Investigation of time-resolved volumetric MRI to enhance MR-guided radiotherapy of moving lung tumors

Moritz Rabe

SIGILL · UNIVERSITAT · LUDOVIC · MAXIM ·

München 2021

Investigation of time-resolved volumetric MRI to enhance MR-guided radiotherapy of moving lung tumors

Moritz Rabe

Dissertation
an der Fakultät für Physik
der Ludwig-Maximilians-Universität
München

vorgelegt von
Moritz Rabe
aus Berlin

München, den 26.10.2021

Erstgutachterin: Prof. Dr. rer. nat. Katia Parodi
Zweitgutachterin: Prof. Dr. rer. nat. Daniela Thorwarth
Tag der mündlichen Prüfung: 10.01.2022

Zusammenfassung

In der Photonenstrahlentherapie von Lungenkrebs führen atembedingte Bewegungen zu systematischen und statistischen Unsicherheiten während Bestrahlungsplanung und Dosisapplikation. Durch die Integration der Magnetresonanztomographie (MRT) in den Bestrahlungsplanungsprozess in der MR-geführten Strahlentherapie (MRgRT) können diese Unsicherheiten im Vergleich zu modernen röntgenbasierten Ansätzen reduziert werden. Weiterhin ermöglichen integrierte MR-Linearbeschleuniger (MR-Linacs) eine genauere und präzisere Dosisapplikation durch tägliche Adaptionen des Bestrahlungsplans und Echtzeit-MRT-basierte gegatete Bestrahlung. Das Potential MRgRT bewegter Zielvolumina wird jedoch aufgrund des Mangels an zeitaufgelöster vierdimensionaler MRT (4D-MRI) in der klinischen Anwendung derzeit noch nicht voll ausgeschöpft. Ziel dieser Arbeit war es, neue Methoden zur Bewegungscharakterisierung und -abschätzung mittels 4D-MRI für MRgRT von Lungenkrebs zu entwickeln und experimentell zu validieren. Konzepte für alle Phasen des klinischen Arbeitsablaufs – Bestrahlungsplanung, Dosisapplikation und retrospektive Analyse – wurden untersucht.

Zunächst wurde eine neue Methode zur Definition des *internal target volume* (ITV) während der Bestrahlungsplanung entwickelt, die auf der Aufenthaltswahrscheinlichkeit bewegter Tumoren basiert. Diese wurde aus 4D-MRI-Aufnahmen in Echtzeit abgeleitet. Die Fähigkeit der ITVs, die im Laufe mehrerer Wochen auftretenden Veränderungen zu antizipieren, wurde anhand retrospektiver geometrischer Analysen von Lungenkrebspatientendaten bewertet. Im Vergleich zu konventionellen, 4D-Computertomographie (4D-CT) basierten Zielvolumina, wurde eine höhere Robustheit der wahrscheinlichkeitsbasierten, 4D-MRI-abgeleiteten ITVs festgestellt. Die Studie zeigte, dass die durch 4D-MRI in Echtzeit ermöglichte Bewegungscharakterisierung über längere Zeiträume systematische und statistische Unsicherheiten im Vergleich zu heutigen Standardverfahren verringern kann.

Weiterhin wurde eine experimentelle Validierung einer veröffentlichten Methode zur Bewegungsschätzung – der Propagationsmethode – unter realistischen, patientenähnlichen Bedingungen mit einem Schweinelungenphantom durchgeführt. Geschätzte 4D-MRIs mit einer zeitlichen Auflösung von 3,65 Hz wurden auf Grundlage orthogonaler 2D cine-MRT-Aufnahmen erstellt, die mit der Scannereinheit eines MR-Linacs aufgenommen wurden. Der Vergleich dieser Datensätze mit *ground truth* atemphasenkorrelierten 4D-MRIs in geometrischen Analysen zeigte, dass die Propagationsmethode akkurate geschätzte 4D-MRIs erzeugen kann. In Zukunft könnte diese Methode Lokalisierungsfehler der Zielvolumina verringern und eine Bewegungsüberwachung in 3D während der Dosisapplikation am MR-Linac ermöglichen.

Schließlich wurde die Propagationsmethode erweitert, um kontinuierliche zeitaufgelöste geschätzte synthetische CTs (tresCTs) zu erzeugen. Die entwickelte Methode wurde experimentell mit aufeinanderfolgenden Aufnahmen des Schweinelungenphantoms an einem CT-Scanner und einem MR-Linac getestet. Geometrische und dosimetrische Analysen zeigten hohe Übereinstimmungen der Bilder und der entsprechenden Dosisverteilungen zwischen den tresCTs und gemessenen *ground truth* 4D-CTs. Die tresCTs könnten für die zeitaufgelöste Rekonstruktion der applizierten Dosis nach der Bestrahlung verwendet werden, um künftig darauf basierende Adaptionen des Bestrahlungsplans zu ermöglichen.

Diese Studien stellen wichtige Schritte in Richtung einer klinischen Anwendung zeitaufgelöster 4D-MRI-Methoden in der MRgRT von Lungentumoren in naher Zukunft dar.

Abstract

In photon radiotherapy of lung cancer, respiratory-induced motion introduces systematic and statistical uncertainties in treatment planning and dose delivery. By integrating magnetic resonance imaging (MRI) in the treatment planning process in MR-guided radiotherapy (MRgRT), uncertainties in target volume definition can be reduced with respect to state-of-the-art X-ray-based approaches. Furthermore, MR-guided linear accelerators (MR-Linacs) offer dose delivery with enhanced accuracy and precision through daily treatment plan adaptation and gated beam delivery based on real-time MRI. Today, the potential of MRgRT of moving targets is, however, not fully exploited due to the lack of time-resolved four-dimensional MRI (4D-MRI) in clinical practice. Therefore, the aim of this thesis was to develop and experimentally validate new methods for motion characterization and estimation with 4D-MRI for MRgRT of lung cancer. Different concepts were investigated for all phases of the clinical workflow – treatment planning, beam delivery, and post-treatment analysis.

Firstly, a novel internal target volume (ITV) definition method based on the probability-of-presence of moving tumors derived from real-time 4D-MRI was developed. The ability of the ITVs to prospectively account for changes occurring over the course of several weeks was assessed in retrospective geometric analyses of lung cancer patient data. Higher robustness of the probabilistic 4D-MRI-based ITVs against interfractional changes was observed compared to conventional target volumes defined with four-dimensional computed tomography (4D-CT). The study demonstrated that motion characterization over extended times enabled by real-time 4D-MRI can reduce systematic and statistical uncertainties associated with today's standard workflow.

Secondly, experimental validation of a published motion estimation method – the propagation method – was conducted with a porcine lung phantom under realistic patient-like conditions. Estimated 4D-MRIs with a temporal resolution of 3.65 Hz were created based on orthogonal 2D cine MRI acquired at the scanner unit of an MR-Linac. A comparison of these datasets with ground truth respiratory-correlated 4D-MRIs in geometric analyses showed that the propagation method can generate geometrically accurate estimated 4D-MRIs. These could decrease target localization errors and enable 3D motion monitoring during beam delivery at the MR-Linac in the future.

Lastly, the propagation method was extended to create continuous time-resolved estimated synthetic CTs (tresCTs). The proposed method was experimentally tested with the porcine lung phantom, successively imaged at a CT scanner and an MR-Linac. A high agreement of the images and corresponding dose distributions of the tresCTs and measured ground truth 4D-CTs was found in geometric and dosimetric analyses. The tresCTs could be used for post-treatment time-resolved reconstruction of the delivered dose to guide treatment adaptations in the future.

These studies represent important steps towards a clinical application of time-resolved 4D-MRI methods for enhanced MRgRT of lung tumors in the near future.

Contents

List of Figures

List of Tables

List of Abbreviations

AP	**A**nterior-**P**osterior
ART	**A**daptive **R**adiation **T**herapy
bSSFP	**b**alanced **S**teady **S**tate **F**ree **P**recession
CAD	**C**omputer-**A**ided **D**esign
CBCT	**C**one-**B**eam **C**omputed **T**omography
CNN	**C**onvolutional **N**eural **N**etwork
CPE	**C**harged **P**article **E**quilibrium
CPU	**C**entral **P**rocessing **U**nit
CT	**C**omputed **T**omography
CTV	**C**linical **T**arget **V**olume
DIR	**D**eformable **I**mage **R**egistration
DVF	**D**eformation **V**ector **F**ield
DVH	**D**ose-**V**olume **H**istogram
DSC	**D**ice **S**imilarity **C**oefficient
DSV	**D**iameter of **S**pherical **V**olume
EPID	**E**lectronic **P**ortal **I**maging **D**evice
FFF	**F**lattening-**F**ilter-**F**ree
FID	**F**ree **I**nduction **D**ecay
FOV	**F**ield **O**f **V**iew
GPU	**G**raphics **P**rocessing **U**nit
GRAPPA	**G**ene**R**alized **A**utocalibrating **P**artially **P**arallel **A**cquisition
GRE	**G**radient **R**ecalled **E**cho
GTV	**G**ross **T**umor **V**olume
HU	**H**ounsfield **U**nit
ICRU	**I**nternational **C**ommission on **R**adiation **U**nits and Measurements
IGRT	**I**mage **G**uided **R**adiation **T**herapy
IMRT	**I**ntensity-**M**odulated **R**adiation **T**herapy
IS	**I**nferior-**S**uperior
ITV	**I**nternal **T**arget **V**olume
MI	**M**utual **I**nformation
midV	**mid-V**entilation target volume
MLC	**M**ulti**L**eaf **C**ollimator
MRgRT	**M**agnetic **R**esonance imaging-**g**uided **R**adio**T**herapy
MRI	**M**agnetic **R**esonance **I**maging
MSE	**M**ean **S**quared **E**rror
NIST	**N**ational **I**nstitute of **S**tandards and **T**echnology
NMR	**N**uclear **M**agnetic **R**esonance
NSCLC	**N**on-**S**mall **C**ell **L**ung **C**ancer
NTCP	**N**ormal **T**issue **C**omplication **P**robability
OAR	**O**rgan **A**t **R**isk
PET	**P**ositron **E**mission **T**omography
POP	**P**robability-**O**f-**P**resence
PRE	**PRE**cision (positive predictive value)

PTV	**P**lanning **T**arget **V**olume
QA	**Q**uality **A**ssurance
QUANTEC	**QU**antitative **A**nalysis of **N**ormal **T**issue **E**ffects in the **C**linic
RF	**R**adio**F**requency
RL	**R**ight-**L**eft
SBPT	**S**tereotactic **B**ody **P**roton **T**herapy
SBRT	**S**tereotactic **B**ody **R**adio**T**herapy
SE	**S**pin **E**cho (Chapter 2)
SE	**SE**nsitivity (true positive rate; Chapter 4)
SENSE	**SENS**itivity **E**ncoding
SI	**S**uperior-**I**nferior
SNR	**S**ignal-to-**N**oise **R**atio
TCP	**T**umor **C**ontrol **P**robability
tresCT	**t**ime-**r**esolved **e**stimated **s**ynthetic **CT**
TWIST	**T**ime-resolved angiography **W**ith **I**nterleaved **S**tochastic **T**rajectories
VMAT	**V**olumetric intensity-**M**odulated **A**rc **T**herapy

Chapter 1

Introduction

With an estimated 19.3 million new cases and 10.0 million deaths per year, cancer is one of the leading causes of death worldwide [1]. Cancer is most commonly treated with surgery, radiotherapy, chemotherapy, immunotherapy, or a combination thereof [2]. Approximately half of all patients receive radiotherapy as part of their treatment [2, 3]. Radiotherapy aims to deposit a sufficiently high radiation dose to the tumor to eliminate all proliferating cancer stem cells while minimizing the radiation-induced damages to the surrounding healthy tissue [4]. Different radiation delivery techniques exist, including brachytherapy and external beam radiotherapy with photons, electrons, protons, or heavy ions [5–9]. Most patients are treated with external photon beam radiotherapy delivered in several fractions over the course of a few days or weeks [10].

Lung cancer is the second most commonly diagnosed cancer type, with an estimated number of 2.2 million annual new diagnoses worldwide (11.4% of all cases) [1]. Owing to the relatively poor five-year overall survival rate ($\sim$20% in Germany [11]), lung cancer is by far the leading cause of cancer mortality (18% of all cancer deaths) [1, 3]. The majority of cases (80–85% [12]) are histologically classified as non-small cell lung cancer (NSCLC). Approximately 20% of NSCLC cases are diagnosed in an early stage before the tumor has spread to regional lymph nodes [13]. The standard-of-care is surgery in these situations, and five-year overall survival rates of 50–70% are reached [14]. However, some patients refuse to undergo surgery, are medically inoperable, or have a high risk for complications due to comorbidities. Stereotactic body radiotherapy (SBRT) has become the standard treatment choice for these patients over the last years [3, 13, 15]. While the current standard treatment for locally advanced NSCLC patients is concurrent chemoradiotherapy with a conventional dose prescription, the feasibility and safety of a combination of chemotherapy and hypofractionated SBRT for these patients are currently under investigation in phase I clinical studies [16–18].

In SBRT, substantially higher doses (up to a factor of 17 for lung SBRT [19]) than in conventional radiotherapy are delivered to the tumor in only a few treatment fractions [2, 13]. Consequently, radiation dose delivery with high accuracy and precision is crucial to avoid underdosage of the tumor, which would result in a reduced local control probability [4]. At the same time, the dose to surrounding healthy tissues has to be minimized to limit the risk of acute and late toxicities [2, 20]. This is particularly challenging for lung SBRT, where the target and organs at risk (OARs) can move by up to several centimeters due to respiratory and cardiac motion [4, 21]. Critical organs such as the trachea, esophagus, heart, and spinal cord can be located in the proximity of lung tumors [3]. Furthermore, anatomical changes, such as tumor shrinkage, patient weight loss, pleural effusion, or atelectasis between treatment fractions frequently occur [13, 21, 22], causing an offset between the initially planned and actually delivered dose distribution [21].

There have been several important technological developments in radiotherapeutic treatment planning, patient positioning, imaging, and beam delivery over the last decades. This includes the clinical introduction of inverse treatment planning, intensity-modulated radiotherapy (IMRT), four-dimensional computed tomography (4D-CT) imaging, image-guided radiotherapy (IGRT) based on daily acquired volumetric in-room imaging data, and motion management techniques such as respiratory gating [4, 15]. These key technologies have allowed a safe and precise deposition of highly conformal dose distributions in lung SBRT [2, 3, 20], where similar survival rates compared to those after surgery are now achieved [23–25].

Another major technological advancement in radiation oncology in the last decade was the clinical introduction of the MR-Linac – an imaging and treatment delivery system that combines a magnetic resonance imaging (MRI) scanner with a medical linear accelerator (linac) for MR-guided radiotherapy (MRgRT) with photons [20]. Today, two MR-Linac devices are commercially available, and two further systems are under investigation and development at academic research centers [26–29]. The outstanding features of MR-Linacs compared to conventional linacs are the potential for higher target delineation accuracy enabled by the enhanced soft tissue contrast of MRI, the possibility to adapt the treatment plan based on the observed anatomy of the day, and the capability of gated beam delivery based on motion information obtained with real-time MRI during patient irradiation [4, 13, 30]. The combination of these features enables the safe delivery of highly conformal dose distributions with unprecedented accuracy and precision. This allows the definition of smaller safety margins around the target than used for treatments at conventional linacs, which in turn enables target dose escalation or sparing of dose to OARs [20, 31]. The ability to continuously monitor and account for target motion renders the MR-Linac especially well suited for SBRT treatments of lung tumors [13, 15].

MR-guided lung SBRT patient treatments only started a few years ago [32], and data are still being compiled to test the hypothesis that stereotactic MR–guided online adaptive radiotherapy can achieve higher local control rates or lower toxicities compared to SBRT with conventional linacs. Therefore, clinical evidence – ideally obtained from randomized controlled clinical trials – that would justify the higher costs and workload associated with MRgRT is still lacking to date [15]. Nevertheless, first clinical reports showed promising results suggesting that high ablative doses can be delivered with low rates of high-grade toxicity, even to challenging sites such as central or ultracentral lung tumors [33, 34] in few [35] or even single fractions [19].

After over two decades of research and development by academic institutions and companies [36–38], important technological challenges and open medical physics research questions related to MRgRT in general, and MR-guided lung tumor treatments in particular, remain [30, 31, 39]. One of the main challenges that hinders the exploitation of the full theoretical potential of MR-Linacs in clinical practice is the lack of imaging sequences for continuous real-time motion monitoring of the patient anatomy in 3D with high temporal and spatial resolution [40, 41]. The topic of this thesis is temporally resolved volumetric MRI (commonly referred to as 4D-MRI) for characterization and estimation of target motion in MRgRT of lung tumors [31, 40, 41]. The aim of this dissertation was to contribute to the active field of 4D-MRI for MRgRT research by conducting three experimental and computational studies, each focused on a different phase of the radiotherapeutic workflow: the treatment planning phase before patient irradiation (Chapter 4), during (Chapter 5), and after beam delivery at the MR-Linac (Chapter 6).

While the number of clinically operational MR-Linacs is rapidly increasing [42, 43], the vast majority of patients is still treated at conventional linacs. At the same time, more and more radiation oncology departments have access to MRI scanners [44]. The aim of the study presented in Chapter 4 was to investigate whether a 4D-MRI-based internal target volume (ITV) definition can yield more representative and robust target volumes for treatments at conventional linacs than achievable with today's standard 4D-CT-based approaches. A probabilistic ITV definition based on the probability-of-presence distribution of moving lung tumors characterized with real-time 4D-MRI is proposed to prospectively account for inter- and intrafractional changes in the treatment planning phase. The suggested approach is compared to conventional 4D-CT-based target volume definition concepts in a retrospective geometrical analysis of data from three lung cancer patients scanned at a diagnostic MRI scanner over the course of several weeks.

One of the two currently commercially available MR-Linac systems – the MRIdian by ViewRay [26] – was installed at the Department of Radiation Oncology at the University Hospital, LMU Munich, and patient treatments started in January 2020. Time-resolved MRI during beam delivery at this system is currently limited to 2D planes [45]. Therefore, no information about potential through-plane motion of the target and OARs in the thorax can be derived from these images. While real-time 4D-MRI could decrease the target localization error and enable time-resolved motion monitoring in 3D, these sequences are currently not offered by the vendor due to technical limitations [31]. This has motivated several research groups to develop methods to create so-called estimated 4D-MRI based on time-resolved 2D MRI data [40]. One of these methods, the propagation method by Paganelli et al. [46], achieved the highest target tracking accuracy among several compared techniques in an *in silico* study [47]. However, this method has thus far only been tested with computational phantoms and sample patient data. The aim of the research study presented in Chapter 5 was to adapt the propagation method for use at the ViewRay MRIdian MR-Linac and to perform validation measurements and a geometric accuracy assessment of the adapted method with a porcine lung phantom [48]. This phantom allows the acquisition of reproducible ground truth data, therefore, enabling the lacking experimental validation of the propagation method under realistic patient-like conditions.

To fully exploit the potential of MRgRT treatments at MR-Linacs, the treatment plan needs to be adapted between consecutive treatment fractions or within the treatment fraction itself based on the actually delivered dose [49]. For this dose reconstruction, linac logfiles and time-resolved volumetric synthetic CT data are needed [50]. These imaging data are currently not available at the ViewRay MRIdian MR-Linac due to the 2D restriction of the cine MRI data acquired during beam delivery [45]. The aim of the research study presented in Chapter 6 was to create continuous time-resolved estimated synthetic CTs (tresCTs) for this purpose by extending the propagation method by Paganelli et al. [46]. The follow-up project to the study presented in Chapter 5 included an experimental validation with measurements at a CT scanner and a MRIdian MR-Linac with the porcine lung phantom. The tresCTs generated with the proposed methodology were compared to measured ground truth 4D-CT datasets to assess the geometric and dosimetric accuracy.

The thesis is structured in the following way: Chapter 2 introduces the physical and technological background of photon radiotherapy, X-ray-based imaging modalities, and MRI. Furthermore, image registration and motion management techniques for application in radiotherapy are explained. MRgRT is reviewed in depth in Chapter 3, with a special focus on the MR-Linac, 4D-MRI, and motion modeling techniques. The research studies conducted in the scope of this thesis are presented in Chapters 4–6. The retrospective proof-of-concept study on real-time 4D-MRI-based ITV definition is described in Chapter 4. Chapter 5 presents the experimental validation study of the propagation method, conducted with the porcine lung phantom at a low-field MR-Linac. The follow-up study on the creation and experimental validation of tresCTs is described in Chapter 6. The thesis is concluded by Chapter 7, where the main research findings are summarized, and future research perspectives are outlined.

Chapter 2

Fundamentals of imaging modalities and photon radiotherapy

This chapter summarizes the principal physical, technological and clinical aspects of tomographic imaging modalities, image registration, and radiotherapy with photons. Firstly, section 2.1 introduces the interaction processes of X-ray photons with matter, followed by a definition of the absorbed dose D. In section 2.2, the X-ray-based imaging modalities computed tomography and cone-beam computed tomography are described. The fundamental physical principles of nuclear magnetic resonance and the technical implementation of MRI are explained in section 2.3. In radiotherapy, the images acquired with different modalities or at different time points have to be registered to combine the complementary image information. For this purpose, image registration is used, which is introduced in section 2.4. Section 2.5 gives an overview of the different workflow steps of photon radiotherapy treatment planning. The chapter is concluded by section 2.6, where a description of motion management and image guidance techniques used in modern radiotherapy is given.

2.1 Physical interaction of X-ray photons with matter

When X-ray photons [51] with energies used for imaging (20–150 keV; section 2.2) and photon radiotherapy (up to 6–15 MeV; section 2.5) pass through matter, such as patient tissue, the main physical interactions that occur are Rayleigh scattering, photoelectric absorption, Compton scattering, pair production, and photonuclear interactions [52].

Common to all of these processes is their stochastic nature, characterized by single interactions in which the photons either scatter elastically (Rayleigh scattering) or transfer a fraction or all of their energy to secondary particles. Secondary charged particles, such as electrons, subsequently deposit their kinetic energy through many small Coulomb-force interactions in the absorbing material, resulting in the ionization of atoms along the particles' paths. Therefore, photons are classified as indirectly ionizing radiation [6].

The number of photons contained in a beam can be quantified by the fluence Φ [52]:

$$\Phi = \frac{\mathrm{d}N}{\mathrm{d}A} \qquad [\Phi] = \mathrm{m}^{-2}, \tag{2.1}$$

where $\mathrm{d}N$ denotes the number of photons incident on a sphere of cross-sectional area $\mathrm{d}A$. For a parallel beam of monoenergetic photons traveling through a homogeneous medium, the interaction probability between a photon and the medium is constant per unit length. Through each of the five interaction processes listed above, photons are either scattered away from their original path or are absorbed. The fluence of the primary beam after passing through an absorber with thickness d is then described by an exponential decay, the *Lambert-Beer's law* [10]:

$$\Phi(d) = \Phi_0 \cdot \exp(-\mu d) \qquad [\mu] = \mathrm{m}^{-1}, \tag{2.2}$$

where Φ_0 is the original fluence impinging on the absorber and μ is the *linear attenuation coefficient*. Defining $x = \rho \cdot d$ as the mass thickness of a material with mass density ρ and thickness d, Equation 2.2 can be rewritten as [53]:

$$\Phi(x) = \Phi_0 \cdot \exp\left(-\frac{\mu}{\rho}x\right) \qquad \left[\frac{\mu}{\rho}\right] = \mathrm{m}^2\,\mathrm{kg}^{-1} \qquad [x] = \mathrm{kg}\,\mathrm{m}^{-2}\,, \tag{2.3}$$

where μ/ρ is the *mass attenuation coefficient*, which depends on the photon energy E_γ and the absorbing material. The interaction probability for a specific process is proportional to the cross section σ [10]:

$$\sigma = \frac{N_{\mathrm{int}}}{\Phi} \qquad [\sigma] = \mathrm{barn} = 10^{-28}\,\mathrm{m}^2, \tag{2.4}$$

with the number of interacting photons N_{int} per fluence Φ. The total mass attenuation coefficient is proportional to the total cross section of all possible processes, σ_{tot} [54]:

$$\frac{\mu}{\rho} = \frac{N_A}{A}\,\sigma_{\mathrm{tot}}\,, \tag{2.5}$$

where N_A is the Avogadro number, and A is the atomic mass number of the absorber material. Figure 2.1 depicts the interaction-specific mass attenuation coefficients in the energy range relevant for X-ray imaging modalities and photon radiotherapy for the absorber materials water and cortical bone.

During Rayleigh scattering, the photon elastically scatters with an atom, and no energy is transferred. Photonuclear interactions, where an atomic nucleus absorbs the photon, only become physically possible above energies of a few MeV. For Rayleigh scattering and photonuclear interactions, the mass attenuation coefficients for X-ray photons for materials with low atomic numbers – as found in patient tissue – are one to several orders of magnitude smaller than for the remaining interaction processes [52, 53]. For a thorough description of these interactions, the interested reader is referred to the textbook by Attix [52].

With the mass attenuation coefficients for photoelectric absorption (τ/ρ), Compton scattering (σ_C/ρ), and pair production (κ/ρ) the total mass attenuation coefficient in Equation 2.5 can be approximated by [52]:

$$\frac{\mu}{\rho} \approx \frac{\tau}{\rho} + \frac{\sigma_C}{\rho} + \frac{\kappa}{\rho}\,. \tag{2.6}$$

The mechanisms of these three dominating physical interactions are schematically depicted in Figure 2.2 and described in the following sections.

2.1.1 Photoelectric absorption

In the photoelectric absorption, first described by Einstein in 1905 [55], a photon is absorbed by a bound electron of an atom of the transversed material (Figure 2.2a). The atom is ionized through this process, and the photoelectron leaves the atom with a kinetic energy T_{e^-} equivalent to the photon energy E_γ, reduced by the binding energy E_b of the electron and negligible kinetic energy that is transferred to the atom T_a [52]:

$$T_{e^-} = E_\gamma - E_b - T_a \approx E_\gamma - E_b\,. \tag{2.7}$$

Therefore, the photon energy must be larger than the binding energy for the process to be possible to occur. In combination with the decreasing interaction probability for increasing photon energies [52], this leads to characteristic edges of the photoelectric mass

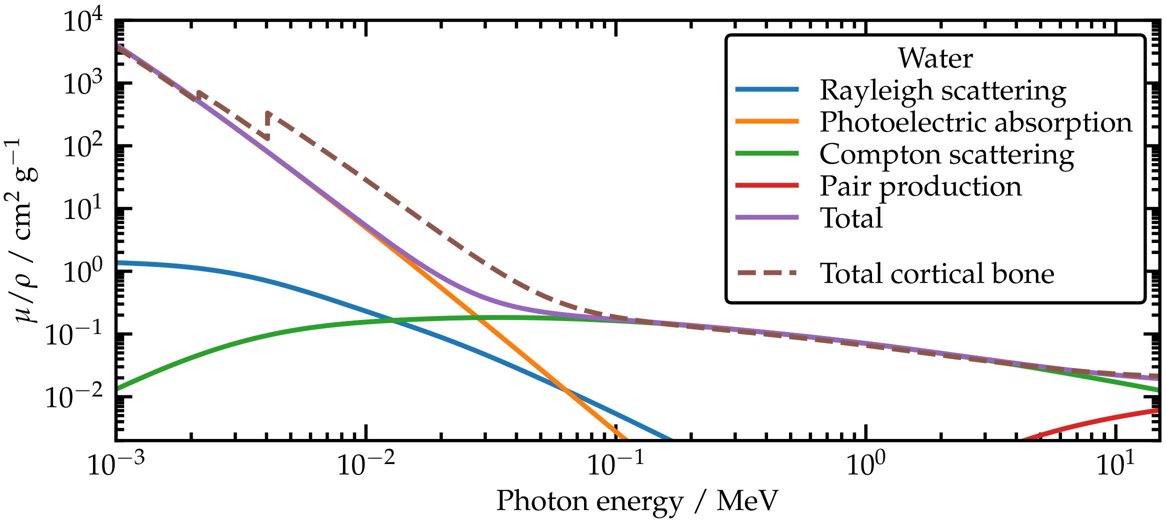

FIGURE 2.1: **Mass attenuation coefficients for water and bone.** The mass attenuation coefficients for the different interaction processes of X-ray photons with water are plotted against the photon energy (photonuclear interactions are not shown here). The total mass attenuation coefficient for cortical bone is additionally drawn as a dashed line. The data was retrieved from the XCOM database by the National Institute of Standards and Technology (NIST) [53].

attenuation coefficient, as observable for cortical bone in Figure 2.1. The photoelectric mass attenuation coefficient (τ/ρ) rapidly decreases with the photon energy E_γ and strongly increases with an increasing atomic number Z of the absorber material [6]. For photons with $E_\gamma < 20\,\text{keV}$, where the photoelectric effect is the dominating interaction process for water (cf. Figure 2.1) [6, 53], the proportionalities can be approximated by [52]:

$$\frac{\tau}{\rho} \propto \frac{Z^3}{E_\gamma^3}\,. \tag{2.8}$$

For increasing photon energies, the photoelectrons are primarily emitted in the forward direction, where they deposit their energy by further ionization of atoms [52]. The photoelectric effect is followed by the emission of characteristic X-radiation and Auger electrons when the photoelectron vacancies are filled with electrons from outer shells [6].

2.1.2 Compton scattering

The binding energy of electrons for low-Z material atoms is small compared to the energy of X-ray photons in the keV–MeV range. Therefore, the electrons can be regarded as loosely bound or quasi-free [52]. In Compton scattering (Figure 2.2b), a photon scatters with such a quasi-free electron [57]. Depending on the scattering angle ϑ relative to the incident photon's direction, the X-ray photon experiences a wavelength shift $\Delta\lambda$ of [10]:

$$\Delta\lambda = \frac{h}{m_\mathrm{e}c}(1-\cos\vartheta) = \lambda_\mathrm{C}(1-\cos\vartheta)\,, \tag{2.9}$$

with the *Compton wavelength* λ_C. The lost energy is transferred to kinetic energy of the recoiling electron. Since the total energy and momentum of the photon-electron system have to be conserved, the scattering angle of the photon, ϑ, and recoil electron, ϕ, are correlated, with $\vartheta \in [0^\circ, 180^\circ]$ and $\phi \in [0^\circ, 90^\circ]$ [52]:

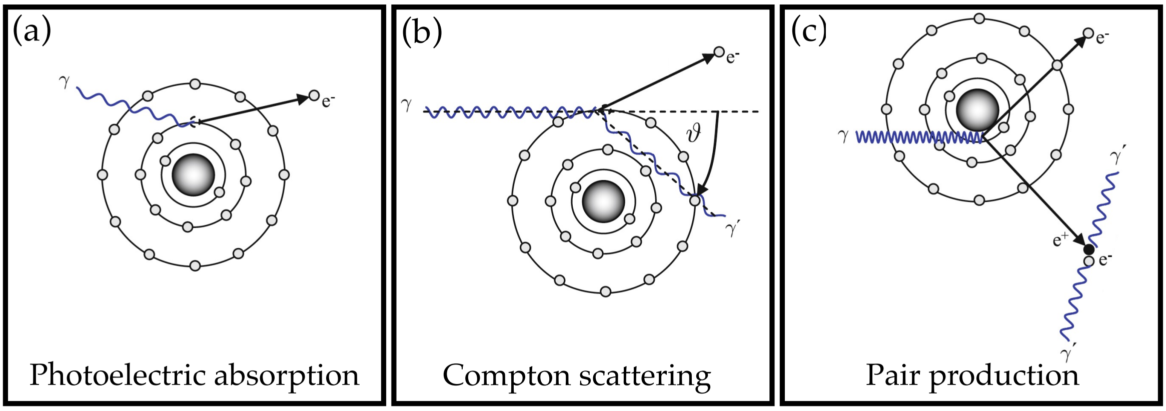

FIGURE 2.2: **Dominant photon-matter interactions.** The most relevant interaction processes for X-ray imaging and photon radiotherapy are schematically depicted. (a) Photoelectric absorption with incoming photon γ and emitted electron e^-. (b) Compton scattering with incoming photon γ, outgoing electron e^- and gamma γ' with scatter angle ϑ. (c) Pair production with incoming photon γ, outgoing electron e^- and positron e^+ and two annihilation photons γ'. Figure adapted from [56].

$$\cot\phi = \left(1 + \frac{E_\gamma}{m_0 c^2}\right)\tan\left(\frac{\vartheta}{2}\right) . \tag{2.10}$$

The maximum energy transfer occurs for $\vartheta = 180°$, i.e., when the photon is scattered in backward and the electron in forward direction with an energy of $m_e c^2/2 = 255.5\,\text{keV}$. The energy-dependent differential cross section for photon scattering at an angle ϑ per unit solid angle and per electron is described by the *Klein-Nishina formula* [58], derived from quantum electrodynamics [52]:

$$\frac{\mathrm{d}\sigma_\mathrm{e}}{\mathrm{d}\Omega} = \frac{r_0^2}{2}\left(\frac{E'_\gamma}{E_\gamma}\right)^2\left(\frac{E_\gamma}{E'_\gamma} + \frac{E'_\gamma}{E_\gamma} - \sin^2\vartheta\right), \tag{2.11}$$

with the energy of the scattered photon [52]:

$$E'_\gamma = \frac{E_\gamma}{1 + \frac{E_\gamma}{m_0 c^2}(1 - \cos\vartheta)}, \tag{2.12}$$

and the *classical electron radius* [52]:

$$r_0 = \frac{e^2}{m_0 c^2} . \tag{2.13}$$

The Klein-Nishina formula describes that the relative probability for small photon scattering angles ϑ increases for increasing photon energies.

The Klein-Nishina cross section per atom, σ_a, scales with the number of electrons per atom and thus, the atomic number Z:

$$\sigma_a = Z \cdot \sigma_\mathrm{e} . \tag{2.14}$$

With Equation 2.5, the mass attenuation coefficient for Compton scattering is given by [52]:

$$\frac{\sigma_\mathrm{C}}{\rho} = \frac{N_A Z}{A}\sigma_\mathrm{e} , \tag{2.15}$$

with the Avogadro constant N_A, atomic number Z, and atomic mass number A. For atoms contained in the human body (with exception of hydrogen), Z/A ranges between 0.4 and 0.5, and thus the mass attenuation coefficient is approximately independent of Z [52].

Compton scattering is the dominant interaction of radiotherapeutic photons with energies between 20 keV–10 MeV (cf. Figure 2.1) [53]. In this energy range, the Compton scattering mass attenuation coefficient (σ_C/ρ) decreases with increasing photon energy [6].

After the scattering process, the scattered photon and electron can undergo further interactions with the transversed material. As for the photoelectric absorption, the Compton scattering process can be followed by the emission of characteristic X-radiation and Auger electrons [6].

2.1.3 Pair production

The third important interaction process is pair production (Figure 2.2c), which was first experimentally observed for cosmic rays by Blackett and Occhialini in 1933 [59]. In the Coulomb force field near an atomic nucleus, the photon is converted to an electron-positron pair with kinetic energies $T_{m_{e^-}}$ and $T_{m_{e^+}}$ [52]:

$$E_\gamma = 2m_e c^2 + T_{m_{e^-}} + T_{m_{e^+}} = 1.022\,\text{MeV} + T_{m_{e^-}} + T_{m_{e^+}}. \tag{2.16}$$

A negligible amount of the photon energy E_γ is transferred to kinetic energy of the nucleus. For this process to occur, the photon needs a minimum energy of $2m_e c^2 = 1.022\,\text{MeV}$, i.e., twice the rest mass of an electron m_e or positron, respectively. To conserve the momentum of the incident photon, the angle ϕ between the original photon direction and the outgoing directions of the electron or positron, respectively, is [52]:

$$\phi \approx \frac{2m_e c^2}{T_{m_{e^-}} + T_{m_{e^+}}} = \frac{2m_e c^2}{E_\gamma - 2m_e c^2} \qquad [\phi] = \text{rad}. \tag{2.17}$$

For increasing photon energies E_γ, the angle ϕ decreases, and the electron and positron are emitted increasingly in the forward direction.

In the photon energy range relevant for imaging and radiotherapy, the pair production mass attenuation coefficient (κ/ρ) roughly increases logarithmically with the photon energy [52]. Furthermore, with the approximation $Z/A \approx$ const. introduced above, κ/ρ is proportional to the atomic number of the material Z [6]:

$$\frac{\kappa}{\rho} \propto Z \log(E_\gamma). \tag{2.18}$$

In radiotherapy, the mass attenuation coefficient of pair production in water and tissue is only of relevance for therapeutic photons with high energies ($E_\gamma > 10\,\text{MeV}$) [6]. Pair production can also occur in the Coulomb force field of an electron (*triplet production*) [52]. Since the minimal required photon energy for this process is $4m_e c^2 = 2.044\,\text{MeV}$ and κ/ρ for triplet production is about one order of magnitude smaller than for pair production (for $E_\gamma > 5\,\text{MeV}$ in water [53]), this effect is of minor importance for radiotherapeutic photons [52].

After the pair production, the electron deposits its kinetic energy in the absorber. The positron is slowed down in Coulomb scattering processes and can form a positronium system with an electron. The positron then undergoes an annihilation process with an electron, where typically two 511 keV photons are emitted in approximately opposite directions. The angular emission distribution depends on the residual momentum of the positronium system. The annihilation quanta can in turn undergo interactions with the absorber material [10, 56].

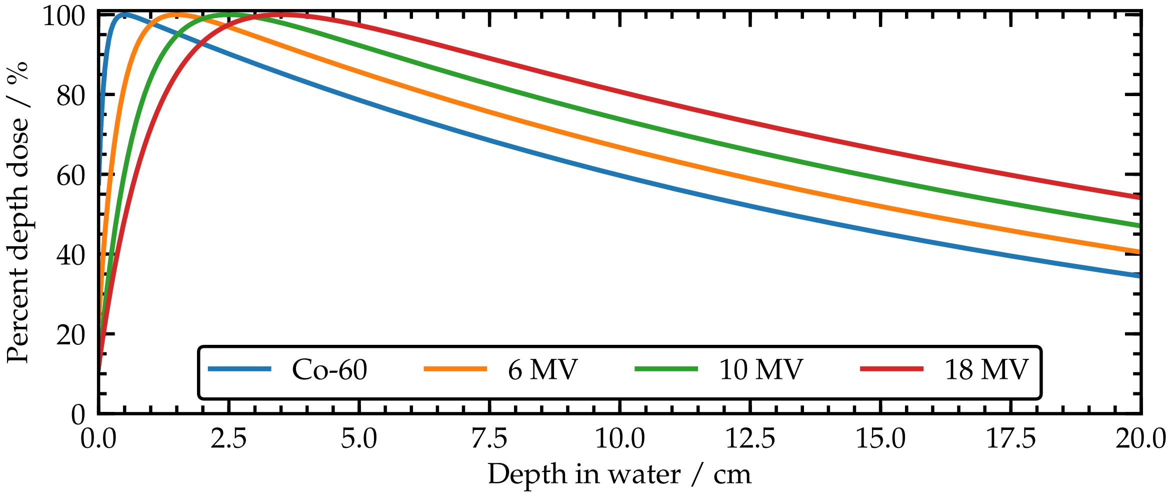

FIGURE 2.3: **Depth-dose curves for photon beams in water.** The percent depth dose curves relative to their maximum are plotted as a function of depth in water for a Cobalt-60 beam and photon beams produced with linacs at four different acceleration voltages (6, 10, and 18 MV). The data was obtained with the analytical expression described in [60] and parameters derived from Table 6.4 in [6].

2.1.4 Definition of dose

Through the interaction processes described above, the energy of the primary photons is transferred to secondary charged particles, which subsequently further deposit their energy in a medium, such as patient tissue. To simulate a radiotherapeutic treatment plan and predict the outcome of such a treatment, a metric is needed that links a physically measurable quantity related to the energy deposition to an observable clinical effect. The most important metric in radiotherapy that is used for these purposes is the absorbed energy *dose* D [10]:

$$D = \frac{\mathrm{d}\bar{\varepsilon}}{\mathrm{d}m} = \frac{1}{\rho}\frac{\mathrm{d}\bar{\varepsilon}}{\mathrm{d}V} \qquad [D] = \mathrm{J\,kg^{-1}} = \mathrm{Gy}, \tag{2.19}$$

where $\bar{\varepsilon}$ is the mean energy of ionizing radiation that is absorbed by a medium with mass m, volume V and mass density ρ. The dose is measured in units of Gray (Gy) and is used to prescribe and report radiotherapeutic treatments in a standardized way. It can be indirectly determined through dosimetric measurements and can be accurately simulated in the treatment planning process (section 2.5). Based on clinical studies, predictions of the physiological response of a tissue that is exposed to a dose D can be made [10].

2.1.5 Depth-dose distributions for photons in matter

When a beam of high-energy monoenergetic photons impinges on a thick absorber such as a water phantom, the fluence of the primary photons decreases exponentially along the beam path in the absorber material (Equation 2.2). Due to the two-step process of the dose deposition – the creation of mainly forward-directed secondary electrons in the interaction processes followed by their energy deposition – the dose first increases along the beam path until the *charged particle equilibrium* (CPE) is reached. Beyond the point of the CPE, a *transient CPE* is present, and the deposited dose is described by an exponential decay [10].

The beams produced by medical linacs are polyenergetic (section 2.2.1), where the shape of the energy spectrum depends on the design of the accelerator head (section 2.5.4) and the maximum photon energy is determined by the acceleration voltage of the electrons. Figure 2.3 depicts the depth-dose curves of a Cobalt-60 beam and photon beams produced by a linac (section 2.5.4) along their path in water. The depth of the dose maximum depends, among other factors, on the absorber material and the acceleration voltage of the linac, with increasing depth for increasing mean photon energies. The existence of this so-called *build-up effect* is exploited in radiotherapeutic treatments, where the severity of acute skin reactions can be lowered through a reduction of superficially deposited dose when higher energy photon beams are used. The depth of the dose maximum is generally not deep enough to coincide with the patient's tumor tissue. To reach a considerably higher dose in the target than in the surrounding healthy tissue, the patient is irradiated from many different directions to reach a high cumulative dose in the tumor. The photon beams used in radiotherapy are polychromatic and a patient's body consists of tissues with varying material compositions and densities. Due to the E_γ- and Z-dependency of the mass attenuation coefficient (Figure 2.1), the dose deposition is more complex than in the simple case depicted in Figure 2.3. For this reason, the fluence of the photon beams and the deposited dose in the patient's body have to be modeled accurately in a treatment planning process, which is described in section 2.5 [6, 10, 61].

2.2 X-ray-based imaging modalities

This section describes the physical and technical aspects of computed tomography (CT) and cone-beam computed tomography (CBCT). The images acquired with these modalities contain morphological information about the patient's anatomy needed for cancer diagnosis and accurate patient positioning in IGRT (section 2.6). Furthermore, CT images provide the 3D spatial electron density distributions within the patient's body needed for radiotherapeutic dose calculation and treatment planning (section 2.5). Therefore, today's standard-of-care photon radiotherapy relies on images acquired with these modalities.

2.2.1 X-ray tube and spectrum

The X-ray photons used for CT and CBCT are produced in X-ray tubes, such as sketched in Figure 2.4. Electrons are emitted from a heated cathode and are accelerated towards a target anode to an energy depending on the applied tube voltage. When the electrons are stopped in the anode material, a small fraction ($\sim 1\%$) of their kinetic energy is emitted as X-radiation, whose intensity is proportional to the atomic number Z of the anode material. The remaining 99% of the kinetic energy is dissipated as thermal energy. The anode must be designed to withstand high temperatures and to quickly distribute the heat away from the focal point, where the electrons strike the anode. Tungsten (W), with its high atomic number ($Z = 74$), density ($\rho = 19.3\,\mathrm{g/cm^3}$), melting point ($T_\mathrm{m} = 3422°\mathrm{C}$) and thermal conductivity ($\lambda = 170\,\mathrm{W/(m\,K)}$) is most often used as anode material [56, 62].

When the electrons decelerate and deflect in the Coulomb force field of target nuclei, the lost kinetic energy is emitted as electromagnetic bremsstrahlung. Additionally, the energy of the electrons can be transferred to electrons bound to atoms, which can result in their ionization. After the ionization of target atoms, electrons transition from outer to inner shells, and the energy difference is emitted as target material-specific characteristic X-radiation [52]. Therefore, the emitted spectrum is a superposition of the continuous bremsstrahlung spectrum and the line spectrum of the characteristic X-radiation [56].

Figure 2.5 shows exemplary X-ray spectra emitted from an X-ray tube. Due to inherent filtration in the anode and other X-ray tube components, a major proportion of photons with energies below 10 keV are removed from the spectrum (Figure 2.5a; blue line). Thin aluminum and copper sheets are added in the beam path to filter out the remaining low-energy photons (Figure 2.5a; orange line). Due to the high photoelectric mass attenuation

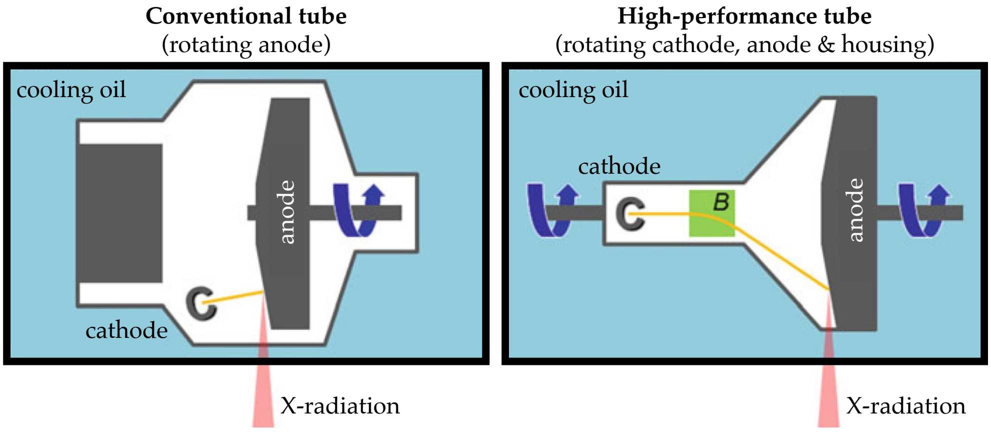

FIGURE 2.4: **Sketch of an X-ray tube.** The main components of a conventional (left) and high-performance (right) tube are depicted. Electrons are liberated in a cathode and accelerated towards a rotating anode. The emitted X-radiation is sketched in red. Cooling oil is needed to prevent the melting of anode material at the focal spot. B: bending magnet. Figure adapted from [10] and [61].

coefficient for low energy X-radiation (cf. section 2.1), these photons would otherwise primarily deposit dose in the patient without improving the image quality since they would not penetrate through the patient [62]. The maximal photon energy in the spectrum is determined by the electron acceleration voltage (Figure 2.5b). Adjusting the tube current leads to a scaling of the whole fluence spectrum (Figure 2.5c) [56, 62]. The choice of these values depends on the composition and spatial extent of the anatomy of interest and the desired image quality and tolerable dose level. Typical values of the acceleration voltage lie between 40–150 kV for diagnostic imaging [62].

2.2.2 Computed tomography (CT)

Computed tomography (CT) is a volumetric quantitative imaging modality based on the attenuation of X-radiation in the transversed material, yielding 3D maps proportional to the attenuation coefficient distribution of the object of interest. Hounsfield described the prototype of a CT scanner in 1973 [64]. Only through the steady increase of computational power in the following decades, CT imaging was established in clinical routine in radiology departments [61]. In radiotherapy, as one of the first steps of every treatment planning process (section 2.5), a CT scan of the anatomy of interest, i.e., the tumor and surrounding healthy tissue, is acquired.

The main technical components of a CT scanner are sketched in Figure 2.6. While the X-ray tube of the CT scanner is rotating around the patient in the axial plane, transmission profiles are acquired by the multi-channel multi-row X-ray detectors mounted on the opposite side of the gantry. At the same time, the patient couch is moved through the bore of the scanner at a constant speed, such that the trajectory of the X-ray tube relative to the patient's body describes a helical path [65]. To quantify this path, the pitch value p is used. It is a scanning protocol-specific parameter that depends on the desired slice thickness and image quality, with typical values between 0.2–1.5 [10], and is defined as [10]:

$$p = \frac{d}{C}, \tag{2.20}$$

where d is the distance that the couch moves during one full rotation of the X-ray tube and C is the collimation of the CT scanner detector array in craniocaudal direction. The pitch value depends on the gantry rotation speed, the couch speed, and the detector design.

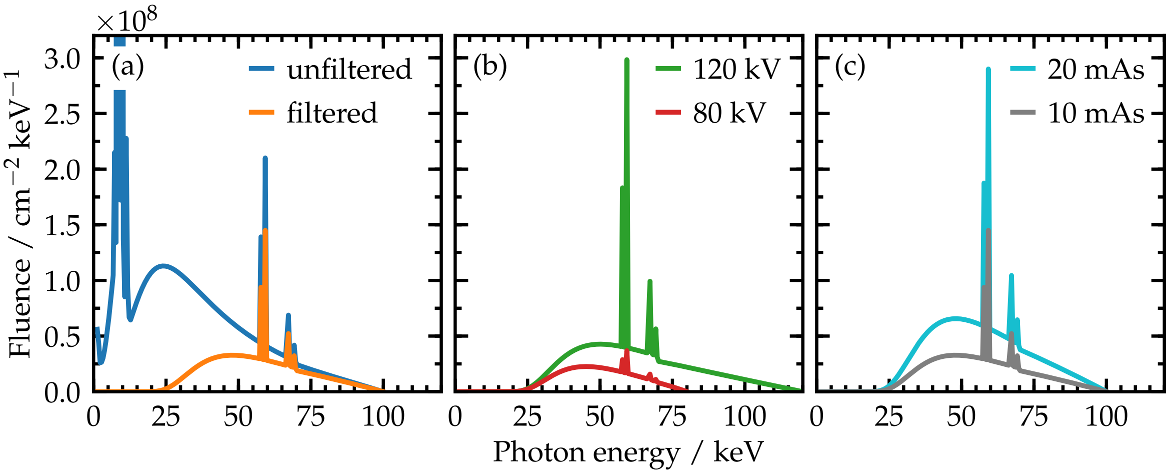

FIGURE 2.5: **Exemplary X-ray spectra.** (a) The effect of filtering the original spectrum (*unfiltered*) with a 1 mm aluminum and 0.2 mm copper sheet (*filtered*) is demonstrated (100 kV; 10 mAs). (b) Filtered spectrum for two different acceleration voltages (80 and 120 kV) and a constant tube current of 10 mAs. (c) Filtered spectrum for two different tube currents (10 and 20 mAs) and a constant acceleration voltage (100 kV). All spectra were created with the Python package spekpy [63], simulating a tungsten anode with tilt angle $\alpha = 12°$.

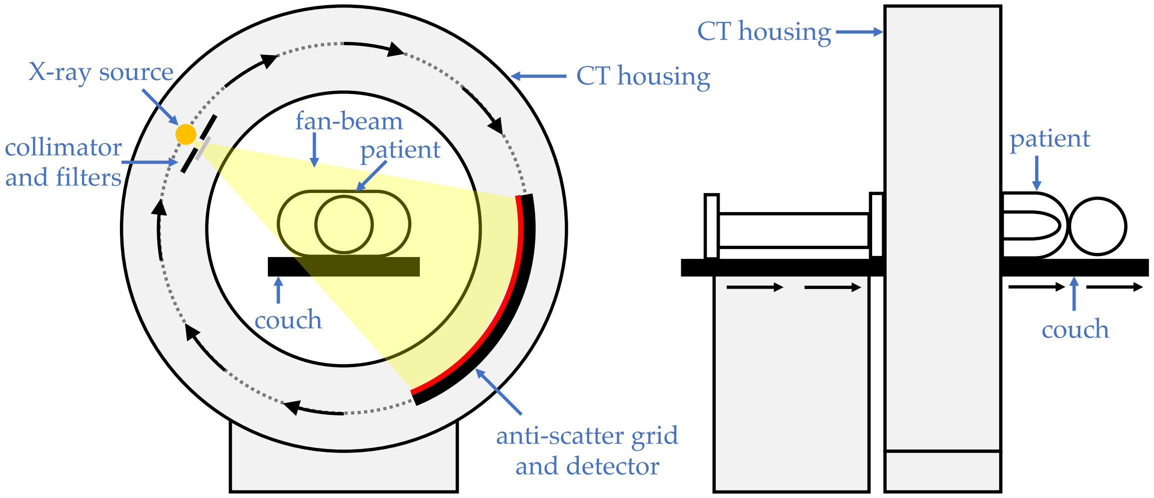

FIGURE 2.6: **Sketch of a CT scanner.** The patient is lying on a couch that is moved through the gantry inside the CT housing at a constant speed. At the same time, an X-ray tube is rotating around the patient, producing a fan beam, which is shaped by collimators and filters in the beam path. After passing through the patient's body, the X-radiation is detected by multi-row multi-channel detectors mounted to the opposite side of the gantry.

During CT scanning, the integral attenuation along straight lines between the focal spot of the X-ray tube and the detector pixels are measured for different slice positions from many different angles [61]. With the typical photon energies between 40–150 keV used for diagnostic imaging [62], the main photon-matter interaction processes are the photoelectric absorption and Compton scattering (cf. section 2.1). Assuming an ideal detector and monoenergetic photons, the intensity I that is measured at a detector pixel is given by the Lambert-Beer's law (cf. Equation 2.2) [61]:

$$I = I_0 \cdot \exp\left(- \int_L \mathrm{d}L \, \mu(x,y,z) \right) , \tag{2.21}$$

where I_0 is the intensity of the beam before entering the patient's body, $\mu(x,y,z)$ describes the 3D spatial distribution of linear attenuation coefficients within the volume of interest, and L is the line that connects the focal spot of the X-ray tube with the detector element. Since a polychromatic X-ray spectrum is used for imaging, in reality, Equation 2.21 is an approximation of the real measured intensity. Defining $p(L)$ as the projection value along the line L, formula 2.21 can be rewritten as [61]:

$$p(L) = -\ln\left(\frac{I(L)}{I_0} \right) = \int_L \mathrm{d}L \, \mu(x,y,z) \, . \tag{2.22}$$

When projections from many different angles covering at least 180° are measured for a fixed slice position, the CT image $f(x,y,z)$, proportional to the attenuation coefficient distribution map $\mu(x,y,z)$, can be derived through image reconstruction [61]. The mathematical foundation of the reconstruction was described by Radon in 1917 [66], long before the invention of the CT scanner. For a single-slice CT scan at slice position z, with the X-ray tube moving on a circular instead of helical path, the image reconstruction can be performed by a *filtered backprojection* [61]:

$$f(x,y,z) = \int_0^{\pi} \mathrm{d}\vartheta \, p(\vartheta,\xi) * k(\xi) \Big|_{\xi = x\cos\vartheta + y\sin\vartheta} \, . \tag{2.23}$$

The angles ϑ and ξ parameterize the position and direction of the line L, where ϑ describes the angle and ξ the distance to the center of rotation of the X-ray tube [10]. In the filtered backprojection, the projection data $p(\vartheta,\xi)$ is convolved with a reconstruction kernel $k(\xi)$, followed by a backprojection into the image domain. The chosen reconstruction kernel determines the sharpness and noise of the reconstructed image. For a spiral CT scan, the projection data must be interpolated at the different longitudinal axial slice positions (*z-interpolation*) [61]. For a thorough mathematical derivation and description, the interested reader is referred to medical physics textbooks [10, 56, 61].

In clinical practice, instead of displaying the linear attenuation coefficient distribution $\mu(x,y,z)$, these values are converted to *CT numbers* in Hounsfield Units (HU), defined as [56]:

$$\mathrm{CT} = \frac{\mu - \mu_{\mathrm{water}}}{\mu_{\mathrm{water}}} \times 1000 \, \mathrm{HU} \, , \tag{2.24}$$

where μ_{water} is the attenuation coefficient of water and μ is the attenuation coefficient of the voxel of interest. The Hounsfield scale is linear and defined such that water has a CT number of 0 HU and air of -1000 HU. The CT numbers depend on the effective atomic number of the absorber material Z, the photon energy E_γ and the mass density ρ. Consequently, the CT number increases with increasing Z and mass density ρ (cf. section 2.1). Due to the markedly different effective Z and ρ of bone, soft, and lung tissue, the contrast of CT images is large

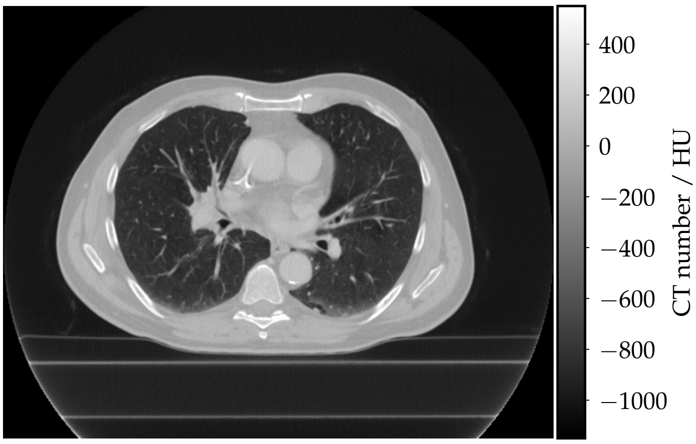

Organ or tissue	CT number
Air	-1000
Lung	-900 to -500
Adipose tissue	-100 to -70
Water	0
Kidney	20 to 40
Pancreas	20 to 50
Blood	30 to 60
Liver	40 to 70
Spongy bone	70 to 350
Cortial bone	350 to 2000

FIGURE 2.7: **Exemplary CT image and typical CT numbers of various tissues.** (Left): An axial CT slice of a lung cancer patient is depicted, where the level and window were chosen to enhance the displayed contrast in the lung tissue ($\ell = -300\,\mathrm{HU}$, $w = 1700\,\mathrm{HU}$). (Right): Table with typical CT numbers in HU of various tissues. Table adapted from [10].

between these different tissues. Different soft tissues have similar effective atomic numbers and mass densities, leading to a low soft tissue contrast of CT images. Typical CT number values of different tissue types are given in Figure 2.7 (right). Due to the large range of the Hounsfield scale, in clinical practice, the image contrast for displaying is adjusted by setting a window w and level ℓ value to enhance the contrast in the tissue of interest. Voxels with a CT number higher than $\ell + w/2$ are displayed as white, and voxels with a CT number lower than $\ell - w/2$ in black [61] and everything in between in different gray tones. Figure 2.7 (left) shows an exemplary axial slice of a CT scan of a lung cancer patient, where ℓ and w were chosen to enhance the contrast within the lung tissue.

The CT image quality can be affected by several imaging artifacts, including metal, scattering, beam hardening, noise, truncation, motion, and aliasing artifacts [10]. Failing to identify and correct these artifacts can lead to inaccurate CT numbers and, consequently, dose calculations during radiotherapy treatment planning (section 2.5).

Compared to MRI (section 2.3), the advantages of CT include the geometric accuracy of the obtained images, the short acquisition time of a few seconds, and the high spatial resolution with typical in-plane pixel sizes of around $1 \times 1\,\mathrm{mm}^2$ and slice thicknesses of 1–5 mm [56]. Most relevantly for radiotherapy, CT images are used to derive the voxelized quantitative 3D spatial distribution of the electron densities within the patient's tissue, which is needed for radiotherapeutic treatment planning (section 2.5).

The main drawback of CT is the radiation dose in the order of a few mSv per scan that is deposited in the patient's tissue [10]. This dose is small compared to the dose delivered to normal tissue over the course of a radiotherapeutic treatment. Nevertheless, to minimize the risk of radiation-induced secondary cancer over the course of the patient's lifespan, radiation exposure has to be minimized, and the acquisition of CT images has to be justified and clinically indicated [61]. Furthermore, compared to MRI, the contrast between tumor tissue and different soft tissues with similar elemental compositions and densities is low, which can be challenging for accurate tumor and OAR delineation (section 2.5), especially in the abdominal and pelvic region.

Current research and development by vendors and academic institutions is focused on the development of new detector types, such as photon-counting detectors, dual-energy or spectral CT scanners, phase-contrast CT, and CT imaging using protons or heavier ions [68–70]. These new techniques could improve the accuracy of target and OAR segmentation and dose calculation during treatment planning for photon and particle therapy (section 2.5).

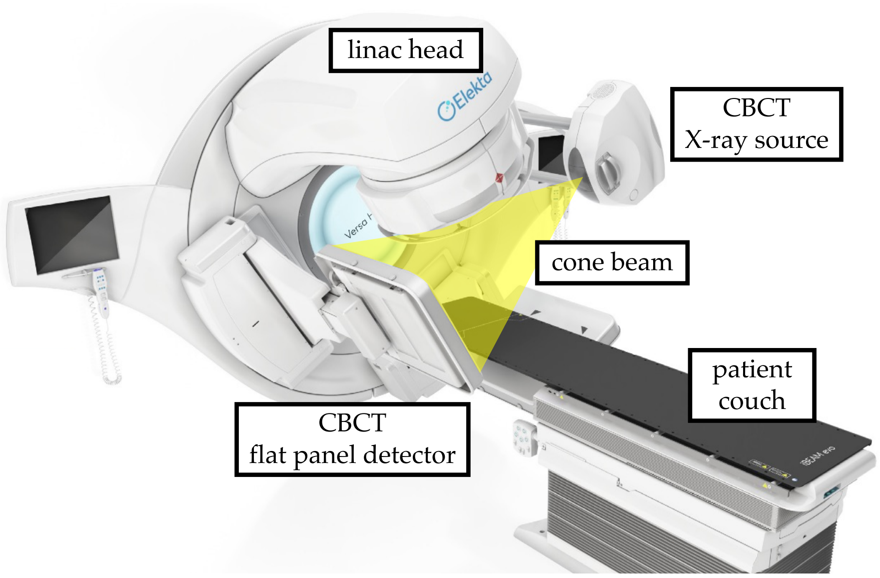

FIGURE 2.8: **CBCT scanner mounted to a linac gantry.** The main components of a CBCT scanner are shown. The X-ray source and flat-panel detector are mounted at 90° relative to the linac head. The cone-beam emitted by the X-ray source (sketched in yellow) is collimated and filtered before passing through the patient (not shown) lying on the treatment couch. Figure adapted from [67].

2.2.3 Cone-beam computed tomography (CBCT)

CBCT in the context of radiotherapy is a kilovoltage X-ray-based imaging modality, where the X-ray tube and detector are directly mounted to the medical linacs used for patient treatments (Figure 2.8). The flat-panel imager technology that is used in today's CBCT scanners was introduced in the early 2000s [71]. Today, CBCT scanners are widely used in radiotherapy of lung tumors to ensure accurate patient positioning before each treatment fraction (section 2.6.4) and assess potential interfractional patient variations (section 2.6.2) [72].

In contrast to conventional CT imaging, the patient couch is not moved during imaging, and a cone-beam instead of a fan-beam is used. This way, the volumetric dataset is acquired in one single gantry rotation. To reconstruct the CBCT image, the 3D volumetric data is directly reconstructed from 2D projection data. This is most often done using the *Feldkamp, Davis and Kress (FDK) algorithm* [73], which is an extension of the filtered backprojection algorithm used in conventional CT imaging [74].

The main advantages and drawbacks of CBCT imaging are similar to the ones of CT imaging. The soft tissue contrast of CBCT images is limited, and the images can be affected by similar artifacts such as beam hardening or ring artifacts due to miscalibrated or defect detector elements [75]. Compared to CT imaging, the overall image quality of CBCT images is lower, mainly caused by the increased contribution of scatter radiation at detector level, which can partly be corrected by using dedicated methods [76, 77]. The measured CBCT numbers cannot be readily used for dose calculations, preventing plan adaptations based on the CBCT images in routine clinical practice. Due to the regulatory restriction of the gantry rotation speed to 1 rotation/min, CBCT images are prone to motion artifacts, especially in body sites with pronounced motion, such as the lung. While 4D-CBCT imaging, where separate images for the different phases of a breathing cycle are reconstructed, can reduce these artifacts, this technique is so far only being used by academic radiotherapy centers [74, 78]. The same concerns about radiation-induced normal tissue damages as for CT imaging apply, since CBCT images are frequently acquired in IGRT (section 2.6.4). Especially for radiosensitive OARs that already receive a radiation dose close to the tolerance doses during the treatment, potential radiation-induced side effects have to be considered [75].

2.3 Magnetic resonance imaging (MRI)

MRI is based on the physical phenomenon of nuclear magnetic resonance (NMR). The measured signal intensities are proportional to the nuclear spin densities of the tissue and their specific relaxation times [79, 80]. In contrast to CT, MRI is typically not quantitative and contains no information about the electron densities needed for radiotherapy treatment planning. MR images have a high soft tissue contrast and are – besides diagnostic imaging – clinically used to guide delineations of tumors in soft tissues such as the brain and prostate [81]. Since no ionizing radiation dose is deposited, repeated time-resolved MRI with frame rates of a few Hz is possible in 2D, which is particularly important for MRgRT (Chapter 3) [40, 82]. Functional MRI can furthermore provide information on physiological processes within the tissue of interest [81]. Drawbacks of MRI compared to CT include the lower image resolution and longer acquisition times [15]. A further challenge for radiation oncology applications are geometric distortions of images that need to be considered and accounted for [83, 84]. The following sections summarize the physical principles and technological aspects of NMR and MRI.

2.3.1 Nuclear magnetic resonance (NMR)

While MRI can theoretically be performed with all nuclei with a non-zero spin, only the NMR of hydrogen nuclei is usually exploited in clinical routine. The spin quantum number I of the hydrogen nucleus is $1/2$ and its z-component I_z can take two different values [85]:

$$I = \frac{1}{2}, \qquad I_z = \pm\frac{1}{2}. \tag{2.25}$$

The magnetic moment $\boldsymbol{\mu}$ of a nucleus is proportional to the *gyromagnetic ratio* γ, which is a characteristic constant for each nucleus. For hydrogen nuclei [80, 86]:

$$\boldsymbol{\mu} = \gamma \boldsymbol{I} \qquad \gamma = 2.675 \times 10^8 \, \frac{1}{\mathrm{T\,s}}. \tag{2.26}$$

The bold font indicates that $\boldsymbol{\mu}$ and $\boldsymbol{I}$ are vectors. The high abundance of hydrogen atoms in the human body and the relatively large gyromagnetic ratio provide a higher detectable signal than when different nuclei are used (e.g., in magnetic resonance spectroscopy) [10].

Without an external magnetic field, all orientations of the magnetic moment $\boldsymbol{\mu}$ have the same potential energy. For a static homogeneous magnetic field, oriented along the z-direction, $\boldsymbol{B_0} = (0, 0, B_0)^{\mathrm{T}}$, the hydrogen nuclei can be in one of two potential energy states [85]:

$$E = -\mu_z B_0, \qquad \mu_z = \pm\frac{1}{2}\gamma\hbar, \qquad [\mu_z] = \mathrm{J\,T^{-1}}. \tag{2.27}$$

Transitions between these two states can only be induced through a time-dependent electromagnetic field $\boldsymbol{B_1}$ perpendicular to $\boldsymbol{B_0}$ [85]. For the transition to occur, the energy needs to be equal to the difference between the two energy states, i.e., $\Delta E = \hbar\omega_0$ with the *Larmor frequency* ω_0. Therefore, for transition to occur, the resonance condition has to be fulfilled [80]:

$$\omega_0 = \gamma B_0 \qquad [\omega_0] = \mathrm{Hz}. \tag{2.28}$$

For a typical diagnostic scanner with a magnetic field strength of 1.5 T, the resonance frequency $f = \omega_0/2\pi$ is 63.87 MHz and for a 0.35 T MRI scanner, such as used for the experimental studies of this thesis (Chapters 5 and 6), it is 14.90 MHz.

2.3.2 Macroscopic magnetization

In a probe containing hydrogen atoms, without the presence of an external magnetic field, all nuclear spins point in arbitrary directions. In this case, the probe does not have a macroscopic magnetization. With the external magnetic field $\boldsymbol{B_0}$, the hydrogen nuclei spins precess around the z-axis in one of the two possible energy states (Equation 2.27). Due to the small energy difference, the lower energy state (with $\mu_z = -1/2\,\gamma\hbar$) is populated more. At room temperature and a magnetic field strength of 1.5 T, the resulting population difference is in the order of 10^{-6}. This leads to an equilibrium macroscopic magnetization M_0 along the z-axis (*nuclear paramagnetism*), described by the Boltzmann statistics from classical mechanics [10, 85]:

$$M_0 = \frac{N}{V}\langle\mu_z\rangle = \frac{\rho\gamma^2\hbar^2 B_0}{4kT} \qquad [M_0] = \mathrm{J\,T^{-1}\,m^{-3}}\,, \tag{2.29}$$

with the expectation value of the z-component of the magnetic moment $\langle\mu_z\rangle$, the spin density ρ (the number of hydrogen atoms N in a given volume V), the probe temperature T and the Boltzmann constant k. The macroscopic magnetization $\boldsymbol{M}$ in thermal equilibrium is parallel to $\boldsymbol{B_0}$.

2.3.3 Equation of motion of magnetization

The temporal evolution of the magnetization $\boldsymbol{M}(t)$ in an arbitrary time-dependent magnetic field $\boldsymbol{B}(t)$ is described by the equation of motion [10, 87]:

$$\frac{\mathrm{d}\boldsymbol{M}(t)}{\mathrm{d}t} = \gamma\boldsymbol{M}(t) \times \boldsymbol{B}(t)\,. \tag{2.30}$$

In MRI, an external time-dependent electromagnetic radiofrequency (RF) pulse with frequency ω_1, perpendicular to $\boldsymbol{B_0}$, $\boldsymbol{B_1}(t) = (\cos(\omega_1 t), \sin(\omega_1 t), 0)^{\mathrm{T}}$, is applied to the object of interest [10]. In a transformed coordinate system that rotates around the z-axis with frequency ω_1, Equation 2.30 can be written as [87]:

$$\begin{aligned}\frac{\mathrm{d}\boldsymbol{M}(t)}{\mathrm{d}t} &= \gamma\boldsymbol{M}(t) \times (\boldsymbol{B_0} + \boldsymbol{B_1}(t)) &(2.31)\\ &= \gamma\boldsymbol{M}(t) \times \left(B_1\hat{\boldsymbol{e}}_x + \left(B_0 - \frac{\omega_1}{\gamma}\right)\hat{\boldsymbol{e}}_z\right). &(2.32)\end{aligned}$$

If the resonant excitation condition $\omega_1 = \omega_0$ is fulfilled, the component in z-direction vanishes and $\boldsymbol{M}$ precesses around the transformed x-axis. For an RF pulse with amplitude B_1 that is applied over a duration Δt, the magnetization $\boldsymbol{M}$, originally oriented along the z-axis, is tilted by the *flip angle* α with respect to the z-axis [10]:

$$\alpha = \gamma B_1 \Delta t\,. \tag{2.33}$$

The flip angle can be adjusted by the duration of the RF pulse and its amplitude. After the application of such an RF pulse, the magnetization vector has a longitudinal magnetization $M_z = M\cos\alpha$ and a transverse magnetization $M_{xy} = M\sin\alpha$ component. While the magnetization vector is stationary in the rotating coordinate system, it is precessing around the z-axis with the Larmor frequency ω_0 in the laboratory frame [80, 85].

2.3.4 Relaxation and Bloch equations

After the application of an RF pulse, *relaxation* processes occur that lead to a restoration of the thermal equilibrium state with a pure longitudinal macroscopic magnetization. This

TABLE 2.1: **Relaxation times at 0.35 T for various tissues.** The T_1 and T_2 relaxation times are given in ms for various tissues at a magnetic field strength of $B_0 = 0.35\,\mathrm{T}$. Table adapted from [89].

Tissue type	T_1	T_2
Water	3500	3500
Adipose tissue	200	60
Liver	285	65
Muscle	500	45
Cerebrospinal fluid	3300	2200
White matter	500	110
Gray matter	800	125
Oxygenated blood	900	240

was first observed by Bloch in 1946 [79] and is described by the differential *Bloch equations* (in the rotating coordinate system) [85]:

$$\frac{\mathrm{d}M_{xy}(t)}{\mathrm{d}t} = -\frac{M_{xy}(t)}{T_2}, \tag{2.34}$$

$$\frac{\mathrm{d}M_z(t)}{\mathrm{d}t} = \frac{M_0 - M_z(t)}{T_1}, \tag{2.35}$$

with the relaxation times T_1 and T_2. The solution to these equations in the rotating coordinate system is [87]:

$$M_{xy}(t) = M_{xy}(0) \cdot \exp\left(-\frac{t}{T_2}\right), \tag{2.36}$$

$$M_z(t) = M_0 - (M_0 - M_z(0)) \cdot \exp\left(-\frac{t}{T_1}\right). \tag{2.37}$$

The recovery of the longitudinal component of the magnetization is called *spin-lattice relaxation*. It is caused by fluctuating local magnetic fields due to the translations and rotations of molecules, electrons, or other nuclei (the *lattice*), which induce spin transitions. The released energy is dissipated as heat until the magnetization has reached its thermal equilibrium state [10]. The exponential decrease of the transversal magnetization is termed *spin-spin relaxation*. Random fluctuations of the local magnetic field lead to slightly different precession frequencies of the nuclear spins, which cause a loss of the original phase coherence. No energy transfer occurs in spin-spin relaxations [10, 80]. In real NMR experiments and MRI, the dephasing of the transversal magnetization occurs at a rate $1/T_2^*$ that is faster than $1/T_2$. This is caused by small inhomogeneities of the B_0-field, described by the relaxation time T_2' [80, 88]:

$$\frac{1}{T_2^*} = \frac{1}{T_2} + \frac{1}{T_2'}. \tag{2.38}$$

In general, T_1 strongly depends on the strength of the homogeneous magnetic field B_0 and is longer than T_2. Different tissues have different relaxation times, even if their elemental composition is similar. In MRI, the measured image intensity depends on the proton density ρ and relaxation times (section 2.3.7), explaining the high soft tissue contrast of MRI [85, 89]. Table 2.1 lists relaxation times of exemplary tissues for a magnetic field strength of 0.35 T.

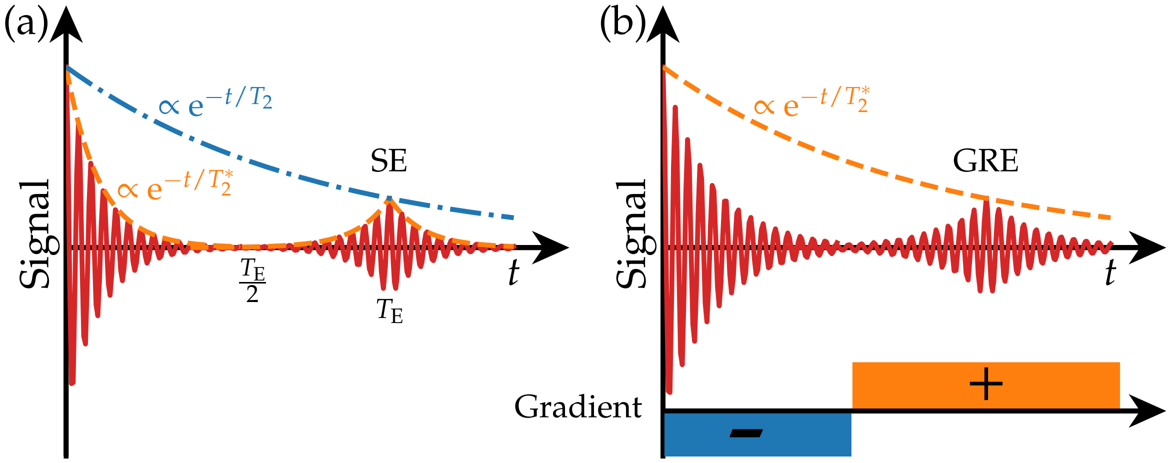

FIGURE 2.9: **Spin echo and gradient recalled echo.** (a): Directly after the application of an excitation RF pulse at $t = 0$, the FID signal can be measured as a damped oscillation with exponentially decaying amplitude at a rate $1/T_2^*$ in the receiver coil. When a 180° pulse is applied at time point $t = T_E/2$, a SE signal is produced, which reaches a maximum signal amplitude proportional to $\exp(-t/T_2)$ at $t = T_E$ due to signal loss caused by irreversible dynamic spin-spin interactions. (b): After the application of the RF pulse, a gradient field is superimposed, which leads to a dephasing at a faster rate than observed in the FID. When the polarity of this gradient field is switched after a set time, the dephasing due to the position-dependent gradient field can be reversed, which leads to the formation of a GRE. The sketch is based on Figure 11.10 in [85].

2.3.5 Free induction decay, spin echo, and gradient recalled echo

Equations 2.36 and 2.38 describe the temporal evolution of the transversal magnetization component $M_{xy}(t)$ after application of an RF pulse in the rotating frame. In the laboratory frame, M_{xy} precesses around the z-axis, which induces the measurable time-dependent signal $S(t)$ in a receiver coil (section 2.3.8). This signal has the shape of a damped oscillation, the *free induction decay* (FID), with Larmor frequency ω_0 and exponentially decreasing amplitude [85, 87]:

$$S(t) \propto M_{xy}(t) = M_{xy}(0) \cdot \exp\left(i\omega_0 t - \frac{t}{T_2^*}\right). \tag{2.39}$$

The spin-spin relaxation caused by random fluctuations of the magnetic field leads to an irreversible loss of transversal magnetization. The dephasing due to inhomogeneities of the external $\boldsymbol{B}_0$-field can be reversed, when at a time $T_E/2$ after the excitation pulse a 180° RF pulse is applied to the volume of interest. The 180° RF pulse flips the transversal magnetization vector in the x-y-plane. After waiting for an additional time $T_E/2$, the different components of M_{xy} rephase again. This leads to the formation of a measurable signal in the receiver coil, the *spin echo* (SE) with *echo time* T_E, illustrated in Figure 2.9a. Imaging sequences exploiting this measurement scheme are called *SE sequences* [80, 85, 88].

In a different type of sequence, the so-called *gradient recalled echo* (GRE) is measured. To produce this echo, after the application of the excitation pulse, an additional position-dependent magnetic gradient field is superimposed with the static B_0-field. The resulting position-dependent Larmor frequency causes accelerated dephasing of the transversal magnetization components. This dephasing can be reversed by applying an inverted gradient field with the same strength but opposite polarity after a set time. This leads to the formation of a measurable GRE signal, illustrated in Figure 2.9b. The MRI sequences used in clinical practice are derived from the basic SE and GRE pulse sequences [85, 87, 88].

2.3.6 Spatial encoding and image reconstruction

For the reconstruction of an MR image, the spatial positions of the object's voxels need to be encoded in the detected signal. In a homogeneous $\boldsymbol{B}_0$-field, the Larmor frequency does not depend on the position within the field-of-view (FOV). For the spatial encoding, the $\boldsymbol{B}_0$-field is superimposed with magnetic gradient fields. These fields all point in z-direction (parallel to $\boldsymbol{B}_0$) but vary in strength along the x-, y- or z-axis [80, 85]:

$$B_x = G_x \cdot x\,, \qquad B_y = G_y \cdot y\,, \qquad B_z = G_z \cdot z\,, \qquad \left[G_{x/y/z}\right] = \mathrm{T\,m^{-1}}\,, \tag{2.40}$$

where G_x, G_y and G_z indicate the slope of the gradient fields with typical values between 20–80 mT/m [10]. In an MRI sequence, these gradient fields are used in three different ways to encode the signal in x-, y-, and z-direction: *slice selection*, *phase encoding* and *frequency encoding*.

Slice selection

When B_z is switched on, the Larmor frequency ω depends on the z-position [85]:

$$\omega(z) = \gamma\left(B_0 + G_z \cdot z\right). \tag{2.41}$$

If this gradient field is present during the application of the excitation RF pulse, the resonance condition is fulfilled in a 2D slice with a fixed z-position. Only the spins within the voxels of this slice are excited. In order to achieve a selective excitation in one plane, the RF pulse has a sinc-function shape, containing a small spectrum of frequencies within a bandwidth $\Delta\omega$. The position of the excited slice is adjusted by tuning the central frequency of the RF pulse or the offset of G_z. The thickness of the excited slice Δz depends on the bandwidth of the excitation pulse and the slope G_z [10]:

$$\Delta z = \frac{\Delta\omega}{\gamma G_z}\,. \tag{2.42}$$

***k*-space**

In MRI, the signal detected with the receiver coils is a superposition of the RF waves emitted at different voxels within the excited slice. These waves have different amplitudes, depending on the local transversal magnetization magnitudes. Furthermore, the location within this slice is encoded using the gradient fields in x- and y-direction, which results in differences in frequencies and phases of the RF waves. During readout, the amplitudes of the signal are collected as a function of their discretized frequency and phase. These data points are saved in a matrix, referred to as *k-space* which is equivalent to the Fourier space of spatial frequencies. As soon as the k-space has been fully sampled, the MR image can be reconstructed using a 2D Fourier transformation [10].

Phase and frequency encoding

To encode the signal along the x-axis, the phase-encoding gradient field B_x is switched on for a duration Δt_p after the slice-selective excitation. During this time, spins at different x-positions precess with slightly different Larmor frequencies. After switching off the gradient field, the magnetization vectors at different x-positions have accumulated different phase shifts φ_p [10], proportional to the k_p value:

$$\varphi_\mathrm{p}(x) = \gamma x G_x \Delta t_\mathrm{p} = k_\mathrm{p} x\,. \tag{2.43}$$

As the last step of the spatial encoding, the frequency-encoding gradient field B_y is switched on during the read-out of the signal for the duration Δt_{r}. Through the varying Larmor frequencies, the y-position is encoded in the acquired signal in terms of different k_{r} values [10]:

$$k_{\mathrm{r}} = \gamma G_y \Delta t_{\mathrm{r}} \,. \tag{2.44}$$

Different k_{r} values are sampled during one signal read-out, but several iterations with different k_{p}-values have to be performed. If the number of pixels in the phase-encoding direction in the final image is N_{p}, the acquisition time for one slice is $T_{\mathrm{acq,\,sl}} = N_{\mathrm{p}} \cdot T_{\mathrm{R}}$, where the *repetition time* T_{R} is the duration of each iteration [80]. Measuring the signal for different k_{r} and k_{p} values this way is termed *cartesian k-space sampling* [88].

Image reconstruction

The acquired signal in the excited 2D slice as a function of the k_{p} and k_{r} values in k-space is given by [10]:

$$S(k_{\mathrm{p}}, k_{\mathrm{r}}) = \iint\limits_{x,y} |M_{xy}(x,y)| \cdot \exp\left[-i(k_{\mathrm{p}} x + k_{\mathrm{r}} y)\right] \mathrm{d}x\, \mathrm{d}y \,. \tag{2.45}$$

An MR image displays the distribution of the transversal magnetization $M_{xy}(x,y)$ and can be reconstructed by a 2D Fourier transformation of the measured signal [10]:

$$M_{xy}(x,y) = \frac{1}{2\pi} \iint\limits_{k_{\mathrm{p}},k_{\mathrm{r}}} S(k_{\mathrm{p}}, k_{\mathrm{r}}) \cdot \exp\left[i(k_{\mathrm{p}} x + k_{\mathrm{r}} y)\right] \mathrm{d}k_{\mathrm{p}}\, \mathrm{d}k_{\mathrm{r}} \,. \tag{2.46}$$

To obtain a 3D image, the spatial encoding and the reconstruction steps are repeated for N_z different slice positions. The total acquisition time for the 3D volume is then given by [80]:

$$T_{\mathrm{acq,\,tot}} = N_z \cdot T_{\mathrm{acq,\,sl}} = N_z \cdot N_{\mathrm{p}} \cdot T_{\mathrm{R}} \,, \tag{2.47}$$

which is typically in the order of several tens of seconds up to a few minutes. The spatial resolution of the reconstructed image is given by the slice thickness Δz (Equation 2.42) and the in-plane-resolution Δx and Δy [10]:

$$\Delta x = \frac{2\pi}{\gamma G_x \Delta t_p} \,, \qquad \Delta y = \frac{2\pi}{\gamma G_y \Delta t_r} \,. \tag{2.48}$$

Typical values for the slice thickness used in clinical practice are in the order of a few millimeters. The in-plane resolution depends on the sequence, can be as small as 1 mm for diagnostic and in the order of a few millimeters for temporally resolved sequences [40, 41].

2.3.7 Imaging sequences

An MRI *pulse sequence* is a combination of different RF excitation pulses and the application of gradient fields for spatial encoding and read-out (Figure 2.10). A multitude of different imaging contrasts can be achieved for different clinical applications through the use of SE or GRE, the variation of the repetition time T_{R}, the echo time T_{E}, the flip angle α, the bandwidth of the excitation pulse $\Delta\omega$, the gradient strengths for spatial encoding, through the use of additional preparation pulses to suppress the signal of certain tissues and through different k-space sampling schemes (cartesian, spiral, radial) [80, 88].

For instance, in a SE sequence, the signal strength depends on the sequence-specific parameters T_{R} and T_{E} and the tissue-specific proton density ρ and relaxation times T_1 and

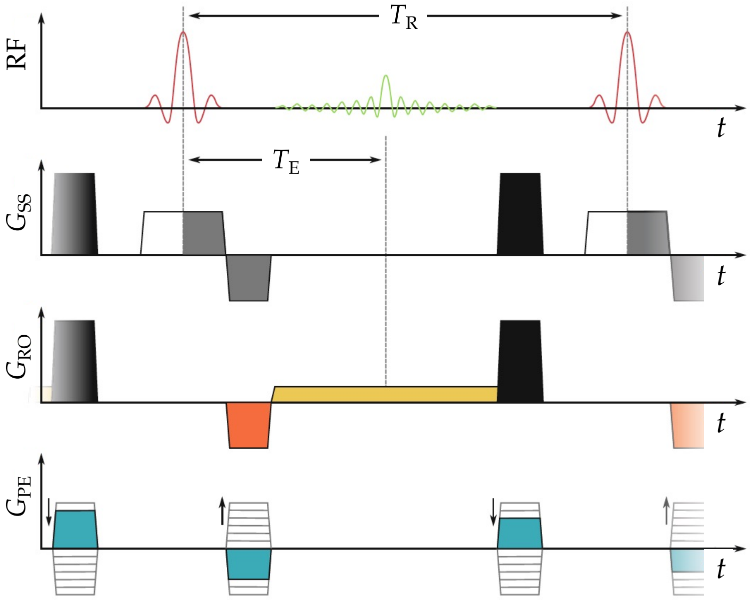

FIGURE 2.10: **Schematic of a gradient echo sequence.** The RF pulses, GRE signal, and gradient fields are schematically plotted as a function of time t. During the application of an excitation pulse, a slice selection gradient G_{SS} is switched on, which is followed by a free precession period during which one k_p-value is encoded by applying the phase-encoding gradient G_{PE}. The transversal magnetization is dephased and rephased by the read-out gradient G_{RO} with opposite polarities, which leads to the formation of a GRE after the echo time T_E. The signal is dephased through the application of spoiler gradients (shown in black) before the pulse sequence is repeated with a different G_{PE} strength after the repetition time T_R. Figure adapted from [10].

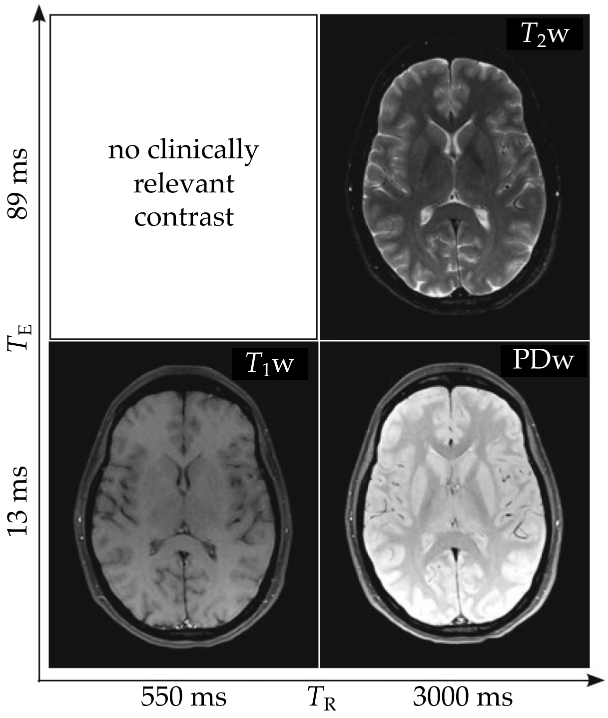

FIGURE 2.11: **Illustration of different MR image contrasts.** An axial slice of a patient's head is shown for different echo times T_E and repetition times T_R. Depending on the combination of T_E and T_R, a T_1-weighted (T_1w), T_2-weighted (T_2w) or proton density weighted (PDw) contrast is obtained. Figure adapted from [10].

T_2 [85]:

$$S_{\mathrm{SE}} = \rho \left[1 - \exp\left(-\frac{T_{\mathrm{R}}}{T_1}\right)\right] \cdot \exp\left(-\frac{T_{\mathrm{E}}}{T_2}\right). \tag{2.49}$$

Figure 2.11 shows the effect of varying the repetition and echo time on the contrast of the image allowing for the acquisition of T_1-weighted (T_1w), T_2-weighted (T_2w) or proton density-weighted (PDw) images.

In addition to the image contrast variation of a static region of interest, dedicated fast MRI sequences can be used to observe the motion of tumors or organs (Chapter 3) [40]. Furthermore, functional imaging sequences like diffusion-weighted imaging can provide valuable data on physiological processes for diagnosis and radiotherapy treatment planning [81, 90].

Similar to CT and CBCT images, MR images can suffer from a series of artifacts, which include aliasing, metal, motion, chemical shift, susceptibility artifacts, and geometric distortions [10]. Since the geometric fidelity of MR images is crucial in MRgRT (Chapter 3) [84, 91], geometric distortions are explained in more detail in section 2.3.9.

2.3.8 Main technical components of MRI scanners

The main technical components of an MRI scanner are sketched in Figure 2.12. The patient is placed on a couch that is moved inside the scanner's bore to position the volume of interest at the imaging isocenter. A superconducting coil, cooled with liquid helium at a temperature of 4 K, provides the strong static homogeneous magnetic field $\boldsymbol{B_0}$ in the cranio-caudal direction (z-axis) to create the macroscopic magnetization. Typical field strengths of diagnostic scanners are 1.5 T and 3.0 T. The housing of the MRI contains RF transmit coils to apply the electromagnetic excitation pulse $\boldsymbol{B_1}$, perpendicular to $\boldsymbol{B_0}$, and gradient coils, used for the spatial encoding of the NMR signals. Receiver coils, specially designed for each body site, are positioned close to the scanned volume to detect the weak signal of the precessing transversal magnetization. A Faraday cage surrounds the room of the MRI scanner to minimize RF contamination that would spoil the detection of the NMR signal. The detected signal is processed, and the image is reconstructed and displayed in a control room outside of the Faraday cage [10, 80].

2.3.9 Geometric distortions

A challenge of MRI that is of particular interest in the context of MRgRT (Chapter 3) is that the reconstructed images can be geometrically distorted. While this is of minor importance in radiology, where the images are used for diagnostic purposes, these distortions need to be accounted and corrected for when used in a radiotherapeutic treatment planning workflow [41, 84]. During treatments with an MR-Linac (section 3.1), 3D-MRI are used for daily treatment adaptations (section 2.6.5), and temporally-resolved 2D-MRI are acquired to track the motion of the target [26, 92]. Therefore, without accounting for geometric distortions, this can result in inaccurate image registrations, delineations, and dose calculations which can lead to an underdosage of tumor tissue [91].

The geometric fidelity of MR images is lower for a larger FOV and generally decreases with the distance to the imaging isocenter. At the edges of the FOV, geometric errors can be in the order of several millimeters [93–95]. The three main sources of geometric distortions are system-related gradient nonlinearities and $\boldsymbol{B_0}$-inhomogeneities, as well as patient-related susceptibility artifacts [83, 96]. Of these sources, the nonlinearities of the gradient fields (Figure 2.13) used for the spatial encoding of the image have the largest contribution [84, 91].

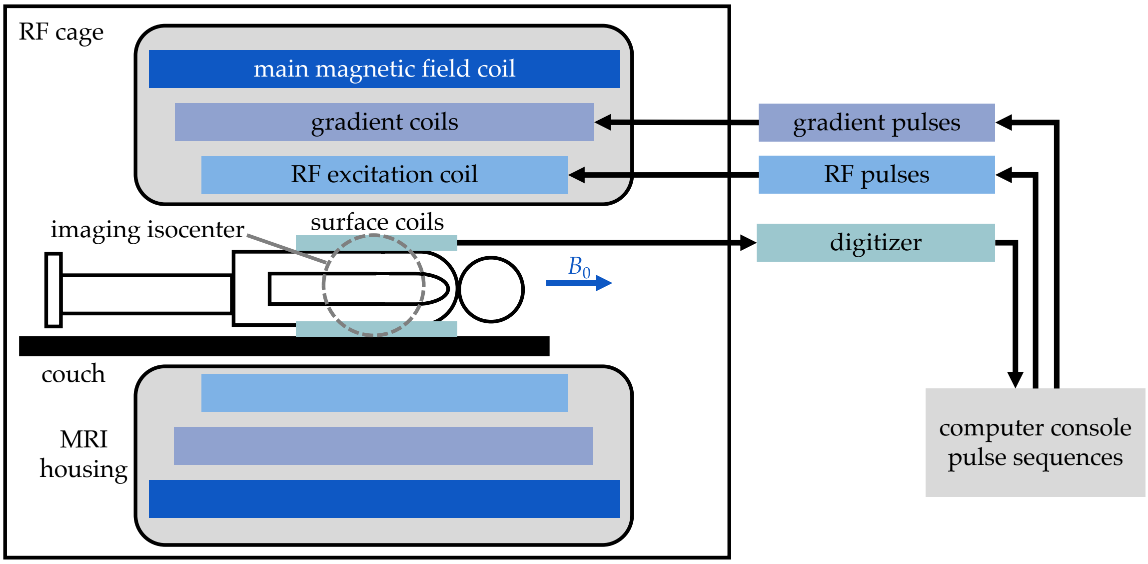

FIGURE 2.12: **Sketch of an MRI scanner.** The main technical components of an MRI scanner are schematically depicted and described in the text. The sketch is based on Figure 9.3 in [10].

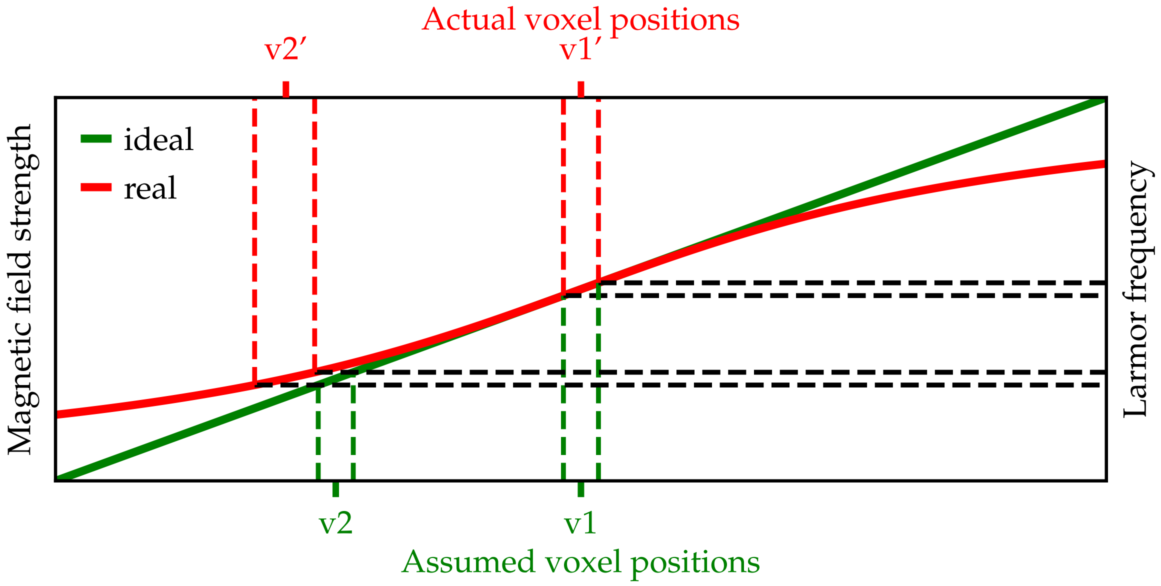

FIGURE 2.13: **Illustration of the effect of gradient nonlinearities.** For the spatial encoding of the NMR signals, Equation 2.40 assumes ideal linearity of the applied gradient fields (green line). In reality, the gradient coils produce nonlinear magnetic fields, represented by the red curve. The position-dependent Larmor frequency encodes the voxel location. While the voxel position close to the isocenter (v1) is correctly encoded for both curves, the position of a voxel located further away from the isocenter (v2) is not correctly encoded when gradient nonlinearities are present. This can lead to a displacement of v2 by several mm in the reconstructed image. This figure is based on Figure 3.2 in [97].

Geometric distortions can be corrected through the design of the imaging sequences (e.g., with a high read-out gradient) or retrospectively by applying manufacturers' proprietary correction methods in 2D or 3D [91, 96]. In research articles, a frequently chosen approach to correct for gradient nonlinearities is to determine correction deformation vector fields (DVF), where a 3D-MRI of an object (distortion phantom) containing well-defined grid points is compared to a ground truth image which can be a geometrically accurate CT scan or a computer-aided design (CAD) model [93–95]. The DVF can then be obtained through an optimization process by determining the weights of spherical harmonics coefficients that minimize the distances of the grid points in the ground truth and geometrically corrected 3D-MRI [91, 98]. This approach was chosen in section 5.2.6, where it is described in more detail.

2.4 Image registration

Image registration is a crucial tool in modern radiotherapy. Applications include the use for patient positioning in IGRT (section 2.6.4), the assessment of motion, synthetic CT generation (section 3.3.2) and the transfer of structures between datasets (section 3.1.6). Image registration aims to find a transformation that maps one image (called *moving* or *target* image) to another image (called *fixed* or *reference* image) to find the relationship of spatial coordinates of corresponding points in the two images [99, 100]. This is achieved by determining the transformation that maximizes the similarity between the fixed and the moving image in an iterative process [99]. The images can contain morphological or functional information, can be acquired with different modalities (*multimodal registration*) or with the same modality (*monomodal registration*) at different time points.

2.4.1 Image registration steps

Three image registration types exist (illustrated in Figure 2.14): rigid registration, affine transformation, and deformable image registration (DIR) [101]. In rigid registration, the moving image is globally translated and rotated to match the fixed image. In affine transformations, the image can be additionally scaled and sheared. In DIR, the image is transformed locally by moving the individual voxels of the moving image by means of a DVF. In the studies presented in Chapters 4–6 of this thesis, automatic rigid registration and DIR was used.

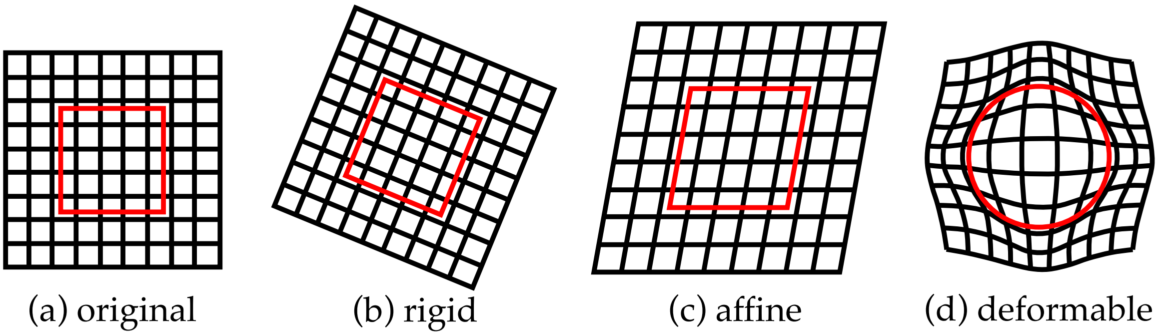
(a) original (b) rigid (c) affine (d) deformable

FIGURE 2.14: **Image registration types.** The effect of the transformation of the schematic original image (a) with each of the three image registration types is illustrated. (b) Image after translation and rotation in a rigid registration. (c) Image after shearing and scaling in an affine transformation. (d) Image after transformation through DIR. Figure adapted from [101].

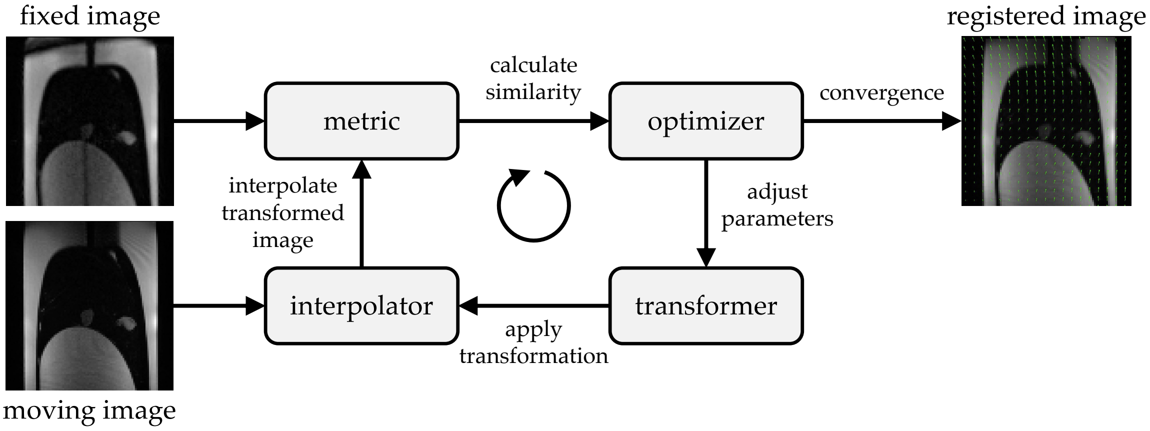

FIGURE 2.15: **Components of an image registration algorithm.** The components and steps of the iterative image registration optimization process are sketched. In this example, two cine MR images in two different breathing states are deformably registered. The final DVF transforming the moving to the fixed image is overlayed on the registered image (green arrows). The sketch was created based on [100] with data from Chapter 6.

While rigid registration can be done manually or automatically, DIR is always performed in an iterative automatic optimization. Independent of the registration type, automatic registration uses an algorithm consisting of a transformer, interpolator, similarity metric, and optimizer (Figure 2.15). In each iteration of the optimization process, the (initial or transformed) moving image is interpolated to match the coordinate system of the fixed image. The similarity metric between the current interpolated transformed moving image and the fixed image is calculated. The optimizer adjusts the parameters of the specific registration type. The transformer then applies the transformation described by the updated parameters to the moving image. The process is terminated either if the similarity metric value converges (i.e., when the difference of the cost function between two iterations is below a predefined threshold), or when a predefined number of iterations is reached. In the final step of the image registration process, the registered image and the transformation parameters are output [100].

2.4.2 Rigid and affine registration

In a rigid registration, the moving image can be translated in all three spatial directions and rotated around all three orientations to match the fixed image. This leads to a total of six degrees-of-freedom for the optimizer [100]. In routine IGRT, the couch is translated and rotated to accurately position the patient with respect to the delivery beam (section 2.6.4). The couch translations and rotations are derived from the rigid registration of the daily acquired CBCT image to the planning CT [99].

In an affine registration, the image can be additionally scaled and sheared along each image axis, leading to a total of twelve degrees-of-freedom for the optimizer for a 3D image registration [101].

2.4.3 Deformable image registration (DIR)

The limited number of degrees-of-freedom of rigid and affine registrations is insufficient to model the complex local changes of moving organs, particularly in the abdomen and thorax. Physiologically induced motion, like breathing or the heart beating, can cause organs or tumors to change their position, orientation, volume, and shape [102]. DIR aims to model these variations by determining a DVF that describes how the voxels from the moving image have to be transformed so that the correspondence with the fixed image is maximized [100]. Many different DIR algorithms exist, including Demons, optical flow, finite element modeling, free form definition, and B-spline registration [100].

DIR using B-splines as basis functions for the transformation model is often used in clinical practice. This type of registration was also chosen in Chapters 4–6 of this thesis. A grid of automatically selected uniformly spaced control points is overlaid on the moving image for this algorithm [100, 102]. The transformation $T_{\mathrm{DIR}}(x,y,z)$ that maps the voxels of the moving image to that of the fixed image is parametrized as a tensor product of 1D cubic B-splines [103]:

$$T_{\mathrm{DIR}}(x,y,z) = \sum_{l=0}^{3}\sum_{m=0}^{3}\sum_{n=0}^{3} B_l(u)B_m(v)B_n(w)\phi_{i+l,j+m,k+n}\,, \tag{2.50}$$

where $\phi_{i,j,k}$ represents the mesh of equally spaced control points with a grid size of $n_x \times n_y \times n_z$ and a spacing of $\delta_x \times \delta_y \times \delta_z$, and:

$$i = \left\lfloor \frac{x}{n_x} \right\rfloor - 1\,, \qquad j = \left\lfloor \frac{y}{n_y} \right\rfloor - 1\,, \qquad k = \left\lfloor \frac{y}{n_y} \right\rfloor - 1\,, \tag{2.51}$$

$$u = \frac{x}{n_x} - \left\lfloor \frac{x}{n_x} \right\rfloor, \qquad v = \frac{y}{n_y} - \left\lfloor \frac{y}{n_y} \right\rfloor, \qquad w = \frac{z}{n_z} - \left\lfloor \frac{z}{n_z} \right\rfloor. \tag{2.52}$$

The B-spline basis functions, with $r \in [u,v,w]$, are given by [102, 103]:

$$B_0(r) = (1-r)^3/6\,, \tag{2.53}$$

$$B_1(r) = (3r^3 - 6r^2 + 4)/6\,, \tag{2.54}$$

$$B_2(r) = (-3r^3 + 3r^2 + 3r + 1)/6\,, \tag{2.55}$$

$$B_3(r) = r^3/6\,. \tag{2.56}$$

The displacements at the control points are optimized in the iterative process to maximize the similarity between the fixed and transformed moving images. The final DVF is then interpolated onto the image voxel grid to get the displacement vectors at each individual voxel position. Any control point can be moved in any of the three spatial directions, leading to a total of $3 \times n_x \times n_y \times n_z$ free parameters to be optimized. Displacing one of the control points only affects the surrounding control points, leading to a local change of the DVF. The smaller the distance between the control points, the smaller the region affected by this change [102].

The registration is performed in several steps for improved performance of the DIR in terms of speed, accuracy, and robustness. The registration is initiated with a coarse image resolution and control point grid. After convergence, or after the maximum number of iterations is reached, the next step is started with a finer image resolution and smaller spacing between the control points. The final transformation parameters of the previous step are thereby used as the starting point for the next resolution step [99, 102]. This technique helps to achieve faster convergence and to model relatively large deformations, and improves robustness by avoiding getting stuck in local minima during optimization [99]. Additionally, a regularization term can be included in the cost function to obtain more realistic and smooth transformation fields [100, 102]:

$$C_{\mathrm{tot}} = C_{\mathrm{sim}}\left(A, T(B)\right) + \lambda C_{\mathrm{smooth}}\,, \tag{2.57}$$

where C_{tot} is the total cost function, C_{sim} is the term quantifying the similarity between the fixed image A and the transformed moving image $T(B)$, and C_{smooth} is the regularization term that ensures the smoothness of the DVF [103]:

$$C_{\text{smooth}} = \frac{1}{V} \int_0^X \int_0^Y \int_0^Z \left[\left(\frac{\partial^2 T}{\partial x^2} \right)^2 + \left(\frac{\partial^2 T}{\partial y^2} \right)^2 + \left(\frac{\partial^2 T}{\partial z^2} \right)^2 \right. \tag{2.58}$$

$$\left. +2 \left(\frac{\partial^2 T}{\partial xy} \right)^2 + 2 \left(\frac{\partial^2 T}{\partial xz} \right)^2 + 2 \left(\frac{\partial^2 T}{\partial yz} \right)^2 \right] \mathrm{d}x \mathrm{d}y \mathrm{d}z \, , \tag{2.59}$$

with the volume of the image V. A typical value of the parameter balancing the two cost function terms is $\lambda = 0.05$ [102].

2.4.4 Applications of DIR

DIR is applied in several workflow steps in adaptive radiotherapy (ART; section 2.6.5) and MRgRT (section 3.1.6). The frequency of its use is expected to further grow in the future [99]. DIR is used to propagate the electron density maps from planning CT images to MR images during treatment planning at the MR-Linac [100] (section 3.1). In the adaptive MRgRT workflow, the structures defined on the planning MRI are transferred to the setup MRI acquired at the start of each fraction using the DVF output by a DIR [99] (section 3.1.6). During gated treatments at the MR-Linac, the reference image is deformably registered to the continuously acquired cine MRI frames to determine the current position of the target structure with respect to the gating boundary (section 3.1.7). Furthermore, DIR is used in dose accumulation studies to compare originally planned and the delivered dose distributions in the same frame of reference [99]. In this thesis, DIR was used to register MR images acquired in different breathing phases to propagate target structures and assess their range of motion. This is described in more detail in Chapters 4–6.

2.4.5 Challenges of DIR

DIR is an ill-posed underconstrained problem, where multiple solutions exist [99]. It is also not trivial to assess whether the obtained image registration accurately describes the real translations and deformations of the tissue since no ground truth is available and the validation of DIR algorithms is difficult [104]. This is especially the case for multimodal registrations, which are inherently more challenging than monomodal registrations due to the different contrast of the images [100]. While B-spline registrations can achieve accurate results, the large number of degrees-of-freedom leads to long computation times, preventing its use for real-time applications [102].

Pronounced anatomical or physiological changes can occur between the acquisition of two images at different time points. Examples include the filling or depletion of digestive organs and tumor shrinkage or growth. In these cases, it is difficult or impossible to obtain a meaningful registration between the images since DIR cannot model the appearance or disappearance of objects [99, 100]. Lastly, sliding motion can occur at tissue boundaries, such as between the lung and the rib cage. Depending on the extent of motion and level of regularization used in the registration, this sliding motion cannot be modeled by DIR [99]. A solution of how this sliding motion can appropriately be accounted for is presented in section 5.2.7. Alternatively, more complex dedicated tissue and anatomy models are required.

2.4.6 Similarity metrics

The similarity metric quantifies how well the transformed moving image is matched to the fixed image [105]. The choice of this metric depends on the type of the registration task.

Three groups of similarity metrics exist, which are either point-based, feature-based, or intensity-based [100]. In point-based registrations, the distances between anatomical landmarks are minimized. The landmarks need to be automatically or manually predefined on the fixed and moving images. In feature-based registrations, manually or automatically selected features such as lines, curves, point clouds, or surfaces must be defined on both images. These features are then matched during the registration process [99, 100]. In the studies in this thesis, intensity-based metrics were exclusively used. In this case, the similarity metric value is automatically calculated from the intensity values of the voxels in the moving and fixed image. The registration process can be fully automated and is generally more robust than when point-based or feature-based similarity metrics are used. This comes at the cost of longer computation times [99, 105]. Examples of intensity-based similarity metrics include mean squared error (MSE), correlation coefficient, mutual information (MI), and gradient magnitude [100, 105]. The intensity-based similarity metrics most commonly used in radiotherapy today include the MSE and MI [100].

Let A be a fixed image and B a moving image to which the transformation T is applied and which is then interpolated to match the coordinate system of A. The MSE between the intensity values of the voxels in the two images is then calculated on a voxel-by-voxel basis, given by [105]:

$$\mathrm{MSE}(A,B) = \frac{1}{N}\sum_{\vec{x}} \left[A(\vec{x}) - T\left(B(\vec{x})\right)\right]^2 , \tag{2.60}$$

where $\vec{x}$ denotes the spatial coordinates of the images and N the number of pixels in the overlapping region in the two images. This metric is often chosen for registrations of images acquired with the same modality (monomodal registration) at different time points. The two images A and B must have intensity values in the same range, which is why MSE cannot be used for multimodal registrations, e.g., between a CT and an MR image [105].

The similarity metric MI is derived from information theory to quantify how well one image describes the other by using the concept of entropy of the images [100]. The Shannon-Wiener entropy H of an image gives a measure of the average information provided by its intensity values i [105]:

$$H = -\sum_i p_i \log p_i \, , \tag{2.61}$$

where p_i is the probability of the image intensity i. When a indicates the intensity values of the voxels in image A, and b the values in image B, the joint entropy $H(A,B)$ of the two images is given by [105]:

$$H(A,B) = -\sum_a \sum_b p_{AB}(a,b) \log p_{AB}(a,b) \, , \tag{2.62}$$

where $p_{AB}(a,b)$ is the joint probability of pairs of the image intensity values a and b occurring together. The more similar the images are, the lower the joint entropy gets compared with the sum of the individual entropies. The MI between images A and B, $\mathrm{MI}(A,B)$, is given by [105]:

$$\mathrm{MI}(A,B) = H(A) + H(B) - H(A,B) \, . \tag{2.63}$$

Using the relations between the probability mass functions p_A and p_B, and the joint probability mass function of A and B, p_{AB} [106]:

$$p_A(a) = \sum_b p_{AB}(a,b) \qquad \text{and} \qquad p_B(b) = \sum_a p_{AB}(a,b) \, . \tag{2.64}$$

Equation 2.63 can be rewritten as [105]:

$$\mathrm{MI}(A,B) = \sum_a \sum_b p_{AB}(a,b) \log \frac{p_{AB}(a,b)}{p_A(a)p_B(b)} \,. \tag{2.65}$$

The joint entropy is minimized, and the MI is maximized during image registration. MI is the most frequently used metric for multimodal registrations, e.g., between the planning CT and a planning or setup MRI in an adaptive MRgRT workflow (section 3.1.6) [100, 105].

2.5 Photon radiotherapy treatment planning

The main goal of radiotherapeutic treatments is delivering a high dose to malignant tumor cells while at the same time minimizing radiation-induced damages to healthy tissue. On the one hand, with increasing doses delivered to the tumor, the tumor control probability (TCP) increases. On the other hand, a higher dose delivered to healthy tissue results in a higher normal tissue complication probability (NTCP). The purpose of radiotherapeutic treatment planning is to find the optimal trade-off between the TCP and NTCP.

There are several techniques to deposit radiation dose in a patient's body. In brachytherapy [5], a radioactive nuclide is temporarily or permanently placed in the tumor tissue. In charged particle therapy, the patient is irradiated with electrons [7], protons [8] or heavier ions such as carbon ions [9]. The technique that is most often used in clinical practice – and that this thesis is focused on – is radiotherapy with high-energy photons. This section summarizes the physical, biological, and clinical aspects of the main steps of photon radiotherapy treatment planning with a conventional medical linac. These steps include imaging (section 2.5.1), structure segmentation (section 2.5.2), dose prescription (section 2.5.3), choice of the delivery technique (section 2.5.4), treatment plan optimization (section 2.5.5), and quality assurance (QA; section 2.5.6) measurements. Advanced treatment planning techniques and workflow steps specific to MRgRT are described in section 2.6 and Chapter 3.

2.5.1 Image acquisition for treatment planning

The decision of whether a cancer patient is treated with radiotherapy is based on radiological, histopathological, and clinical data. As the first step of the radiotherapy workflow, a planning CT (section 2.2.2) centered around the tumor target is acquired. The extent of the CT image in the craniocaudal direction has to be long enough to capture the whole anatomy that is expected to receive a non-negligible dose during treatment. The energy range of photons used for CT imaging is one to two orders of magnitude smaller than that of radiotherapeutic photons. The photon attenuation coefficients correlated to the HUs of the CT images can thus not be directly used as input for dose calculations, since these depend on the photon energy (Figure 2.1). The CT number distributions are converted to electron densities maps using calibration curves derived from measurements with phantoms containing tissue-equivalent materials. The electron density distributions are needed for the dose calculations during simulation of the treatment plan (section 2.5.5) [10]. For tumors in the thoracic and abdominal region for which significant respiratory-induced motion is expected, today's standard-of-care is to additionally acquire a respiratory-correlated 4D-CT scan (section 2.6.2) to assess the range of motion for one averaged breathing cycle [10, 61].

2.5.2 Definition of target and organs at risk (OARs)

After the image acquisition, different target and OAR structures need to be contoured on the planning CT, following the guidelines defined by the *International Commission on Radiation*

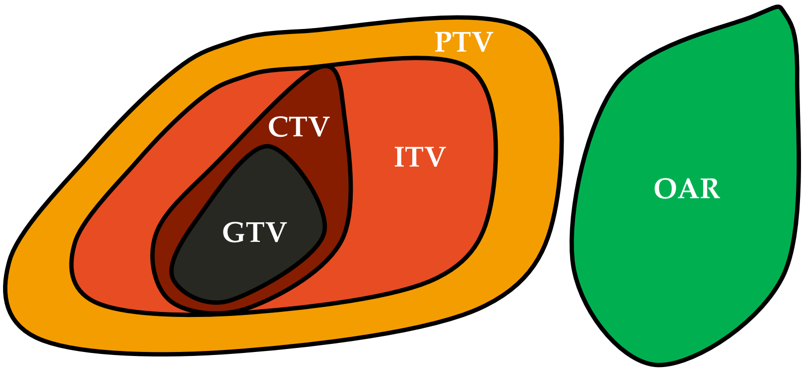

FIGURE 2.16: **Target and normal tissue structures defined by the ICRU** [107]. The different volumes are defined in the text. GTV: gross tumor volume. CTV: clinical target volume. ITV: internal target volume. PTV: planning target volume. OAR: organ at risk.

Units and Measurements (ICRU). In the radiotherapy planning and delivery process, several uncertainties exist that can lead to statistical and systematic errors during treatment delivery which can potentially compromise the patient outcome. Report 83 of the ICRU [107] defines several volumes and margins to account for these uncertainties and to ensure that a sufficient dose is delivered to the tumor tissue with a high probability. The most important volumes used in clinical practice are illustrated in Figure 2.16 and described in the following.

The *gross tumor volume* (GTV) "is the gross demonstrable extent and location of the tumor" [107]. This is the volume in the imaging data in which the tumor tissue is clearly visible and distinguishable from the surrounding anatomy. For some tumor entities, additional MRI or positron emission tomography (PET) images can be acquired to obtain complementary morphological information through the superior soft tissue contrast of MR images or functional data on physiological processes of the tumor tissue. These images are registered (section 2.4) to the planning CT dataset and can be used for a more accurate GTV segmentation [107]. Current clinical studies investigate whether a dose-escalation (termed *boost* or *dose painting by numbers* [108, 109]) in sub-regions within the GTV, identified through functional imaging data, can lead to a higher TCP and improved patient outcome.

The *clinical target volume* (CTV) "is a volume of tissue that contains a demonstrable GTV and/or subclinical malignant disease with a certain probability of occurrence considered relevant for therapy" [107]. The CTV includes the GTV, expanded by a margin to include suspected microscopic tumor spread around the GTV or regional infiltration into lymph nodes that cannot be identified on imaging data [107]. The GTV and CTV delineation is one of the most crucial steps in the radiotherapeutic workflow. An erroneous segmentation introduces systematic errors that directly impact all subsequent steps in the radiotherapy workflow chain [110]. Since the GTV and CTV segmentation depend on the physician's clinical experience, multiple studies could demonstrate that a high inter- and intra-observer variability of target structure delineations exists, which remains one of the major challenges in clinical radiation oncology [111].

The *internal target volume* (ITV) is defined as the "CTV plus a margin taking into account uncertainties in size, shape, and position of the CTV within the patient" [107]. The ITV is only defined for moving targets and is described in detail in section 2.6.3.

The *planning target volume* (PTV) consists of the CTV or ITV, expanded by an additional margin to "specifically [account] for uncertainties in patient positioning and alignment of the therapeutic beams during the treatment planning, and through all treatment sessions" [107]. While the GTV and CTV are purely anatomical volumes derived from imaging data, the PTV additionally depends on the patient positioning accuracy, motion management strategy (section 2.6), image guidance (section 2.6.4), treatment plan adaptation (section 2.6.5), radiation quality, delivery technique, and beam directions (in particle therapy) used during treatment. In clinical practice, the PTV margin is often a generic isotropic expansion of the CTV or ITV based on studies investigating the systematic and statistical uncertainties [107]. A formula to derive the extent of this margin is presented in section 2.6.3 [110]. Due to the volumetric effect, the PTV margin considerably enlarges the high-dose volume. Technical advancements in radiation oncology aim to reduce the aforementioned uncertainties to allow a safe reduction of the PTV margin to achieve a higher normal tissue sparing while keeping the TCP constant.

The *organs at risk* (OARs) "are tissues that if irradiated could suffer significant morbidity and thus might influence the treatment planning and/or the absorbed-dose prescription" [107]. In the treatment plan optimization process (section 2.5.5), the dose to these OARs is minimized to reduce the NTCP and the risk of acute or late side effects.

Today, the CT images are still segmented manually or with the aid of semi-automatic algorithms by physicians, based on their clinical experience. The latest developments in artificial intelligence, such as convolutional neural networks (CNNs) for organ segmentation, will likely lead to an increasing application of automatic algorithms in clinical routine [112]. In the future, this could enable a more consistent target and OAR delineation and would significantly accelerate the definition of the critical structures on the imaging data.

2.5.3 Dose prescription and treatment fractionation

The goal of a radiotherapeutic treatment is to kill or inactivate all clonogenic malignant tumor cells. This is achieved by the dose deposition in the tumor cells, through which the DNA is damaged. If the DNA damage is complex and severe enough, the cell will undergo apoptosis or lose its ability for cell division. However, small damages to the DNA, such as single-strand breaks, can be repaired by the cell. Increasing the dose to the tumor tissue increases the probability of lethal DNA damages, the TCP, and the chances of a cancer cure. At the same time, the probability and severity of acute or late side effects are correlated to the dose delivered to healthy tissue [10]. The physician prescribes a minimum dose value to be delivered to the target to achieve an acceptable TCP based on guidelines and study protocols. By following guidelines such as from the *Quantitative Analysis of Normal Tissue Effects in the Clinic* (QUANTEC) review [113], the maximum tolerable doses to the individual OARs are prescribed.

Except for stereotactic radiosurgery, the prescribed dose is not delivered in a single radiotherapy session but is split up into partial dose deliveries over the course of several weeks with typically five treatment sessions per week. This concept is called *fractionation* and is motivated by the observation that most healthy tissue cells have a higher recovery rate from radiation-induced damages than tumor cells. Through the multiple treatment fractions, a higher total dose can be delivered to the tumor tissue than if the dose was only delivered at once. Otherwise intolerable normal tissue damages would occur. Due to several biological processes, the clinically observable effects of the radiation dose do not solely depend on the total delivered dose accumulated over all fractions but also depend on the irradiated tissue-type, the number of fractions n and the fractional dose d. In clinical practice, the *biologically effective dose* (BED) is considered [10]:

$$\mathrm{BED} = nd\left(1 + \frac{d}{\alpha/\beta}\right) \qquad [\mathrm{BED}] = \mathrm{Gy}\,, \tag{2.66}$$

where α/β is a tissue-specific parameter of the *linear quadratic model*. The description of this model and the underlying biological principles is beyond the scope of this thesis. The interested reader is referred to radiobiology textbooks [10, 114]. In conventional fractionation schemes, n is in the order of 20–30 and d approximately 2 Gy [10]. With the steadily improving dose conformality of modern IGRT and the, in turn, reduced PTV margins, less dose is delivered to OARs. This allows a *hypofractionation* where d is increased and n is reduced. As examples of hypofractionation schemes, with the MR-Linac (section 3.1), it is feasible to safely deliver 8×7.5 Gy or 5×11 Gy to central lung tumors [35].

2.5.4 Medical linear accelerator and treatment delivery techniques

Within the field of photon radiotherapy, different models of medical linacs from different vendors exist, which offer different techniques for the delivery of the planned dose to the patient. Over the last decades, important technical and computational advancements allowed for the development of treatment delivery techniques with steadily increasing precision. The increased flexibility of these techniques allows the delivery of highly conformal dose distributions to the target at the cost of higher complexity of the treatment machine and treatment planning algorithms. An exemplary medical linac with its main components is depicted in Figure 2.17. The rotating gantry of a linac enables irradiation from all angles around the patient's craniocaudal axis. The multileaf collimator (MLC) allows the treatment field's shaping and decomposition into small partial fields, called segments, for a fixed gantry angle. In IMRT, modulation of the intensity of the treatment beam over time adds further degrees of freedom for the optimization. Important treatment delivery techniques used in clinical practice today are *step-and-shoot IMRT*, *dynamic IMRT*, and *volumetric intensity-modulated arc therapy* (VMAT). In step-and-shoot IMRT – the only delivery technique currently available at the ViewRay MRIdian MR-Linac (section 3.1.4) – multiple segments with varying intensities are delivered for fixed beam angles while the gantry and MLC leafs are stationary. A faster delivery time and even higher number of degrees of freedom can be achieved through dynamic IMRT, where the MLC moves at fixed gantry angles, or VMAT, where the beam is continuously turned on during continuous gantry rotation and MLC movement [6, 10, 61, 115].

Besides physical considerations based on the desired conformality and flexibility of the beam delivery, the choice of the delivery technique depends on the availability and capabilities of the systems at the radiation oncology facility and practical considerations (workload) and economic aspects (patient throughput) [10].

2.5.5 Treatment plan optimization

Once the segmentation, the choice of the treatment delivery technique, and the dose prescription have been finished, a clinical medical physicist performs a patient-specific and delivery system-dependent treatment plan optimization. Today, the beam angles or start and endpoint angles of the arcs in VMAT have still to be set manually to reduce the overall complexity of the optimization problem. The prescribed target dose and maximum tolerable OAR doses serve as planning objectives. Each objective is assigned a weight that determines the impact of the corresponding term in the total cost function. In the automatic inverse iterative optimization process, the cost function value is calculated based on the fulfillment of the planning objectives. The optimal trade-off between the competing objectives is determined by the variation of the MLC positions, the number of segments, and the corresponding fluences for each beam angle. Due to the high number of degrees of freedom in IMRT, finding the optimal solution is not trivial and computationally demanding [10].

In each iteration of the optimization, the dose distribution in the patient's tissue needs to be computed based on the currently planned segments. Several dose calculation algorithms

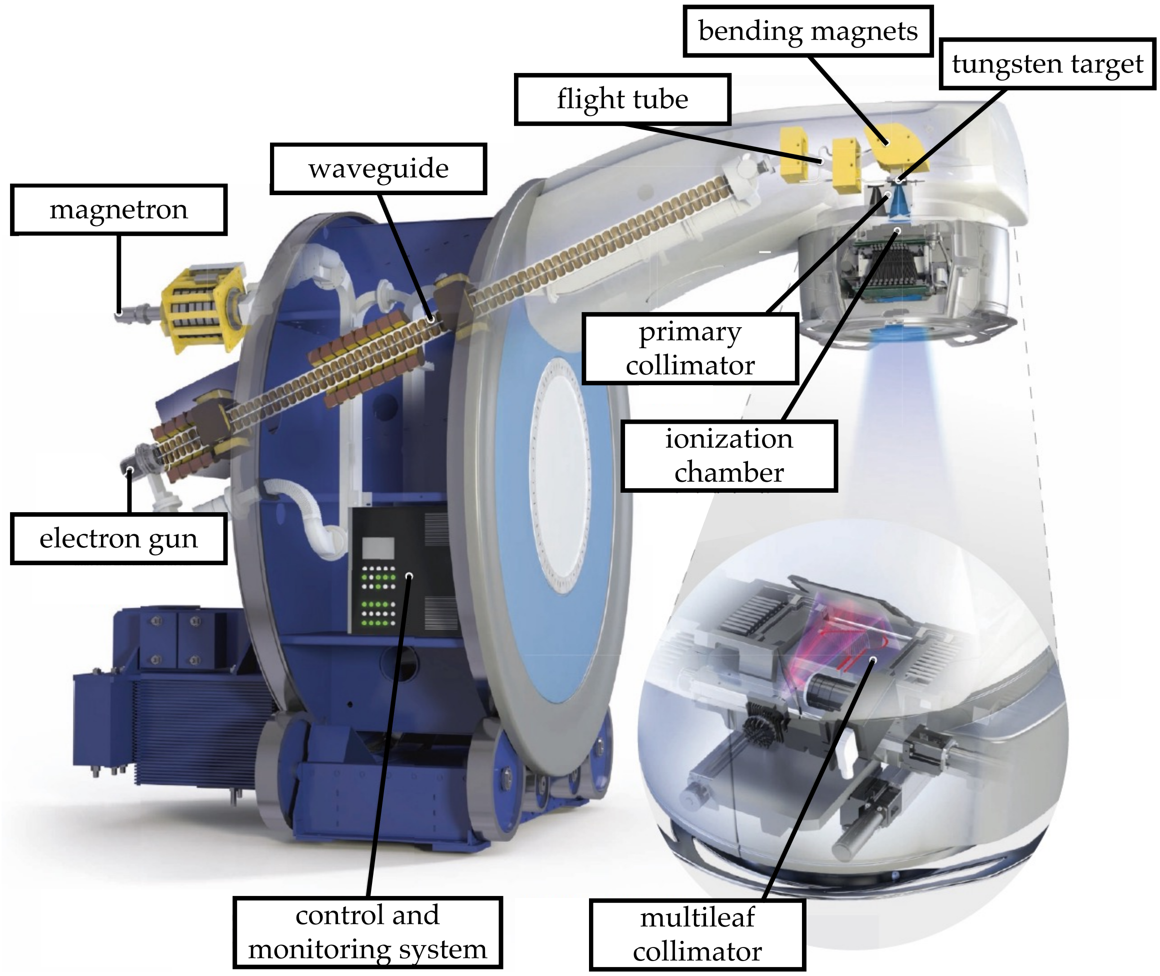

FIGURE 2.17: **Main technical components of an exemplary medical linac.** In the depicted linac, electrons are produced in an electron gun and accelerated in the waveguide by an RF field provided by the magnetron. The electron beam is deflected by bending magnets onto a tungsten target where the photon bremsstrahlung used for the treatment is produced. The photon beam is collimated, shaped by a MLC, and monitored by ionization chambers in the linac head. Figure adapted from [10].

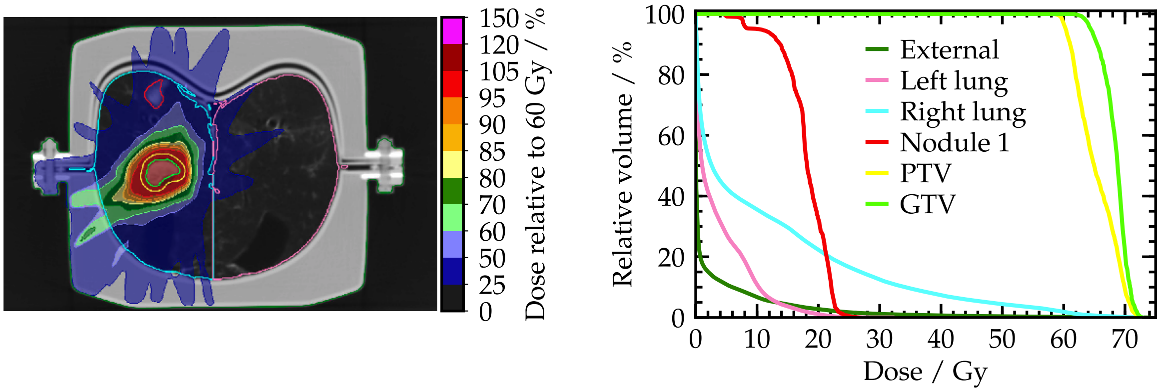

FIGURE 2.18: **Dose distribution and dose-volume histograms.** An exemplary dose distribution on an axial CT slice (left) of a porcine lung phantom and the corresponding cumulative DVHs (right) are depicted. A dose of 60 Gy was prescribed to the PTV, shown in yellow. The DVH curves represent the fractional volumes of the target structures and OARs that receive at least the dose level indicated on the x-axis. These figures were created based on data from Chapter 6.

exist for this purpose, including kernel-based superposition and convolution methods, such as pencil beam and collapsed cone algorithms, and Monte Carlo simulations. These algorithms use different degrees of simplifications to reduce the computational effort. The reduced complexity comes at the cost of a lower accuracy of the resulting dose distribution, particularly in heterogeneous tissues like the lung. The most accurate but most computationally demanding methods are Monte Carlo simulations, where the different interaction processes described in section 2.1 are explicitly stochastically modeled. Modern treatment planning systems allow graphics processing unit (GPU)-accelerated Monte Carlo dose calculations with high accuracy and acceptable calculation times in the order of a few minutes [6, 10].

When the clinical physicist has determined an acceptable solution for the given clinical objectives, a radiation oncologist assesses the plan from a clinical standpoint. The quality of the plan is judged based on the dose distribution maps overlayed on the delineated planning CT image. Additionally, the dose distributions within the different target and OAR structures are typically assessed by cumulative *dose-volume histograms* (DVHs), defined as [107]:

$$\mathrm{DVH}_s(D) = 1 - \frac{1}{V} \int_{0}^{D_{\max}} \frac{\mathrm{d}V(D)}{\mathrm{d}D}\,\mathrm{d}D\,, \tag{2.67}$$

where one DVH_s for each structure s is calculated by considering only the dose distribution within the respective structure volume. Figure 2.18 depicts an exemplary dose distribution and the corresponding DVHs. If the treatment plan is deemed unsatisfactory, another iteration of treatment plan optimization is performed based on altered clinical objectives, e.g., to achieve a further reduction of dose to an OAR or a higher or more homogeneous dose distribution within the PTV. If the plan quality is deemed sufficient, a patient-specific QA check is performed [6, 10].

2.5.6 Quality assurance (QA)

As the last step of the conventional treatment preparation process, QA measurements or independent dosimetric calculations (section 3.1.6) are performed to ensure the patient's safety. In regular machine-related QA measurements, clinical medical physicists and radiotherapy technologists check whether all linac components are working properly within certain tolerance limits. To verify that the intended treatment machine can actually deliver the planned dose distribution, patient-specific QA measurements with dedicated phantoms and detectors are performed to measure the delivered dose distributions in 2D or 3D. If all QA checks are passed, the patient is treated according to the treatment plan [6, 10, 61].

2.6 Motion management techniques and image guidance

In conventional radiotherapy, a treatment plan is generated on a 3D planning CT image, acquired several days before the start of treatment (section 2.5.1). This plan is then delivered to the patient over the course of several weeks. A patient's anatomy can change on different time scales, affecting the relative position between the treatment beam, the tumor target, and the OARs. This section summarizes motion management and image-guidance techniques to account for the different types of changes that can occur over the course of radiotherapeutic treatment delivery.

Section 2.6.1 defines inter- and intrafractional changes, followed by an overview of methods to quantify these in section 2.6.2. In section 2.6.3, passive motion management techniques are described that aim to prospectively account for these uncertainties in the treatment planning phase. The principles behind IGRT and ART are explained in sections 2.6.4 and 2.6.5. The chapter is concluded by a description of active motion management techniques that are applied during beam delivery in section 2.6.6.

2.6.1 Inter- and intrafractional changes

On each day of treatment, the goal is to position the patient, in particular the tumor tissue, in the same way as during the planning CT acquisition to ensure that the dose is delivered to the patient as planned. However, changes on different time scales can occur that lead to variations in the position, orientation, or shape of the target with respect to the treatment beam. These include anatomical alterations between different treatment fractions (*interfractional changes*) or physiologically-induced motion occurring on shorter time scales, within a treatment session (*intrafractional changes*). Interfractional changes frequently observed during lung cancer radiotherapy include tumor growth or shrinkage, weight loss of the patient, or normal tissue changes such as pleural effusion and the onset or resolution of atelectasis [13, 21, 22, 116]. For tumors located in the lung, intrafractional changes caused by respiration or rhythmic cardiac motion are the main causes of motion. Respiratory-induced target motion can be larger than 2 cm, patient-specific, difficult to predict, irregular, and can change from one day to another [13, 40, 116–121]. The assessment and management of this motion are of major importance. These movements can lead to an underdosage of the tumor target or OAR overdosage when unaccounted for, particularly in hypofractionated treatments (section 2.5.3) [118, 122].

2.6.2 Assessment of respiratory-induced target motion for treatment planning

The most commonly used method to investigate the extent of respiratory-induced target motion is 4D-CT. For helical 4D-CT, projections of the patient are continuously acquired along with a surrogate signal that is correlated with the position of the tumor. Examples of such a surrogate signal include spirometry devices, abdominal pressure belts, and optical surface scanners [82]. After the raw data acquisition, the surrogate signal is used to assign the projections to several breathing cycles according to its phase or amplitude. This is followed by a reconstruction of 3D images of the different breathing states. Oversampling the respiratory motion during the raw data acquisition is needed to not miss slices in the reconstructed images. Multislice respiratory-correlated spiral 4D-CT was introduced in the early

2000s. Over the years, it has become the standard modality to assess the range of motion of tumors in the thoracic and abdominal region [123–128]. As described in section 2.6.3, this information can be incorporated into the treatment planning process.

4D-CT imaging is associated with several limitations and drawbacks. This includes the increased imaging dose compared to 3D-CT and a sub-optimal breathing phase assignment when the surrogate signal is poorly correlated with the target motion [82]. An important uncertainty associated with the motion assessment based on 4D-CT data is that only a single averaged breathing cycle is reconstructed. It is questionable whether the motion sample that is acquired over a typical time-span of 10 seconds is sufficiently long to representatively characterize the target motion that is expected during radiotherapy treatment delivery. The purpose of several studies in literature has been to answer this question [129–133], including the study presented in Chapter 4 of this thesis [116].

A further X-ray-based motion assessment modality is 4D-CBCT (section 2.2.3), where the patient is imaged in treatment position on the couch of the linac directly before beam delivery. These scans can potentially increase the patient setup accuracy [134] but the motion information is so far not used clinically for online adaptations of the treatment plan (section 2.6.5).

Respiratory-induced target motion can furthermore be assessed using time-resolved 2D or 3D-MRI scans [40, 41] (section 3.2.2). A proposal of how real-time 4D-MRI scans could be incorporated in the treatment workflow with a conventional linac is presented in Chapter 4.

2.6.3 Passive motion management techniques

Passive motion management techniques aim to prospectively account for intra- and interfractional changes in the treatment planning phase. These techniques include the definition of motion-encompassing margins, or abdominal compression to reduce the motion amplitudes within the lung and abdomen.

The definition of motion-encompassing target volumes enables a time-efficient treatment delivery and – except for the 4D-CT scan – no special equipment is needed. Different approaches can be used to account for respiratory-induced target motion, including the ITV [107], the mid-ventilation [135], and the mid-position techniques [136] which are described in the following.

Internal target volume (ITV)
As defined in section 2.5.2, the ITV accounts for the CTV's intrafractional motion-related uncertainties [107]. For the delineation of the ITV, a 4D-CT scan is acquired to assess the typical motion trajectory of the CTV. The ITV is then obtained by delineating the CTV on ideally all (and at least in the inhale and exhale) breathing phases and calculating the union of all CTV positions [120]. This concept assumes that the motion observable on the 4D-CT represents all possible positions of the CTV that occur throughout the course of treatment [132]. The validity of this assumption is investigated in Chapter 4. The ITV is expanded by a PTV margin, as described further below. The ITV concept yields large PTV volumes, particularly for tumors in the lower lung, which can move by few centimeters. As a consequence, a large volume of healthy tissue is inevitably irradiated with a high dose.

Mid-position and mid-ventilation target volume (midV)
Due to the large volumes of the ITV, the mid-ventilation and mid-position concepts were developed as alternative passive motion management techniques. In the mid-ventilation approach, the centroid position of the CTV centroids in all breathing phases of a 4D-CT image (section 2.6.2) is calculated. The CTV with the minimal distance of its centroid to this point is then defined as the mid-ventilation target volume (midV) [135]. The mid-position

concept is a refinement of the mid-ventilation approach, where the target volume is the geometric time-weighted mean tumor position, reconstructed from the CTV positions in all phases of the 4D-CT image, using DIR [136]. For both of these target volumes, the motion uncertainty is then explicitly included in the PTV definition, which typically results in smaller PTVs than for the corresponding ITVs [119, 137] (Chapter 4).

Planning target volume (PTV)
During radiotherapeutic treatments over the course of typically a few weeks, systematic and statistical uncertainties in the position and shape of the GTV or CTV occur. The PTV is used during treatment planning to prospectively account for these uncertainties. Since, by definition, the inter- and intrafractional changes that occur during treatment are a priori unknown, generic PTV margins are derived from large patient cohorts. Van Herk et al. [110] proposed an analytical *margin recipe* to calculate the PTV margin $\boldsymbol{m}_{\mathrm{PTV}}$, based on the systematic (*preparation variations*) and statistical uncertainties (*execution variations*), $\boldsymbol{\Sigma}$ and $\boldsymbol{\sigma}$, which is widely used for PTV definitions in clinical practice today:

$$\boldsymbol{m}_{\mathrm{PTV}} = \alpha\boldsymbol{\Sigma} + \beta\boldsymbol{\sigma} - \beta\sigma_{\mathrm{p}}\,, \tag{2.68}$$

where σ_{p} describes the width of the treatment beam penumbra, and α and β are parameters based on cumulative probability distributions, derived in the original publication [110]. As an example, to ensure a minimum of 95% of the prescribed dose to the target for 90% of the patients, these values are $\alpha = 2.5$ and $\beta = 1.64$ [110] (see Table 4.1 for typical values of $\boldsymbol{\Sigma}$, $\boldsymbol{\sigma}$, and σ_{p}). Depending on the nature of the uncertainties $\boldsymbol{\Sigma}$ and $\boldsymbol{\sigma}$, the PTV margin can be anisotropic, especially when including intrafractional target motion. The different contributing systematic and statistical uncertainties in radiotherapy of lung tumors are described in more detail in section 4.2, where PTV margins are calculated for different ITVs and midVs.

2.6.4 Image-guided radiotherapy (IGRT)

IGRT describes the use of imaging modalities to visualize the patient's anatomy directly before or during beam delivery. The main purpose of today's IGRT techniques is to accurately position the patient and the target volume on the treatment couch at the linac. These images also serve to detect potential deviations with respect to the planning images that would have to be addressed by creating a new adapted treatment plan (section 2.6.5) [10].

A multitude of imaging modalities has been developed for IGRT in the past [82]. A survey of the American Society for Radiation Oncology members [72], conducted in 2014, reported that for lung cancer treatments, 77% of the departments used kV or MV CBCT (section 2.2.3), 51% used planar kV X-ray imaging, and 22% used MV portal imaging with an electronic portal imaging device (EPID) as IGRT technique. In 78% of cases, the IGRT techniques were used daily. Further modalities with a lower prevalence or that are used for entities other than lung cancer include ultrasound imaging, surface scanners, in-room CT scanners, and RF receivers to locate implanted electromagnetic fiducial markers [22, 72, 82, 118, 119]. The MR-Linac, described in detail in section 3.1, is an IGRT device relying on in-room MRI that was introduced in clinical practice only a few years ago. While it is not widespread at the moment, it is expected to gain importance and prevalence in the coming years.

Some of the IGRT modalities yield only static 2D or 3D images before treatment, while others can be used for real-time imaging during the treatment itself. The acquired motion information can be used for gating the delivery beam (section 2.6.6). IGRT is considered a standard in modern radiotherapy. The high patient positioning accuracy achievable with modern IGRT techniques allows smaller PTV margins than without using these methods [10, 72]. The full potential of the described imaging modalities can only be exploited by ART, described in the next section.

2.6.5 Adaptive radiotherapy (ART)

The concept of ART was already discussed in 1997 [138], but only through the technological developments in the last years, ART could transition from an academic concept to clinical reality. In ART, the treatment plan is adapted based on the image information provided by in-room IGRT modalities. This way, observed interfractional changes such as a variation of the patient weight, tumor volume, or biological parameters can be accounted for and an optimal treatment plan can be delivered in each fraction [122, 139]. Thus, ART intends to safely deliver the planned dose to the patient through the systematic monitoring of and timely reaction to anatomical variations [138].

The treatment plan can be adapted offline after completing a treatment fraction. This can be necessary when interfractional changes are detected that are deemed severe enough to compromise the accuracy of the dose delivery in the remaining treatment fractions. For instance, such a replanning process could be triggered by the observation of significant tumor shrinkage or patient weight loss detected on CBCT images that, if not accounted for, could lead to a deteriorated dose deposition in the next treatment fractions [76]. Through the clinical introduction of the MR-Linac (section 3.1), dedicated adaptation workflows, and fast dose optimization techniques, the re-optimization of the treatment plan while the patient is lying on the treatment couch has become feasible [140]. This is called online-ART and is described in more detail in section 3.1.6.

2.6.6 Active motion management techniques

In contrast to passive motion management techniques (section 2.6.3), active techniques aim to account for intrafractional changes during beam delivery, instead of in the treatment planning phase. These methods include active breathing control and breath-hold techniques, gated beam delivery based on a motion surrogate (section 3.1.7), or tracking [82].

In gating, a surrogate signal or 2D image is acquired during beam delivery with a temporal resolution that is high enough to resolve the physiological process that is inducing the target motion. Gating is primarily used for targets affected by respiratory motion, requiring a temporal resolution of a few Hz. The intrafractional motion monitoring can be achieved using different techniques, including MV portal imaging with an EPID, fluoroscopic planar or stereotactic imaging of the target itself, or implanted fiducial markers in the vicinity of the target, surface imaging, abdominal pressure belts, or cine MRI (section 3.1.7). The delivery beam is only switched on when the target or surrogate signal is located within a predefined tolerance region. The margins used for the residual motion within the gating window are considerably smaller than ITV or mid-position target volumes. A better sparing of OARs, a reduced integral dose to healthy tissue, a dose escalation to the target, and a hypofractionation of the treatment can potentially be achieved by gated beam delivery. As a drawback, through a reduced treatment beam usage efficiency, the overall treatment time is prolonged, and the overall complexity of the workflow and required equipment is increased [10, 82, 118, 119, 122, 128]. The overall system latency, i.e., the time that passes after detecting an out-of-tolerance deviation from the reference position until the delivery beam is switched off, is recommended to be shorter than 500 ms [21]. The clinical implementation of gated treatments at an MR-Linac is described in section 3.1.7.

In tracking, the treatment beam follows the motion of the tumor, thus enabling a 100% duty cycle during beam delivery [21]. This is achieved by adaptation of the MLC leafs in real-time based on a high-frequency and low-latency surrogate signal correlated to the tumor motion [82]. These systems need to be able to anticipate the target motion with prediction algorithms for an accurate dose delivery [21]. Tracking has been implemented at conventional linac systems at few academic centers [82], and is currently under development for MR-Linacs (section 3.1) [141]. Compared to passive motion management techniques, active methods can potentially reach a higher dose conformality and a decreased integral dose delivered to healthy tissue. On the contrary, these techniques are generally more complex, prolong the treatment time, and require specialized equipment and staff training [82, 118].

For these reasons, passive motion management techniques are widely used clinically today, particularly in conventionally fractionated radiotherapy [22, 116, 128]. A major advancement for active motion management techniques was the clinical introduction of MRgRT and MR-Linacs, that allow gated beam delivery based on real-time imaging data. In combination with daily treatment plan adaptations based on MR images acquired at the beginning of each treatment fraction, this enables beam delivery with higher conformality than achievable with conventional IGRT and passive motion management techniques. This is the topic of the next chapter.

Chapter 3

Magnetic resonance imaging-guided radiotherapy (MRgRT)

One of the latest major technological advancements in radiation oncology was the clinical introduction of combined MRI and linac devices (MR-Linac). The technological and clinical aspects of MRgRT with MR-Linacs are presented in section 3.1. A key technique for improved motion assessment in MRgRT is 4D-MRI, which is summarized in section 3.2. The chapter is concluded by section 3.3, where an overview of techniques under investigation in research to model the time-resolved patient anatomy before, during, or after beam delivery is given.

3.1 MRI-guided linear accelerator (MR-Linac)

The idea of combining an MRI scanner with a linac for advanced image guidance in radiotherapy was proposed at the 19th Annual ESTRO Meeting in 2000 by Lagendijk and Bakker [36]. The motivation behind this idea was the potential for improved treatment position verification enabled by the high soft tissue contrast of MRI and the possibility to acquire time-resolved 2D images during irradiation without additional dose to the patient. Lagendijk and Bakker hypothesized that "the integration of an MRI system with a linear accelerator [would] revolutionize radiotherapy" [36]. The main advantages of MRgRT compared to CBCT-based IGRT are further discussed in section 3.1.1. At the same time, they recognized that the design of such an integrated system involves major engineering problems due to the potential interactions between the MRI and the linac [36]. The main challenges that had to be solved before the clinical integration of such systems and further drawbacks of MRgRT are described in section 3.1.2.

The first prototype of an MR-Linac with a stationary horizontally oriented accelerator was constructed at the University Medical Center Utrecht, the Netherlands. The first proof-of-concept study of simultaneous MRI and irradiation was conducted with this prototype, published in 2009 [37, 142]. Four vendors and research institutes developed different combined systems in the following years. These systems are briefly presented in section 3.1.3.

The first clinical MRgRT system – the MRIdian by ViewRay Inc. (Oakwood Village, OH, USA) with three Cobalt-60 sources instead of a linac – was installed at Washington University in St. Louis, MO, USA. The first patient was treated with this system in January 2014 [15, 140]. In May 2017, the first patient worldwide was treated with an MR-Linac system, the Unity MR-Linac by Elekta AB (Stockholm, Sweden), at the University Medical Center Utrecht [143]. The use of Cobalt-60 sources requires more elaborate radiation protection compared to a linac and the beams produced by these sources have broader penumbras [144]. For these reasons, ViewRay developed their own MR-Linac system, presented in section 3.1.4, which started clinical operation in July 2017 at the Henry Ford Health System in Detroit, MI, USA [15]. This system uses a balanced Steady State Free Precession (bSSFP) sequence for imaging, which is described in section 3.1.5. As of 2021, more than sixty MR-Linac systems are in clinical use, with a steadily increasing number of institutions commencing patient treatments around the globe [42, 43].

MR-Linacs enable daily ART treatments with an altered clinical workflow compared to conventional CBCT-based IGRT, and gated treatments, which is described in sections 3.1.6 and 3.1.7.

3.1.1 Motivation for combining MRI and Linac

The development of MR-Linac systems was motivated by several advantages of MRI compared to CBCT imaging. In MRI, no additional dose is delivered to the patient. This enables frequent and time-resolved image acquisitions for treatment planning and monitoring without healthy tissue damages induced by ionizing radiation. This is particularly of interest for pediatric patients, for whom the avoidance of late side effects has a high priority [30]. The high and variable soft tissue contrast of MRI (section 2.3) enables a more accurate visualization and localization of tumor tissue compared to X-ray-based imaging modalities, especially in the abdominal region [15, 30, 45]. Combining frequent and online imaging with improved target localization allows daily treatment adaptations based on the latest anatomy [15, 140], and gated treatments [30, 92, 145] (sections 2.6.5 and 2.6.6) through real-time monitoring of the target motion with cine MRI during beam delivery. The higher accuracy of MR-guided treatment delivery potentially enables a reduction of PTV margins, hypofractionation, and target dose escalation without increasing side-effects [18, 20]. This allows a safe treatment delivery, even in challenging entities such as ultracentral thorax malignancies [34, 35]. High-dose adaptive MRgRT has the potential to increase the overall patient survival without increasing the risk for acute toxicity, as indicated by the promising results of the first clinical studies describing MR-guided treatments of inoperable pancreatic cancer [146].

Further techniques enabled by MR-Linacs that are not routinely used today could play an important role in the future. Synthetic CT methods (section 3.3.2) could make the planning CT acquisition obsolete, which is referred to as “MR-Only” radiotherapy [147]. The functional MRI information acquired with the patient in treatment position could be integrated in the plan adaptation process (*biology-guided adaptive radiotherapy*) [30, 90, 148]. The frequent imaging with different contrasts and the retrospective analysis of the delivered dose using machine log files and cine MRI during treatment could serve as input data for advanced treatment adaptation methods and dose-response assessment studies [20, 30, 45, 50, 145]. The high precision achievable through real-time beam-on imaging can furthermore enable the treatment of non-oncological pathologies [149, 150]. A case study on the radioablation of sustained ventricular tachycardia with an MR-Linac has recently been published [151].

3.1.2 Challenges of MRgRT

Several technical challenges caused by the mutual electromagnetic interference of MRI and linac components had to be solved by the vendors and research institutes during the development of MR-Linacs [20].

The fringe magnetic fields of the MRI scanner disturb the path of the electrons in the accelerator components due to the Lorentz force. The electromechanical controls of moving elements such as the motors attached to the leafs of the MLC may not function properly in a magnetic field. Therefore, the sensitive linac components have to be shielded from the main magnetic field. This can be achieved by using shielding material or through active shaping of the fringe fields [20].

Ionization chambers are often employed for reference dosimetry. When used for the QA of MR-Linacs, the trajectories of the electrons in the sensitive air volume of the chambers are affected by the magnetic field. As a result, the detected charge and dose deviate from measurements without the presence of a magnetic field. The detector response depends on the magnetic field strength and the orientation of the ionization chamber with respect to the magnetic field direction. Correction factors have to be applied to the detected signal to account for these effects [152, 153].

Surface receiver coils are placed on the patient's body around the volume of interest to maximize the signal-to-noise ratio (SNR) of MR images. The coils used in MRgRT have to be placed in the beam path and specially designed, using low-density material to minimize the attenuation and avoid radiation-induced currents [20].

The Lorentz force affects the dose deposition within the patient's body, with increasing severity for higher magnetic field strengths [154]. This needs to be accounted for during treatment planning. Depending on the orientation of the beam path relative to the static magnetic field (perpendicular or parallel), this can lead to a skewing of the dose distribution or beam focusing effects, respectively. Furthermore, the skin dose can be increased through the so-called *electron return effect* [155]. These effects need to be modeled in Monte Carlo simulation during treatment planning.

Not only can the MRI influence the linac components, but also vice versa. RF signals produced by the linac components can introduce noise in the MR images. When ferromagnetic materials, such as the MLC and bending magnets, are placed within the static B_0 field, the magnetic field changes, and its homogeneity decreases. This can lead to a degraded quality or geometric distortions of the MR images. These effects can be minimized through RF shielding of the linac components. A proof-of-concept study by Kontaxis et al. [156], performed at the Elekta Unity MR-Linac, demonstrated that the MR image quality is negligibly affected by the linac if such measures are taken, even during VMAT delivery with gantry rotations and MLC movements during imaging.

Further challenges that have to be considered in MRgRT include geometric distortions of the MR images (section 2.3.9). These can introduce systematic errors in the treatment planning process [30, 84, 91]. The MR images lack electron density information needed for treatment planning (section 2.5.1). These have to be either propagated from CT datasets to create synthetic CTs (section 3.3.2) using multimodal DIR (section 2.4), or can be obtained from bulk density assignments [157] or deep learning methods [158, 159]. Depending on the design of the MR-Linac, the photon beam quality is deteriorated when it has to penetrate through MRI components [27]. Furthermore, compared to conventional linacs, MR-Linac patient couches have a limited range of motion and do not allow rotations [27, 45]. This restriction, however, can be compensated for by treatment plan adaptations [157].

The installation and maintenance of MR-Linacs are considerably more expensive compared to conventional linacs equipped with CBCT scanners. The number of patients that can be treated per day is reduced through the prolonged fraction times. Patients that suffer from claustrophobia or experience intolerable pain in the lying treatment position cannot be treated at these machines [32]. The higher conformality and precision of the dose delivery achievable with MR-Linacs in combination with the increased overall complexity leads to a higher sensitivity to treatment delivery errors caused by technical or human failures. For instance, if PTV margins are chosen too small, this will lead to an underdosage of tumor tissue at the edges of the target volume [110]. Moreover, today's clinical workflow (section 3.1.6) relies on DIR (section 2.4) of CT to MR images [100] for the creation of pseudo-CTs generated based on MRI data [40]. This can be challenging and a potential error source [30].

MRgRT still needs to demonstrate that these drawbacks are sufficiently traded off by improved local control, reduced toxicities, or improved overall survival compared to today's standard-of-care IGRT treatments [30].

TABLE 3.1: **Specifications of MR-Linac systems.** The technical specifications of the four MR-Linac systems described in section 3.1.3 are summarized based on information provided in [20, 31, 38]. The beam orientation relative to the main magnetic field – perpendicular ($\perp$) or parallel ($\|$) – is indicated.

System	MRIdian	Unity	Aurora	Australian
Company/institution	ViewRay	Elekta	MagnetTx University of Alberta	Ingham Institute
Field strength	0.35 T	1.5 T	0.5 T	1.0 T
Linac	6 MV (formerly ^{60}Co)	7 MV	6 MV	4/6 MV
Beam orientation	$\perp$	$\perp$	$\|$	both
Commercial	yes	yes	not yet	no
First patient treated	02/14 (^{60}Co) 07/17 (linac)	05/17	-	-
References	[26, 45]	[27, 157]	[29]	[28]

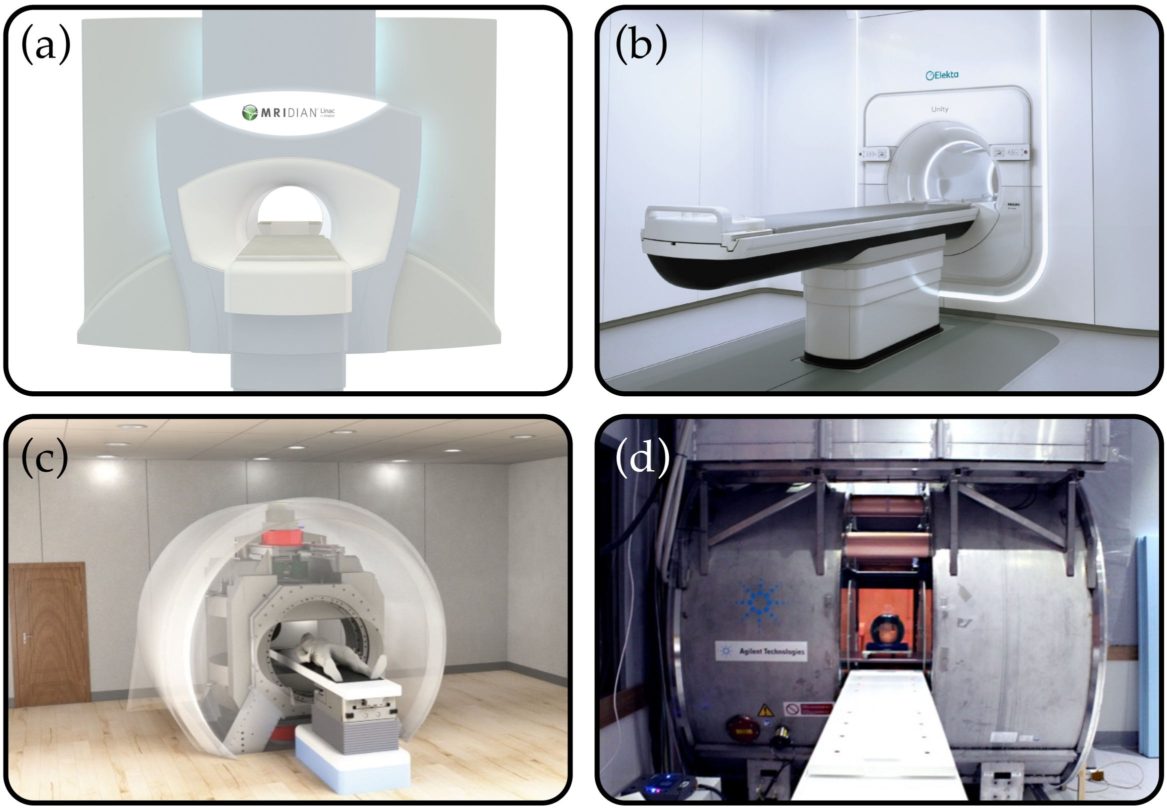

FIGURE 3.1: **Overview of MR-Linac systems.** (a) Photograph of the ViewRay MRIdian MR-Linac [42]. (b) Photograph of the Elekta Unity MR-Linac [43]. (c) CAD drawing of the MagnetTx Aurora system [160]. (d) Photograph of the Australian MR-Linac [161].

3.1.3 Overview of available MR-Linacs

At the time of writing, two MR-Linac systems are commercially available: the ViewRay MRIdian [26, 45] and the Elekta Unity [27, 157]. Two further systems are under development at university-based research institutions: the Australian MR-Linac [28] and the MagnetTx Oncology Solutions Aurora system [29]. Table 3.1 summarizes the main technical features of these four devices, depicted in Figure 3.1. The main differences between the systems are their magnetic field strength, the magnet and MLC design, and the orientation between the magnetic field and the beam direction.

The experimental studies in Chapters 5 and 6 of this thesis were conducted on MRIdian systems. This MR-Linac is presented in more detail in the following section. A thorough description of the other systems can be found in the respective references given in Table 3.1, in a book chapter by Whelen et al. [20], and the review article by Liney et al. [38].

3.1.4 The ViewRay MRIdian MR-Linac

The ViewRay MRIdian MR-Linac imaging unit is a 0.35 T split superconducting magnet with a 28 cm gap between the two magnet halves and a 70 cm wide bore. The RF transmit coils and gradient coils with a strength of 18 mT/m are located inside the MRI housing. Two surface receiver coil pairs are available: a coil pair with 2 × 6 channels for the treatment of malignancies in the thoracic, abdominal, or pelvic region and a coil pair with 2 × 5 channels for the treatment of head and neck tumors. The coils are embedded in low-density foam for minimal beam attenuation. The vendor assures a geometric accuracy of the MR images better than 1 mm on average within a 20 cm diameter of spherical volume (DSV) and better than 2 mm on average within a 35 cm DSV for the available MRI sequences. The first clinical version of the MRIdian only allowed imaging with a bSSFP sequence. This sequence was used in the experimental studies in Chapters 5 and 6 and is described in more detail in the next section. The latest clinical version of the MRIdian allows acquiring additional MR images with Turbo Spin Echo sequences yielding a T_1- or T_2-weighted contrast, or diffusion-weighted images [162, 163].

The patient is positioned on a treatment couch with the aid of in-room lasers and is then moved inside the bore to position the tumor target at (or in proximity to) the coinciding MRI and linac isocenter. The treatment couch can be moved in craniocaudal and, to a certain degree, in right-left (RL) and anterior-posterior (AP) direction for accurate positioning. All 6 MV flattening-filter-free (FFF) linac components are assembled on a gantry at the position of the gap between the two magnet halves. The components are surrounded by cylindrical layered ferromagnetic shields for magnetic field shielding and "RF buckets" (Figure 3.2) consisting of copper and carbon fiber for RF shielding (section 3.1.2). In the original version of the MRIdian, three Cobalt-60 sources were used instead of a linac. The linac has a dose rate of 6 Gy/min and a source-to-axis distance of 90 cm. The beam path is perpendicular to the magnetic field. It is shaped by a double-stack, double-focused MLC, which allows the collimation of fields with sizes between $0.2 \times 0.4\,\text{cm}^2$ and $27.4 \times 24.1\,\text{cm}^2$. The dedicated treatment planning and delivery system supports step-and-shoot IMRT treatments, on-table plan adaptations (section 3.1.6), and automatic beam gating based on cine MRI and structure tracking (section 3.1.7) [26, 45].

3.1.5 The balanced Steady State Free Precession (bSSFP) sequence

The ViewRay MRIdian MR-Linac offers 3D-MRI and cine MRI with a bSSFP sequence (Figure 3.3) [45, 92]. A train of equally-spaced RF pulses is applied in this sequence. The RF pulses are interleaved by periods of *free precession* with a duration of the repetition time $T_R \ll T_2 \leq T_1$, where T_R is in the order of a few ms, and an echo formation at $T_E \approx T_R/2$. The

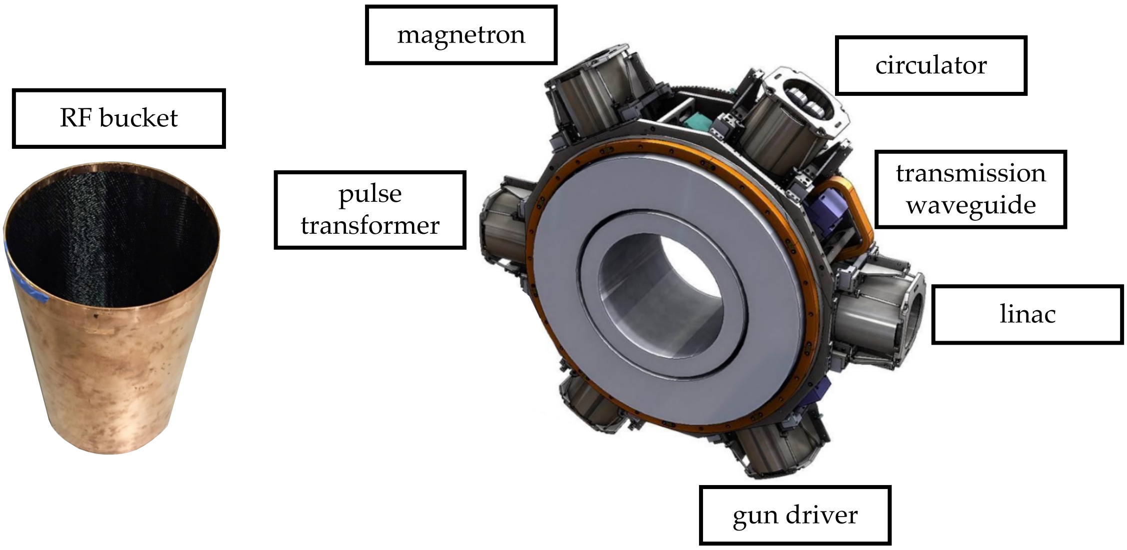

FIGURE 3.2: **MRIdian linac component shielding.** The left photograph shows an empty cylindrical compartment (*RF bucket*) used for RF shielding, consisting of an outer copper and an inner carbon fiber surface. The linac components are additionally surrounded by cylindrical layered ferromagnetic material to shield them from the magnetic field. All linac components indicated in the right CAD drawing are mounted on the gantry around the MR scanner. Figure adapted from [164].

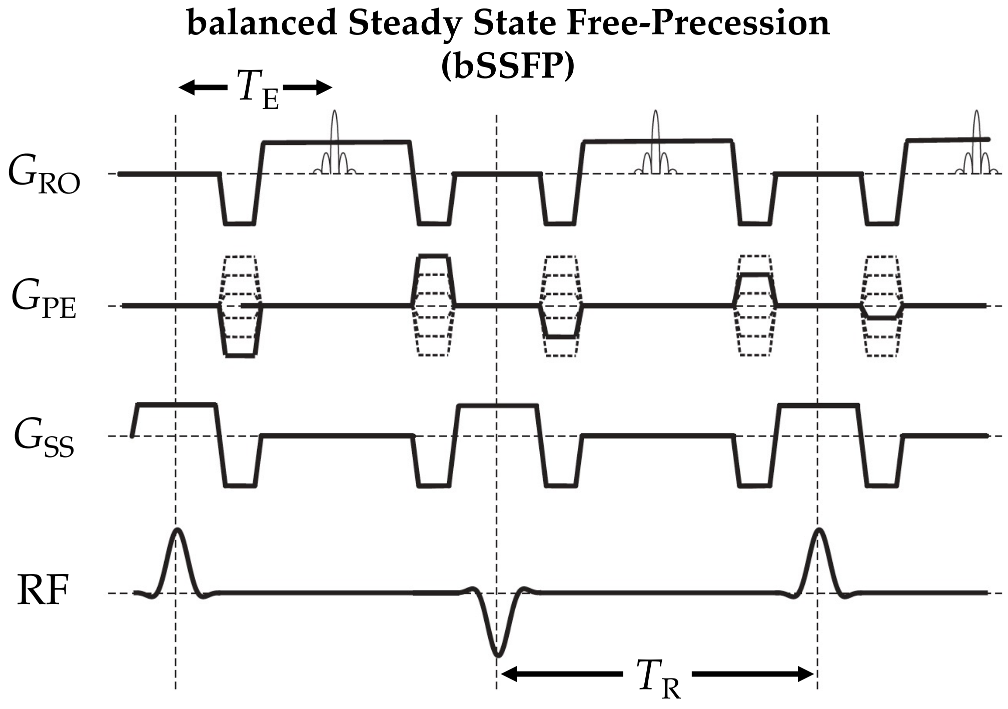

FIGURE 3.3: **bSSFP pulse sequence.** The sketch shows the applied gradients and RF pulses of the bSSFP sequence. The signal detected by the receiver coils is indicated in the same row as the read-out gradient G_{RO}. The sign of the RF pulse alternates with each repetition. The integral of all applied gradients over each repetition time T_R is zero. Figure adapted from [165]. SS: slice selection. PE: phase-encoding. RO: read-out (frequency-encoding). T_E: echo time. T_R: repetition time. RF: excitation pulse.

applied gradient moments are fully balanced between two consecutive excitation pulses. In the transient state directly after the start of imaging, the images are prone to artifacts, and the image contrast is changing in a complex fashion. After a few seconds, a steady state is reached, where the longitudinal and transversal magnetization vector amplitudes reach a dynamic equilibrium, and the image contrast does not change anymore. The time until this steady state is reached can be shortened by the application of preparation pulses. In the steady state, the magnetization is a superposition of different transversal and longitudinal states, leading to T_2/T_1-weighted contrast [166]:

$$S \propto \frac{M_0}{2}\sqrt{\frac{T_2}{T_1}}, \tag{3.1}$$

with the signal S and thermal equilibrium magnetization M_0. The image contrast depends on the tissue-specific properties (T_1 and T_2 relaxation times) and sequence-specific parameters (T_R, T_E, and α) [166]. In bSSFP images, fats and fluids appear bright, and other tissues appear darker [165]. Advantages of the bSSFP sequence include the high frame rates (typical acquisition times of 180–500 ms per 2D frame [40]), low sensitivity to motion artifacts, and a high SNR due to the steady magnetization and fully balanced gradients. A disadvantage of this sequence is that it is prone to banding artifacts originating from slight off-resonances and B_0 inhomogeneities, visible as dark lines in the images [166].

3.1.6 Clinical workflow of online-adaptive MR-Linac treatments

This section describes the clinical workflow for online-adaptive treatments at the ViewRay MRIdian MR-Linac, sketched in Figure 3.4. For a description of the (in many aspects similar) workflow at the Elekta Unity MR-Linac, the interested reader is referred to references [143] and [157].

For treatment planning, a 3D-MRI of the patient in treatment position is acquired at the MR-Linac in addition to the planning CT (section 2.5). A bSSFP sequence (section 3.1.5) with an in-plane resolution of $1.5 \times 1.5\,\text{mm}^2$ and a slice thickness of 1.5 mm or 3 mm is used for this purpose. For moving targets, this image is acquired in breath-hold to obtain a reference image for gated treatments (section 3.1.7) and reduce motion artifacts.

The planning CT is rigidly or deformably registered (section 2.4) to the planning MRI to transfer the electron density maps needed for treatment planning. The target and relevant OARs are segmented on the planning MRI. A step-and-shoot IMRT plan is optimized with a Monte Carlo dose algorithm on the planning synthetic CT. The static magnetic field is explicitly taken into account during the dose calculation and optimization. The planning phase is concluded by reviewing and approving the treatment plan by a physician and a physicist before performing QA checks (section 2.5.6) [15, 45].

In each fraction during the course of treatment delivery, the patient is set up in treatment position at the MR-Linac, and a setup 3D-MRI similar to the planning MRI is acquired. The target and OAR contours as well as the electron density maps are transferred from the planning image to this setup MRI using DIR. The deformed structures are checked and, if necessary, are recontoured by a physician [15, 45]. Once the contours have been approved, the original treatment plan is recalculated on the daily segmented synthetic CT. The resulting dose distribution and DVHs are compared to the initial treatment plan. The operator can decide whether to treat the patient with the original plan or whether the observed differences are unacceptable, in which case an adapted treatment plan is created. After optimization and review of the adapted plan, QA checks have to be performed. This cannot be done by measurements since the patient is lying on the treatment couch during the adaptation process. Therefore, the adapted plan is checked with an independent secondary Monte Carlo

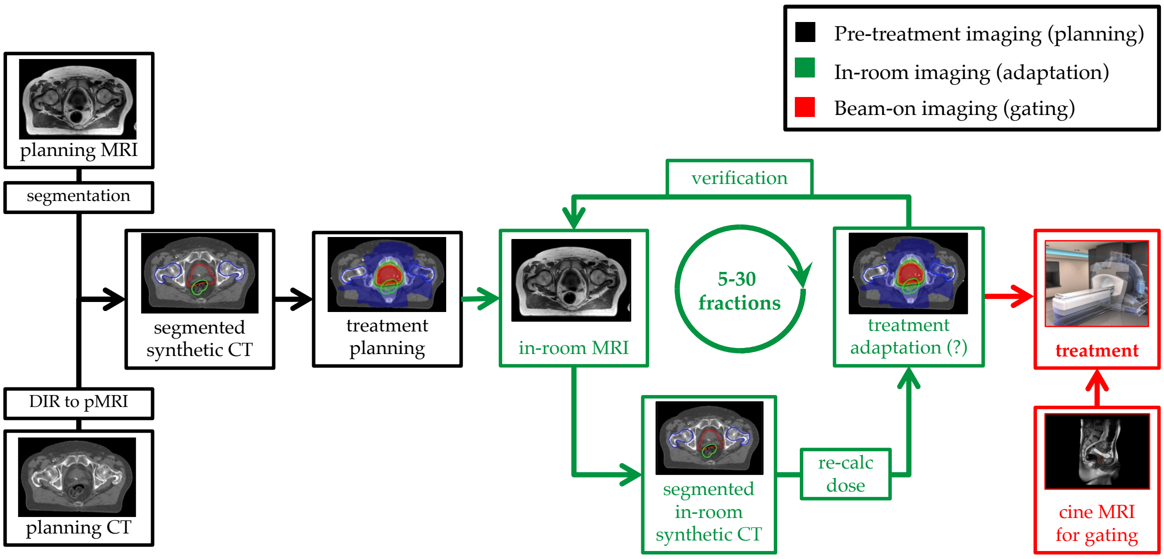

FIGURE 3.4: **Online-adaptive MR-Linac treatment workflow.** The main planning, adaptation, and beam delivery steps of an online-adaptive gated treatment at the ViewRay MRIdian are schematically depicted. The workflow steps are described in more detail in section 3.1.6. Figure courtesy of Dr. Christopher Kurz.

simulation and by comparing treatment plan parameters, such as the number of segments, segment shapes and weights, and Monitor Units. An additional verification 3D-MRI scan can be acquired after the QA calculation to check whether the patient has moved during the replanning procedure [15, 45].

Depending on the entity and complexity of the clinical case, plan adaptation can be time-consuming. In the first publication on clinically applied MR-guided ART by Acharya et al. [140], the authors reported that a median time of 26 min was needed for recontouring, reoptimization, and QA. Several studies have demonstrated that the prolonged treatment time is traded off by improved dose distributions. For instance, Finazzi et al. [33] reported that on-table plan adaptations in MRgRT of central lung tumors could improve the PTV coverage while the number of OAR planning constraint violations was significantly ($p < 0.05$) reduced.

As the final step of the adaptive treatment planning process, the dose is delivered to the target. In the case of non-negligible target motion, the beam delivery is gated based on real-time cine MRI, which is described in the next section.

3.1.7 Gated treatments at the ViewRay MRIdian MR-Linac

Gating is an active motion management technique (section 2.6.6) in which the beam delivery is interrupted and resumed based on a surrogate signal or 2D image. For this purpose, the MR-Linac allows the acquisition of continuous fast cine MRI in 2D with a temporal resolution of a few Hz [40]. Cine MRI is theoretically feasible in arbitrary orientations [31, 167]. In clinical practice at the ViewRay MRIdian MR-Linac, the images used for gated treatments can only be acquired in sagittal orientation [45, 92]. The bSSFP sequence variant most commonly applied in clinical practice [31, 168, 169] uses a cartesian read-out scheme, has a frame rate of 4 Hz, an in-plane resolution of $3.5 \times 3.5\,\mathrm{mm}^2$, and a slice thickness of 5, 7, or 10 mm [45]. A new sequence variant using a radial read-out scheme at 8 Hz with a spatial resolution of 2.7 mm has obtained FDA approval in 2019 and was recently clinically introduced [162, 170].

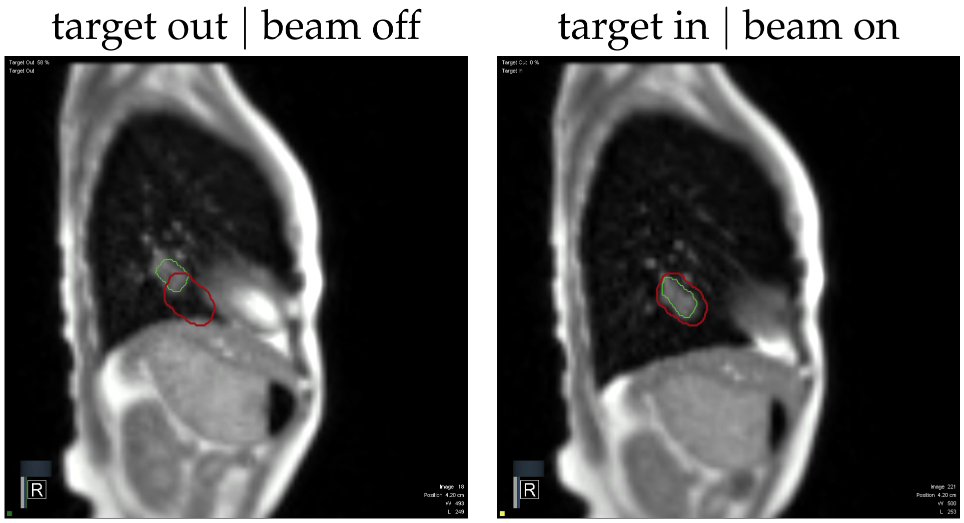

FIGURE 3.5: **Gating at the ViewRay MRIdian MR-Linac.** The images show snapshots of the delivery cine MRI videos of a lung cancer patient treated with gating. The target structure is shown in green and the gating boundary in red. In the left image, the target out percentage is above the predefined threshold, and the beam delivery is paused. In the right image, the target is located fully within the gating boundary and the beam delivery is switched on.

The workflow of a gated beam delivery starts with the definition of a target structure and a boundary. The boundary is an isotropic or anisotropic expansion of the target structure defined on the setup MRI dataset (section 3.1.6). During treatment, the system automatically deforms the target structure from the original image to each of the acquired real-time cine MRI frames using an optical flow DIR algorithm (section 2.4). The relative overlap of the deformed target structure with the boundary is calculated and compared with a pre-defined threshold value (*target out percentage*), which is usually between 5–10%. The beam delivery is only switched on if the target out percentage is below this threshold (classification as *target in*). Otherwise (*target out*), the beam delivery is paused (Figure 3.5). AAPM Task Group 76 recommended that the overall gating latency, i.e., the time delay between the target leaving the gating window until the beam is switched off, should be below 500 ms [21]. Kim et al. measured the latency for the ViewRay MRIdian MR-Linac and reported a maximum time delay of 302 ms [170].

Gating allows the use of smaller PTV margins (section 2.6.6) but leads to a prolongation of the treatment. Some radiation oncology departments use in-house developed visual feedback systems through which the patient can see the cine MRI including target and boundary structures on in-room screens while being treated. This technique can improve the reproducibility of repeated breath-hold procedures and therefore can help to increase the duty cycle [169, 171].

3.2 Four-dimensional volumetric MRI (4D-MRI)

As part of the conventional radiotherapy treatment planning for lung tumors, a 4D-CT scan of the moving anatomy is typically acquired (section 2.6.2). In MRgRT, 4D-MRI could enable a dose-free motion characterization of the target and surrounding healthy tissue during treatment planning, directly before or even during treatment. This information could be used to determine mid-position or mid-ventilation images, for 4D robust planning approaches, to select the gating position and gating window size, for more representative ITV definitions (in cases where gating is not deemed beneficial), and improved target localization during gating [41, 116, 145]. The latter could also enable tracking of the actually applied dose in 3D or, in the future, even real-time adaptive treatments [49]. Two different variants of 4D-MRI are described in the literature: respiratory-correlated 4D-MRI, described in section 3.2.1, and real-time 4D-MRI, described in section 3.2.2. Neither respiratory-correlated nor real-time 4D-MRI sequences with a high spatiotemporal resolution are offered by MR-Linac vendors today [41]. Owing to their potential for MRgRT, the interest in the research community in both approaches has steadily increased over the last few years [40, 41].

3.2.1 Respiratory-correlated 4D-MRI

In respiratory-correlated 4D-MRI, the fourth dimension represents the phase of one respiratory cycle, similar to 4D-CT imaging. In most studies described in the literature, these images are obtained by acquiring 2D cine MRI data at different slice positions. The cine MRI frames are then retrospectively sorted using a surrogate signal. One frame per slice position is assigned to each breathing phase to obtain the 4D-MRI dataset [41]. Oversampling during the cine MRI acquisition can ensure that all necessary data are acquired for all breathing phases and slice positions but prolongs the overall acquisition time. The main motion direction of structures in the lung is in the craniocaudal and AP directions. Therefore, the sagittal plane is most often chosen for the 2D cine MRI acquisition for respiratory-correlated 4D-MRI of the lung [40]. This minimizes through-plane motion, which otherwise could lead to artifacts in the final reconstructed images. The signal used for the sorting process can be an external surrogate (e.g., pneumatic bellows or spirometry devices), an additional navigator that is acquired in parallel or interleaved with the cine MRI acquisition (e.g., pencil-beam navigator where a single column of spins is excited in 1D), or can be derived from the reconstructed 2D images themselves (e.g., the diaphragm-lung interface position) [40, 172]. An alternative to the multi-slice 2D acquisition is the repeated acquisition of volumetric MRI using a 3D read-out scheme, where an additional phase-encoding step replaces the slice selection [41]. The breathing phase binning is then performed already in k-space prior to image reconstruction, since the acquisition of one 3D-MRI volume spans over several breathing phases [145].

The underlying principle of the respiratory-correlated 4D-MRI acquisition is similar to that of 4D-CT acquisition. Consequently, the 4D-MRI datasets can suffer from similar artifacts and limitations. Breathing pattern variations and suboptimal sorting can lead to stitching artifacts (Figure 3.6). The final image represents one average breathing cycle, reconstructed from several breathing cycles [40], which prevents the assessment of intercyclic breathing variations. For treatments with the MR-Linac today, the planning 3D-MRI and setup 3D-MRI acquired at the beginning of each treatment fraction are captured during breath-hold to avoid motion artifacts (section 3.1.6). These images contain no information about the magnitude and direction of the target and organ motion during respiration. In the future, respiratory-correlated 4D-MRI could replace the breath-hold 3D-MRI, enabling a motion characterization at the planning stage or directly before beam delivery [145]. The acquisition of the cine MRI data is time-consuming, typically in the order of several minutes [31]. As a drawback, this would prolong the overall time a patient needs to lie on the MR-Linac treatment couch.

A respiratory-correlated 4D-MRI was acquired and reconstructed as part of the experimental study in Chapter 5 to obtain the ground truth motion pattern of a porcine lung phantom. This is described in more detail in section 5.2.5.

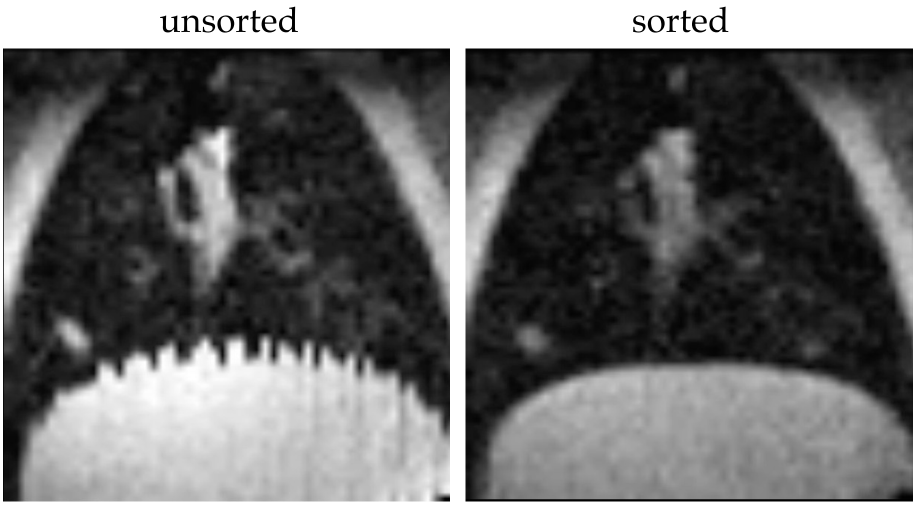

FIGURE 3.6: **Stitching artifacts in respiratory-correlated 4D-MRI.** Coronal views of a phase of an unsorted (left) and sorted (right) 4D-MRI dataset. The 2D cine MRI data were acquired in sagittal orientation, resulting in strong stitching artifacts at the diaphragm-lung transition in the RL direction in the unsorted image. These artifacts are not observed in the sorted image, and the diaphragm surface appears as a smooth curve. This figure was created with data from Chapter 5.

3.2.2 Real-time 4D-MRI

In real-time 4D-MRI, the fourth dimension represents the time, meaning that one full 3D-MRI dataset is acquired at each time point. Due to the intrinsic trade-off between spatial and temporal resolution, no real-time 4D-MRI sequences that can acquire a full 3D volume with sufficient temporal (< 0.5 s) and spatial resolution (2–3 mm) for MRgRT exist today [40, 41]. The maximum acquisition speed of an MRI scanner depends on its specifications, such as the static magnetic field strength, the gradient strengths and speed, and read-out hardware and electronics [82].

Several image acceleration techniques have been developed that already led to shorter 3D-MRI acquisition times in clinical practice and that could allow for real-time 4D-MRI at high spatiotemporal resolution in the future. The general idea behind most of these techniques is to reduce the amount of *k*-space data acquired for each 3D-MRI. This can be achieved by limiting the FOV or spatial image resolution or by undersampled *k*-space acquisition [82]. Undersampling the *k*-space leads to image artifacts, which can be avoided by the methods described in the following. Many of the techniques described below can be combined to achieve a higher image acceleration factor [41].

In *partial Fourier* imaging, a portion of the *k*-space (up to 50% and typically 35%) is deliberately not collected. These missing data are retrospectively filled in, exploiting the property of the Fourier transform that real functions have a conjugate symmetry in *k*-space [41].

Instead of cartesian *k*-space sampling, *radial k-space sampling* can be used. The *k*-space is read out in spokes, each time passing through its center, which contains information about bulk motion. The periphery of the *k*-space, containing information of spatially localized motion, is sampled less frequently. The reconstructed images suffer less from undersampling artifacts than undersampled images obtained with a cartesian read-out scheme, and the reconstructed images are less sensitive to motion artifacts [40, 41].

Generalized Autocalibrating Partially Parallel Acquisition (GRAPPA) and SENSitivity Encoding (SENSE) are *parallel imaging* techniques that allow an acceleration by a factor of up to six. In these techniques, the image is reconstructed based on undersampled *k*-space data using multiple independent receiver coils. The signal that is measured by each receiver coil depends on its position relative to the patient. This additional spatial information can be used during image reconstruction to separate the aliased signal based on spatial sensitivity maps of the read-out coils [41, 173]. Due to lacking receiver coil hardware, the parallel imaging capabilities of MR-Linacs are still limited [45, 82]. Parallel imaging can be combined with a *simultaneous multi-slice acquisition*, where more than one slice position is excited and sampled simultaneously using a multiband RF pulse. The detected aliased signal is then deconvolved using parallel imaging techniques during image reconstruction [145].

A further technique for accelerated image acquisition is to sparsely sample the *k*-space and then use *compressed sensing* to retrospectively reconstruct the images from the undersampled data [174]. The technique relies on the fact that medical images can be sparsely represented. The MR images are obtained through iterative image reconstruction with reconstruction times up to several hours. Therefore, compressed sensing cannot be used for true real-time imaging but only for retrospectively reconstructed 4D-MRI [41, 145].

In the study presented in Chapter 4, a real-time 4D-MRI sequence using *view-sharing*, also referred to as *keyhole imaging*, was used to assess the motion of moving lung tumors. This sequence is explained in more detail in section 4.2.1. The idea of view-sharing is to sample the center and periphery of the *k*-space at different rates, where the center is sampled much more frequently. At each time point, the missing peripheral *k*-space data is then copied in from different time points before image reconstruction. This technique allows a severalfold image acquisition acceleration [175].

The approach that has the greatest potential to provide real-time 4D-MRI for MRgRT in the near future is the use of deep learning methods. Hyun et al. [176] trained a CNN with pairs of MR images reconstructed from subsampled and fully sampled *k*-space data. The trained network then takes images reconstructed with undersampled *k*-space data with image folding artifacts as an input and outputs high quality artifact-free MR images. An alternative deep learning-based approach could rely on training a deep CNN to directly perform the Fourier transform of the undersampled *k*-space data [177]. Undersampling the *k*-space enables faster image acquisition, which could allow creating real-time 4D-MRI with such CNNs in the future. While the training of deep learning models is time-consuming and computationally expensive, the final model could potentially be applied in near real-time [145].

In the future, real-time 4D-MRI sequences could be used during beam delivery (section 3.1.7). This could enable an improved target and OAR localization in 3D, particularly when prominent out-of-plane motion is present in 2D cine MRI [40, 178]. Furthermore, synthetic 4D-CTs could be created based on these data, which would allow a reconstruction of the actually delivered dose (section 3.3.2) or even real-time treatment adaptation in the future [49].

3.3 Motion modeling for MRgRT

The assessment of inter- and intrafractional changes is of major importance in adaptive MRgRT. As long as no real-time 4D-MRI sequence (section 3.2.2) with sufficient spatiotemporal resolution for MRgRT applications is available, alternative methods are needed to create time-resolved 4D-MRI from lower-dimensional surrogate data. The concept of motion modeling for this purpose is summarized in section 3.3.1. To fully exploit the potential of MRgRT, the dose delivered to the target and OARs during treatment has to be reconstructed. A prerequisite for this dose reconstruction are synthetic 4D-CTs, created based on 4D-MRI data, which is further described in section 3.3.2.

3.3.1 Motion modeling approaches

Following the definition by McClelland et al. [179], "motion models are used when it is not possible or practical to directly measure the actual motion of interest with sufficient temporal resolution during the intended procedure. [...] A motion model refers to a process that takes some surrogate data as input and produces a motion estimate as output". In MRgRT research, motion models can be used to derive time-resolved 4D-MRI datasets of the thorax or abdomen based on surrogate signals or 2D cine MRI data [40]. In the future, these 4D-MRI could be used for the motion assessment in the treatment planning stage or serve as input for the creation of synthetic 4D-CT datasets (section 3.3.2) [180].

The typical approach of motion modeling is sketched in Figure 3.7. In the following, the creation of a respiratory motion model based on 2D cine MRI data and respiratory-correlated 4D-MRI reconstruction for motion assessment is described. Series of 2D cine MRI data at different slice locations and one or more surrogate signals are acquired simultaneously to create the training data needed for motion modeling. These signals can be an external surrogate signal or a navigator signal acquired in parallel or interleaved with the imaging data. In the published literature, this surrogate signal was often directly derived from the acquired cine MRI data. In this case, specific features such as the diaphragm or chest position are extracted from the 2D images [181]. Alternatively, the surrogates can be determined by applying a principal component analysis to the image intensities [180]. The imaging data is used to reconstruct a respiratory-correlated 4D-MRI dataset. The different phases of this 4D-MRI are deformably registered to characterize the observed motion. The motion states, parametrized by the DVFs of the DIR, are fitted as a function of the surrogate signal to create the motion model [40]. For the model application, the surrogate signal is measured and used as input for the motion model to estimate the corresponding DVF and motion states in 3D. If a patient was treated at an MR-Linac, the cine MRI for building the motion model could be acquired during treatment planning or on each day of treatment at the start of each fraction. The cine MRI acquired for gating could then be used to drive the motion model during beam delivery [180].

Motion models have been proposed for a wide range of applications and imaging modalities [40, 179]. In the context of MRgRT, several models have been developed using cine MRI data to estimate time-resolved 3D data, including the ones by Fayad et al. [182], Harris et al. [183], Stemkens et al. [184], and McClelland et al. [185]. None of these models have been applied clinically yet. A thorough description of the models is given in the original publications and the comparative *in silico* analysis conducted by Paganelli et al. [47].

Motion models can provide volumetric time-resolved 4D-MRI with high temporal and spatial resolution without special hardware. The model application is fast and can enable near real-time creation of volumetric datasets [145]. The reliance on the correlation of the surrogate signal with the motion states is a drawback of these methods. This correlation can deteriorate over time due to breathing pattern or anatomy changes [40]. Not all motion models can correctly model intracyclic motion variability, such as the hysteresis trajectories of lung tumors [179, 186]. The reconstruction of respiratory-correlated 4D-MRI for the motion characterization can introduce further systematic uncertainties. While the motion models can be tested with virtual or physical motion phantoms, their validation with patient data is challenging since no ground truth information is available. Lastly, the data acquisition and training phase to build the motion model is time-consuming. This may prevent its use in an adaptive MRgRT workflow to limit the overall time the patient has to lie in treatment position [40].

In this thesis, two approaches were chosen to address some of these limitations. Firstly, a porcine lung phantom was used for the experimental validation measurements in Chapters 5 and 6. This phantom can be regarded as a link between phantoms with reproducible

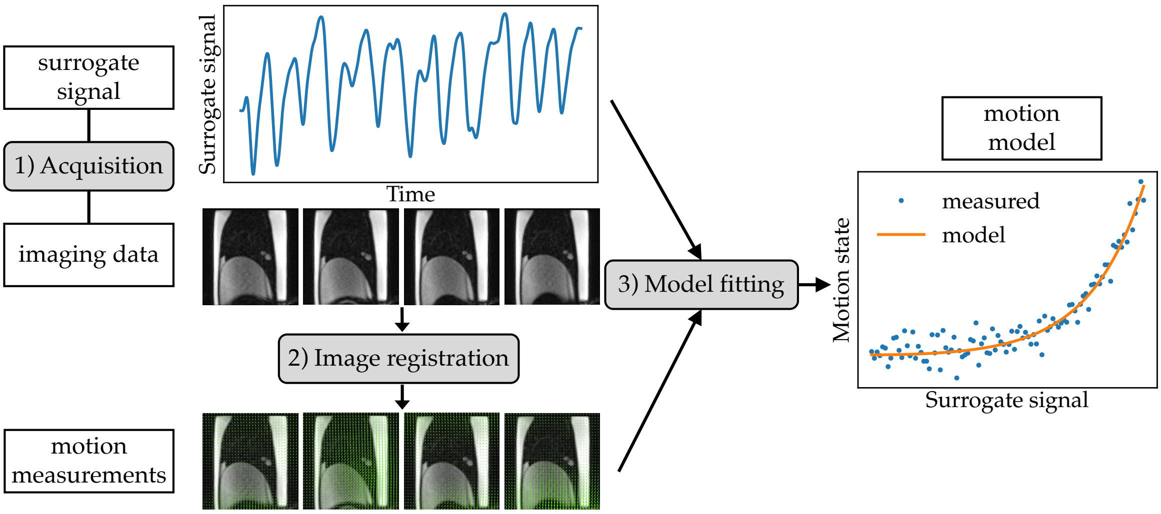

FIGURE 3.7: **Motion modeling workflow.** The steps of the creation of a motion model are schematically depicted. (1) One or several surrogate signals are acquired simultaneously to the time-resolved imaging of the region of interest. (2) The images are deformably registered to parametrize the different motion states. (3) The measured motion state parameters are fitted as a function of the measured surrogate signal(s) to build a motion model. This sketch was created based on Figure 1 in [180] with data from Chapter 6.

motion patterns and realistic patient data. Secondly, an alternative method to create estimated time-resolved 4D-MRI based on cine MRI data, the *propagation method* [46], was applied. This method does not rely on surrogate signals, can model intracyclic variations, and does not require model training. The propagation method is described in detail in section 5.2.7.

3.3.2 Synthetic 4D-CT

MR images contain no information about the electron density distribution of the imaged tissue (section 3.1.2). Since there is no direct physical correlation between MR image intensities and electron densities, synthetic CTs have to be generated based on the MR images alone or with the aid of a static CT image of the same anatomy to enable dose calculations (section 3.1.6). Different synthetic 3D-CT generation methods have been proposed and partly clinically implemented at the ViewRay MRIdian and Elekta Unity MR-Linacs (section 3.1.3). These methods include DIR, bulk density assignments, atlas-based segmentation, and deep learning methods. A systematic review of these 3D approaches was conducted by Johnstone et al. [187].

In the future, real-time, respiratory-correlated, or motion model-based 4D-MRI could be used in MRgRT workflows for a dose-free motion assessment for planning and treatment evaluation. When the morphological and motion information from these 4D-MRI is combined with the electron density maps of a CT image, the resulting *synthetic 4D-CTs* could be used for 4D treatment planning and – in combination with linac log files – retrospective reconstruction of the delivered dose [40, 41]. The reconstructed dose distributions could then be used to guide interfractional or even intrafractional treatment plan adaptations [49]. This is particularly of interest in the thorax, where large respiratory-induced motion and inhomogeneous tissues are present [40]. A review of synthetic 4D-CT generation methods proposed in the literature is given in Chapter 6 of this thesis. The purpose of the study presented in that chapter was to create continuous time-resolved estimated synthetic 4D-CT datasets by using the estimated 4D-MRI output by the propagation method.

Chapter 4

Real-time 4D-MRI-based internal target volume definition

This chapter presents a research project that was conducted by the author in the scope of this dissertation. The presented methodology and results have been published as an article in *Medical Physics* in 2020 [116], including all figures, Table 4.2, and Table 4.4. The text was adapted, and Table 4.1 and Table 4.3 were added to increase the readability and consistency within this thesis.

The goal of the retrospective proof-of-concept study was to investigate whether the integration of real-time 4D-MRI data into treatment planning can improve the ITV definition for radiotherapeutic treatments of lung cancer at conventional linacs. The motivation for the real-time 4D-MRI-based target definition is given in section 4.1. The data acquisition and processing workflow, the probability-of-presence-based target definition, and the evaluation steps are described in section 4.2. The results of the study are presented in section 4.3 and discussed in section 4.4. Finally, the drawn conclusions are summarized in section 4.5.

4.1 Motivation for MRI-based target definition

In radiotherapy of lung cancer, inter- and intrafractional changes (section 2.6.1), such as anatomical variations and respiratory-induced target motion, have to be considered in the treatment planning and delivery process through active and passive motion management techniques (sections 2.6.3 and 2.6.6). Motion-encompassing target definitions are most commonly used for conventionally fractionated lung cancer treatment to prospectively account for these uncertainties during treatment planning [78]. This includes the definition of ITV, midV, and mid-position target volumes (section 2.6.3) [22, 128]. While the midV and mid-position concepts generally result in smaller PTVs, their clinical use is still limited compared to the ITV approach [78]. In any case, today's standard is to define the targets based on 4D-CT scans (section 2.6.2) [119].

4D-CT images can be affected by motion artifacts, and only a single averaged breathing cycle is reconstructed from projection data acquired over just a few breathing cycles. Respiratory-induced motion is patient-specific, irregular, and difficult to predict (section 2.6.1). Therefore, the target motion sampled during the short time period is subject to statistical uncertainties [188]. Interfractional changes frequently occur for lung cancer patients, which can lead to breathing pattern and positional changes over the course of treatment [13, 21, 22]. The breathing motion is furthermore affected by psychological factors, such as patient anxiety or relaxation [186]. These factors introduce statistical and systematic uncertainties in the target definition, leading to inferior target coverage or increased OAR doses [128, 131]. For these reasons, several authors have raised the question whether a single 4D-CT scan is sufficient for a representative quantification of the respiratory-induced target motion [129, 130, 132, 133, 189].

These uncertainties can be reduced by daily adaptive gated treatments at MR-Linacs (section 3.1.7). However, the worldwide availability of these machines is limited so far. The majority of patients are still treated with conventional linacs and CBCT imaging for IGRT (section 2.6.4) [30]. At the same time, the availability of MRI scanners for treatment planning in radiation oncology departments has increased over the last decade [44]. The MR images can be integrated into the conventional radiotherapeutic workflow to complement the planning CT images [190, 191].

Several research groups have investigated the motion of lung tumors with 2D cine MRI [40, 169, 192–196]. This technique enables repeated continuous time-resolved dose-free imaging over extended time periods with high soft tissue contrast [13, 40] (section 3.1.1). Cai et al. [197] demonstrated that the lung tumor motion characterization with 2D cine MRI is more representative than with 4D-CT imaging. This was mainly attributed to the improved statistics through the long acquisition times of 5 min enabled by cine MRI [188].

The purpose of the first study in the scope of this thesis was to develop and evaluate a method to integrate the motion information obtained by time-resolved MRI in the planning of treatments delivered at conventional linacs. Probabilistic ITVs were defined based on the target motion extracted from real-time 4D-MRI (section 3.2.2) with the aid of DIR (section 2.4.3). The use of volumetric MRI instead of 2D cine MRI allows a direct assessment of the 3D target motion, including translations, rotations, and deformations. It was investigated whether the proposed probabilistic ITV definition can reduce the statistical and systematic uncertainties associated with today's 4D-CT-based approaches (midV and conventional ITV definition).

4.2 Material and Methods

4.2.1 Patient data and imaging protocols

Three lung cancer patients were retrospectively included in the study. All patients had tumors located in the lower or middle lobe of the right lung. MRI in treatment position was performed at a 1.5 T Avanto scanner (Siemens Healthineers, Forchheim, Germany). For each patient, seven to nine imaging sessions were distributed over eleven to twelve weeks, leading to a total of 24 imaging sessions for all patients accumulated. At the beginning of each session, a 3D-MRI in breath-hold, denoted as 3DMRI, was acquired. A bSSFP sequence (section 3.1.7) was used for this purpose (TrueFISP; axial slices; slice thickness: 4–5 mm; in-plane resolution: $0.88 \times 0.88\,\mathrm{mm}^2$; TR/TE: 380/1.16 ms; flip angle: 63°; FOV: $45 \times 45 \times 24\,\mathrm{cm}^3$; receiver bandwidth: 1030 Hz/px; acquisition time: 20–24 s) with parallel imaging (GRAPPA; section 3.2.2) for image acceleration.

A real-time 4D-MRI (section 3.2.2) dataset, denoted as 4DMRI, was subsequently acquired to capture the respiratory-induced tumor motion while the patient was breathing freely (TWIST; coronal slices; slice thickness: 10 mm; in-plane resolution: $3.91 \times 3.91\,\mathrm{mm}^2$; TR/TE: 1.47/0.61 ms; flip angle: 5°; FOV: $50 \times 50 \times 36\,\mathrm{cm}^3$; receiver bandwidth: 1565 Hz/px; parallel imaging: GRAPPA).

The TWIST sequence (time-resolved angiography with interleaved stochastic trajectories) [198] by Siemens uses view-sharing and undersampling of the *k*-space periphery, which allows an acceleration of up to 20 times compared to full *k*-space acquisition. In this sequence, the *k*-space is divided into two regions: region A, which includes the low frequencies responsible for the overall image contrast, and region B, which includes the outer *k*-space, responsible for image details. To shorten the acquisition time, the sampling of regions A and B is alternated. In each iteration, the full region A is sampled, but only a part of region B is sampled in a random fashion. The different *k*-space points in regions A and B are thus sampled at different rates. The missing k-space information of region B is copied in from several B intervals before reconstruction of the image at each time point [198].

During 4D-MRI, 157 volumetric MRIs were acquired in 80 s with a temporal resolution of 2 Hz. The distortion correction methods provided by the vendor were applied to 3DMRI and 4DMRI to minimize geometric distortions (section 2.3.9), which is crucial in a radiotherapy workflow. The GTV (section 2.5.2) was contoured on 3DMRI and approved by a radiation oncologist.

The first imaging session ($n = 1$) for each patient was defined as the reference imaging session, serving as a surrogate for the imaging during treatment planning. The remaining imaging sessions, $n \in [2, ..., N]$, where N is the patient-specific total MRI session number, were taken as surrogates for the treatment fractions in the geometric analyses described below.

4.2.2 Overview of image processing and analysis workflow

The time-dependent GTV positions within the 4DMRI datasets were analyzed and used as input for the target volume definitions. The image processing and analysis workflow is sketched in Figure 4.1, with the following main workflow steps:

1. Breathing state determination and matching between 3DMRI and 4DMRI,
2. GTV contour propagation from 3DMRI to best matching image within 4DMRI at time point t', 4DMRI(t'),
3. GTV contour propagation from 4DMRI(t') to the whole 4DMRI dataset,
4. ITV and midV target volume definition,
5. PTV definition,
6. time-averaged 4DMRI generation,
7. rigid registration between averaged 4DMRI of day 1 and n,
8. geometrical overlap analysis between the reference PTV ($\mathrm{PTV_r}$) and the ITVs from day n (ITV_n).

These steps are indicated in Figure 4.1 and explained in the following.

4.2.3 Step 1: Breathing state determination

As the first data analysis step, the breathing states of the 3DMRI and at all time points of the 4DMRI were parametrized with an image processing-derived surrogate signal. This step aimed to find the 3D image within 4DMRI with the closest resemblance to 3DMRI in order to minimize the DIR uncertainty in the next step.

At first, a region-of-interest containing parts of the diaphragm-lung transition in the contralateral (left) lung was manually selected. This partial volume was converted to a binary image based on its voxel intensity distribution using Otsu's thresholding method [199]. A value of zero was assigned to voxels with low intensities (air and lung tissue) and a value of one to voxels with higher intensities (abdominal tissue). The binary images were summed over the AP and RL image axes, resulting in a 1D surrogate signal in superior-inferior (SI) direction. The position of the steepest gradient of this signal was defined as the diaphragm position. The absolute differences between the surrogate signal value of 3DMRI and all 3D images of 4DMRI were calculated. The time point t' at which this difference was minimal was determined. The 3D-MRI at this time point, 4DMRI(t'), was used for all subsequent DIRs.

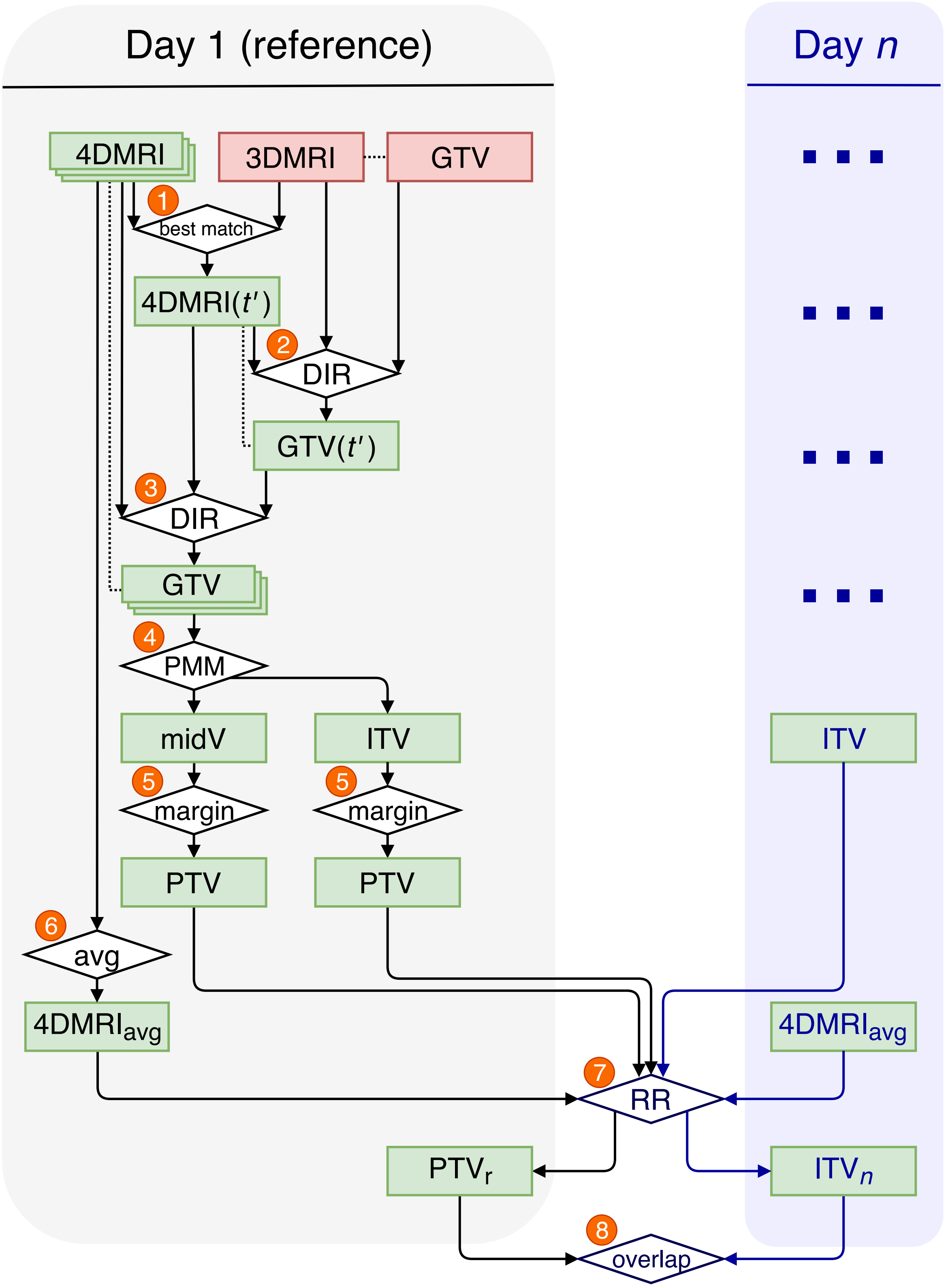

FIGURE 4.1: **Image processing and analysis workflow.** The schematic depicts the main data processing and analysis steps, indicated by the small numbers. These are described in the text. The ellipses indicate that the same analysis steps as depicted for day 1 were performed for day n. PTV_r is the reference PTV and ITV_n the ITV on day n. GTV: gross tumor volume; DIR: deformable image registration; PMM: passive motion management; midV: mid-ventilation target volume; ITV: internal target volume; PTV: planning target volume; RR: rigid registration. Figure reprinted from [116].

4.2.4 Steps 2 and 3: GTV contour propagation

3DMRI and 4DMRI were resampled to an isotropic grid with a voxel size of $2 \times 2 \times 2\,\mathrm{mm}^3$ using trilinear interpolation. The resampled images were used for all remaining image registration and analysis steps. The open-source software Plastimatch [200] was used to deformably register 3DMRI to 4DMRI(t') in a multi-level B-spline DIR (section 2.4.3) with MI as similarity metric (section 2.4.6). The cost function included a regularization term (section 2.4.3) to smooth the DVFs. The DIR was focused on the region surrounding the target by using a binary mask derived from the GTV in 3DMRI, expanded by an isotropic margin of 10–18 mm. The GTV was transformed from 3DMRI to 4DMRI(t') by applying the DVF obtained from the DIR.

The GTV was subsequently propagated from 4DMRI(t') to all remaining 4DMRI(t_i), with $i \in [1, ..., 157]$. This was done by applying the DVFs output by multi-level B-spline DIRs of 4DMRI(t') and 4DMRI(t_i), focused on the GTV with MSE as similarity metric and including regularization.

An alternative approach would have been to register 3DMRI to all 4DMRI(t_i) directly. However, 3DMRI and 4DMRI were acquired with different sequences, resulting in dissimilar image contrast. This affects the accuracy of the DIR, particularly when the images represent different breathing states. The DIR between images with similar contrast, 4DMRI(t') and 4DMRI(t_i), was expected to be more accurate. For this reason, the contour propagation was split into the two steps described above.

The GTV motion amplitudes in each breathing cycle captured by 4DMRI were measured by calculating the centroid positions of GTV(t_i) at all time points t_i, finding the inhale and exhale positions, and calculating the difference between each inhale position relative to the median exhale position.

4.2.5 Step 4: ITV and midV target volume definition

The target volumes ITV$^{5\%}$ and ITV$^{10\%}$ were defined based on the POP distribution of the GTV for all reference and follow-up imaging sessions. Additionally, the target volumes ITV$_\mathrm{r}^{80\,\mathrm{s}}$, ITV$_\mathrm{r}^{10\,\mathrm{s}}$ and midV were defined to compare the POP-based ITVs with conventional motion-encompassing structures. These target volumes were only created for the reference imaging session on day 1.

ITV$^{5\%}$ and ITV$^{10\%}$ The binary images GTV(t_i) were summed over all t_i and normalized by dividing the voxel values by the total number of time points $N = 157$. The resulting 3D image values indicate the percentages of time that a part of the GTV was present at the voxels' positions during the image acquisition. Under the assumption that the 4DMRI acquisition time was long enough to sample the motion of the day representatively, this image can be interpreted as a probability-of-presence (POP) map. POP-based ITVs were defined based on this 3D distribution by using threshold values of 5% (ITV$^{5\%}$) and 10% (ITV$^{10\%}$). All voxel values smaller than these thresholds were set to 0, while all other voxel values were set to 1.

ITV$_\mathrm{r}^{80\,\mathrm{s}}$ A POP threshold value of 0% was used to define this ITV. This target volume includes all GTV positions observed during the whole 4DMRI acquisition time.

ITV$_\mathrm{r}^{10\,\mathrm{s}}$ The 4DMRI was split up into eight 10 s periods. An ITV was defined for each of the eight segments by including all GTV positions that occurred during the respective time periods. These target volumes served as surrogates for conventional 4D-CT-based ITVs,

TABLE 4.1: **Uncertainties for PTV definition.** The systematic (Σ) and statistical uncertainties (σ) used for the PTV margin calculation in Equation 4.2 are summarized. All values are given in millimeters. p.s.: patient-specific.

Symbol	Error type	Description	Value	Reference
Σ_{setup}	systematic	CBCT-based patient positioning setup error	0.8	[203]
Σ_{BL}	systematic	baseline shifts over course of treatment	0.99	[204]
Σ_{del}	systematic	delineation uncertainties	1.7	[201]
σ_{setup}	statistical	CBCT-based patient positioning setup error	0.8	[203]
σ_{BL}	statistical	baseline shifts over course of treatment	1.08	[204]
$\sigma_{\text{br,d}}$	statistical	standard deviation of motion in direction d	p.s.	[135]
σ_{p}	statistical	Gaussian beam penumbra width in lung	6.4	[137]

since the typical acquisition time of a 4D-CT scan is around 10 s (section 2.6.2). This method was proposed and used by Thomas et al. [195].

midV Following the work by Ehrbar et al. [201] and Thomas et al. [202], a midV was defined based on the full 4DMRI. The centroid of the centroids of all $N = 157$ GTV positions within 4DMRI was calculated. The GTV within 4DMRI with the smallest euclidean distance of its centroid to this point was then defined as the midV.

4.2.6 Step 5: PTV definition

The reference ITVs and midV were expanded by margins to create PTV_r (section 2.6.3). Isotropic margins of 5 mm were used for the ITVs based on current clinical practice [72]. The van Herk margin recipe (Equation 2.68) [110] was used to calculate the anisotropic margins m_d in directions d (with $d \in [\text{RL}, \text{SI}, \text{AP}]$) for the midV:

$$\begin{aligned} m_d &= \alpha\boldsymbol{\Sigma} + \beta\boldsymbol{\sigma} - \beta\sigma_\text{p} && (4.1)\\ &= \alpha\sqrt{\Sigma^2_{\text{setup}} + \Sigma^2_{\text{BL}} + \Sigma^2_{\text{del}}} + \beta\left(\sqrt{\sigma^2_{\text{setup}} + \sigma^2_{\text{BL}} + \sigma^2_{\text{br},d} + \sigma^2_{\text{p}}} - \sigma_\text{p}\right). && (4.2)\end{aligned}$$

For the individual contributions to the systematic $\boldsymbol{\Sigma}$ and statistical $\boldsymbol{\sigma}$ uncertainties, values published in the literature were used. These are summarized in Table 4.1. The systematic uncertainties were assumed to be isotropic, while the statistical uncertainties include the direction-dependent uncertainty $\sigma_{\text{br},d}$. This uncertainty describes the standard deviation of the respiratory-induced GTV motion in direction d. Its value was approximated by $\sigma_{\text{br},d} = A^d_{\text{cen}}/3$, where A^d_{cen} is the median GTV centroid motion amplitude on day 1 in direction d [201]. Following the margin recipe by van Herk et al. [110], $\alpha = 2.5$ and $\beta = 1.64$ were used for the calculations to ensure a minimum of 95% of the prescribed dose to the target for 90% of the patients. The margin values m_d were rounded up to integer millimeter values. All ITV and midV margin expansions were conducted on a $1 \times 1 \times 1\,\text{mm}^3$ grid and then resampled back to the original $2 \times 2 \times 2\,\text{mm}^3$ grid. For each patient, steps 1–5 in Figure 4.1 were performed for the reference imaging session on day 1 to create twelve PTV_r: $\text{PTV}^{5\%}_\text{r}$, $\text{PTV}^{10\%}_\text{r}$, $\text{PTV}^{80\,\text{s}}_\text{r}$, eight $\text{PTV}^{10\,\text{s}}_\text{r}$, and $\text{PTV}^{\text{midV}}_\text{r}$.

4.2.7 Steps 6 and 7: Time-averaged 4DMRI generation and rigid registration

The 4DMRIs acquired on different days need to be in the same frame of reference for the target volume overlap analysis described in the next section. The time-averaged 4DMRI

($4DMRI_{avg}$) of day 1 and day n were calculated. These images were rigidly registered (section 2.4.2) using Plastimatch with MI as similarity metric, focused on the target region. The registration of the time-averaged 4DMRI was used to mimic patient positioning in an IGRT workflow, where the 3D-CBCT images are inevitably blurred due to breathing motion [118].

4.2.8 Step 8: Geometrical overlap analysis

A geometrical overlap analysis between the different reference PTVs (PTV_r) and the ITVs from day n (ITV_n) was performed. The purpose of this analysis was to assess whether the PTV_r, derived from the motion in the imaging session on day 1, can appropriately account for the GTV motion that is observed in the imaging sessions on days n, with $n \in [2, ..., N]$.

The PTV_r were used as surrogate for the structures used in treatment planning before the start of treatment. The ITV of day n with a POP threshold of 5% ($ITV_n^{5\%}$) was used as a surrogate for the true motion that would be observed during beam delivery on day n. This POP threshold was chosen to ensure a minimum dose of 95% to the GTV [110]. PTV_r and $ITV_n^{5\%}$ are rigidly registered binary images, defined on the same $2 \times 2 \times 2\,\text{mm}^3$ image grid. These images were compared on a voxel-by-voxel basis. The PTV_r and $ITV_n^{5\%}$ voxel values can be interpreted in the following way: A PTV_r voxel with a value of 1 is a prediction that a part of the GTV will be located at the voxel's position with a non-negligible probability during beam delivery. A $ITV_n^{5\%}$ voxel with a value of 1 indicates that a part of the GTV is actually present at the voxel's position during at least 5% of the time. To each of the voxels in the image grid, one of four labels was assigned (illustrated in Figure 4.2):

true positive: voxels with a value of 1 in PTV_r and $ITV_n^{5\%}$.

true negative: voxels with a value of 0 in PTV_r and $ITV_n^{5\%}$.

false positive: voxels with a value of 1 in PTV_r and 0 in $ITV_n^{5\%}$.

false negative: voxels with a value of 0 in PTV_r and 1 in $ITV_n^{5\%}$.

TP, FP, and FN are defined as the total number of voxels with labels true positive, false positive, and false negative, respectively. The geometrical volume overlap of PTV_r with $ITV_n^{5\%}$ can be quantified in terms of the *sensitivity*, the *precision*, and the *Dice similarity coefficient*, defined as:

Sensitivity (SE; *true positive rate*):

$$\mathrm{SE} = \frac{\mathrm{TP}}{\mathrm{TP} + \mathrm{FN}} = \frac{\mathrm{PTV_r} \cap \mathrm{ITV}_n^{5\%}}{\mathrm{ITV}_n^{5\%}} . \tag{4.3}$$

Precision (PRE; *positive predictive value*):

$$\mathrm{PRE} = \frac{\mathrm{TP}}{\mathrm{TP} + \mathrm{FP}} = \frac{\mathrm{PTV_r} \cap \mathrm{ITV}_n^{5\%}}{\mathrm{PTV_r}} . \tag{4.4}$$

The Dice similarity coefficient (DSC) can be expressed as a function of SE and PRE:

$$\mathrm{DSC} = \frac{2 \cdot \mathrm{TP}}{2 \cdot \mathrm{TP} + \mathrm{FP} + \mathrm{FN}} = \frac{2 \cdot (\mathrm{PTV_r} \cap \mathrm{ITV}_n^{5\%})}{\mathrm{PTV_r} + \mathrm{ITV}_n^{5\%}} = 2 \cdot \frac{\mathrm{SE} \cdot \mathrm{PRE}}{\mathrm{SE} + \mathrm{PRE}} . \tag{4.5}$$

The PTV is designed to ensure that a curative dose is delivered to the GTV while considering the different uncertainties associated with the treatment planning and delivery process. In terms of the metrics defined above, increasing the PTV margin increases TP (target hit) and

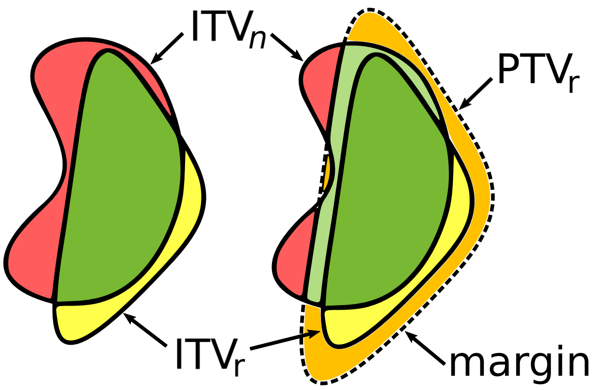

FIGURE 4.2: **Illustration of target volume overlaps.** The left sketch shows the overlap of a reference ITV (ITV_r) with an ITV from day n (ITV_n). The colors represent the labels defined in section 4.2.8: true positive (dark green), false positive (yellow), and false negative (red). The right sketch demonstrates the effect of adding a margin (indicated by the dashed line) to ITV_r to create PTV_r. The true positive area increases (light green), which leads to a decrease of the false negative area (red) at the cost of an increased false positive area (orange). Figure reprinted from [116].

decreases FN (target miss). This comes at the cost of an increased FP (normal tissue damage). The scalar metrics SE and PRE quantify the target coverage and normal tissue sparing relative to the target volume. The optimal values of SE and PRE are 100%. Increasing the PTV margin increases SE while PRE decreases and vice versa. The goal of treatment planning is to define a PTV that represents an acceptable trade-off between SE (tumor coverage) and PRE (normal tissue sparing). For each patient, the $(N-1)$ SE, PRE and DSC overlap values were calculated for each PTV_r and all $ITV_n^{5\%}$. Out of the eight $PTV_r^{10\,s}$, the PTV with the highest (“best”) and lowest (“worst”) SE was determined.

4.3 Results

4.3.1 Motion amplitudes

During the 80 s acquisition time of the 4DMRI, 12–24 breathing cycles were recorded with a median value of 15.5. The corresponding breathing rates were between 9 and 18 cycles per minute with a median value of 12 cycles per minute. The breathing patterns varied between the imaging sessions acquired on different days and between patients regarding regularity, breathing amplitude, and frequency. The GTV centroid motion trajectories for an exemplary patient are shown in Figure 4.3a. The motion amplitudes of all breathing cycles within each imaging session relative to the median exhale position are presented for all patients in Figures 4.3b–d.

No clear trend of the median breathing amplitudes over time was observed for Patients 1 and 2. Patient 3 developed pulmonary edema in the tumor-bearing (right) lung with increasing severity over the course of the observation period. This led to a systematic baseline shift of the GTV position and a variation of the GTV centroid motion in different MRI sessions. A gradual decrease of the motion amplitude in SI direction was observed. The loss in amplitude was partially compensated by an increase of motion in RL direction while the 3D amplitude decreased slightly (Figure 4.3d).

Table 4.2 summarizes the median motion amplitudes in 3D, and split up into the different motion directions for each patient. For all patients and MRI sessions combined, the largest motion was observed in SI direction with a median motion amplitude of 8.8 mm. Similar median motion amplitudes were measured in RL direction (2.7 mm) and AP direction (2.2 mm).

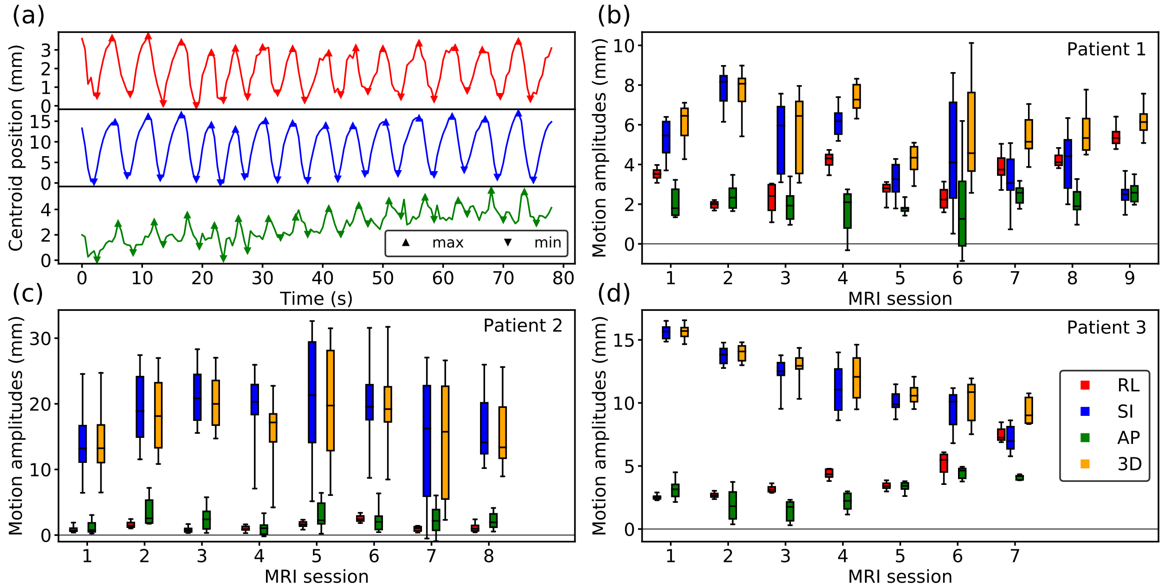

FIGURE 4.3: **GTV centroid motion amplitudes.** (a) The GTV centroid trajectory for an exemplary imaging session is shown, split up into RL (red), SI (blue), and AP (green) direction. The amplitudes were measured relative to the median exhale position. The triangular markers indicate the detected maxima (max) and minima (min) for each breathing cycle. (b–d) The motion amplitudes in RL, SI, AP direction, and in 3D are summarized in box plots and are plotted as a function of the MRI session for each patient separately. The whiskers of the box plots indicate the 5th and 95th percentiles. The subplots do not share the same y-axis. Figure reprinted from [116].

TABLE 4.2: **Patient-specific GTV motion characteristics.** The table summarizes the median GTV centroid motion amplitudes, averaged over all imaging sessions for each patient. The motion amplitudes A^d_{cen} in direction d are given, with $d \in [\text{3D}, \text{RL}, \text{SI}, \text{AP}]$. The volume of the GTV and the median ratio between the volumes of $\text{ITV}^{80\,\text{s}}$ and the GTV are additionally given. Table reprinted from [116].

Patient	GTV position	$A^{\text{3D}}_{\text{cen}}$ mm	$A^{\text{RL}}_{\text{cen}}$ mm	$A^{\text{SI}}_{\text{cen}}$ mm	$A^{\text{AP}}_{\text{cen}}$ mm	GTV ml	$\frac{\text{ITV}^{80\,\text{s}}}{\text{GTV}}$
1	middle right lobe	6.0	3.3	4.4	2.1	273	1.29
2	lower right lobe	17.2	1.2	18.4	2.0	16	3.25
3	lower right lobe	12.1	3.4	11.5	3.0	190	1.58

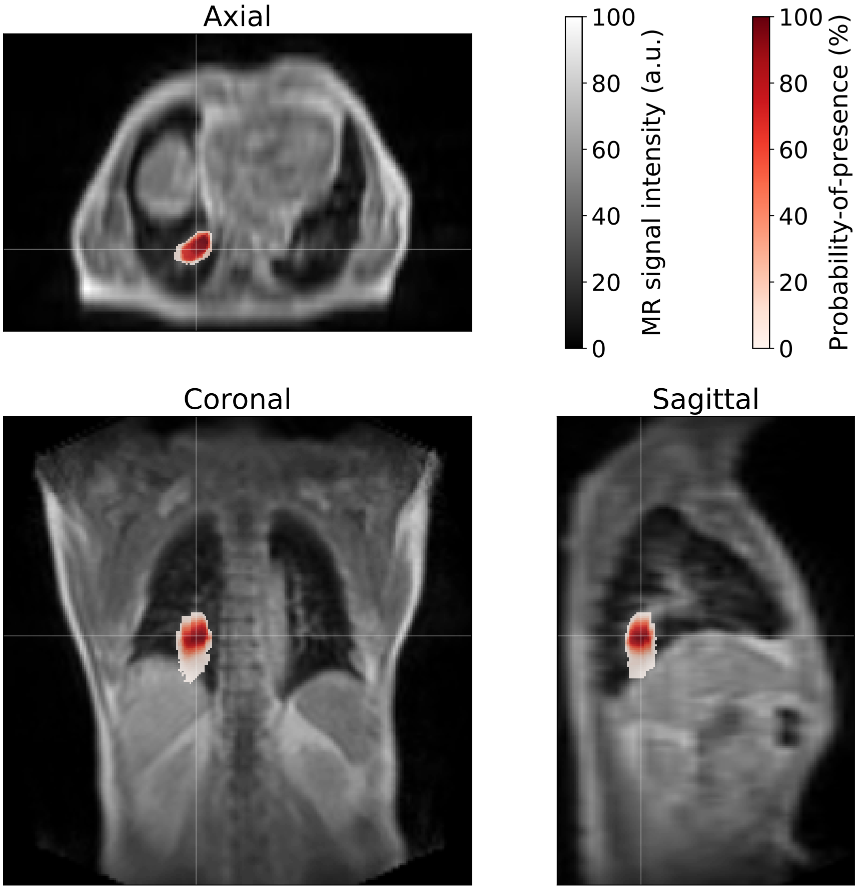

FIGURE 4.4: **Three-dimensional POP distribution.** The 4DMRI(t') image of the reference imaging session of Patient 2 is shown in axial, coronal, and sagittal orientation. The crosshairs indicate the slice positions in the respective views. The POP is color-encoded and superimposed on this image. Figure reprinted from [116].

4.3.2 Probability-of-presence ITV and midV

The 3D POP distribution maps were derived for all imaging sessions. Figure 4.4 illustrates an exemplary map for Patient 2. Sharp gradients were measured in the directions of small motion amplitudes (RL and AP) and shallow gradients in the main direction of motion (SI). The $\mathrm{ITV}^{80\,\mathrm{s}}$ includes all voxels with a non-zero POP. The median volume ratios of $\mathrm{ITV}^{80\,\mathrm{s}}$ to GTV, averaged over all imaging sessions, are listed in Table 4.2. This ratio depended on the GTV size and the motion amplitude. Values between 1.29 (Patient 1) and 3.25 (Patient 2) were measured. The mean distance between the centroid of all GTV centroid positions and the midV centroid, averaged over the reference imaging sessions of the three patients, was 0.5 mm.

4.3.3 PTV definition

The direction-dependent uncertainty $\sigma_{\mathrm{br},d}$ for the midV PTV margin was derived from the median motion amplitudes in RL, SI, and AP direction observed during the reference imaging session (cf. Figure 4.3). These motion amplitudes and the respective anisotropic PTV margins are summarized in Table 4.3. The margins in RL and AP direction were 6 mm for all three patients and 6 mm, 8 mm, and 9 mm in SI direction for Patients 1, 2, and 3, respectively.

TABLE 4.3: **PTV margins around midV.** The median motion amplitudes A^d_{cen} in RL, SI and AP direction observed in the reference imaging session are given. The anisotropic PTV margins were derived based on these amplitudes. All values are given in millimeters.

Patient	Median A^d_{cen}			PTV margins		
	RL	SI	AP	RL	SI	AP
1	3.5	5.5	1.8	6	6	6
2	0.7	13.2	0.8	6	8	6
3	2.5	15.7	3.2	6	9	6

TABLE 4.4: **Median geometrical overlap values.** The median DSC, SE and PRE values of the geometrical overlap analysis of the different PTV_r with the $\text{ITV}^{5\%}_n$ are given in percent. The volumes of the PTV_r relative to the $\text{PTV}^{80\,\text{s}}_\text{r}$ volume (V_{rel}) were additionally calculated. Table reprinted from [116].

	Patient 1				Patient 2				Patient 3			
	DSC	SE	PRE	V_{rel}	DSC	SE	PRE	V_{rel}	DSC	SE	PRE	V_{rel}
$\text{PTV}^{80\,\text{s}}_\text{r}$	72	100	57	100	58	99	41	100	72	98	56	100
$\text{PTV}^{10\,\text{s}}_\text{r}$ (best)	76	100	63	90	63	99	46	89	75	97	60	93
$\text{PTV}^{10\,\text{s}}_\text{r}$ (worst)	75	100	61	94	60	80	49	67	74	95	60	92
$\text{PTV}^{\text{midV}}_\text{r}$	78	99	67	84	66	68	66	44	78	90	68	77
$\text{PTV}^{5\%}_\text{r}$	75	100	62	91	68	90	55	69	75	96	61	91
$\text{PTV}^{10\%}_\text{r}$	77	100	64	88	68	83	59	60	76	95	63	87

4.3.4 Geometrical volume overlap analysis

The DSC, SE, and PRE were calculated for each patient for all twelve PTV_r from the reference imaging session with the $\text{ITV}^{5\%}_n$ from the remaining imaging sessions. Figure 4.5 shows the results of this geometrical overlap analysis for the three patients separately and all patients accumulated. The median overlap values are summarized in Table 4.4 along with the PTV_r volumes relative to the $\text{PTV}^{80\,\text{s}}_\text{r}$ volumes.

The $\text{PTV}^{80\,\text{s}}_\text{r}$ had the largest volumes, the highest SE, but lowest PRE values of all defined PTVs, with median SE values between 98 and 100% and median PRE values in the range 41–57%.

The $\text{PTV}^{10\,\text{s}}_\text{r}$ with the highest and lowest median SE (averaged over all imaging sessions) were labeled "best" and "worst", respectively. The differences of the SE and PRE values of these two target volumes depended on the regularity of the breathing pattern observed during the reference imaging session. These differences were small ($\leq$ 2%) for Patients 1 and 3, whose breathing patterns on day 1 were very stable, as indicated by the small variance of the motion amplitudes in Figure 4.3b&d. The breathing pattern variability of Patient 2 during the reference imaging session was high (Figure 4.3c), which led to a difference of 19% between the SE of the best and worst $\text{PTV}^{10\,\text{s}}_\text{r}$ (99% vs. 80%). While the SE of the best $\text{PTV}^{10\,\text{s}}_\text{r}$ were comparable to those of the $\text{PTV}^{80\,\text{s}}_\text{r}$ (differences $<$ 1%), higher PRE values of up to 6% were measured for all patients. This increase originated from the smaller $\text{PTV}^{10\,\text{s}}_\text{r}$ compared to the $\text{PTV}^{80\,\text{s}}_\text{r}$, with volumetric differences up to 11%. By definition, the SE of the $\text{PTV}^{10\,\text{s}}_\text{r}$ cannot be larger than that of the $\text{PTV}^{80\,\text{s}}_\text{r}$. While no or a small decrease of the SE of the worst $\text{PTV}^{10\,\text{s}}_\text{r}$ compared to the $\text{PTV}^{80\,\text{s}}_\text{r}$ were observed for Patients 1 (0%) and 3 (3%), a large difference was measured for Patient 2 (19%).

The midV concept was developed to achieve a target volume reduction compared to the ITV approach by using motion-dependent anisotropic PTV margins [135]. Volume reductions between 16 and 56% compared to the $\text{PTV}^{80\,\text{s}}_\text{r}$ were achieved for the $\text{PTV}^{\text{midV}}_\text{r}$ for the

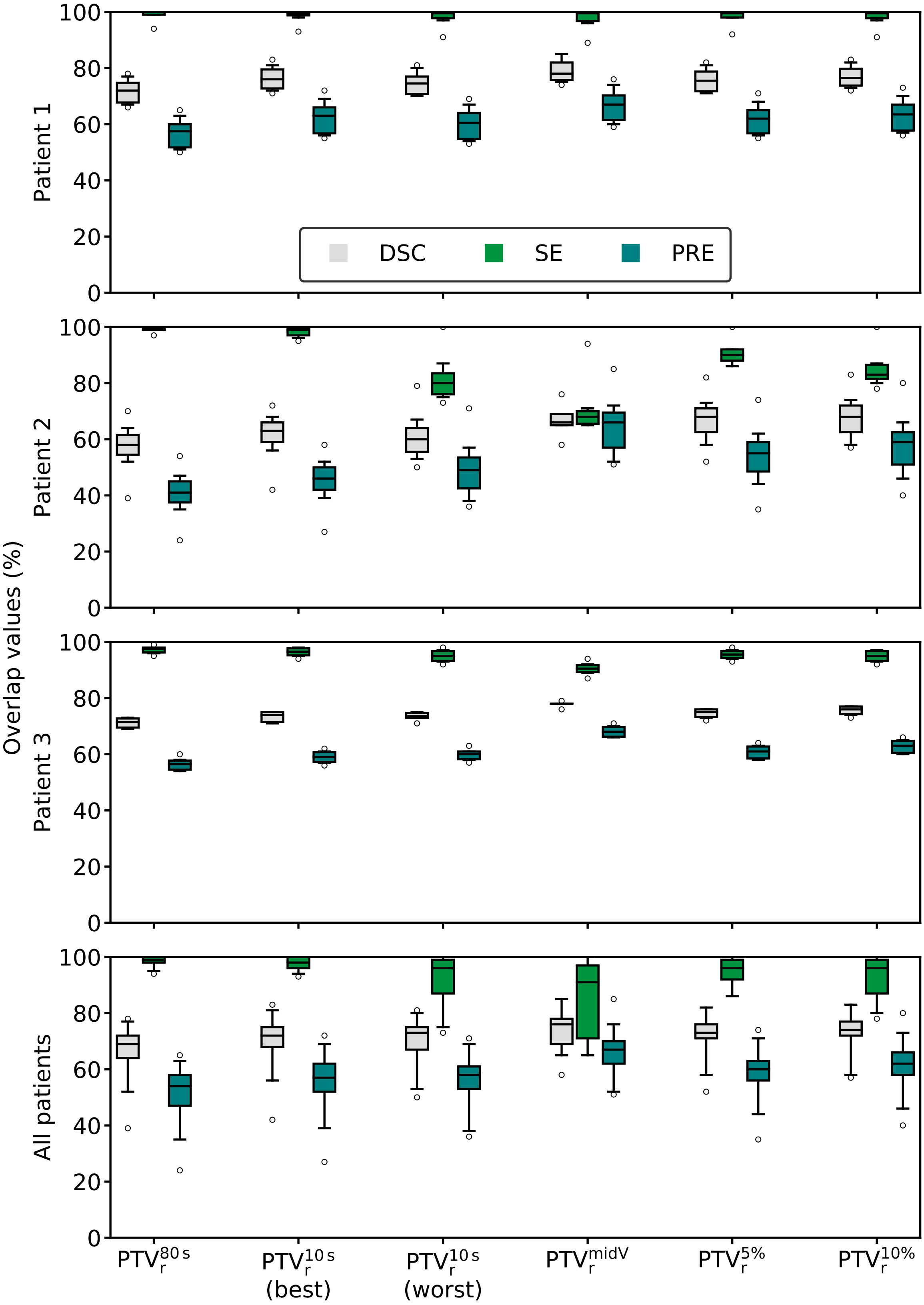

FIGURE 4.5: **Geometrical overlap analysis results.** The DSC, SE, and PRE of the different PTV_r with the $ITV_n^{5\%}$ are summarized in box plots. The results are plotted for each patient individually (top three rows) and all patients accumulated (bottom row). $PTV_r^{10\,s}$ (best/worst) are defined as the $PTV_r^{10\,s}$ with the highest/lowest median SE value. The whiskers of the box plots indicate the 5th and 95th percentiles. Figure reprinted from [116].

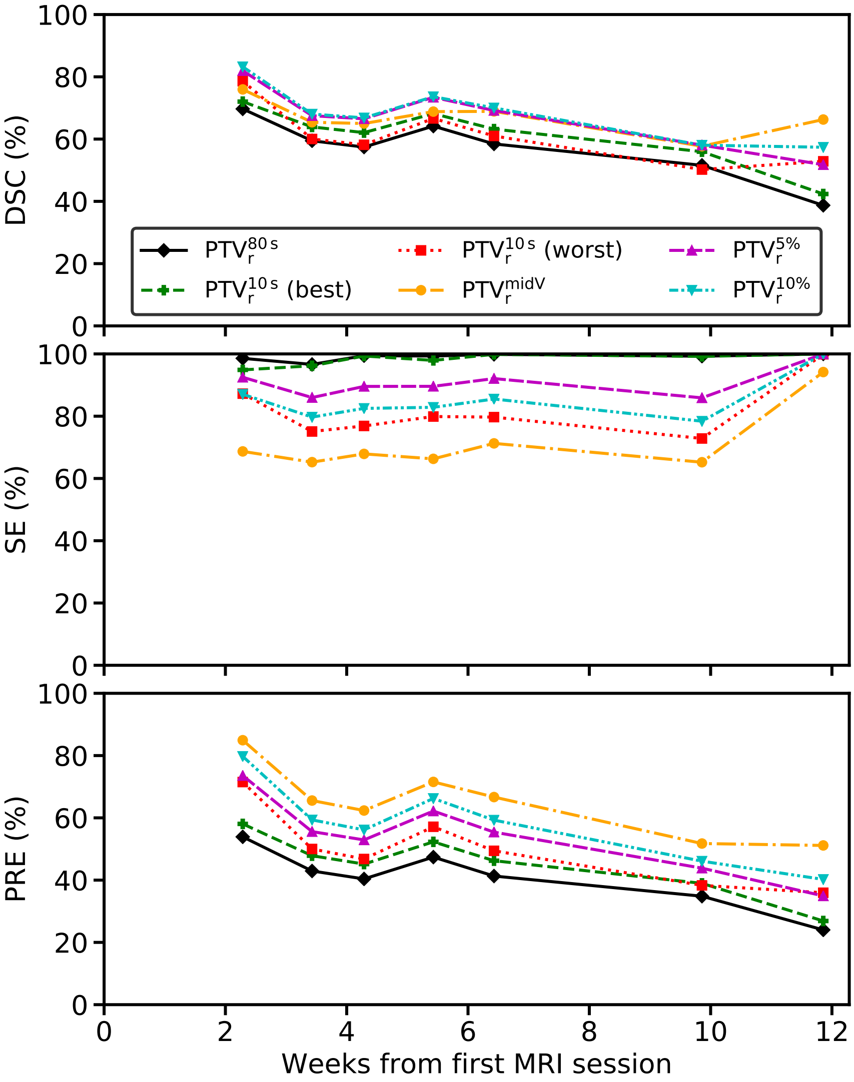

FIGURE 4.6: **Time development of geometrical overlap values.** The DSC (top row), SE (center row), and PRE (bottom row) values of the different PTV_r with $ITV_n^{5\%}$ are plotted as a function of the time difference between the reference imaging session and the sessions on day n for Patient 2. Figure reprinted from [116].

three patients. Consequently, the smallest volumes and highest PRE values (≈ 67% for all patients) among all PTV_r were measured, at the cost of decreased SE values. The largest SE difference of 31% was observed for Patient 2, with a median SE value of 68% for the PTV_r^{midV} compared to 99% for the $PTV_r^{80\,s}$.

The PTVs could be reduced by 9–31% compared to the $PTV_r^{80\,s}$ when a 5% POP threshold was used to create the $PTV_r^{5\%}$. The median SE values of the $PTV_r^{5\%}$ compared to the $PTV_r^{80\,s}$ were similar for Patients 1 and 3 (differences $\leq 2\%$), but 9% smaller for Patient 2 (90% vs. 99%). Compared to the PTV_r^{midV}, the SE of the $PTV_r^{5\%}$ was higher by up to 22%, and the PRE was smaller by up to 11% due to the increased PTV. When using a POP threshold of 10% instead of 5% for the creation of the $PTV_r^{10\%}$, the PRE increased by up to 4%, while the SE decreased by up to 7%.

In addition to the comparison of the median SE and PRE values averaged over all imaging sessions, their development over time was investigated in patient-specific analyses. Interfractional changes such as tumor shrinkage or different breathing patterns on different days impact these values. Figure 4.3b&d show that the differences of the median amplitudes on different days were small for Patient 1 (the standard deviation of the median 3D centroid motion amplitude was 1.3 mm) and that the median 3D motion amplitudes of Patient 3 were decreasing over time. This led to only small changes of the SE over time for these two patients, with a standard deviation of smaller than 4% for both patients and all $\mathrm{PTV_r}$. The median GTV motion amplitudes measured in the first and last imaging session of Patient 2 were 13 mm and substantially larger (16–20 mm) in the remaining imaging sessions (Figure 4.3c). Figure 4.6 shows that this led to a higher variance of the SE of the different $\mathrm{PTV_r}$ over time. The tumor of this patient was shrinking over the course of the treatment, which led to a gradual decrease of the PRE over time for all $\mathrm{PTV_r}$.

4.4 Discussion

ITVs and midV were defined based on the lung tumor motion assessed with real-time 4D-MRI for three lung cancer patients. A new concept for the definition of the ITV based on the sampled target POP was proposed. The ability to account for interfractional changes over the course of several weeks was quantified in terms of the volume overlap metrics DSC, SE, and PRE.

The GTVs were mainly moving in SI direction. The motion amplitudes measured for GTVs located in the lower lobe (Patients 2 and 3) were considerably larger than in the middle lobe (Patient 1). Hysteresis GTV centroid motion in SI and AP direction was observed in some of the 4DMRIs, as commonly seen for lung tumors [21, 186]. These observations are consistent with other studies published in the literature [21, 119, 122, 205].

The metrics SE and PRE were used to quantify the volume overlap of the $\mathrm{PTV_r}$ with the $\mathrm{ITV}_n^{5\%}$. A high SE (target coverage) is generally more important than a high PRE (normal tissue sparing) in radiotherapy. Due to these different priorities, the interpretation of the overlap results based on the DSC alone was found to be insufficient since the DSC merely sets a lower limit on the SE and PRE. As can be derived from Equation 4.5, the PRE and SE can be very different for a given DSC, e.g., for a DSC of 80%, the SE can take any value in the range [67%, 100%].

The most conservative target volume concept investigated in this study was the $\mathrm{PTV_r^{80\,s}}$. This volume was defined by calculating the union of all GTV positions captured during 4D-MRI, including improbable GTV positions that rarely occur. While this led to the highest SE values of all compared $\mathrm{PTV_r}$, the PTVs might be unacceptably large from a clinical perspective.

The $\mathrm{PTV_r^{10\,s}}$ were used as surrogates for today's standard PTVs derived from 4D-CT-based ITVs. The statistical uncertainties due to the limited motion sampling time period of 10 s become systematic errors when the ITV definition is based on these data. These errors can impact the whole radiotherapeutic treatment. This was observed for Patient 2, for whom large differences between the SE of the best and worst $\mathrm{PTV_r^{10\,s}}$ were detected.

The smallest PTVs and highest PRE values were found for the $\mathrm{PTV_r^{midV}}$. For Patients 1 and 3, the median SE values were 99% and 90% for these target volumes, respectively. These patients could benefit from the midV-based instead of an ITV-based PTV definition. The smallest median SE value of all investigated $\mathrm{PTV_r}$ and patients was observed for the $\mathrm{PTV_r^{midV}}$ for Patient 2 with a value of 68%. This indicated that the GTV motion captured during the reference imaging session was not representative of the target's motion in the follow-up imaging sessions. Figure 4.3c shows that the variance of the GTV motion in SI direction in the reference imaging session on day 1 was high. The direction-dependent PTV margin around the midV was calculated using only the median motion amplitudes. In this simplification step, the rich GTV motion information was lost, and the extent of motion was underestimated. This led to low SE values when the $\mathrm{PTV}_\mathrm{r}^\mathrm{midV}$ was compared with the $\mathrm{ITV}_n^{5\%}$ of the follow-up imaging sessions.

Ehrbar et al. [201] and Thomas et al. [202] performed dosimetric studies, comparing the midV and ITV concepts. They concluded that by using a midV instead of an ITV, the dose delivered to healthy lung tissue could be reduced while keeping the tumor coverage constant. In both studies, the dose was recalculated on the same 4D-CT images used for the target volume definition, neglecting the impact of interfractional changes or breathing pattern variations. The present study results suggest that these changes can strongly deteriorate the SE, which was used as a surrogate metric for the tumor coverage. The definition of the $\mathrm{ITV}_\mathrm{r}^{5\%}$ based on the GTV POP was found to be more robust than the midV concept in these cases.

The motivation for using non-zero cutoffs for the $\mathrm{PTV}_\mathrm{r}^{5\%}$ and $\mathrm{PTV}_\mathrm{r}^{10\%}$ definition was to avoid the potentially substantial increase of the ITV through rare extreme positions of the GTV (e.g., when the patient coughs), which are not representative for the typical target motion. The probabilistic approach used for the $\mathrm{PTV}_\mathrm{r}^{5\%}$ definition could decrease statistical uncertainties in the PTV definition. This led to high median SE values with low variance (cf. Figure 4.5) and higher robustness against interfractional changes compared to the $\mathrm{PTV}_\mathrm{r}^{10\,\mathrm{s}}$ and $\mathrm{PTV}_\mathrm{r}^\mathrm{midV}$.

In Figure 4.4, a volume with a POP of 100% exists. This volume depends on the GTV size and the magnitude of the GTV motion. It can take any value between zero and the $\mathrm{ITV}^{80\,\mathrm{s}}$ size. Voxels with a POP of 100% are the essential voxels that have to be targeted in radiotherapy. A miss of voxels with a lower POP would be less critical. The use of non-zero thresholds for the POP-based ITV definitions led to a considerable reduction of the PTV. This resulted in increased PRE and DSC values compared to the $\mathrm{PTV}_\mathrm{r}^{80\,\mathrm{s}}$. Increasing this POP threshold value bears the risk of underdosing the GTV at its edges. The derivation of the optimal threshold is not trivial, is expected to be patient-specific, and necessitates additional dosimetric analyses. In this study, the use of a 10% instead of a 5% threshold resulted in only small PRE increases while the SE was reduced. For these patients, the higher normal tissue sparing (higher PRE) might not justify the decreased target coverage (decreased SE).

The volume with a POP of 100% in Figure 4.4 is surrounded by a distribution in which the POP is transitioning to a value of 0%. The gradients of this distribution depend on the extent of motion in the respective directions. In this study, the different ITVs were expanded by isotropic 5 mm margins to create the PTVs. As a potential future extension of the proposed method, non-isotropic PTV margins, similar to those surrounding the midV, could be derived based on these gradients. An alternative approach could be to incorporate the POP distributions in the treatment planning process directly. Following the work by Shusharina et al. [206] on probabilistic treatment planning, this could be achieved by defining an "internal target distribution" instead of a binary ITV using these POP maps.

In general, the results suggest that patients could benefit from the additional 4D-MRI which allows a longer and more representative target motion assessment than achievable with today's 4D-CT-based method. The standard treatment planning and delivery workflow could be adapted in the following way:

- Real-time 4D-MRI acquisition – ideally in treatment position – instead of or in addition to 4D-CT imaging for treatment planning,
- ITV definition based on the derived POP distributions with an appropriately chosen threshold,
- PTV definition with isotropic or anisotropic margins to prospectively account for potential interfractional changes,
- treatment delivery at a conventional linac with CBCT-based image guidance to monitor interfractional anatomical changes,

- repetition of real-time 4D-MRI and subsequent target volume overlap analyses for target volume verification and patient-specific QA, ideally followed by a dosimetric evaluation,
- replanning, if large interfractional changes are detected on the CBCT images or in the target volume overlap analysis.

Thomas et al. [195] summarized studies on the lung tumor motion assessment with cine MRI (cf. Table 1 in [195]). While the number of patients in the proof-of-concept study presented in this chapter was limited to three, the number of MR imaging sessions was higher by a factor of 2–4 compared to these published studies. The real-time 4D-MRI acquisition time was limited to 80 s due to technical reasons. In the future, the acquisition time could be prolonged to improve statistics and to reach convergence of the probability density function of the GTV positions on the day of imaging [188]. The proposed method relies on several DIR steps, and the MR images were corrected for geometric distortions. These two factors introduce uncertainties that are difficult to quantify, but the higher robustness of the POP-based ITVs is expected to outweigh these. The proposed workflow requires dedicated imaging sessions and analyses, which are associated with additional costs and workload. Future dosimetric evaluations will have to quantify whether this is appropriately traded off by an improved target coverage or a reduced integral dose to healthy tissue. The spatiotemporal resolution of the real-time 4D-MRI sequences available today is limited. This includes the TWIST sequence used in this study. A coarse image resolution affects the accuracy of the DIR and the target delineation. A temporal resolution below 2 Hz can lead to apparent enlargements of moving structures and underestimations of the inhale and exhale positions [207]. This can result in an underdosage of the GTV edges. In the imaging sessions included in this study, a median breathing rate of 12 cycles/min was measured. With the temporal resolution of 2 Hz, a median of ten volumetric images were acquired per breathing cycle. Therefore, for breathing rates of 12 cycles/min, the uncertainty due to the underestimated motion is expected to be comparable to that of 4D-CT imaging, where typically ten images are reconstructed (section 2.6.2). This effect is of higher importance and must be considered for breathing frequencies higher than 12 cycles/min. The interest in the development of real-time 4D-MRI sequences has increased in the last few years. This was driven by the potential application of these sequences for MRgRT treatments at the MR-Linac [41]. New developments in this field (section 3.2.2) are expected to lead to the development of new sequences with higher spatial and temporal resolution compared to the sequence used in this study. These improvements would directly translate to lower uncertainties of the proposed method associated with the limited spatiotemporal resolution discussed above.

4.5 Conclusions

A novel concept for the ITV definition for lung cancer patients based on real-time 4D-MRI data was proposed. The ITVs were derived from the POP of the GTV in 3D, assessed over a time period of 80 s. This target volume was expanded by a PTV margin to account for interfractional anatomical and breathing pattern changes prospectively. The resulting PTVs were compared to a conservative target definition that included all observed positions ($\mathrm{PTV}_\mathrm{r}^{80\,\mathrm{s}}$) and PTVs mimicking target concepts used in current clinical practice ($\mathrm{PTV}_\mathrm{r}^{10\,\mathrm{s}}$, $\mathrm{PTV}_\mathrm{r}^{\mathrm{midV}}$). The different target volume concepts were evaluated in overlap analyses of the PTVs with the $\mathrm{ITV}_n^{5\%}$ of follow-up imaging sessions. The results suggest that the proposed method has the potential to reduce the statistical and systematic uncertainties associated with the target definition of today's standard-of-care 4D-CT-based workflow. This was attributed to the longer motion sampling times enabled by the real-time 4D-MRI sequence, which resulted in improved representativity and robustness of the target volumes. The higher complexity of the proposed clinical workflow need to be weighed against the potential increase in SE and PRE and the observed higher robustness of the target volumes. These overlap values were used as surrogates for target coverage and normal tissue sparing, which needs to be verified by future dosimetric evaluations. This study focused on the motion of lung tumors. The method can be straightforwardly adapted for other tumor sites strongly affected by respiratory-induced motion, such as tumors in the liver and pancreas.

The real-time 4D-MRI sequence used in this study enabled a continuous motion assessment in 3D through which intra- and intercyclic breathing pattern variations could be resolved. Such imaging sequences are attractive for application during beam delivery at MR-Linacs for 4D motion assessments (Chapter 5) and synthetic 4D-CT generation for dose reconstruction (Chapter 6). In this study, the patients were imaged at a diagnostic MRI scanner with a field strength of 1.5 T. At the ViewRay MRIdian MR-Linac (section 3.1.4), due to the limitations of the parallel imaging hardware (section 3.2.2) in combination with the low field strength of 0.35 T, no real-time 4D-MRI sequences are clinically available today. Therefore, different research groups have tried to fill this gap by building motion models driven by surrogate signals that can provide continuous time-resolved 4D-MRI with a high spatial and temporal resolution (section 3.3.1). An alternative method to create such estimated 4D-MRIs is the propagation method [46], which uses orthogonal cine MRI to estimate the motion states. This method was adapted for the MRIdian MR-Linac and experimentally validated in the scope of this thesis with a porcine lung phantom, which is described in the next chapter.

Chapter 5

Experimental validation of estimated 4D-MRI for low-field MR-Linacs

This chapter presents an experimental validation study conducted by the author in the scope of this dissertation. The methods and results of this study have been published as an article in *Physics in Medicine & Biology* in 2021 [178]. Figures 5.1, 5.2, 5.3, 5.7, 5.8, 5.9, and Tables 5.2 and 5.3 were included in this research article. Figures 5.4 and 5.5 have been published as supplementary material to the article. Table 5.1, Figures 5.6 and 5.10 were added to this chapter and the text was adapted to provide additional information and increase the readability within this thesis.

The aim of this study was to assess the accuracy of time-resolved estimated 4D-MRI created with the propagation method by Paganelli et al. [46] in experiments conducted with a porcine lung phantom at a low-field MR-Linac. The motivation for estimated 4D-MRI for MRgRT is presented in section 5.1. The data acquisition, processing, and analysis steps are described in section 5.2. The accuracy of the estimated 4D-MRI was visually and quantitatively assessed, and the results of these analyses are summarized in section 5.3. The main findings, the limitations, and the advantages of the propagation method are discussed in section 5.4, and the conclusions are given in section 5.5.

5.1 Motivation for estimated 4D-MRI for MRgRT

Hypofractionated SBRT (Chapter 1 and section 2.5.3) of early-stage NSCLC has become an alternative treatment to surgery [13, 208, 209]. This was enabled by technological advancement in the last years, including the clinical introduction of the MR-Linac (section 3.1). These machines can precisely deliver highly conformal doses to moving lung tumors through daily plan adaptations and gated beam delivery (section 3.1.6) [18, 168, 210].

At the ViewRay MRIdian MR-Linac (section 3.1.4) [26, 45], the target movement is visualized with real-time cine MRI during irradiation. The bSSFP sequence (section 3.1.5) used in clinical practice is limited to the acquisition of a single sagittal slice with a frame rate of 4 Hz or 8 Hz (section 3.1.7) [92, 162, 168, 169, 211]. This slice is positioned to intersect the moving target. In the case of strong out-of-plane motion, the limitation to two dimensions can lead to target localization errors. Furthermore, no information about the 3D motion of the target and the surrounding normal tissues can be inferred from this 2D slice [40].

Time-resolved 4D-MRI acquired at the MR-Linac would enable the motion monitoring of the whole thorax during beam delivery. These images could improve the target localization in 3D for gating, which could help avoid tumor underdosages and OAR toxicities [13, 122, 212]. In the future, these images could be used for performing tracking (section 2.6.6) and serve as input data for creating synthetic 4D-CTs (section 3.3.2 and Chapter 6) for real-time treatment adaptation or post-beam 4D reconstruction of the delivered dose [40, 41, 49].

Real-time 4D-MRI would be the natural sequence of choice for this purpose, but the spatiotemporal resolution of these sequences is still too poor for these applications (section 3.2.2 and Chapter 4) [40, 41, 116].

Several approaches have been proposed in the literature to infer the 4D anatomy from data with lower dimensionality. These methods include acquiring multiple parallel slices [26, 213], the interleaved [46, 194, 214, 215] or simultaneous [216, 217] acquisition of orthogonal slices and surrogate-driven motion models (section 3.3.1) [179, 185, 218].

In the study presented in this chapter, the propagation method, originally proposed by Paganelli et al. in 2018 [46], was employed and experimentally validated. The propagation method generates continuous estimated 4D-MRI, derived from the DIR of a 3D reference image to orthogonal 2D cine MRI data. The accuracy of these 4D-MRI was assessed in the original proof-of-concept study with digital phantom data simulating exemplary patient images [46]. Furthermore, the propagation method was compared to four other methods that estimate 4D-MRI based on 2D cine MRI data in an *in silico* study by Paganelli et al. [47]. The methods were tested with a digital MRI phantom that simulated the breathing patterns of six NSCLC patients [47]. In this comparison, the propagation method achieved the lowest tumor tracking error.

While the computational phantoms used in these two studies allow a comparison of the estimated motion state to a ground truth image, these phantom images are idealized simulations without image artifacts. A validation of the method with patient data acquired under realistic conditions would be desirable. However, the patient data cannot be used for accurate validation since no ground truth images can be acquired due to the unavoidable irregularity of human breathing. Thus, a porcine lung phantom [48] was used for the experiments described in this chapter. This phantom simulates patient-like breathing motion with *ex vivo* porcine lungs and has been used for experimental studies with CT, CBCT, and MRI scanners in the past [219–222]. The unique characteristics of the phantom allow acquiring realistic and reproducible imaging data that are needed for a thorough validation of motion estimation methods before their potential clinical implementation.

The purpose of this study was an experimental validation of the propagation method for MRgRT with this porcine lung phantom. The propagation method was adapted for the use at the low-field MRIdian MR-Linac by ViewRay. The estimated 4D-MRI output by the method were compared to respiratory-correlated 4D-MRI that served as ground truth to assess their accuracy and identify factors influencing it.

5.2 Material and Methods

5.2.1 Porcine lung phantom

The MR-compatible porcine lung phantom artiCHEST (PROdesign GmbH, Heiligkreuzsteinach, Germany) [48] used for the validation measurements in this study is depicted in Figure 5.1. This phantom allows reproducible simulation of breathing motion with *ex vivo* porcine lungs in a geometry that resembles a human thorax. The main components of the phantom are two double-walled shells that surround the lungs, an artificial silicone diaphragm located inferior to the lungs, tubes, and hoses connecting the phantom with vacuum and pressure pumps, and a control system. The shells were filled with a nickel(II) sulfate ($NiSO_4$) solution with a concentration of 1.25 g/l to simulate the MR signal in the human chest wall [220].

Ex vivo porcine lungs were purchased from local slaughterhouses and checked for airtightness and tissue damages. Gelatin powder (TreeHouse Foods, Inc., Oak Brook, IL, USA) was dissolved in water with a concentration of 0.3 g/ml by heating up to approximately 50 °C. The mixture was injected into the lung tissue at four to eight positions per lung. Upon

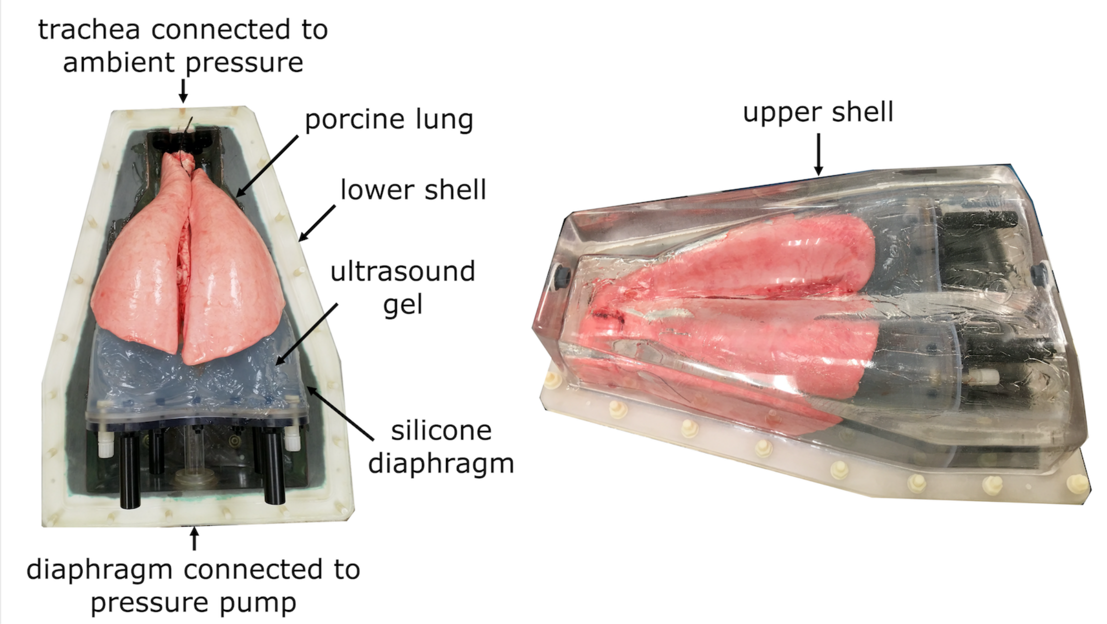

FIGURE 5.1: **Porcine lung phantom.** The photos show the phantom with its main components indicated by the arrows and labels. The left photo shows a view from the top onto the lower shell on a porcine lung and the water-filled silicone diaphragm. In the right photo, the phantom was closed with the upper shell and hermetically sealed. The lung is passively inflated by evacuating the volume surrounding it with vacuum pumps (not depicted). Figure reprinted from [178].

contact with the cold tissue, this mixture solidified and formed structures with volumes of 1.3–13 cc. These nodules were used as surrogate target lesions and were comparable in size to stage T1 NSCLC lesions [223]. The injected mixture amount was deliberately varied to test the 4D-MRI estimation for a range of different nodule sizes. The lungs and the inner surfaces of the two phantom shells were lubricated with ultrasound gel to reduce friction between the tissue and plastic surfaces. This allowed the simulation of sliding motion as occurring during human breathing. The lungs were mounted into the phantom by connecting the trachea to a tube at ambient pressure and placing the lung onto the silicone diaphragm. The phantom was hermetically sealed by mounting the upper shell. The lungs were passively inflated by applying an underpressure with two vacuum pumps connected via hoses to the phantom.

The control system allows the simulation of arbitrary periodical diaphragm movements for a range of different breathing frequencies and amplitudes. The breathing motion is induced by applying air pressure to the water-filled silicone diaphragm with an external pump connected via a pressurized hose to its base plate. The diaphragm expands and contracts and thereby passively moves the lungs within the phantom.

5.2.2 MRI scanner

The measurements were conducted at the 0.35 T MRI scanner unit of a research version of the commercial MRIdian MR-Linac by ViewRay (section 3.1.4), located in Oakwood Village, OH, USA. The scanner has the same imaging capabilities as the clinical version. The phantom was positioned on the treatment couch with the vendor's torso coils designed for the treatment of abdomino-thoracic lesions. The estimated centroid of the lungs in inferior-superior (IS), AP, and RL direction was aligned to in-room lasers indicating a virtual isocenter. The phantom was then moved into the scanner's bore to position this reference point at the imaging isocenter. When the MRI is operated in clinical mode, the parameters of the

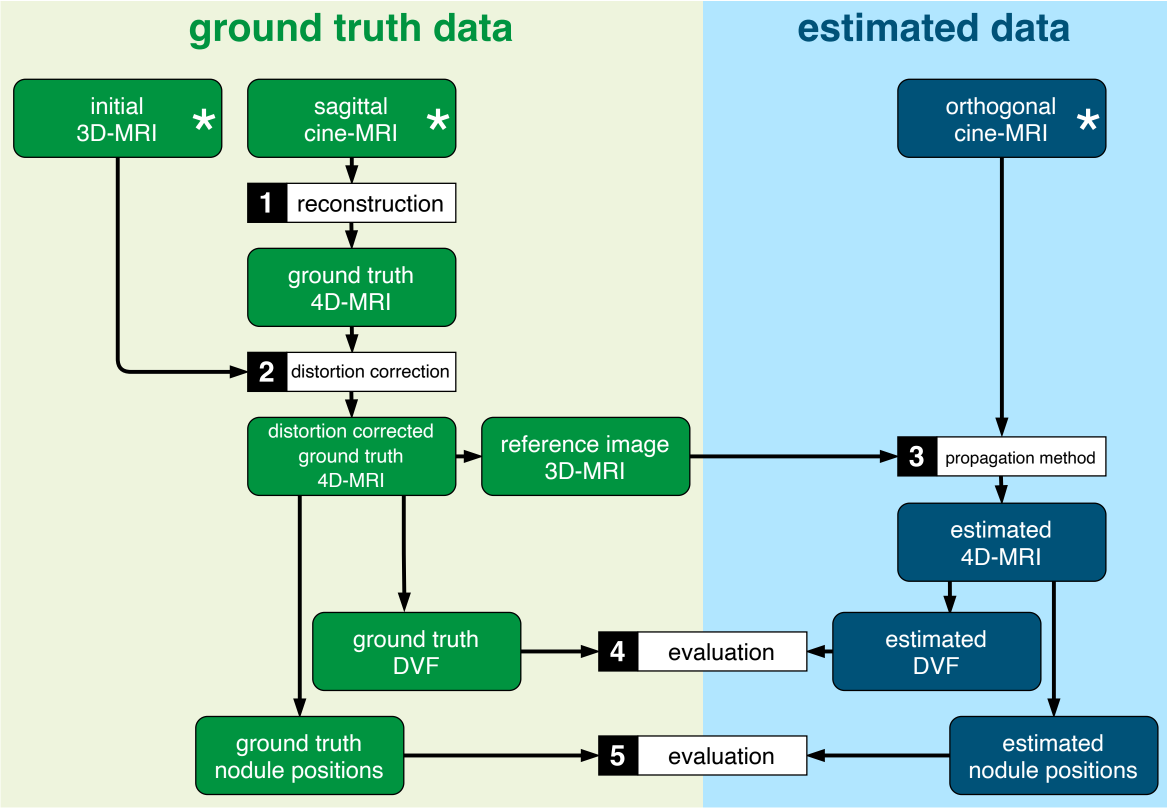

FIGURE 5.2: **Data acquisition, analysis, and evaluation workflow.** Ground truth (left) and estimated (right) 4D-MRI datasets were reconstructed from 3D and 2D cine MRI data (steps 1–3). In steps 4 and 5, these datasets were compared in geometrical DVF and nodule position analyses to quantify the accuracy of the propagation method. Data fields marked with an asterisk (*) represent acquired images, and all other data fields represent post-processed data. Figure reprinted from [178].

imaging sequences cannot be modified. Therefore, all images were acquired in QA mode, which allowed the use of custom sequence parameters. The image acquisition, data processing, and analysis workflow is depicted in Figure 5.2 and described in the following sections.

5.2.3 Image acquisition

Initial 3D-MRI

After positioning, the breathing motion was paused at the inhale phase since this is the most stable position determined by the phantom's design. The clinical bSSFP sequence (sections 3.1.5 and 3.1.6) was used to acquire a 3D-MRI of the phantom (TrueFISP; sagittal slices; 5 mm slice thickness; $1.2 \times 1.2\,\mathrm{mm}^2$ in-plane resolution; TR/TE: 3.4/1.4 ms; 554 Hz/pixel bandwidth; 60° flip angle; 334 × 260 acquisition matrix). The image was corrected for geometric distortions in 3D by applying the vendor's proprietary method.

Cine MRI for ground truth 4D-MRI

Retrospectively sorted respiratory-correlated 4D-MRIs (section 3.2.1) served as ground truth image datasets for the geometrical evaluation of the propagation method. These datasets were reconstructed from 2D cine MRI data acquired at different slice positions. After the acquisition of the initial 3D-MRI, the periodic breathing motion of the phantom was initiated. Fifty 2D cine MRI frames in sagittal orientation were acquired at each fixed slice position. This number of frames was chosen to capture 1.2–3.0 breathing cycles (depending on the set breathing frequency) at each slice position to avoid missing frames in the retrospective sorting process. The slice position was incrementally shifted by the slice thickness to cover all positions of the phantom in RL direction. The clinical bSSFP sequence (section 3.1.7) with a slice thickness of 5 mm and a frame rate of 4 Hz was chosen for this purpose [45, 92, 168, 169, 211] (TrueFISP; 3.5 × 3.5 mm^2 in-plane resolution; TR/TE: 2.4/1.1 ms; 1002 Hz/pixel bandwidth; 60° flip angle; 78 × 78 acquisition matrix; number of averages: 2). All cine MRI frames were corrected for geometric distortions in 2D with the vendor's proprietary method. The 2D cine MRI data were reviewed to identify nodules at different RL, IS, and AP positions that showed pronounced motion. Four of these nodules (two in each hemithorax) were selected for the subsequent orthogonal cine MRI acquisition.

Orthogonal cine MRI

A series of orthogonal cine MRIs was acquired for each selected nodule (TrueFISP; 5 mm slice thickness; 3.5 × 3.5 mm^2 in-plane resolution; TR/TE: 2.4/1.1 ms; 1000 Hz/pixel bandwidth; 60° flip angle; 100 × 100 acquisition matrix; number of averages: 1). The orthogonal images were acquired in sagittal and coronal orientation in an alternating fashion and were positioned to intersect the moving nodule. The phantom was breathing with the same motion patterns as during cine MRI for the ground truth 4D-MRI creation. For each nodule, 600 frames (300 in each orientation) were collected within 82 s, corresponding to a frame rate of 7.3 Hz. All images were corrected for in-plane geometric distortions in 2D using the vendor's method. The number of recorded breathing cycles depended on the set breathing frequency and ranged from 8 (6 cycles/min) to 20 (15 cycles/min).

Verification 3D-MRI

After orthogonal cine MRI, the breathing motion of the phantom was paused at the inhale position. A verification 3D-MRI with the same sequence parameters as for the initial 3D-MRI was subsequently acquired. This image served to quantify potential changes of the lung tissue and the gelatin nodules over time. The similarity of the initial and verification 3D-MRI was inspected in overlay views to check for potential changes due to nodule baseline shifts or lung tissue deflation between the two image acquisitions. To quantify the positional changes within the lung, the initial and verification 3D-MRI were deformably registered in a multi-stage B-spline DIR with MSE as the similarity metric using Plastimatch [200]. The median and 95th percentile values of the vector lengths in the output DVF within the lungs were calculated.

5.2.4 Motion pattern variation

All imaging protocols described above were repeated with different lungs and motion patterns to assess the accuracy and robustness of the propagation method under varying conditions. For this, the breathing frequency and amplitude, as well as the rotation of the phantom around its AP axis were varied. The goal of the phantom rotation was to change the extent of motion in RL direction and thereby the through-plane motion with respect to the sagittal slice. The measurements were performed with three porcine lungs to create eight datasets in total. Table 5.1 summarizes the dataset-specific motion parameters. The baseline pressure of the diaphragm that controls the lung's maximum inflation state was additionally changed between the acquisition of datasets 6, 7, and 8 (not indicated in Table 5.1).

5.2.5 Ground truth 4D-MRI reconstruction

The respiratory-correlated 4D-MRIs used as ground truth datasets were reconstructed from the planar cine MRI data (step 1 in Figure 5.2). For each slice position, the median image intensity was calculated and plotted as a function of time. Based on these plots, the first 10–15

TABLE 5.1: **Dataset-specific motion parameters.** The table summarizes the motion parameters set for the acquisition of the eight datasets. The motion amplitude is given relative to the diaphragm motion amplitude of dataset 1. The phantom was rotated around its AP axis.

Dataset	Lung	Breathing frequency (cycles/min)	Relative amplitude (%)	Phantom rotation (°)
1	1	15	100	0
2	1	6	100	0
3	2	7	100	0
4	2	7	100	-5
5	2	7	100	+5
6	3	7	120	0
7	3	7	80	0
8	3	7	100	0

frames of each cine MRI series were discarded since, at these frames, the steady state had not been reached yet (section 3.1.5). For the remaining frames, a surrogate signal was derived from the image intensities by calculating the sum of all pixels in a binary thresholded region of interest that included parts of the moving diaphragm. This signal was used to determine the frame number of the first inhale position. Starting at this frame, the subsequent images were assigned to 40 (6 cycles/min), 35 (7 cycles/min) or 16 (15 cycles/min) breathing phase bins, respectively. This procedure was repeated at each slice position to reconstruct the ground truth 4D-MRI with a spatial resolution of $3.5 \times 3.5 \times 5\,\mathrm{mm}^3$, representing the motion during one average breathing cycle with a frame rate of 4 Hz.

5.2.6 Geometric distortion correction

The geometric distortion of MR images, mainly caused by gradient nonlinearities, needs to be considered and corrected for MR-Linac treatments [91] (section 2.3.9). Several authors have investigated the geometric fidelity of 3D-MRI, and the in-plane distortion of 2D cine MRI acquired with the MRIdian MR-Linac after application of the vendor's correction methods [93–95]. The residual geometric distortion of these images was reported to be negligible within a 10 cm DSV (section 3.1.4) around the isocenter. The 2D cine MRI used in current clinical practice are, however, only corrected for in-plane distortions in 2D, but not for through-plane distortions [91]. When these images are used for gating (section 3.1.7) this is of minor importance since the target is mainly located at the center of the images where through-plane distortions are smaller than at the edges of the FOV. In this study, the accuracy of the propagation method was assessed in the whole lung, necessitating a correction of the through-plane distortions observed in the 4D-MRI since these can be in the order of several millimeters [91].

Keesman et al. [91] reported on the correction of slice-based respiratory-correlated 4D-MRI at the Unity MR-Linac (section 3.1.3). A similar approach was chosen in this study to correct for through-plane distortions of the reconstructed ground truth 4D-MRI (step 2 in Figure 5.2). The distortion correction was conducted for each of the eight datasets separately. For each dataset, the distortion-corrected initial 3D-MRI in inhale phase was defined as the undistorted fixed reference image. The inhale phase of the ground truth 4D-MRI was defined as the moving image to be deformed to match the fixed image. The aim of the correction method was to find the DVF that, when applied to the moving image, maximizes the similarity between the deformed and fixed images. The weights of spherical harmonics coefficients that parametrize this DVF were determined in an iterative optimization process

[91, 98]. In each iteration, a 3D vector field was calculated based on the intermediate weights of the coefficients up to the seventh order. The DVF was restricted to only correct for the RL distortions of the sagittal slices of the ground truth 4D-MRI. The intermediate DVF was applied to the moving image using Plastimatch [200]. The MI (section 2.4.6) between the deformed and fixed images was calculated and passed to the optimizer to update the weights using the constrained optimization by linear approximation (cobyla) method implemented in the Python package lmfit [224]. After convergence, the final DVF and deformed image were visually assessed for plausibility with overlay plots. The median and 95th percentile DVF vector lengths were calculated for all datasets accumulated to quantify the effect of the distortion correction. The correction DVF was applied to each phase of the ground truth 4D-MRI to correct for the through-plane distortions. The orthogonal cine MR images used in the propagation method were not retrospectively corrected for through-plane distortions. The motivation for this was that this type of correction is currently not available for the cine MRI acquired during patient treatments in clinical practice.

5.2.7 Estimated 4D-MRI generation

Estimated 4D-MRIs were generated with the propagation method by Paganelli et al. [46] (step 3 in Figure 5.2). Briefly summarized, the estimated motion states were derived by deformably registering 2D slices extracted from a 3D reference image to the orthogonal cine MRI data. The DVFs output by these registrations were extrapolated to 3D and applied to the reference image to obtain the estimated motion states. The individual steps of this method are described in more detail in the following.

Reference image determination
3D images at different breathing phases (inhale, mid-exhale, exhale, and mid-inhale) were extracted from the distortion-corrected ground truth 4D-MRI and used as reference images. The intention behind this was to test the influence of the reference image breathing phase on the performance of the propagation method.

Deformable image registration
Sagittal and coronal 2D images at the locations of the respective orthogonal slices were extracted from the 3D reference image. These reference slices were deformably registered to each of the sagittal and coronal frames of the orthogonal cine MRI series. Each DIR was performed in 2D in a multi-stage B-spline DIR using Plastimatch with gradient magnitude as the similarity metric (Figure 5.3). The cost function included a regularization term (section 2.4.3) to smooth the DVFs. The sliding motion between the lung and the inner phantom shell surfaces cannot be appropriately modeled by DIR (section 2.4.5), especially if a regularization term is included in the cost function [104]. This problem was circumvented by splitting up the DIR into two regions, as suggested in the literature [185, 225–227]. For this, the phantom cavity, including the lungs and the diaphragm, was segmented. The phantom shells surrounding this structure were assumed to be stationary, while the lungs and the diaphragm were assumed to be movable. The binary image of the phantom cavity structure was resampled at the orthogonal slice positions. These resampled binary images were used to mask the 2D DIR to ignore any stationary phantom parts in the registration process. All DVFs outside of the segmented cavity were then set to zero after the DIR.

Weighted extrapolation of DVFs
The motion information from consecutively acquired orthogonal cine MR images in the two orientations was combined to obtain 3D DVFs for the estimation of the motion states. The

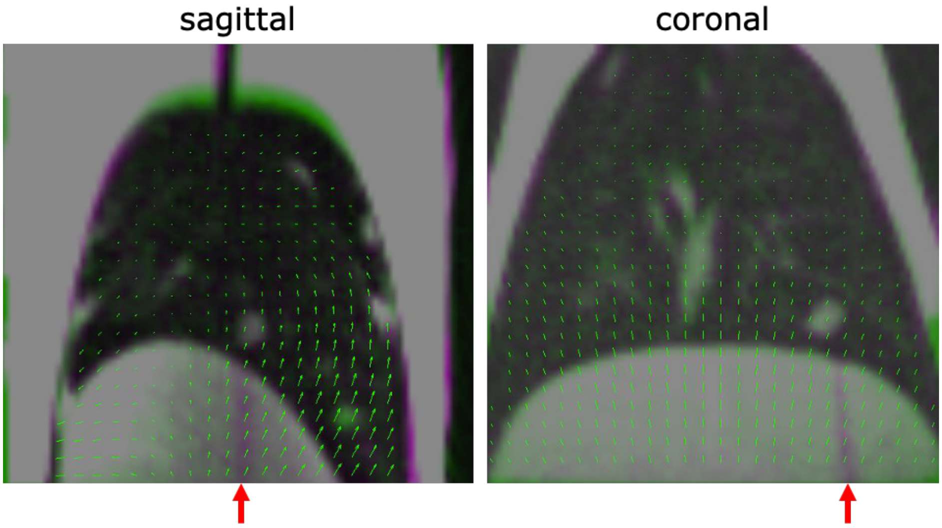

FIGURE 5.3: **DIR of reference and orthogonal slices.** Exemplary results of the 2D DIRs in sagittal and coronal orientation that are part of the propagation method are shown. The deformed 2D reference image slices are shown in purple, and the orthogonal cine MRI frames in green. The DVFs are depicted as green arrows. All DVF components outside of the phantom cavity were set to zero. The location of the orthogonal slice intersection, positioned at a nodule in the left lung, is indicated by the red arrows. The signal intensities at this position are reduced in the orthogonal images since the voxels located on this line are exited during imaging in both orientations. Figure reprinted from [178].

sagittal images of the orthogonal cine MRI series captured the motion in IS and AP direction, and the coronal images in IS and RL direction. All DVF components in AP direction of the sagittal DIR were replicated to all other sagittal slice positions within the 3D reference image. Therefore, the AP components of the DVF at voxels with the same IS and AP, but different RL positions were the same. Correspondingly, the DVF components in RL direction of the coronal DIR were replicated to all other coronal slice positions.

The motion in IS direction was captured by both the sagittal and coronal orthogonal images. The DVF component in IS direction within the 3D reference image volume was determined by calculating a weighted average of the IS vector components of the DIRs in the two orientations. In the proof-of-concept study by Paganelli et al. [46], constant weighting factors of 0.5 were used for this step, independent of the voxel position within the image volume. The theoretical considerations illustrated in Figure 5.4 showed that the constant weighting factors can introduce a systematic bias of IS components at the orthogonal slice positions or lead to DVF discontinuities in the vicinity of the orthogonal slices. Motivated by these findings, a different weighting factor method was developed in this study.

The weighting factors at the voxel position (x, y) for the IS DVF component of the sagittal DIR ($W^{\text{sag}}_{x,y}$) and the coronal DIR ($W^{\text{cor}}_{x,y}$) were calculated for all voxels within the reference image volume. These weighting factors depend on the normal distances of the voxel to the sagittal and coronal slices of the orthogonal images. The motion in IS direction in the left and right lung at the same lateral distances to the mid-sagittal plane was assumed to be similar. Hence, the distance of the voxel to the mirrored sagittal slice position with respect to the mid-sagittal plane at the center of the phantom in RL direction was additionally considered for the weighting factor calculation.

A coordinate system was defined in the following way: the x-axis was oriented along the RL direction, the y-axis along the AP direction, and the z-axis along the IS direction. The origin of the coordinate system was positioned at the center of the phantom, such that the mid-sagittal plane was located at $x = 0$. The RL position of the sagittal orthogonal slice is defined as x_0 and the AP position of the coronal orthogonal slice as y_0. The weighting

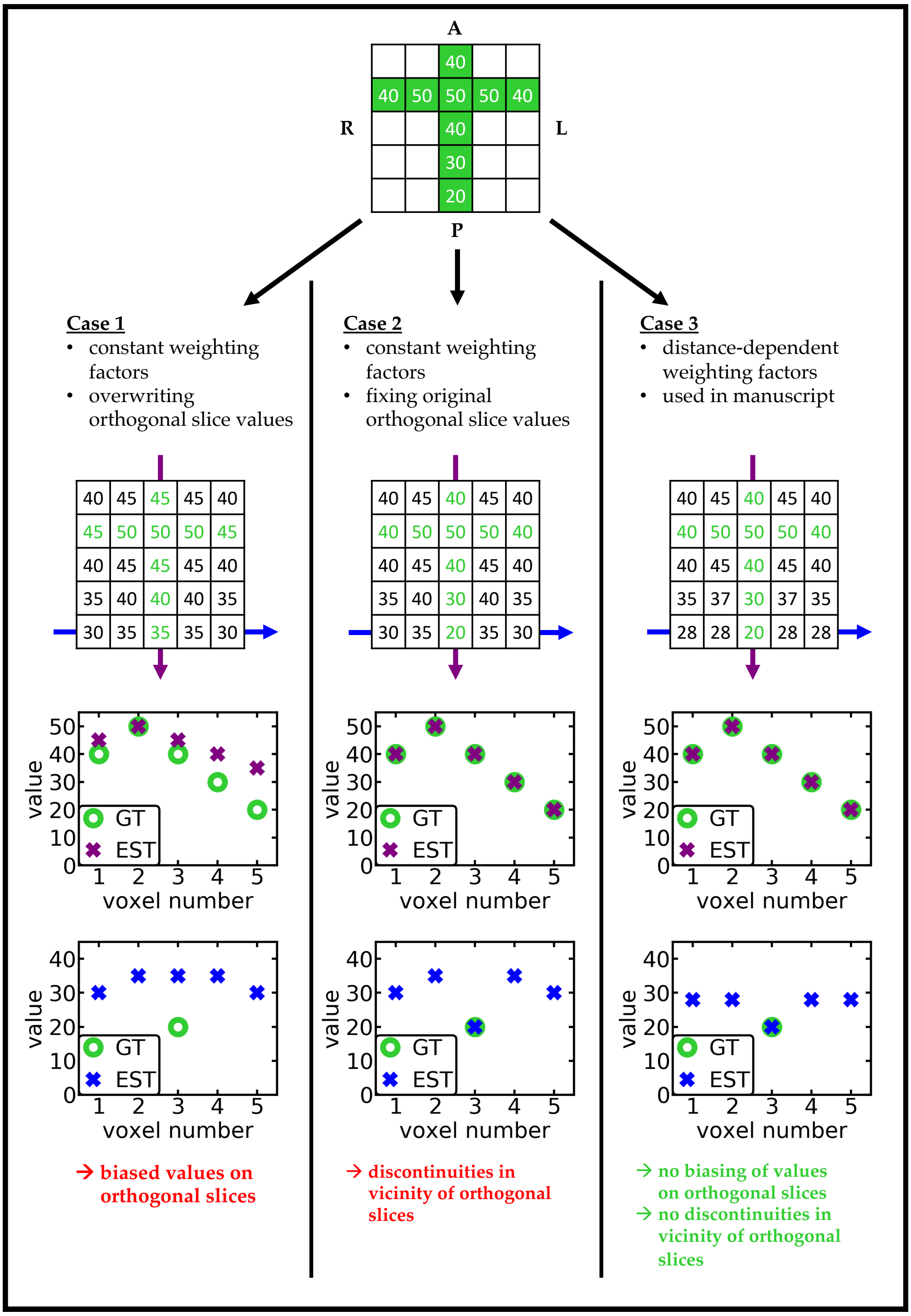

FIGURE 5.4: **Motivation for the change of the IS weighting method.** Exemplary ground truth IS vector field components are shown in the matrix in green for an axial slice (top image). The IS components in the axial slice are extrapolated using three different weighting methods (cases 1–3), and the resulting values are given in the matrices below the case descriptions. The ground truth (GT) and estimated (EST) IS vector field components along the sagittal orthogonal slice (purple arrow in AP direction) and along a coronal slice parallel to the coronal orthogonal slice (blue arrow in RL direction) are plotted as profiles in the lower two rows. While a systematic bias at the orthogonal slice positions and discontinuities along the coronal profile can be observed for case 1 (used in the feasibility study by Paganelli et al. [46]) and case 2, no biased values or discontinuities are introduced when the distance-dependent weighting factors (case 3; method proposed in this work) are used. This figure was published as supplementary material to [178].

factors at the voxel with position (x, y) were then defined as:

$$W_{x,y}^{\text{sag}} = \frac{|y - y_0|}{\min\left(|x - x_0|, |x + x_0|\right) + |y - y_0|}, \tag{5.1}$$

$$W_{x,y}^{\text{cor}} = \frac{\min\left(|x - x_0|, |x + x_0|\right)}{\min\left(|x - x_0|, |x + x_0|\right) + |y - y_0|}. \tag{5.2}$$

The weighting factors do not depend on the z-position. The normal distances between the voxel located at (x, y) to the sagittal and coronal slices were defined as $\Delta\text{RL} = |x - x_0|$ and $\Delta\text{AP} = |y - y_0|$, respectively. The distance of the voxel to the sagittal slice mirrored at the mid-sagittal plane was defined as $\Delta\text{RL}^{\text{m}} = |x + x_0|$. The weighting factors can then be rewritten as:

$$W_{x,y}^{\text{sag}} = \frac{\Delta\text{AP}}{\min\left(\Delta\text{RL}, \Delta\text{RL}^{\text{m}}\right) + \Delta\text{AP}}, \tag{5.3}$$

$$W_{x,y}^{\text{cor}} = \frac{\min\left(\Delta\text{RL}, \Delta\text{RL}^{\text{m}}\right)}{\min\left(\Delta\text{RL}, \Delta\text{RL}^{\text{m}}\right) + \Delta\text{AP}} = 1 - W_{x,y}^{\text{sag}}. \tag{5.4}$$

The weighting factors at $\Delta\text{RL} = \Delta\text{AP} = 0$ are not defined in these equations and were both set to 0.5. These voxels lie on the intersection line of the coronal and sagittal slices. The smaller the distance between the voxel and the sagittal or coronal slice, the larger the weighting factor of the corresponding slice orientation.

Estimated 4D-MRI

For each pair of consecutively acquired orthogonal images, the 3D DVF was calculated by superimposing the replicated RL and AP components and the IS components calculated with the weighting method described above. The 3D reference image was then deformed with these 3D DVFs to create the estimated 4D-MRI with a spatial resolution of $3.5 \times 3.5 \times 3.5\,\text{mm}^3$. In each orthogonal cine MRI series, 600 frames were acquired, thereof 300 in sagittal and 300 in coronal orientation. Analogous to the planar cine MRI data, the first 30 frames (15 in each orientation) were discarded since these images were acquired in the transient phase of the bSSFP sequence. Therefore, each estimated 4D-MRI consisted of 285 3D-MRI with a duration of 78 s and a temporal resolution of 3.65 Hz. This frame rate is half of the orthogonal slice acquisition frame rate (7.3 Hz) since the motion information from two consecutive images was combined. The breathing phase was determined at each time step of the estimated 4D-MRI. The same surrogate signal-based method as described in section 5.2.5 was applied to the sagittal slice of the corresponding orthogonal slice pair for this purpose. One estimated 4D-MRI was created for each orthogonal cine MRI series. In total, this yielded 32 estimated 4D-MRI – one for each of the four nodules in each of the eight datasets.

5.2.8 Estimated 4D-MRI evaluation

To evaluate the estimated 4D-MRI output by the propagation method, these images were geometrically compared to the ground truth 4D-MRI in a DVF analysis and a nodule centroid position analysis.

Deformation vector field analysis

The accuracy of the propagation method was assessed in the whole lung by directly comparing the ground truth and estimated DVFs (step 4 in Figure 5.2). The estimated DVFs were created through the DIR and extrapolation steps described in the previous section. To obtain the ground truth DVFs, the reference image extracted from the ground truth 4D-MRI was defined as the moving image. This moving image was registered to all remaining breathing phases of the ground truth 4D-MRI by 3D multi-stage B-spline DIR with MSE as the similarity metric (section 2.4.6), including a regularization term using Plastimatch. Similar to the DIR in the propagation method, these DIRs were masked with the segmented binary image of the phantom cavity to allow the modeling of sliding motion between the lungs and the phantom's shells. All DVFs outside of this structure were set to zero since these phantom parts were assumed to be stationary. The resulting DVFs were used as the breathing phase-dependent ground truth DVFs.

The ground truth and the estimated DVFs were subsampled to the same isotropic grid with a resolution of 10.5 mm. This corresponds to three times the in-plane resolution of the ground truth and orthogonal images. The subsampling was performed since the variance of the DVFs of neighboring voxels was expected to be low due to the regularization of the ground truth DIR and the 2D DIRs in the propagation method. The porcine lung was segmented with image processing algorithms on the motion-averaged ground truth 4D-MRI. The estimated and ground truth DVFs were exclusively compared within the segmented lung volume to not bias the results by including stationary phantom parts. For each time step of the estimated 4D-MRI, the 3D differences between the subsampled estimated and ground truth DVFs in the corresponding breathing phase were calculated. The median and 95th percentile differences were calculated at different breathing phases (reference, inhale, and exhale phase) and averaged over all phases. The influences of the motion amplitude and the distance of the grid points to either of the orthogonal slices on the estimation error were investigated.

Nodule centroid position analysis

The four selected nodules were contoured on the inhale image of the ground truth 4D-MRI, resampled to an isotropic image grid with a spatial resolution of $1.2 \times 1.2 \times 1.2\,\mathrm{mm}^3$. The structures were then converted to binary images. These images were propagated with the ground truth DVFs to all remaining breathing phases. The centroid positions of the four nodules in each breathing phase were determined by calculating the centroid of the transformed binary masks. These positions served as the ground truth nodule centroid locations. The estimated nodule centroid positions were determined analogously by transforming the binary nodule masks defined on the reference image to all other time points of the estimated 4D-MRI with the respective estimated DVFs and calculating their centroid positions.

The four nodules in each of the four estimated 4D-MRI per dataset were assigned to one of three categories. This classification was based on the normal distances of the individual nodule centroids in the reference image to the sagittal (ΔRL) and coronal slice locations (ΔAP) of the respective orthogonal slice series:

Category 1: Nodule was intersected by both orthogonal slices, with $\Delta\mathrm{RL} \leq 2\,\mathrm{cm}$ and $\Delta\mathrm{AP} \leq 2\,\mathrm{cm}$.

Category 2: Nodule was intersected by one of the orthogonal slices, with ($\Delta\mathrm{RL} \leq 2\,\mathrm{cm}$ and $\Delta\mathrm{AP} > 2\,\mathrm{cm}$) or ($\Delta\mathrm{RL} > 2\,\mathrm{cm}$ and $\Delta\mathrm{AP} \leq 2\,\mathrm{cm}$), respectively.

Category 3: Nodule was not intersected by either of the orthogonal slices, with $\Delta\mathrm{RL} > 2\,\mathrm{cm}$ and $\Delta\mathrm{AP} > 2\,\mathrm{cm}$.

The 3D distances between the estimated and ground truth nodule centroid positions in the corresponding breathing phases were determined. The median and 95th percentile values were calculated for each category and dataset, and for all datasets accumulated (step 5 in Figure 5.2).

Partial volume effect analysis

The limited spatial resolution of the cine MRI, with an in-plane resolution of $3.5 \times 3.5\,\mathrm{mm}^2$ and a slice thickness of 5 mm, introduced uncertainties in the nodule centroid position determinations due to the partial volume effect. The magnitude of this effect was estimated in a dedicated simulation.

Binary images of spheres with varying volumes (0.3–13.6 cc) were created on a high-resolution image grid ($0.2 \times 0.2 \times 0.2\,\mathrm{mm}^3$) and resampled onto a coarse grid ($3.5 \times 3.5 \times 5.0\,\mathrm{mm}^3$) with the same image resolution as the ground truth 4D-MRI using nearest neighbor interpolation. The centroid position of each sphere in the high-resolution image grid (c_{HR}) was exactly known by definition. The centroid position of the resampled sphere on the low-resolution grid (c_{LR}) was derived from the resampled binary images, analogously to the centroid determination described above. The centroid position determination error due to the partial volume effect (δ) is given by the Euclidean distance between c_{LR} and c_{HR}:

$$\delta = \|c_{\mathrm{LR}} - c_{\mathrm{HR}}\| \,. \tag{5.5}$$

This error was calculated each time after applying 250 random shifts to the sphere centroid in all directions in the high-resolution image before resampling. The random shifts were discretized to multiples of the high-resolution grid size (0.2 mm) up to one low-resolution voxel dimension in each direction (i.e., 3.5 mm in IS and AP, and 5.0 mm in RL direction) with a uniformly sampled distribution. The analysis was repeated for different sphere volumes in the range 0.3–13.6 cc. The median absolute position determination error due to the partial volume effect (σ_{PVE}) was calculated for each sphere volume.

In this study, the centroid position estimated error (e) was calculated based on the Euclidean distance between the ground truth and estimated nodule centroid positions, c_{GT} and c_{EST}:

$$e = \|c_{\mathrm{EST}} - c_{\mathrm{GT}}\| \,. \tag{5.6}$$

The partial volume effect uncertainty σ_{PVE} affects the precision of both the ground truth and the estimated centroid position determination. The total error due to partial volume effect σ_e can then be estimated as:

$$\sigma_e = \sqrt{2}\,\sigma_{\mathrm{PVE}} \,. \tag{5.7}$$

This error was compared to the nodule centroid estimation error for the different nodule volumes used in the study.

5.3 Results

5.3.1 Initial and verification 3D-MRI

No verification 3D-MRIs were acquired for datasets 1 and 2. The time differences between the acquisition of the initial and the available verification 3D-MRI (datasets 3–8) ranged between 26 and 69 min with a median value of 44 min. The images were analyzed in overlay plots for potential changes that could have occurred in this time period. No systematic changes were observed for any of these datasets. The overall median (95th percentile) vector length of the DVFs, obtained from initial to verification 3D-MRI DIR, within the lungs was 0.8 mm (2.6 mm), corresponding to 0.7 (2.2) times the in-plane resolution of the 3D-MRI. These results indicate that the lung tissue was stable over extended time periods, which confirms the suitability of the phantom for the intended purpose of the study.

5.3.2 Ground truth 4D-MRI

The regular and reproducible breathing motion of the phantom facilitated the retrospective breathing phase binning of the cine MRI frames for the reconstruction of the ground truth 4D-MRI. Stitching artifacts caused by erroneous binning would be visible as discontinuities at the diaphragm surface when viewed in a coronal or axial orientation. The reconstructed images featured only minor stitching artifacts (cf. coronal views of the 4D-MRI in Figure 5.5) caused by the residual uncertainties in the surrogate determination process and the finite breathing phase bin sizes. These were deemed negligible when compared to the uncertainties of the DIR to extract the ground truth DVFs.

The lack of through-plane distortion correction of the acquired sagittal 2D cine MRI led to geometric distortions of up to 10 mm in RL direction in the ground truth 4D-MRI. The 3D-MRI and the inhale phase of the ground truth 4D-MRI before, and after applying the through-plane distortion correction DVF determined in the optimization process are depicted in Figure 5.5. The distortions in the uncorrected image were increasing towards the edges of the FOV. The lower right difference plot in Figure 5.5 demonstrates that these distortions could be substantially reduced by applying the correction method. The differences between the corrected image and the initial 3D-MRI close to the imaging isocenter were negligible. Averaged over all eight datasets, the median (95^{th} percentile) distortion correction DVF vector lengths within the segmented lung masks were 1.5 mm (4.9 mm).

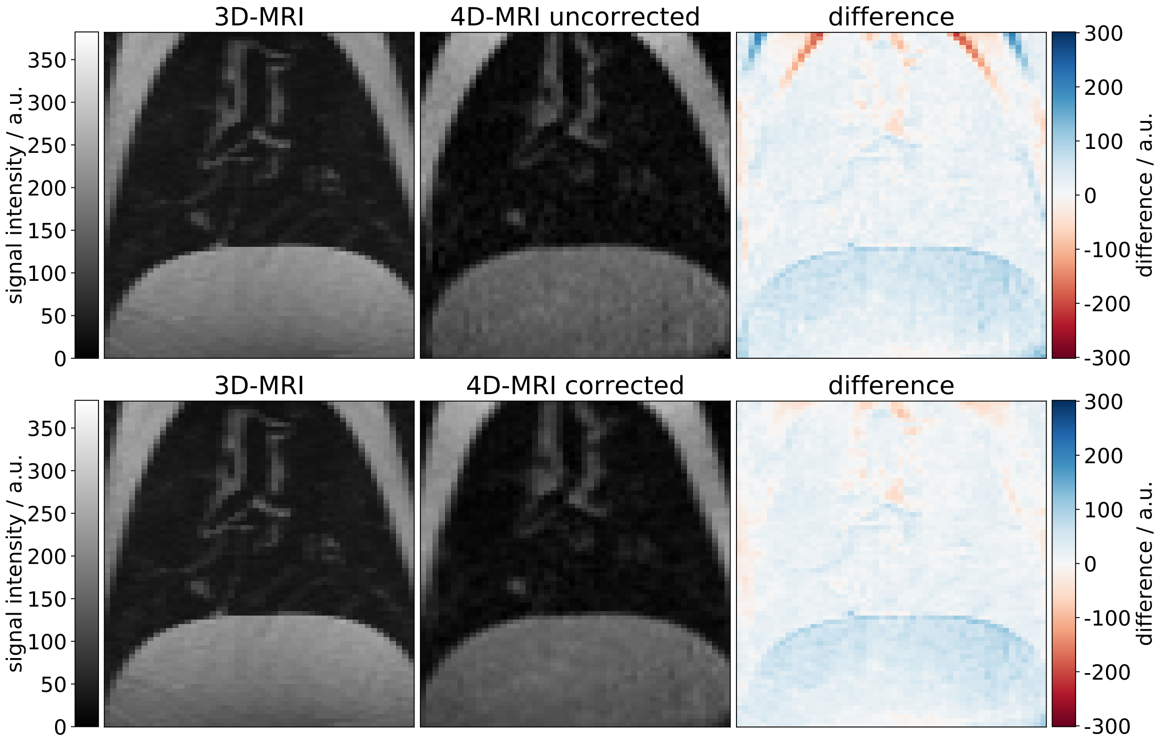

FIGURE 5.5: **Through-plane distortion correction.** The left column shows coronal views of an exemplary 3D-MRI, acquired in inhale breath-hold. The center column depicts the corresponding views of the inhale phase of the ground truth 4D-MRI before (uncorrected; top row) and after (corrected; bottom row) application of the distortion correction DVF. The difference plots in the right column illustrate that the geometric distortions in RL direction could be effectively reduced by the correction method. This figure was published as a supplementary figure to [178].

5.3.3 Estimated 4D-MRI

The orthogonal cine MRI series could successfully be acquired at 7.3 Hz on the low-field MR-Linac. No averaging was used for the orthogonal cine MRI while two images are averaged in the standard clinical 2D cine MRI sequence. In comparison, this led to a decreased SNR of the orthogonal cine MRI. The orthogonal images contained a line of reduced signal intensity at the slice intersection (cf. Figure 5.3) and banding artifacts (section 3.1.5) towards the edges of the images. The reference 2D slices extracted from the ground truth 4D-MRI were corrected for through-plane geometric distortions, while the orthogonal slices were not. This led to some differences between the reference and orthogonal images, which were most clearly visible at the phantom walls (cf. sagittal view in Figure 5.3).

In total, 32 estimated 4D-MRI at 3.65 Hz were created – one for each of the four nodules tracked with the orthogonal cine MRI for each of the eight datasets. The 2D DIRs performed as part of the propagation method were robust against the higher noise level, the intersection line, the banding artifacts, and the geometric distortions in the orthogonal images. No differences in the robustness of the DIRs were observed for the varying sizes of the injected nodules (1.3–13 cc). The same surrogate signal-based breathing phase binning as applied for the ground truth images was used for the sagittal images of the orthogonal cine MRI series. This is illustrated in Figure 5.6, where the high reproducibility of the diaphragm motion can also be seen.

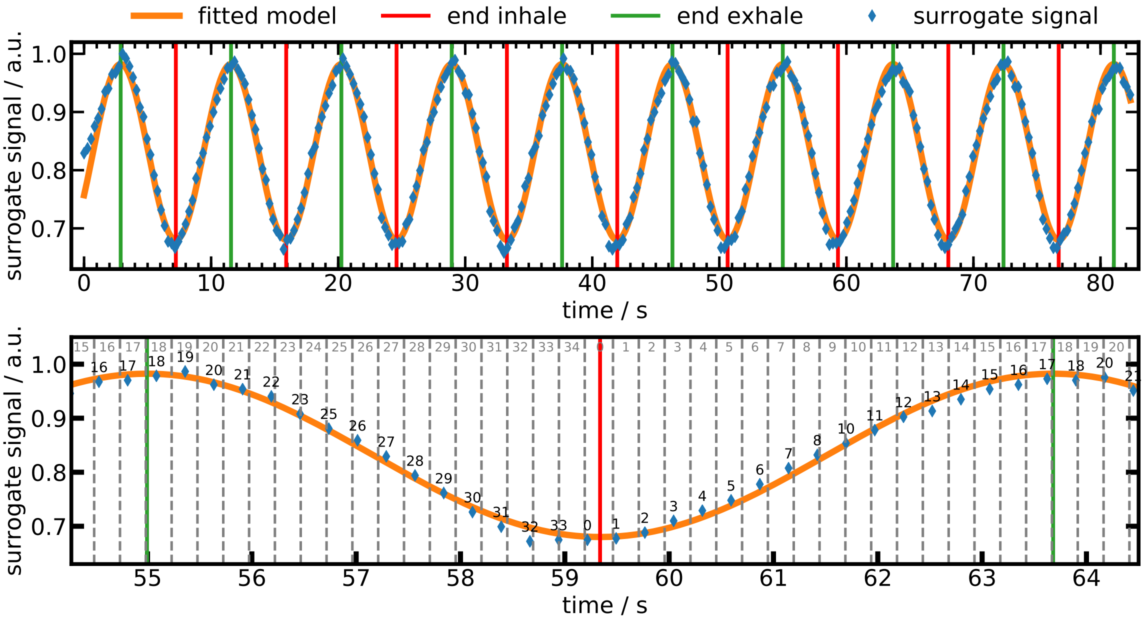

FIGURE 5.6: **Breathing phase determination for estimated 4D-MRI.** The surrogate signal derived with image processing from the sagittal slices of the orthogonal cine MRI is plotted as a function of the whole acquisition time (top row) and zoomed in for one breathing cycle (bottom row) for an exemplary imaging series. The surrogate signal was fitted with a sinusoidal function with four free parameters (frequency, amplitude, phase, and offset). The inhale and exhale phase positions were derived from the fitted model function. Larger deviations between the model and surrogate data points were observed in the first few frames, where the bSSFP sequence was in its transient state. The breathing phase assignment is illustrated in the lower row, where the bin boundaries are plotted as vertical dashed lines. The small numbers indicate the assigned breathing phases next to the surrogate signal data points.

5.3.4 Visual comparison of estimated and ground truth 4D-MRI

Exemplary sagittal and coronal slices of the ground truth and estimated 4D-MRI, and the differences of their image intensities are depicted in Figure 5.7. In this example, the mid-exhale phase was chosen as the reference phase, and images in the inhale phase are shown, where the largest deviations were observed. The depicted slices are located several centimeters away from the positions of the acquired orthogonal slices used as input for the propagation method. In the coronal view, some deviations can be observed at the diaphragm, which are increasing with the distance to the sagittal slice position, indicated by the red arrow. In the sagittal view, deviations at the anterior diaphragm boundary are visible, although this structure was located in the vicinity of the coronal plane of the orthogonal slice set. The estimated and ground truth DVFs were visually compared in this region. The comparison showed that the diaphragm was strongly moving in AP direction in this area due to the design of the phantom. This is also visible in Figure 5.3, where the DVF components in the sagittal view are relatively large in AP direction at this position. The strong AP motion of the diaphragm led to pronounced through-plane motion at the coronal slice of the orthogonal image set in Figure 5.7. In the DIR in coronal orientation, this motion was not accurately modeled due to its restriction to 2D. Therefore, the deviations observed in Figure 5.7 were mainly attributed to out-of-plane motion that was not correctly modeled by the DIR and the extrapolation of the vector fields in the propagation method. Nevertheless, overall, a high agreement between the ground truth and estimated datasets was observed.

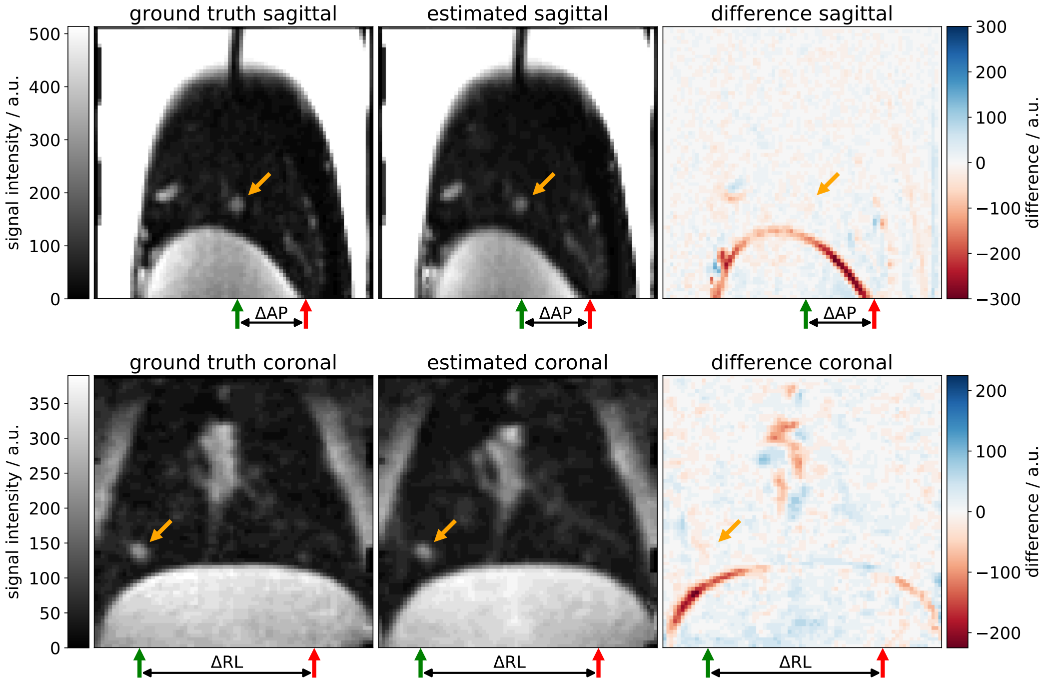

FIGURE 5.7: **Visual comparison of ground truth and estimated 4D-MRI.** Exemplary sagittal (top row) and coronal (bottom row) views of a ground truth (left column) and estimated 4D-MRI (center column) image and their differences (right column) are depicted. The mid-exhale phase was used as the reference phase and the inhale phase is shown. The depicted images were extracted from dataset 3, where the orthogonal slices (not shown) were located at the positions indicated by the red arrows. The green arrows indicate the positions of the respective depicted sagittal and coronal views. The position of the nodule indicated by the orange arrow could be accurately estimated. The normal distances of this nodule to the coronal and sagittal slices of the orthogonal slice set were $\Delta AP = 73.5\,\mathrm{mm}$ and $\Delta RL = 171.5\,\mathrm{mm}$, respectively. Figure reprinted from [178].

5.3.5 Deformation vector field analysis

The ground truth and estimated DVFs were compared at the subsampled grid point positions located within the segmented lung structures. On average, 3400 grid points were included inside the lungs.

Reference phase dependency

The dependency of the DVF error on the breathing phase of the reference image was investigated for a subsample of the estimated motion states. For each estimated 4D-MRI, the corresponding DVFs of the first 70 frames were compared to the ground truth DVFs in four analyses. In each analysis, a different breathing phase of the ground truth 4D-MRI was used as the 3D reference image. The median (95th percentile) DVF errors in 3D were 3.1 mm (9.7 mm) for the inhale phase, 2.3 mm (5.7 mm) for the mid-exhale phase, 2.4 mm (7.9 mm) for the exhale phase, and 2.3 mm (5.6 mm) for the mid-inhale phase as breathing phase of the 3D reference image. Based on these results, the mid-exhale phase of the ground truth 4D-MRI was defined as the 3D reference image in all analyses described below.

Further DVF error dependencies

The dependencies of the DVF error on the estimated breathing phase, the motion amplitude, and the normal distances of the positions of the estimated grid points to the locations of the orthogonal cine MRI slices were investigated. The estimated DVFs at the grid points within the segmented lungs at all 285 time points of each of the 32 estimated 4D-MRI were compared to the ground truth DVFs in an aggregated analysis. The results are shown in Figure 5.8.

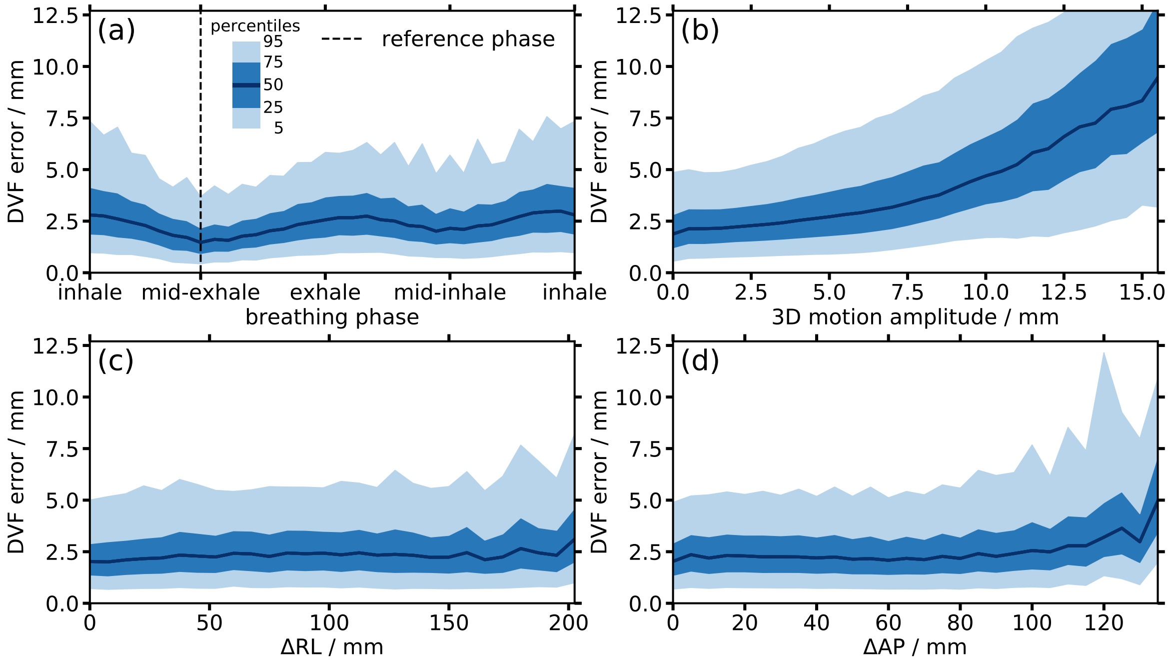

FIGURE 5.8: **DVF error dependencies.** The results of the aggregated DVF error dependency analysis are depicted. The DVF error is plotted as a function of (a) the estimated breathing phase, (b) the 3D motion amplitude relative to the reference phase (mid-exhale), (c) the normal distance of the grid points to the sagittal slice of the orthogonal image set (ΔRL), and (d) the normal distance of the grid points to the coronal slice of the orthogonal image set (ΔAP). The 5th, 25th, 50th, 75th and 95th percentile values are shown. Figure reprinted from [178].

TABLE 5.2: **DVF error dependency on estimated breathing phases.** The median (95th percentile) values of the DVF error are given for different estimated breathing phases for each dataset individually and for all datasets accumulated. Table adapted from [178].

Dataset	Ref. phase (mm)	Inhale (mm)	Exhale (mm)	All phases (mm)
1	2.2 (7.0)	2.8 (8.4)	2.8 (6.8)	2.6 (8.2)
2	1.7 (3.7)	2.5 (7.2)	1.8 (4.1)	2.1 (5.1)
3	1.3 (3.4)	3.0 (6.3)	2.4 (5.3)	2.2 (5.2)
4	1.4 (2.7)	2.8 (6.5)	2.6 (5.0)	2.1 (4.9)
5	1.2 (3.3)	2.6 (5.2)	2.4 (4.7)	2.0 (4.6)
6	1.8 (4.2)	3.5 (9.3)	4.1 (7.4)	3.0 (6.7)
7	1.5 (4.2)	2.6 (6.6)	2.6 (4.8)	2.2 (5.0)
8	1.5 (3.8)	3.2 (7.6)	2.8 (5.2)	2.4 (5.4)
All	1.6 (4.5)	2.8 (7.3)	2.6 (5.9)	2.3 (5.7)

The median and 95th percentile DVF errors were calculated when the reference (mid-exhale), inhale, or exhale phase images were estimated. These values are summarized in Table 5.2 for each dataset individually and for all datasets accumulated. The smallest overall median (95th percentile) value of 1.6 mm (4.5 mm) was measured when the reference phase was estimated. The values for the inhale and exhale phases were 2.8 mm (7.3 mm) and 2.6 mm (5.9 mm), respectively. These results confirm the intuitive assumption that the more similar the estimated images are to the reference image (i.e., more similar breathing phase), the smaller is the DVF error. This relationship can be seen in Figure 5.8a, where the median DVF error depends on the estimated breathing phase. For all phases accumulated, values of 2.3 mm (5.7 mm) were calculated, corresponding to 0.7 (1.6) times the cine MRI in-plane imaging resolution of 3.5 mm.

The DVF dependency on the motion amplitude at the position of the estimated grid points is depicted in Figure 5.8b. The motion amplitude was defined as the ground truth DVF vector length in 3D, measured relative to the reference phase. The mid-exhale phase was used as the reference image for the analyses. Therefore, the total motion amplitudes at the grid points, measured from the inhale to exhale positions, were approximately twice as large. For small to medium motion amplitudes (< 10 mm), a shallow increase of the DVF error as a function of the 3D motion amplitude was observed. A steeper increase was found for large motion amplitudes (> 10 mm). The median DVF error was smaller than one voxel size (3.5 mm) for motion amplitudes < 7.5 mm and below two voxel sizes (7.0 mm) for motion amplitudes up to 12.5 mm.

The DVFs output by the 2D DIRs in sagittal and coronal orientation were extrapolated to 3D in the propagation method to create the estimated motion states. The DVF error is therefore expected to depend on the normal distance of the point at which the motion is estimated to either of the orthogonal slices (ΔRL and ΔAP). The dependencies of the DVF error on these parameters are plotted in Figures 5.8c&d. A shallow increase of the DVF error as a function of ΔRL and ΔAP was observed, with median values below 5 mm even for large distances ($\Delta\text{RL} = 20$ cm and $\Delta\text{AP} = 13$ cm). This indicates that the motion could be accurately estimated within the whole lung.

5.3.6 Nodule centroid position error

For each dataset, 16 nodule classifications were performed (four nodules in each of the four estimated 4D-MRI per dataset). For each dataset, four nodules were assigned to category 1,

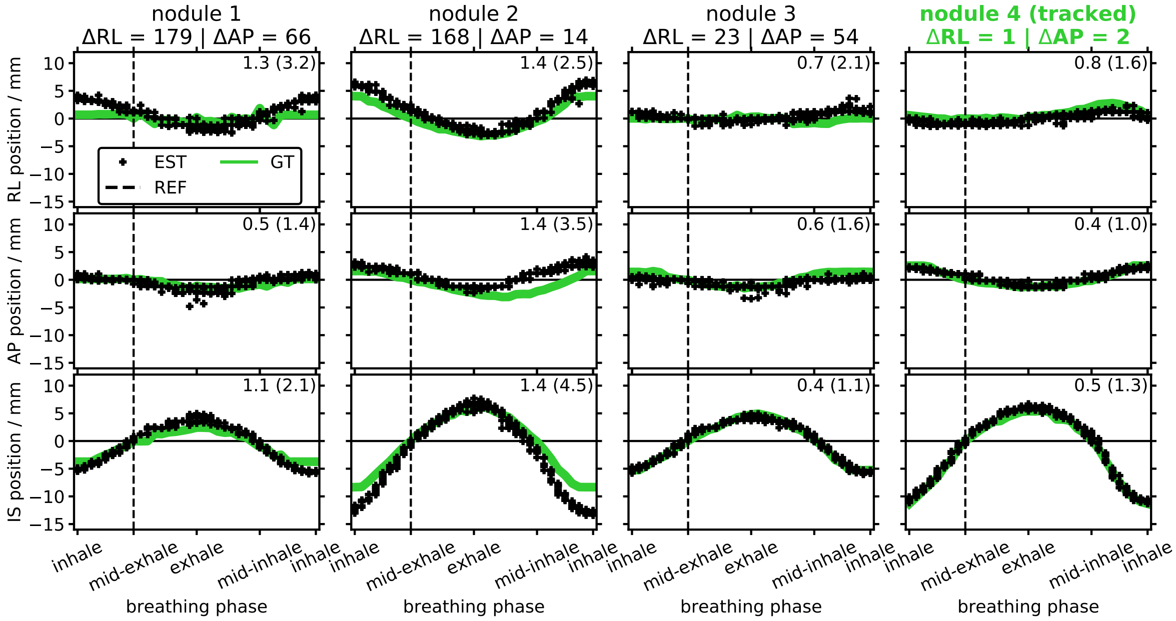

FIGURE 5.9: **Estimated and ground truth nodule positions.** The figure shows the ground truth (GT; green line) and estimated (EST; black markers) centroid positions for the four nodules (columns), split up in the three different motion directions (rows) for an exemplary dataset. The centroid positions are plotted as a function of the breathing phase relative to the ground truth centroid position in the reference phase (REF; mid-exhale). The orthogonal slices were positioned at nodule 4. The distances of the nodule centroids in the reference phase to the orthogonal slices (ΔRL and ΔAP) are given in the figure titles in millimeters. Based on these values, nodule 4 was assigned to category 1, nodule 2 to category 2, and nodules 1 and 3 to category 3. The median (95th percentile) estimation errors in the respective directions are given in millimeters in the upper right corner of each subplot. Figure reprinted from [178].

TABLE 5.3: **Nodule position analysis results.** The range of motion amplitudes of the four nodules in each dataset were calculated relative to the reference phase (mid-exhale). The motion amplitudes are given in IS, AP, and RL direction, as well as in 3D (A_{IS}, A_{AP}, A_{RL}, A_{3D}). The median (95th percentile) estimation errors in 3D were calculated for the three nodule categories. Table reprinted from [178].

	Motion amplitudes				Estimation errors		
Dataset	A_{IS} (mm)	A_{AP} (mm)	A_{RL} (mm)	A_{3D} (mm)	Category 1 (mm)	Category 2 (mm)	Category 3 (mm)
1	2–5	1–1	0–2	2–5	1.5 (2.6)	2.4 (8.4)	1.9 (11.6)
2	3–4	1–2	0–2	3–4	1.1 (3.1)	2.0 (8.9)	2.6 (10.9)
3	4–10	1–3	1–2	4–10	1.6 (3.6)	1.8 (4.1)	1.7 (3.7)
4	4–11	2–3	1–4	4–12	1.5 (2.6)	2.5 (5.5)	2.6 (6.1)
5	4–9	1–3	1–3	4–10	1.4 (3.5)	1.6 (3.6)	1.6 (3.4)
6	4–9	3–6	2–4	5–10	2.0 (6.4)	2.6 (7.1)	2.7 (7.2)
7	2–5	1–3	0–2	3–6	1.5 (5.4)	1.8 (5.1)	1.8 (4.3)
8	4–7	1–5	0–2	4–8	1.7 (7.0)	2.1 (4.8)	2.0 (4.4)
All	2–11	1–6	0–4	2–12	1.5 (3.8)	2.0 (6.2)	2.1 (7.1)

eight nodules to category 2, and four nodules to category 3.

The estimated and ground truth nodule centroid positions are depicted in Figure 5.9 for an exemplary estimated 4D-MRI, where the orthogonal slices intersected nodule 4. All nodule positions in this example could be accurately and precisely estimated, with an exception for nodule 2, where deviations of up to 5 mm in inferior direction were observed.

The motion amplitudes, measured within the ground truth 4D-MRI, and the estimation errors for each nodule category were calculated for each dataset and are summarized in Table 5.3. The main nodule motion was in IS direction with amplitudes up to 11 mm, followed by the AP (up to 6 mm) and RL direction (up to 4 mm). As described above, these amplitudes were measured relative to the reference phase, and their full ranges of motion were approximately twice as large. The median (95$^{\text{th}}$ percentile) estimation error for all datasets combined for nodules of category 1 was 1.5 mm (3.8 mm), for nodules of category 2 was 2.0 mm (6.2 mm) and for nodules of category 3 was 2.1 mm (7.1 mm). Different motion patterns in terms of breathing frequency, amplitude, and extent of through-plane motion were tested for the different datasets (cf. Table 5.1). No clear correlations between the estimation error and the breathing frequency (cf. datasets 1 and 2 in Table 5.3) or motion amplitudes in RL direction (cf. datasets 3, 4, and 5) were identified. The nodule centroid estimation error increased with increasing 3D nodule motion amplitudes (cf. datasets 6, 7, and 8 with relative amplitudes of 120%, 80%, and 100%, respectively). This is in agreement with the results of the DVF error dependency analysis, where an increasing DVF error was measured for increasing 3D motion amplitudes of the estimated grid points (cf. section 5.3.5 and Figure 5.8b).

5.3.7 Partial volume effect uncertainty

The partial volume effect uncertainty was calculated from the resampling analysis of spheres with varying volumes (0.3–13.6 cc). The partial volume error in the nodule centroid position comparison was calculated based on these values. The results are plotted in Figure 5.10. For all nodule sizes investigated in the study (1.3–12.6 cc; red vertical lines in Figure 5.10), the partial volume error (σ_e) was smaller than 0.55 mm, with smaller errors for larger nodule sizes.

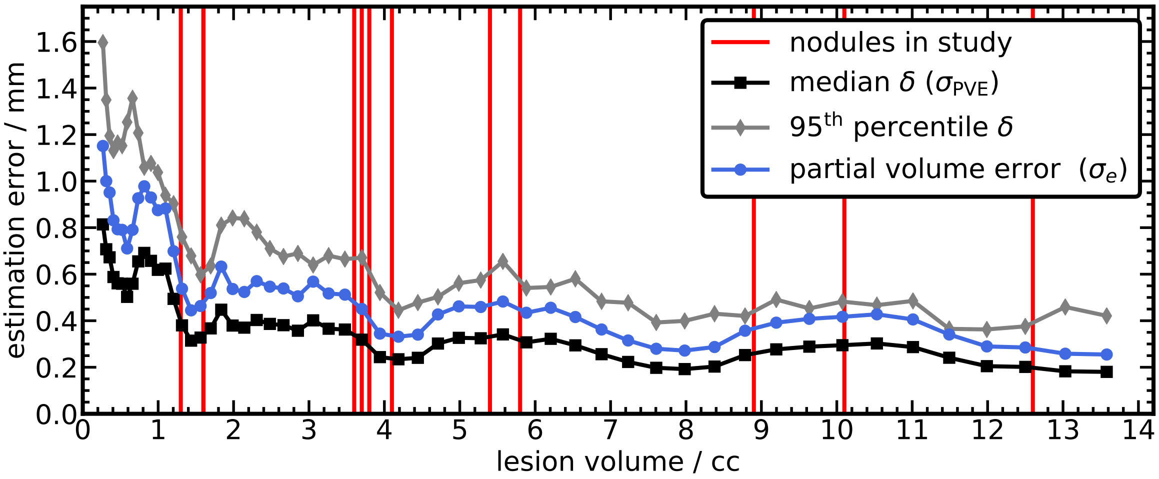

FIGURE 5.10: **Results of partial volume effect analysis.** The median and 95$^{\text{th}}$ percentile centroid determination error δ is plotted as a function of the volume of the simulated spheres. The partial volume error in the nodule centroid position comparison in this study (σ_e) was calculated based on the median δ (σ_{PVE}). The red vertical lines indicate the nodule sizes used in the analyses in this study. The lines connecting the data points serve to guide the eye.

5.4 Discussion

The accuracy of the estimated 4D-MRI created with the propagation method by Paganelli et al. [46] was investigated. The use of a dedicated porcine lung phantom with a highly reproducible and stable breathing motion enabled experimental validation measurements under realistic, patient-like conditions. The feasibility of orthogonal cine MRI and the applicability of the propagation method for a low-field MR-Linac to create continuous estimated 4D-MRI at 3.65 Hz was demonstrated. Overall, a median sub-voxel size DVF estimation error of 2.3 mm, averaged over the whole lung, was achieved. The median nodule centroid position estimation errors for the three categories were between 1.5 and 2.1 mm. The propagation method was robust against different lesion sizes, breathing frequencies, motion amplitudes, and the use of different porcine lungs.

The aim of this study was to assess the overall DVF and nodule centroid position estimation error in an experiment that closely resembles the clinical setting. This error includes uncertainties stemming from different steps of the measurement and data processing workflow, such as the DIR, geometric distortions, out-of-plane motion, partial volume effects, and the DVF extrapolation in the propagation method. With the chosen study design, it is not possible to fully decouple the effects of these different contributions. However, the DIR uncertainty can be estimated by analyzing the centroid position error of category 1 nodules (i.e., nodules intersected by both orthogonal slices) where extrapolation effects play a minor role. This median error was 1.5 mm (cf. Table 5.3), suggesting that the DIR uncertainties were an important, and potentially the dominating, source of uncertainty in this study.

Out-of-plane motion, in particular the pronounced AP motion of the anterior diaphragm that moved orthogonal to the coronal slices, led to increased DVF errors in this study. This was attributed to the inability of the DIR to appropriately model the real motion due to its restriction to 2D. A potential solution could be to register the whole 3D reference image to the fixed 2D orthogonal slices in 3D. While this might improve the accuracy of the motion estimation, the additional degrees of freedom would increase the variance and reduce the precision of the motion estimation.

No through-plane distortion corrections were applied to the orthogonal cine MRI frames since this type of correction is not available for 2D slices at the clinical MRIdian MR-Linac. Deviations between the reference and orthogonal slices were observed (Figure 5.3) since the ground truth images were corrected for this type of distortion. These deviations introduce geometrical errors that can affect the DIR and limit the achievable accuracy of the propagation method. In this study, the treatment couch was not shifted to position the nodule of interest as close as possible to the imaging isocenter. Since through-plane geometric distortions increase with increasing distance to the imaging isocenter [91], this could have reduced the geometric distortions close to the nodule of interest. While for a patient treatment it is generally feasible to position the target at isocenter in IS direction through craniocaudal couch shifts, positioning the target at isocenter in RL and AP direction is not always possible due to the limited size of the bore of the MR-Linac and the restricted couch shifts in these directions [45]. Therefore, using imaging planes offset to the isocenter cannot always be avoided. If the propagation method was used in a clinical scenario, uncertainties due to through-plane geometric distortions would have to be considered.

The bSSFP cine MRI sequence used for the orthogonal slice acquisition had an in-plane resolution of $3.5 \times 3.5\,\text{mm}^2$ with a slice thickness of 5 mm due to the low magnetic field strength of 0.35 T and the limited hardware capabilities of the clinical MRIdian [13, 45, 82]. The coarse spatial resolution leads to partial volume effect errors in the nodule centroid position determination. These errors were estimated to lie between 0.3 and 0.6 mm for the investigated nodule sizes. Future hardware and software upgrades are expected to enable cine imaging with a higher spatial and temporal resolution [31, 162]. This could, in turn, decrease the estimation error of the estimated 4D-MRI created with the propagation method.

The impact of the breathing phase of the reference image on the accuracy of the propagation method was investigated. The lowest median estimation errors were obtained when the mid-exhale or mid-inhale phases were used as the reference image. The subsequent DVF analysis demonstrated that the estimation error is lowest for breathing phases that are similar to the reference image phase. Consequently, if the propagation method was used in a gated MR-Linac treatment, the reference image should be acquired in the breathing phase in which the beam is switched on to maximize the accuracy of the 4D-MRI estimated during beam delivery. The reference image selection and the positioning of the orthogonal slices are the most important steps of the propagation method. The choice of these parameters directly impacts the achievable estimation accuracy. The tumor target has to be clearly visible in the orthogonal slices and the respective slices in the reference image to minimize the DIR uncertainties.

The propagation method was originally proposed by Paganelli et al. in 2018 [46] and compared to other motion estimation methods in an *in silico* study in 2019 [47]. Some adaptations to the originally proposed method were made for this study. Instead of extracting the orthogonal slices from the ground truth dataset, these were acquired in additional cine MRI series to obtain clinically realistic images. In this study, the reference image was extracted from the respiratory-correlated ground truth 4D-MRI instead of using the 3D-MRI acquired in breath-hold. The intention behind this approach was to enable a comparison of different breathing phases as reference images. Different DIR algorithms were used in the original proof-of-concept study (Demons) [46], the *in silico* comparison study (optical flow) [47], and this work (B-spline). Additionally, the weighting factors for the IS components of the DVFs in sagittal and coronal orientation were changed. In the original propagation method, constant weights of 0.5 were used, independent of the location within the FOV. In this study, the weighting factors depended on the normal distances to the orthogonal slices. The motivation for this change was to avoid the potential systematic biasing of IS components in the vicinity of the acquired orthogonal slices (Figure 5.4).

In contrast to the motion models described in section 3.3.1, neither does the propagation method rely on a pre-treatment 4D-MRI or model training, nor is it driven by surrogate signals. Instead, the estimated 4D-MRI are solely created based on a 3D-MRI acquired in breath-hold and the interleaved orthogonal cine MRI. Such a 3D-MRI is already acquired for patient positioning and adaptive planning in MRgRT today (section 3.1.6). Furthermore, as demonstrated in this study, the commercially available MR-Linacs are capable of orthogonal cine MRI [228]. Therefore, the MR-Linacs in clinical operation already have the imaging capabilities needed for the presented method. This could allow a smooth clinical integration for improved 3D target localization for gating in the future.

B-spline DIRs (section 2.4.3) [100, 102, 103] can accurately model the motion within the lung but are computationally demanding and slow. In the current implementation, 1.7 s were needed for the estimation of each time step on a workstation with 72 central processing units (CPUs; Intel Xeon Gold 6254 at 3.10 GHz), of which 1.4 s were attributed to the DIR. To allow for a real-time application of the propagation method, a different DIR method could be chosen, and the DIR could be performed on a GPU instead [229]. A further DIR speed-up could be achieved by using a warm start optimization where the DVF of the previous time point is taken as the starting point for the DIR at the next time step.

Several aspects differ when imaging the *ex vivo* porcine lungs mounted in the phantom from imaging the thorax of a patient. These differences include the beating heart, the moving chest, and the perfused blood vessels in an *in vivo* lung. This will lead to different image contrasts, SNRs, and motion patterns compared to this study. In turn, this might affect the performance of the propagation method.

A proof-of-concept application of the propagation method with patient data was performed in the original publication by Paganelli et al. [46] for two patients scanned at a 1.5 T MRI scanner. A feasibility study of using the propagation method for a large patient cohort with different tumor locations and target motion patterns scanned before and during treatment with an MR-Linac would be desirable to assess the added value of 4D image guidance during treatment. If the same imaging protocols as used in the study in this chapter were chosen, the estimated 4D-MRI would have to be compared to a retrospectively sorted respiratory-correlated 4D-MRI. This would introduce uncertainties in the accuracy assessment since a patient's breathing pattern is generally irregular and the respiratory-correlated 4D-MRI could therefore not be regarded as a ground truth dataset.

5.5 Conclusions

This chapter presented the results of the first application of the propagation method to imaging data acquired at an MR-Linac. The results of the experimental validation with the porcine lung phantom demonstrated that the propagation method based on orthogonal cine MRI generates accurate estimated 4D-MRI at high temporal resolution. Compared to today's standard target motion monitoring based on single planar sagittal cine MRI at the MRIdian, the propagation method has the potential to reduce the target localization error, particularly when significant out-of-plane motion (i.e., RL motion) is present. In addition, the time-resolved volumetric images could allow the motion monitoring of OARs located at arbitrary positions within the whole thorax during gated treatments.

In today's ART at the MRIdian, the treatment plan is only adapted based on anatomical changes observed on the static 3D-MRI acquired before each treatment fraction (section 3.1.6). Kontaxis et al. [49] have proposed a methodology that envisions inter- and intrafractional plan adaptations based on the dose that was actually delivered to the target and OARs in or even during each fraction to fully exploit the potential of MRgRT. To reconstruct the delivered dose, the system-related linac log-files and time-resolved synthetic CTs that accurately represent the patient's anatomy during the beam delivery are needed (section 3.3.2) [20, 30, 45, 50, 145]. The next chapter presents a follow-up study to the work in this chapter, where such time-resolved synthetic CTs were created based on estimated 4D-MRI output by the propagation method.

Chapter 6

Time-resolved estimated synthetic CTs based on orthogonal cine MRI

In this chapter, a follow-up study to the validation experiments of the propagation method described in the previous chapter is presented. A method to create continuous time-resolved estimated synthetic CTs (tresCTs) based on a static 3D-CT and orthogonal cine MRI is proposed and tested with the porcine lung phantom (section 5.2.1). The study was conducted by the author in the scope of this dissertation and a manuscript on the key results is currently under preparation.

Section 6.1 motivates the use of time-resolved synthetic CTs for MRgRT, including a literature review. The methodology of the experiments, tresCT generation, geometric and dosimetric analyses are described in section 6.2. The results of these analyses are presented in section 6.3 and discussed in section 6.4. Finally, the conclusions are summarized in section 6.5.

6.1 Motivation for time-resolved synthetic CTs

In MR-guided ART (sections 2.6.5 and 3.1.6) at the MR-Linac (section 3.1), the treatment plan is adapted once prior to treatment based on the daily patient anatomy to account for interfractional changes (section 2.6.1). In addition, planar sagittal cine MR images are acquired to monitor the target motion during irradiation at the ViewRay MRIdian MR-Linac (section 3.1.4). Today, these 2D images are solely used to gate the beam delivery (sections 2.6.6 and 3.1.7). In the future, real-time volumetric cine MRI could serve as input data for the creation of time-resolved synthetic CTs (section 3.3.2) for improved MRgRT (section 3.1.1) [187]. These synthetic 4D-CTs, in combination with linac log-files, would enable the reconstruction of the dose that was actually delivered to the patient, explicitly accounting for the intrafractional changes and potential interplay effects with the treatment delivery [50]. After each fraction, the treatment plan could be updated for the remaining fractions while considering the dose that was already delivered to the target and OARs. Ultimately, with fast synthetic 4D-CT generation methods, dose calculation and optimization algorithms, the partially delivered dose could be reconstructed and accumulated in real-time during the treatment fraction itself, and the treatment plan could be continuously adapted based on this information [13, 49]. Further applications of such synthetic 4D-CTs include gating window optimization [230], 4D and robust treatment plan optimization [231], and the investigation of interplay effects [232]. Furthermore, the dose reconstructed over the whole treatment course could serve as input for clinical dose-response modeling in the post-treatment phase [30].

Several research groups have developed synthetic 4D-CT methods for the thoracic or abdominal region based on 3D-CT and 4D-MRI data. Boye et al. [233] created synthetic 4D-CTs for proton therapy of liver tumors by mapping the motion with the DVFs obtained from DIR (section 2.4.3) of a retrospectively sorted 4D-MRI (section 2.4.3) to a static 3D-CT image.

They tested their method with patient and volunteer data. Marx et al. [234] took a similar approach but used the real-time 4D-MRI (section 3.2.2) sequence TWIST (section 4.2.1) and tested their method with lung cancer patient data instead. This work was extended by Yang et al. [235], who mapped the motion using a hybrid DIR and biomechanical lung model. Instead of using a respiratory-correlated or real-time 4D-MRI sequence (section 3.2), Müller et al. [181] developed a motion model (section 3.3.1), based on orthogonal cine MRI for the use in MRgRT. The model was built and driven by different surrogate signals, such as the diaphragm and chest position, extracted from the orthogonal cine MRI slices. In this publication, digital phantom data simulating the motion of the lung was used for testing. Freedman et al. [236] also created synthetic 4D-CTs for MRgRT based on a respiratory-correlated 4D-MRI and Dixon MRI. Instead of mapping the motion with a DIR, they applied a three-step method to derive the synthetic 4D-CTs with bulk density assignment, atlas-based segmentation, and lung density correction algorithms. Similar to Boye et al., Meschini et al. [227] mapped the motion extracted from a respiratory-correlated 4D-MRI with DIR to a static 3D-CT to obtain synthetic 4D-CTs (called "virtual 4D-CTs" in their publication) for the treatment of pancreatic and liver tumors with carbon ion radiotherapy.

Neither of these methods can be directly applied during beam delivery at the ViewRay MRIdian MR-Linac. For an accurate dose reconstruction, intrafractional changes must be taken into account by extracting the motion information from continuous time-resolved 4D-MRI instead of respiratory-correlated 4D-MRI (Boye et al. [233], Freedman et al. [236], Meschini et al. [227]). This can be achieved by using real-time 4D-MRI sequences instead (Marx et al. [234], Yang et al. [235]). However, these imaging sequences are not available at the low-field MR-Linac by ViewRay (section 5.1). Alternatively, motion models could be used (Müller et al. [181]) to output continuous time-resolved synthetic CTs at the MR-Linac. These motion models, however, typically rely on additional imaging before treatment for training (section 3.3.1). This would prolong the time that the patient has to lie in the treatment position and decrease the number of patients treated at the MR-Linac per day.

The geometric analyses in Chapter 5 demonstrated that the propagation method (section 5.2.7) could generate accurate continuous estimated 4D-MRI based on orthogonal cine MRI acquired at the MRIdian MR-Linac [178]. This method does not require model training in the pre-treatment phase and can potentially be implemented in the clinic with only a few changes compared to today's workflow (section 5.4). The purpose of this study was to develop and test a method to create continuous tresCTs for use during beam delivery at the MRIdian MR-Linac. These images were created by transforming a static synthetic 3D-CT scan with the DVF from the estimated 4D-MRI output by the propagation method. The geometric and dosimetric accuracy of these synthetic CTs was tested with the porcine lung phantom used for the experimental validation measurements in Chapter 5.

6.2 Material and Methods

6.2.1 Experimental setup

The same porcine lung phantom as described in section 5.2.1 was used for the experiments in this study. Compared to the validation measurements described in Chapter 5, additional 3D-CT and 4D-CT data had to be acquired, thus requiring new experiments at a CT scanner and MR-Linac in close proximity to each other. The measurements described below were repeated three times with different motion patterns for two lungs to create three datasets in total (one dataset for lung 1 and two datasets for lung 2). The *ex vivo* porcine lungs were prepared and mounted in the phantom in the same way as described in Chapter 5. Four (lung 1; dataset 1) or three (lung 2; datasets 2 and 3) artificial gelatin nodules with a concentration of 0.3 g/ml with sizes of 10–17 cc were injected into the lung tissue at various

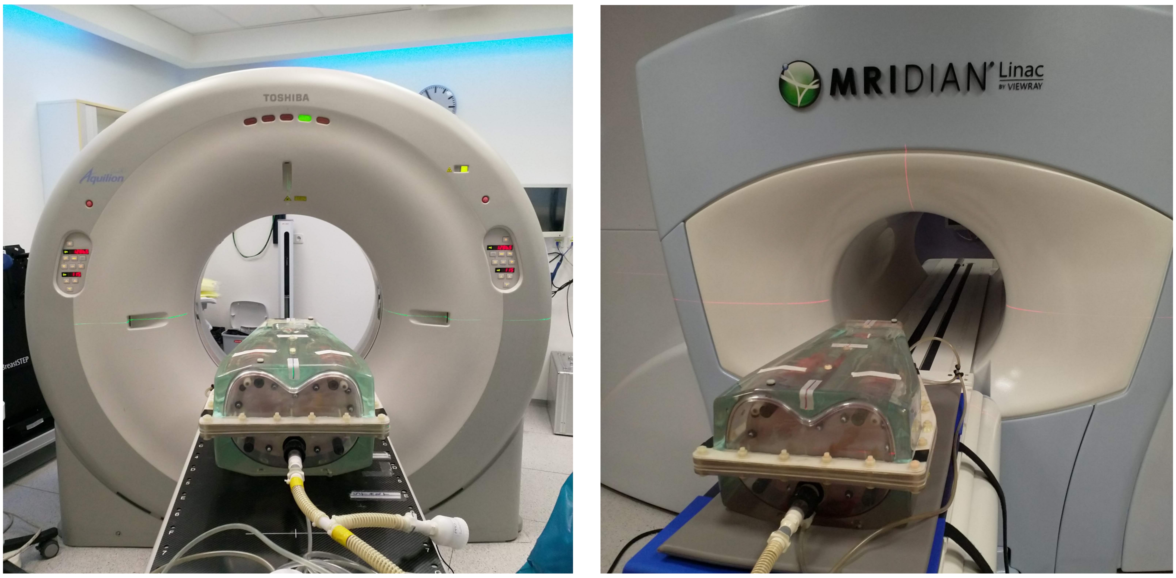

FIGURE 6.1: **Phantom setup at CT scanner and MR-Linac.** Photographs of the porcine lung phantom setup at the CT scanner (left) and the MR-Linac (right) are depicted. The photograph at the MR-Linac was taken before positioning the upper torso receiver coil (not shown) and moving the phantom to the imaging isocenter.

locations following the procedure described in section 5.2.1. These nodules served as surrogate target lesions. Periodic motion patterns with a breathing frequency of 12 cycles/min, varying motion amplitudes, and different baseline pressures were set at the control system for the three datasets.

The porcine lung phantom was first scanned at a CT scanner, then transported to, and scanned at an MR-Linac (datasets 1 and 2). For dataset 3, the phantom was first scanned at the MR-Linac before CT imaging to minimize transport. The breathing motion was manually paused at the inhale position before transport between the two scanners, and the lung position was marked on the upper phantom shell. The experimental setup was connected to an uninterruptible power supply during transport to constantly evacuate the phantom cavity with the vacuum pumps to ensure a stable lung inflation state. The lung position was checked with the marker positions after transport to identify potential deviations between the lung inflation states at the two scanners.

6.2.2 CT data acquisition

The phantom was positioned on the patient couch of a Toshiba Aquilion LB (Canon Medical Systems, Japan) CT scanner (Figure 6.1), used in clinical routine for the acquisition of planning CT images (section 2.5.1) for radiotherapy treatment planning. The phantom motion was paused at the mid-exhale position, and a 3D-CT was acquired (in-plane resolution: $1.074 \times 1.074\,\text{mm}^2$; slice thickness: 3 mm; pixels: 512×512; X-ray tube voltage: 120 kV). Next, the phantom breathing motion was initiated, and projection data for 4D-CT reconstruction (section 2.6.2) were acquired during couch translation with constant speed in craniocaudal direction. Simultaneous to the image acquisition, a surrogate signal correlated to the breathing phase was recorded with a load cell. The load cell is a component of an abdominal pressure belt respiratory gating system (Anzai Medical Co., Ltd., Tokyo, Japan) and was connected to the pressure hose ventilating the diaphragm with a dedicated adapter. The projections were retrospectively assigned to ten breathing phase bins using the vendor's phase-based sorting algorithm to reconstruct a respiratory-correlated 4D-CT

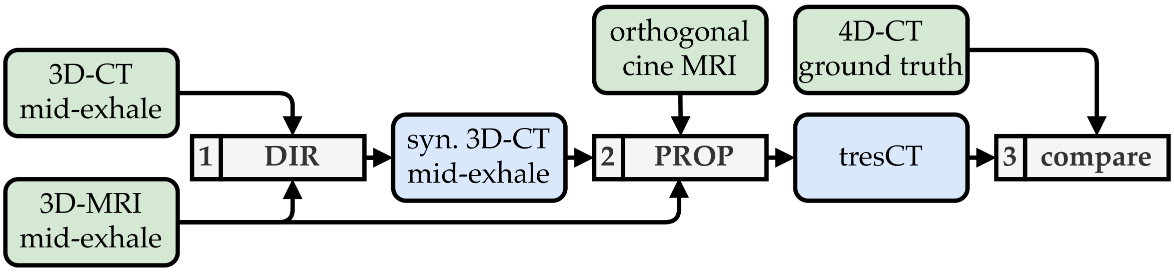

FIGURE 6.2: **Workflow of tresCT creation and comparison.** In step 1, the 3D-CT and 3D-MRI in the mid-exhale position are rigidly and deformably registered to create a synthetic 3D-CT in the mid-exhale phase. In step 2, the 3D-MRI and orthogonal cine MRI serve as input data to the propagation method, and the resulting estimated DVFs are applied to the synthetic CT to create a tresCT. In step 3, this tresCT is compared to the measured ground truth 4D-CT in geometric and dosimetric analyses. Measured data is shown in green, reconstructed data in blue fields.

dataset (in-plane resolution: $1.074 \times 1.074\,\mathrm{mm}^2$; slice thickness: 3 mm; pixels: 512×512; X-ray tube voltage: 120 kV) with ten breathing phases (0%–90% with a 10% step size). This 4D-CT served as the ground truth dataset in the geometric and dosimetric analyses described below.

6.2.3 MR-Linac data acquisition

The MRI data were acquired at a ViewRay MRIdian MR-Linac (section 3.1.4) in clinical operation for MRgRT patient treatments at the Department of Radiation Oncology of the University Hospital of LMU Munich. The scanner was operated in QA mode to allow for orthogonal cine MRI acquisition and modification of the sequence parameters. The phantom was positioned on the patient couch (Figure 6.1) with the torso receiver coils and moved to the imaging isocenter in the same way as described in section 5.2.2.

Similar to section 5.2.3, the MRI data needed as input for the propagation method were collected: First, a 3D-MRI in mid-exhale breath-hold was acquired with a bSSFP sequence (TrueFISP; sagittal slices; 3 mm slice thickness; $1.5 \times 1.5\,\mathrm{mm}^2$ in-plane resolution; TR/TE: 3.0/1.27 ms; 604 Hz/pixel bandwidth; 60° flip angle; 360×310 acquisition matrix; section 3.1.5). This scan was followed by one orthogonal cine MRI series per injected nodule, where the intersection line was positioned at the approximate nodule position. During these scans, the phantom was breathing with the same motion pattern as during 4D-CT acquisition. The same sequence parameters as listed in section 5.2.3 were used. Equivalent to the study described in Chapter 5, 600 frames were acquired (300 in sagittal and 300 in coronal orientation) over a time period of 82 s with a frame rate of 7.3 Hz for each nodule.

6.2.4 Creation of continuous time-resolved estimated synthetic CTs

For each of the ten gelatin nodules of the three datasets, a tresCT was created with the workflow sketched in Figure 6.2. The 3D-CT was rigidly registered to the 3D-MRI with the commercial treatment planning system RayStation (RaySearch Laboratories, Stockholm, Sweden; research version 8.99) with MI as similarity metric (section 2.4.6). The final registration results were visually inspected in overlay plots by assessing the alignment of the inner and outer phantom walls and ten multimodality markers (MR PinPoint, Par Scientific A/S, Odense, Denmark) attached to the outer surface of the upper phantom shell. The optimal translation and rotation parameters output by the registration were applied to the 3D-CT and all 4D-CT datasets to enable a direct comparison of the CT and MRI data in the same frame of reference. All gelatin nodules within the lung tissue were delineated on the 3D-CT image and transferred to all phases of the 4D-CT by regularized B-spline DIRs with MI as similarity metric using Plastimatch [200]. The ground truth nodule centroid positions in all phases of the 4D-CT were extracted with the algorithm described in section 5.2.8.

The mid-exhale 3D-CT was deformably registered to the mid-exhale 3D-MRI with a B-spline DIR with MI as similarity metric using Plastimatch (step 1 in Figure 6.2) to create a synthetic 3D-CT in the mid-exhale phase. The nodule contours were transferred from the 3D-CT to the synthetic 3D-CT by applying the DVFs of this DIR to the individual structures. The mid-exhale 3D-MRI was defined as the reference image and was input to the propagation method together with the orthogonal cine MRI (step 2 in Figure 6.2). The same DIR, extrapolation, IS weighting, and estimated DVF transformation algorithms as described in section 5.2.7 were applied to create an estimated 4D-MRI with 285 frames at 3.65 Hz. The DVFs output by the propagation method were subsequently applied to the synthetic 3D-CT to create the continuous tresCT and to the respective nodules structures (on the synthetic 3D-CT) to obtain the estimated nodule positions at each time point. The surrogate signal-based breathing phase binning method described in section 5.2.5 was applied to the tresCT and ground truth 4D-CT to assign each estimated synthetic 3D-CT and ground truth 3D-CT to one of ten breathing phases. The images in corresponding breathing phases of the tresCT and ground truth 4D-CT were compared in the geometric and dosimetric analyses described in the next sections.

6.2.5 Geometrical analysis

The motion amplitudes of the nodule centroids in the ground truth 4D-CT dataset were measured from the inhale to the exhale phase. The ground truth and estimated nodule positions in the tresCTs in each breathing phase were compared analogously to the nodule centroid position analysis described in section 5.2.8. Each of the tracked and estimated nodules was assigned to one of three categories based on the normal distance of its centroid to the orthogonal slice set. Nodules intersected by both, one or neither of the orthogonal slices were assigned to category 1, 2 or 3, respectively (see section 5.2.8 for category definition).

6.2.6 Dosimetric evaluation

The treatment planning system RayStation was chosen for the dosimetric evaluation instead of the system provided by ViewRay since the RayStation allowed the scripting of several treatment planning and evaluation steps. One treatment plan was created for each of the ten surrogate target lesions in the three datasets. For each plan generation, the mid-exhale phase of the ground truth 4D-CT was used as the planning image, and the nodule structure intersected by the respective orthogonal slices was defined as the GTV. The PTV was created by expanding the GTV with an isotropic margin of 5 mm, similar to clinical practice for stereotactic MR-guided adaptive radiotherapy of lung tumors with the ViewRay MRIdian MR-Linac reported in the literature [211] and at our institution. A step-and-shoot IMRT (section 2.5.4) plan with a dose of $8 \times 7.5\,\mathrm{Gy}$, prescribed to the PTV (section 2.5.3), was optimized to mimic gated stereotactic treatment plans at the MRIdian MR-Linac (section 3.1.4) [211]. A TrueBeam (Varian Medical Systems, Palo Alto, CA, USA) FFF beam model (RSL_TrueBeam_FFF) with 6 MV photon beams was used. Ten beams with an angular spacing of 24° were set up, where angles for which the beam would enter from the non-tumor-bearing lung side were omitted to spare dose to healthy lung tissue. The plans were optimized to achieve a 95% prescription dose coverage of the PTV ($V_{100\%} \geq 95\%\ D_{\mathrm{prescribed}}$) [211], without setting OAR constraints. The dose calculation was performed on an isotropic grid with a voxel size of $3 \times 3 \times 3\,\mathrm{mm}^3$ with a collapsed cone algorithm (section 2.5.5). Exemplary dose distributions and DVHs are depicted in Figure 6.3.

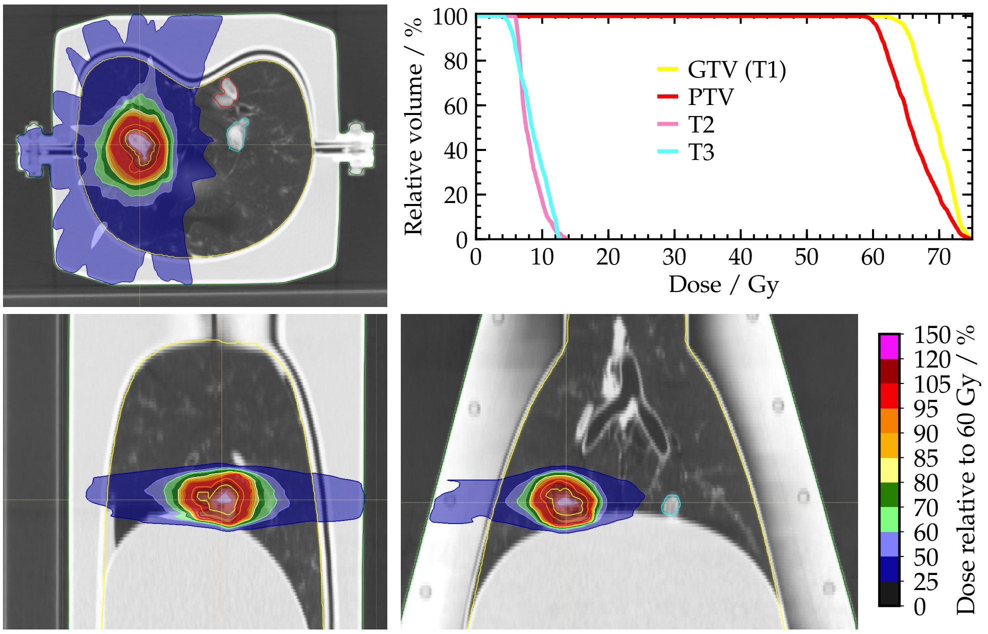

FIGURE 6.3: **Exemplary step-and-shoot IMRT plan.** The figure shows axial (top left), sagittal (bottom left), and coronal (bottom right) views of the dose distributions of an exemplary treatment plan overlayed on the planning CT image. The DVHs of the GTV (dataset 2, nodule 1; T1), PTV, and two further nodules (T2 and T3) are plotted in the upper right graph. A total dose of 60 Gy was prescribed to the PTV, shown as a red contour in the images.

The optimized plan was recalculated on all ground truth 4D-CT phases and ten synthetic CTs, where one image per breathing phase was randomly sampled from the tresCT. One plan for each of the ten nodules was created and was recalculated for all ten breathing phases, yielding 100 dose distributions on the ground truth and the synthetic CTs. The corresponding dose distributions on the ground truth and synthetic CTs were compared in dose difference and DVH (section 2.5.5) analyses. In the global dose difference analysis, the dose distributions on the two images were compared for all voxels with a dose above 10% of the prescribed dose. The pass rates at acceptance levels of 2% and 1% were calculated, defined as the fraction of voxels with an absolute dose difference relative to the prescribed dose below the respective acceptance levels. For the DVH analysis, the PTV and GTV structures defined on the planning CT image were copied to all other ground truth 4D-CT and tresCT datasets. The relative deviations (RD) of the $D_{98\%}$, $D_{50\%}$, and $D_{2\%}$ parameters for the tresCTs were computed relative to the corresponding ground truth (GT) parameters for these PTVs and GTVs:

$$\mathrm{RD} = \frac{D_x^{\mathrm{tresCT}} - D_x^{\mathrm{GT}}}{D_x^{\mathrm{GT}}}, \qquad \text{with } x \in [98\%, 50\%, 2\%]. \tag{6.1}$$

6.3 Results

6.3.1 Geometrical analysis

With the breathing frequency of 12 cycles/min, and the acquisition time of 82 s, approximately 16 breathing cycles were recorded during orthogonal cine MRI acquisition. The motion amplitudes of the nodules, measured from the inhale to exhale phase in the ground truth 4D-CT, were in the range 3–16 mm, with a median value of 7.5 mm. The largest median motion amplitudes were observed for the nodules in dataset 2 (13.0 mm), followed by dataset 1 (7.5 mm), and dataset 3 (7.0 mm).

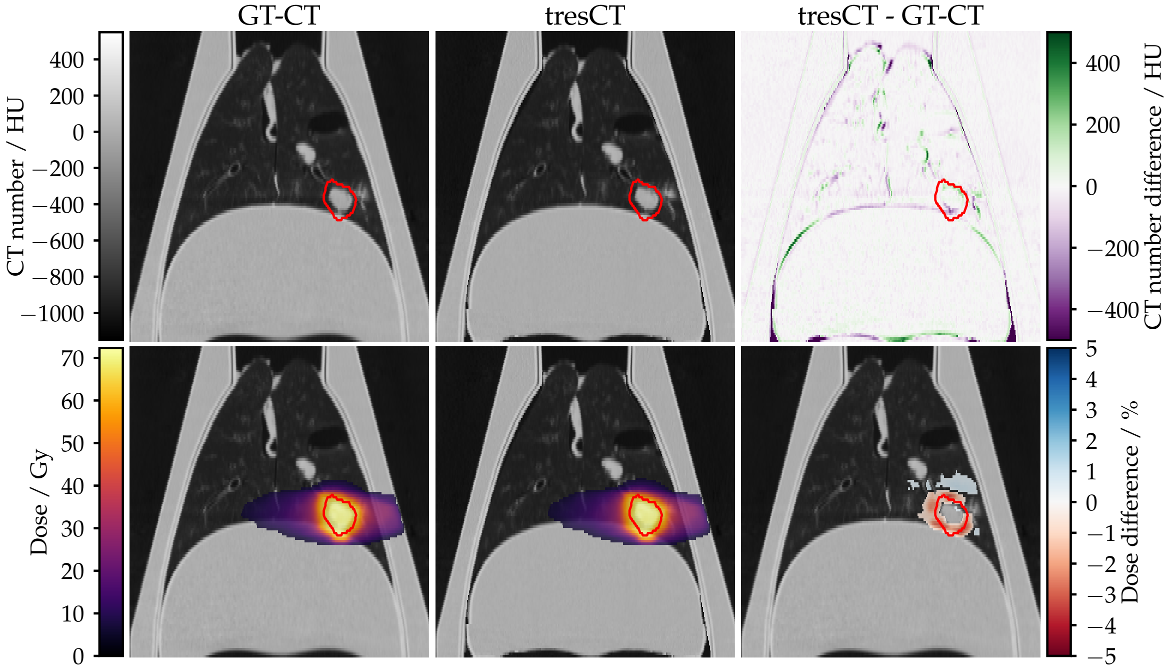

FIGURE 6.4: **Comparison of ground truth 4D-CT and tresCT.** The figure shows exemplary coronal views of the images (top row) and dose distributions (bottom row) of the ground truth dataset in the left column, the tresCT in the center column, and their differences in the right column. The images are shown in the mid-exhale phase, corresponding to the phase of the planning image and reference image for the propagation method. Doses below 10% of the prescribed dose and dose differences below an absolute value of 0.5% were masked for the sake of clearer visualization. The PTV is shown as a red contour.

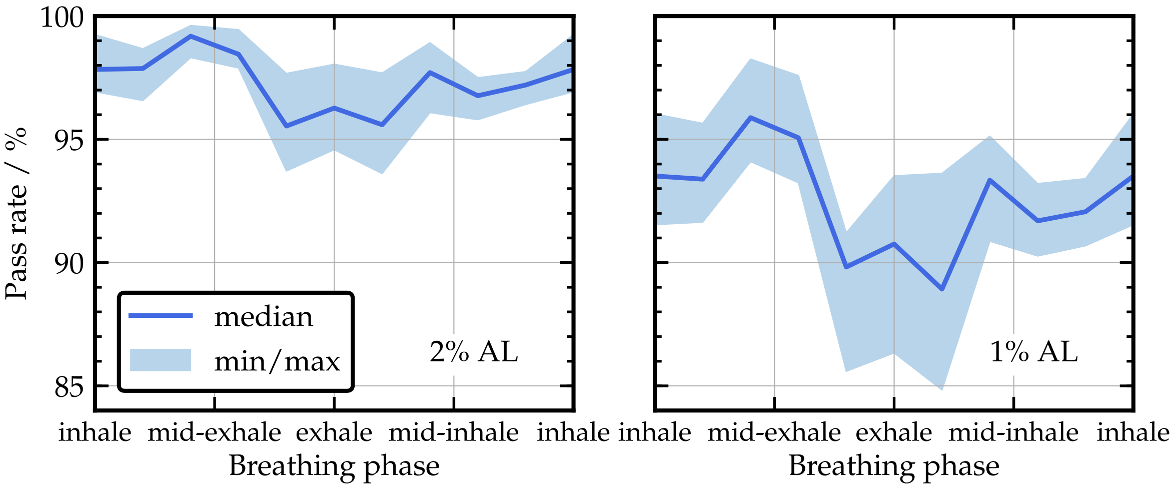

FIGURE 6.5: **Dose difference analysis results.** The pass rates of the dose difference analysis with acceptance levels (AL) of 2% (left) and 1% (right) are plotted as a function of the estimated breathing phase. The minimal (min), maximal (max), and median values of all ten datasets are shown.

Averaged over all time points and all ten datasets, the median (95th percentile) nodule estimation error for nodules of categories 1, 2, and 3 were 1.9 mm (4.6 mm), 2.3 mm (5.1 mm), and 2.7 mm (5.7 mm), respectively. The median (95th percentile) nodule estimation errors for the nodules intersected by both orthogonal slices (category 1) were 1.7 mm (3.3 mm) for dataset 1, 3.4 mm (5.3 mm) for dataset 2, and 1.6 mm (2.6 mm) for dataset 3, respectively.

6.3.2 Dose difference analysis

Exemplary coronal views of the images and dose distributions on the ground truth 4D-CT and the tresCT in mid-exhale phase are depicted in Figure 6.4. Overall, a high agreement between the two CT images and two dose distributions was observed. In the lower right dose difference plot in Figure 6.4, a slight dose underestimation of a few percent in the vicinity of the PTV boundary can be seen.

Figure 6.5 summarizes the results of the dose difference analysis. The highest median pass rates were obtained for the mid-exhale phase, which was the reference phase in the propagation method, followed by the mid-inhale, inhale, and exhale phase. The median pass rates with acceptance levels of 2% and 1%, averaged over all 100 dose distribution comparisons (ten datasets with ten breathing phases each), were 97.4% and 92.4%, respectively. The highest median pass rate at a 1% acceptance level was measured for dataset 1 (94.7%), followed by dataset 3 (92.1%) and dataset 2 (89.8%).

6.3.3 DVH analysis

Exemplary DVHs for the PTV and GTV are depicted in Figure 6.6 for the inhale, mid-exhale, and exhale phases. While the dose was slightly overestimated in the inhale phase, a small underestimation in exhale phase was observed. The relative deviations of the $D_{98\%}$, $D_{50\%}$, and $D_{2\%}$ parameters for the 100 DVH parameter comparisons for the PTV and GTV are summarized in Figure 6.7. Overall a high agreement of these parameters was found, with median relative deviations of –2.0% and –1.4% for the $D_{98\%}$ and below ±1% for the $D_{50\%}$, and $D_{2\%}$, both for the PTV and GTV, respectively.

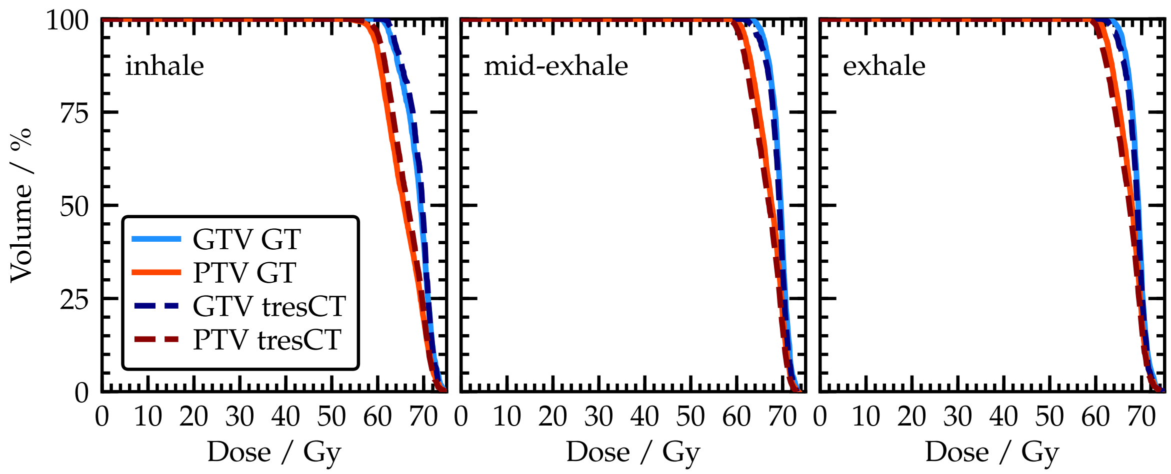

FIGURE 6.6: **Exemplary DVH curves for different breathing phases.** The DVH curves of the GTV and PTV are plotted for an exemplary ground truth (GT) and tresCT dataset (dataset 1 with nodule 4 as GTV) for the inhale (left), mid-exhale (center), and exhale (right) phase. The dose to the GTV and PTV in the tresCT was slightly overestimated in the inhale phase and slightly underestimated in the mid-exhale and exhale phases.

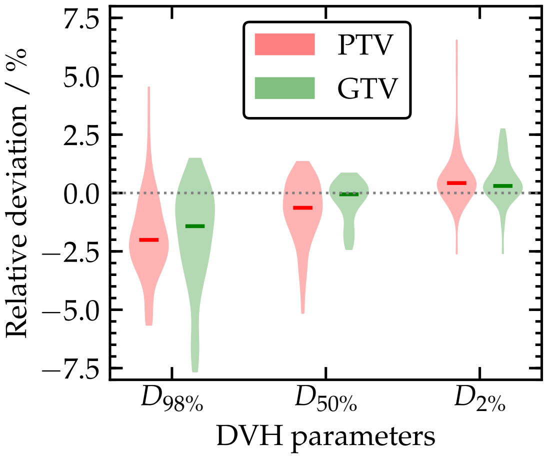

Structure	Parameter	RD (%)
PTV	$D_{98\%}$	−2.0 [−4.9, +0.7]
	$D_{50\%}$	−0.6 [−3.4, +0.8]
	$D_{2\%}$	+0.4 [−0.6, +2.1]
GTV	$D_{98\%}$	−1.4 [−6.6, +0.7]
	$D_{50\%}$	−0.1 [−2.2, +0.7]
	$D_{2\%}$	+0.3 [−0.7, +2.2]

FIGURE 6.7: **DVH parameter analysis results.** (Left): The results of the 100 DVH parameter comparisons for all datasets and breathing phases are summarized in violin plots for the PTV and GTV. The median values are indicated as horizontal lines. (Right): The median [5th percentile, 95th percentile] values of the relative deviations (RD) of the DVH parameters in percent are listed in the table for the PTV and GTV.

6.4 Discussion

The geometric and dosimetric accuracy of tresCTs generated with the propagation method was assessed in porcine lung phantom measurements at a clinical low-field MR-Linac. The median nodule centroid estimation errors for the three categories were smaller than the voxel dimensions of the orthogonal cine MRI images ($3.5 \times 3.5 \times 5\,\mathrm{mm}^3$). A high agreement of the dose distributions calculated on the ground truth 4D-CT and randomly sampled tresCT images was found, with a median dose difference pass rate of 97.4% at a 2% acceptance level. Furthermore, the respective median DVH parameters for the PTV and GTV deviated by only up to ±2%. These results suggest that the tresCT generation method could be a valuable tool for retrospective dose reconstruction or real-time dose adaptation based on imaging data acquired during beam delivery.

From an experimental perspective, the validation measurements of the tresCTs were more challenging than the propagation method validation measurements described in Chapter 5. In Chapter 5, the ground truth images and the input data for the propagation method were acquired at the same scanner. For the accuracy assessment in this chapter, the phantom had to be transported from the CT scanner to the MR-Linac (or vice versa) between the acquisition of the ground truth 4D-CT and the input data for the tresCT generation. The uninterruptible power supply and markers were used to stabilize the lung inflation state during transport and to check for potential positional deviations afterwards. Due to the additional transport, a direct comparison between the nodule centroid estimation errors determined in the study in Chapter 5 and in this chapter is not straightforward, also since the estimation error depends – among other factors – on the nodule motion amplitudes (section 5.3.6). Nevertheless, overall larger errors were measured for all three nodule categories (section 5.3.6 and section 6.3.1) in the study in this chapter, although the median 3D nodule motion amplitudes were smaller (7.5 mm vs. 8.9 mm). This observation appears plausible considering the additional uncertainties introduced by the phantom transport. The geometric errors caused by potential slightly different motion patterns at the two scanners could directly impact and bias the dosimetric analyses. However, the median nodule centroid estimation errors of all categories (1.9–2.7 mm) were smaller than the dose calculation grid (3 mm isotropic).

The dose differences depended on the breathing phase, with the highest pass rates for phases close to the reference image phase of the propagation method. This is in agreement with the results reported in section 5.3.5 and Figure 5.8a, where the DVF error was correlated to the estimated breathing phase. The lowest dose difference pass rates were measured for dataset 2. For this dataset, the largest motion amplitudes and category 1 nodule centroid estimation errors were observed. These nodules are less affected by extrapolation errors introduced by the propagation method (section 5.4), but subject to DIR uncertainties and actual deviations between the motion trajectories at the two scanners. With the chosen experimental study design, it is not feasible to determine the impact of these individual uncertainties on the resulting dose differences.

In the DVH analyses, slight breathing phase-dependent over- or underestimations of the dose to the GTV and PTV were identified (Figure 6.6). In Figure 6.4, the dose deviations were found to be largest in the vicinity of the PTV boundary. Upon closer inspection of the CT images, it was concluded that these deviations originated from lung density variations during the breathing cycle. These caused a variation of the CT numbers in the ground truth 4D-CT, but not in the tresCT since this was not accounted for in the DIRs in the tresCT generation method. The differences in CT numbers affected the electron densities assumed during dose calculation, thus impacting the resulting dose distributions and causing the observed deviations of a few percent. This effect likely also affected the dose difference analysis (Figure 6.5) and partly contributed to the breathing phase-dependent pass rates discussed above. These deviations could potentially be minimized by adopting the CT number correction method proposed by Yang et al. [237]. The authors of this technical note applied voxel-wise correction factors proportional to the Jacobian determinant of the DVF output by a DIR to the CT images of thoracic cancer patients. The Jacobian determinant measures the local volume changes (compression or expansion) of the voxels in a DIR. Therefore, it can be used to correct the CT numbers for the varying lung tissue densities during the breathing cycle.

The study presented in this chapter was subject to similar limitations as discussed in section 5.4 since the same porcine lung phantom and methodology for the estimated 4D-MRI generation with the propagation method were chosen. This includes through-plane distortions of the orthogonal slices, the coarse image resolution of the cine MRI sequence, and the lack of a beating heart and moving chest in the lung phantom. The proposed method requires a synthetic 3D-CT image created with a DIR of a measured 3D-CT to a 3D-MRI. This workflow step introduces additional DIR uncertainties. To minimize these, the 3D-CT and 3D-MRI need to be acquired in a similar breathing phase. This is already done in clinical practice at the ViewRay MRIdian MR-Linac today as part of the routine synthetic 3D-CT generation (section 3.1.6). The tresCT generation could be smoothly integrated into today's clinical treatment workflow by using this synthetic 3D-CT as input data for the proposed method. This could be achieved by replacing the planar cine MRI acquired during beam delivery with orthogonal cine MRI, as discussed in section 5.4. For a potential real-time application of the tresCT generation method, the propagation method would have to be sped up, e.g., by implementing the suggestions discussed in section 5.4 (warm start optimization and GPU implementation of the DIRs).

It would be desirable to verify the computational results of this study with dosimetric validation measurements. Mann et al. [221] demonstrated that the 3D dose distribution within such a porcine lung phantom could be dosimetrically measured with polymer gel. However, this is experimentally challenging, and the accuracy of the polymeric gel measurements is currently limited to 2% [238]. Alternatively, computational [47] or simpler motion phantoms [170] could be used for validation measurements, but these phantoms suffer from the limitations described in section 5.1, representing idealized simulations or oversimplifications of the human anatomy. The method should ideally be additionally validated with patient data. However, the validity of such measurements would be limited due to the lack of a ground truth caused by the poor breathing pattern reproducibility of a patient (section 5.4). Furthermore, this approach would be impractical since the required additional 4D-CT scan would lead to a considerable additional dose deposition to healthy tissue (section 2.6.2).

The porcine lung phantom offers an intermediate step between simple phantom experiments and real patient data acquisition by enabling ground truth measurements under conditions similar to the clinical environment. By stabilizing the lung position with an uninterruptible power supply during transport, reproducible lung tumor motion at the CT scanner and MR-Linac could be achieved.

6.5 Conclusions

In this chapter, a method to create tresCTs at a low-field MR-Linac was proposed and tested in porcine lung phantom experiments. Advantages of this approach include that the method outputs continuous time-resolved volumetric CT data with high geometric accuracy without the need for motion model training. The simplicity of the required imaging sequences could potentially enable a low-threshold clinical implementation. The observed high dosimetric accuracy suggests that tresCTs could be used to reconstruct the delivered dose after patient irradiation or to perform real-time plan adaptation based on real-time orthogonal cine MRI and a pre-treatment synthetic 3D-CT at low-field MR-Linacs in the future.

Chapter 7

Summary and Outlook

The introduction of MRI in the radiotherapeutic treatment workflow can improve the motion assessment and characterization of lung tumors with respect to today's standard-of-care CBCT-based IGRT. In particular, MR-Linacs offer imaging with enhanced soft tissue contrast, daily treatment adaptation to account for interfractional changes, and gating of the beam delivery based on the motion information gained with real-time cine MRI. These features allow the accurate and precise delivery of highly conformal dose distributions in SBRT treatments of lung tumors. Despite these advantages that allow for a substantial reduction of the applied treatment margins, the full potential of MRgRT is not yet fully exploited in clinical practice. Future techniques currently under investigation and development, such as real-time 4D-MRI, could lead to even higher confidence in target localization. In turn, even further reductions of the PTV margin, escalation of the dose to the tumor, or further dose sparing to normal tissues and OARs could become feasible.

This thesis was focused on intrafractional motion characterization and estimation of lung tumors with real-time and estimated 4D-MRI. A special focus lay on the ViewRay MRIdian as one of the two clinically employed MR-Linac systems available today. Three experimental and computational research studies were conducted in the scope of this thesis, investigating applications of time-resolved 4D-MRI in the stage of treatment planning, during beam delivery, and after irradiation for post treatment analyses.

In the proof-of-concept study in Chapter 4, a probabilistic ITV definition method based on real-time 4D-MRI was proposed to prospectively account for motion-related uncertainties in the treatment planning phase. The geometric analysis of imaging data from three lung cancer patients demonstrated that the ITVs derived from the GTV POP maps could achieve higher sensitivity values (surrogate metric for target coverage) with higher robustness against interfractional changes than conventional 4D-CT-based target volume definition concepts. This was attributed to the higher representativity of the captured motion as a result of the extended 4D-MRI acquisition time.

The finding that 4D-MRI could be used for improved ITV definitions was confirmed in an independent study with a similar methodology by Krieger et al. [239], published shortly after the publication of the study described in this thesis [116]. Furthermore, Wikström et al. [240] adopted the POP generation method proposed by the author of this thesis to evaluate the effects of irregular breathing on the ITV definition for lung cancer radiotherapy using cine CT data. Wikström et al. concluded that irregular breathing during 4D-CT acquisition could lead to suboptimal ITVs, which is in agreement with the results presented in this thesis. Consequently, the real-time 4D-MRI-based ITV definition could be a valuable technique for more accurate and precise ITV definitions for lung cancer patients treated at conventional linacs. This is of particular interest for clinics without an MR-Linac (e.g., in Germany, currently only three machines are in clinical use) but with access to a diagnostic MRI scanner.

The number of patients included in the proof-of-concept study in Chapter 4 was limited. However, the number of follow-up imaging sessions was high compared to other cine MRI motion assessment studies published in the literature [195]. A further limitation of the study was the coarse spatiotemporal resolution of the employed TWIST sequence.

Recent developments in the field of real-time 4D-MRI suggest that sequences with higher spatiotemporal resolution could become available in the near future [41]. A clinical introduction of these sequences would facilitate data collection to validate the proposed method with a larger patient cohort. As a further future research project, the method could be adapted to other treatment sites strongly affected by motion, such as the liver or pancreas.

While the first study focused on the use of real-time 4D-MRI in treatment planning for radiotherapy at conventional linacs, the topic of the second study was to create estimated 4D-MRI for motion monitoring at MR-Linacs. These estimated 4D-MRI could enable target and OAR tracking in 3D during beam delivery which could decrease localization errors compared to the 2D tracking based on planar cine MRI employed in clinical practice today. In this context, Chapter 5 presented the first experimental validation study of the propagation method by Paganelli et al. [46] at the scanner unit of a ViewRay MRIdian MR-Linac. The geometric accuracy of the continuous time-resolved estimated 4D-MRI at a frame rate of 3.65 Hz was assessed with the aid of a porcine lung phantom that allows the acquisition of realistic ground truth data for validation purposes. The porcine lung phantom exhibited a high breathing motion reproducibility and was found to be well suited for the intended validation measurements. The median DVF estimation error averaged over all eight datasets was 2.3 mm and the median centroid estimation errors for all 32 tracked nodules were between 1.5 mm and 2.1 mm for the three nodule categories. These errors are well below the in-plane resolution of the orthogonal cine MRI slices ($3.5 \times 3.5\,\mathrm{mm}^2$) used as input data for the propagation method. The estimation error depended on the breathing phase, the motion amplitudes, and the distance to the orthogonal slice set.

To the best of the author's knowledge, the article published on this study [178] was the first report on orthogonal cine MRI acquired at the MR scanner unit of the ViewRay MRIdian system. The study conducted in the scope of this thesis confirmed the computational results of the proof-of-concept study and the *in silico* comparison by Paganelli et al. [46, 47] showing that the propagation method can achieve low estimation errors not only at the tumor position but also at distant locations within the thorax.

Some limitations of the adapted propagation method were identified, including the through-plane geometric distortion of the orthogonal slices, the sensitivity to large out-of-plane motion, the limited spatial resolution of the employed cine MRI sequence, and the lack of chest or heart movements of the phantom. Nevertheless, despite the uncertainties related to the data acquisition and motion estimation, high geometric accuracy was achieved.

The simplicity of the propagation method and the similarity of the required MRI protocols with today's standard MRgRT sequences could allow a smooth clinical integration in the future. As a first future step, the proposed method could be adapted to the newly available 8 Hz sequence with a higher in-plane resolution provided by the vendor [162]. Furthermore, the data processing pipeline could be revised for speed-up of the motion estimation, e.g., by accelerating the DIRs of the propagation method. Motivated by the promising results of this phantom study, a clinical study for the evaluation of the geometric accuracy of the propagation method with a cohort of lung cancer patients was recently started in the scope of an ethics-approved clinical trial (TOSCA, project number 21-0019) at the University Hospital, LMU Munich. For the accuracy assessment with patient data, a sagittal or coronal slice is acquired in addition to the orthogonal slice set used as input data for the propagation method in an interleaved fashion. This additional slice serves as the ground truth motion state to be compared with the estimated motion state.

The experimental validation study in Chapter 5 demonstrated that the propagation method can generate geometrically accurate estimated 4D-MRIs which could enable improved target and OAR tracking in 3D during beam delivery. However, for a reconstruction of the delivered dose based on imaging data acquired during irradiation, time-resolved synthetic CTs are required. For this purpose, a follow-up project to the geometric accuracy assessment study in Chapter 5 was presented in Chapter 6. Continuous tresCTs with native CT resolution at 3.65 Hz were created using imaging data acquired at a CT scanner and a MRIdian MR-Linac. Orthogonal cine MRI and reference 3D-CT and 3D-MRI images served as input data to the extended propagation method, and the porcine lung phantom was again employed for experimental validation of the method. A high agreement of tresCTs and ground truth 4D-CTs in terms of geometric and dosimetric accuracy was achieved, with a median dose difference pass rate of 97.4% at a 2% acceptance level and median relative DVH parameter deviations below ±2% for the PTV and GTV. Thus, the proposed method could be a valuable tool for dose reconstruction after or even during each treatment fraction to guide inter- and intrafractional treatment plan adaptations and for documentation purposes at the low-field MR-Linac by ViewRay in the future.

Compared to other synthetic 4D-CT generation methods published in the literature, the proposed method has the advantage of providing continuous time-resolved volumetric CT data instead of reconstructing only a single breathing cycle [227, 233, 236]. Furthermore, instead of using real-time 4D-MRI sequences that are only available at 1.5 T MRI scanners [234, 235], readily available imaging sequences of the 0.35 T MRIdian MR-Linac were used for the tresCT generation method. Lastly, in contrast to motion models such as the one proposed by Müller et al. [181], no model training is needed before application of the method.

The chosen experimental study design required transport of the phantom between the CT scanner and the MR-Linac. Despite the measures taken to stabilize the lung inflation state, this transport introduced geometric uncertainties in the method evaluation process. Furthermore, compared to the original propagation method, the tresCT generation method requires an additional DIR of a 3D-CT to a 3D-MRI to create the synthetic 3D-CT that is deformed by the DVFs output by the propagation method. This DIR introduces further geometric uncertainties that need to be considered.

One of the next potential steps to further develop the proposed method is to combine the tresCT image data with MR-Linac treatment log files to reconstruct the dose actually delivered to the patient [50]. Further studies should also validate the computational results determined in this study with dosimetric measurements, e.g., by using polymer gel [221, 241]. A necessity for potential future real-time application of the tresCT generation method for real-time 4D dose reconstruction and intrafractional treatment plan adaptation [242] is the speed-up of the propagation method discussed above.

MR-guided radiotherapy of moving lung tumors is an active field of research. Numerous interesting and promising techniques are under investigation that could be implemented in the clinic in the following years [13, 31, 39–41].

From a clinical perspective, a trend towards increasingly hypofractionated SBRT deliveries at MR-Linacs down to a single fraction can be observed [19]. The delivery of a high ablative dose in only a few fractions relies on carefully managing intrafractional changes. The random uncertainties caused by respiratory motion do not average out over several fractions like in conventionally fractionated radiotherapy [110]. Therefore, a future aim should be to systematically reconstruct the dose delivered to the target and OARs in these hypofractionated treatments. The reconstruction will rely on time-resolved synthetic CTs – such as the tresCTs presented in Chapter 6 – generated from real-time imaging data acquired during beam delivery and linac log files [50]. The reconstructed dose could then serve as input for improved dose-response assessments in clinical SBRT studies. First clinical studies suggest that high doses can be safely and accurately delivered with the MR-Linac [35], which needs to be confirmed in future clinical studies with larger patient cohorts and longer follow-up times. Furthermore, MR-Linacs already allow the treatment of central and ultra-central lung tumors [33, 34, 212] and could allow dose-escalated SBRT treatments of stage III NSCLC tumors in the future [18]. A goal of paramount importance should be to systematically build clinical evidence – ideally with randomized controlled clinical trials – that the theoretical potential of MRgRT can translate into actual clinical benefits compared to CBCT-based IGRT [15]. This will answer the question of whether the higher complexity and costs associated with MRgRT are justified [30].

In the context of MR imaging, developing cine MRI sequences with higher frame rates and spatial resolution or different image contrasts could improve the target localization accuracy during gated MRgRT treatments in the short-term perspective [40]. An alternative interesting approach for target tracking with higher accuracy is to determine the optimal spatial orientation of the planar 2D cine MRI slices that minimizes the target localization error in the treatment planning phase [167] or to acquire MRI in beam's-eye-view [243, 244]. The acquisition of interleaved orthogonal slices allowed the creation of accurate estimated 4D-MRIs in this thesis. Several research groups are investigating the acquisition of several parallel slices or the interleaved or simultaneous acquisition of orthogonal slices for improved target tracking [31, 194, 214–217]. In the mid-term perspective, respiratory-correlated 4D-MRI could become available at clinical MR-Linacs. This was already demonstrated by Han et al. [245] on a 0.35 T MRgRT system who acquired self-gated 4D-MRI using rotating cartesian *k*-space acquisition. Such respiratory-correlated 4D-MRI could reduce delineation uncertainties, allow gating window optimization [31, 40] and provide data for global motion models that could be trained before and applied during treatment [185]. In the long-term perspective, real-time 4D-MRI [41] could be clinically introduced at MR-Linac systems. This could be enabled by improving the parallel imaging capabilities of the clinical MR-Linac systems [31, 45] or by accelerated image acquisition and reconstruction of subsampled *k*-space data with deep learning methods [41, 246]. These sequences could be used for similar applications as for respiratory-correlated 4D-MRI, for target and OAR monitoring in 3D during gated treatments, and as input data for the creation of time-resolved synthetic CTs.

Deep learning methods have recently gained a high interest in medical physics research [247] and are expected to play an increasingly important role in research and in the clinic in the coming years [246]. In the context of motion monitoring at MR-Linacs, besides the already discussed application for accelerated MRI acquisition and reconstruction [176, 177, 248], deep learning could be applied for automatic image segmentation of lung tumors during gated treatments [249–251] and prediction of future target positions [252] to avoid target miss related to the imaging and linac latency [170].

An alternative active motion management technique to gating that could directly benefit from such developments is tracking which would have the advantage of reduced treatment times enabled by a high duty cycle. Tracking has been demonstrated in proof-of-concept studies with the Elekta Unity [141], the MagnetTx Aurora system [253], and the Australian MR-Linac [254]. To the best of the author's knowledge, no study on tracking at the ViewRay MRIdian has been published thus far. Besides the clinical introduction of tracking techniques for lung tumor treatments, VMAT treatments could soon become available at the MR-Linac, as demonstrated in the proof-of-concept study by Kontaxis et al. [156] at the Elekta Unity MR-Linac. Both tracking and VMAT could enable a faster treatment delivery with potentially increased dose conformality [255].

In the more distant future, MR-guided proton therapy systems could be clinically implemented [256, 257]. These machines would combine the features provided by MR guidance with the physical advantages of proton therapy, such as the higher dose conformality and the lower integral dose to normal tissues. The potential of MR-guided proton therapy was discussed early on [258], in parallel with the invention of MR-Linacs. The first experimental proof-of-concept of proton beam delivery during MRI with a low-field open MRI scanner and a static proton beam line was achieved by Schellhammer et al. [259]. A randomized phase II study of SBRT versus stereotactic body proton therapy (SBPT) for early-stage NSCLC closed early due to the lack of volumetric imaging in the SBPT group [260]. MR-guided proton therapy could provide these lacking image guidance capabilities needed for the safe delivery of ablative doses with proton therapy. Many of the motion monitoring and 4D-MRI techniques that are currently developed for MR-Linac treatments of lung tumors – including the methods proposed in this thesis – could directly be applied for MR-guided proton therapy.

In conclusion, a novel ITV definition concept based on real-time 4D-MRI, an experimental validation of the propagation method at the scanner unit of an MR-Linac, and a new technique to create tresCTs at the low-field MR-Linac were presented in the scope of this thesis. These studies represent important steps towards a potential clinical application of these methods, which could further increase the accuracy and precision of MRgRT of moving lung tumors in the future.

Bibliography

[1] Hyuna Sung et al. “Global Cancer Statistics 2020: GLOBOCAN Estimates of Incidence and Mortality Worldwide for 36 Cancers in 185 Countries”. *CA: A Cancer Journal for Clinicians* 71.3 (2021), pp. 209–249. DOI: `10.3322/caac.21660`.

[2] Deborah E. Citrin. “Recent developments in radiotherapy”. *New England Journal of Medicine* 377.11 (2017), pp. 1065–1075. DOI: `10.1056/NEJMra1608986`.

[3] Sarah Baker et al. “A critical review of recent developments in radiotherapy for non-small cell lung cancer”. *Radiation Oncology* 11.1 (2016), pp. 1–14. DOI: `10.1186/s13014-016-0693-8`.

[4] Michael Baumann et al. “Radiation oncology in the era of precision medicine”. *Nature Reviews Cancer* 16.4 (2016), pp. 234–249. DOI: `10.1038/nrc.2016.18`.

[5] Jack Venselaar et al. *Comprehensive Brachytherapy: Physical and Clinical Aspects*. Taylor & Francis, 2012.

[6] Ervin B. Podgoršak. *Radiation Oncology Physics*. International Atomic Energy Agency, 2005. URL: `https://www.iaea.org/publications/7086/radiation-oncology-physics`.

[7] Kenneth R. Hogstrom and Peter R. Almond. “Review of electron beam therapy physics”. *Physics in Medicine & Biology* 51.13 (2006), R455. DOI: `10.1088/0031-9155/51/13/R25`.

[8] Wayne D. Newhauser and Rui Zhang. “The physics of proton therapy”. *Physics in Medicine & Biology* 60.8 (2015), R155. DOI: `10.1088/0031-9155/60/8/R155`.

[9] Dieter Schardt, Thilo Elsässer, and Daniela Schulz-Ertner. “Heavy-ion tumor therapy: Physical and radiobiological benefits”. *Reviews of Modern Physics* 82.1 (2010), pp. 383–425. DOI: `10.1103/RevModPhys.82.383`.

[10] Wolfgang Schlegel, Christian P. Karger, and Oliver Jäkel. *Medizinische Physik: Grundlagen – Bildgebung – Therapie – Technik*. Springer Spektrum, 2018. DOI: `10.1007/978-3-662-54801-1`.

[11] Benjamin Barnes et al. “Bericht zum Krebsgeschehen in Deutschland 2016”. *Robert Koch-Institut* (2016). DOI: `10.17886/rkipubl-2016-014`.

[12] Min Yuan et al. “The emerging treatment landscape of targeted therapy in non-small-cell lung cancer”. *Signal Transduction and Targeted Therapy* 4.1 (2019), pp. 1–14. DOI: `10.1038/s41392-019-0099-9`.

[13] Martin J. Menten, Andreas Wetscherek, and Martin F. Fast. “MRI-guided lung SBRT: Present and future developments”. *Physica Medica* 44 (2017), pp. 139–149. DOI: `10.1016/j.ejmp.2017.02.003`.

[14] Kristin A. Higgins et al. “National Cancer Database Analysis of Proton Versus Photon Radiation Therapy in Non-Small Cell Lung Cancer”. *International Journal of Radiation Oncology*Biology*Physics* 97.1 (2017), pp. 128–137. DOI: `10.1016/j.ijrobp.2016.10.001`.

[15] Michael Roach and Carri Glide-Hurst. "MRI at the Time of External Beam Treatment". *MRI for Radiotherapy*. Ed. by Gary Liney and Uulke van der Heide. Springer International Publishing, 2019. Chap. 11, pp. 169–188. DOI: `10.1007/978-3-030-14442-5_11`.

[16] Sameera S. Kumar, Kristin A. Higgins, and Ronald C. McGarry. "Emerging therapies for stage III non-small cell lung cancer: stereotactic body radiation therapy and immunotherapy". *Frontiers in Oncology* 7 (2017), p. 197. DOI: `10.3389/fonc.2017.00197`.

[17] Anurag K. Singh et al. "A pilot study of stereotactic body radiation therapy (SBRT) after surgery for stage III non-small cell lung cancer". *BMC Cancer* 18.1 (2018), pp. 1–8. DOI: `10.1186/s12885-018-5039-5`.

[18] Stefanie Corradini et al. "MR-guidance in clinical reality: current treatment challenges and future perspectives". *Radiation Oncology* 14.92 (2019), pp. 1–12. DOI: `10.1186/s13014-019-1308-y`.

[19] Tobias Finazzi et al. "Delivery of magnetic resonance-guided single-fraction stereotactic lung radiotherapy". *Physics and Imaging in Radiation Oncology* 14 (2020), pp. 17–23. DOI: `10.1016/j.phro.2020.05.002`.

[20] Brendan Whelan et al. "MRI Linac Systems". *MRI for Radiotherapy*. Ed. by Gary Liney and Uulke van der Heide. Springer International Publishing, 2019. Chap. 10, pp. 155–168. DOI: `10.1007/978-3-030-14442-5_10`.

[21] Paul J. Keall et al. "The management of respiratory motion in radiation oncology report of AAPM Task Group 76". *Medical Physics* 33.10 (2006), pp. 3874–3900. DOI: `10.1118/1.2349696`.

[22] Dirk De Ruysscher et al. "European Organization for Research and Treatment of Cancer (EORTC) recommendations for planning and delivery of high-dose, high precision radiotherapy for lung cancer". *Radiotherapy and Oncology* 124.1 (2017), pp. 1–10. DOI: `10.1016/j.radonc.2017.06.003`.

[23] David Palma et al. "Treatment of stage I NSCLC in elderly patients: A population-based matched-pair comparison of stereotactic radiotherapy versus surgery". *Radiotherapy and Oncology* 101.2 (2011), pp. 240–244. DOI: `10.1016/j.radonc.2011.06.029`.

[24] Matthias Guckenberger et al. "Definition of stereotactic body radiotherapy". *Strahlentherapie und Onkologie* 190.1 (2014), pp. 26–33. DOI: `10.1007/s00066-013-0450-y`.

[25] Joe Y. Chang et al. "Stereotactic ablative radiotherapy versus lobectomy for operable stage I non-small-cell lung cancer: a pooled analysis of two randomised trials". *The Lancet Oncology* 16.6 (2015), pp. 630–637. DOI: `10.1016/S1470-2045(15)70168-3`.

[26] Sasa Mutic and James F. Dempsey. "The ViewRay System: Magnetic Resonance–Guided and Controlled Radiotherapy". *Seminars in Radiation Oncology* 24.3 (2014), pp. 196–199. DOI: `10.1016/j.semradonc.2014.02.008`.

[27] Jan J. W. Lagendijk, Bas W. Raaymakers, and Marco van Vulpen. "The Magnetic Resonance Imaging–Linac System". *Seminars in Radiation Oncology* 24.3 (2014), pp. 207–209. DOI: `10.1016/j.semradonc.2014.02.009`.

[28] Paul J. Keall, Michael Barton, and Stuart Crozier. "The Australian Magnetic Resonance Imaging–Linac Program". *Seminars in Radiation Oncology* 24.3 (2014), pp. 203–206. DOI: `10.1016/j.semradonc.2014.02.015`.

[29] B. Gino Fallone. "The Rotating Biplanar Linac–Magnetic Resonance Imaging System". *Seminars in Radiation Oncology* 24.3 (2014), pp. 200–202. DOI: `10.1016/j.semradonc.2014.02.011`.

[30] Marcel van Herk et al. "Magnetic Resonance Imaging–Guided Radiation Therapy: A Short Strengths, Weaknesses, Opportunities, and Threats Analysis". *International Journal of Radiation Oncology*Biology*Physics* 101.5 (2018), pp. 1057–1060. DOI: `10.1016/j.ijrobp.2017.11.009`.

[31] Christopher Kurz et al. "Medical Physics challenges in clinical MR-guided radiotherapy". *Radiation Oncology* 15 (2020), pp. 1–16. DOI: `10.1186/s13014-020-01524-4`.

[32] Benjamin W. Fischer-Valuck et al. "Two-and-a-half-year clinical experience with the world's first magnetic resonance image guided radiation therapy system". *Advances in Radiation Oncology* 2.3 (2017), pp. 485–493. DOI: `10.1016/j.adro.2017.05.006`.

[33] Tobias Finazzi et al. "Role of On-Table Plan Adaptation in MR-Guided Ablative Radiation Therapy for Central Lung Tumors". *International Journal of Radiation Oncology*Biology*Physics* 104.4 (2019), pp. 933–941. DOI: `10.1016/j.ijrobp.2019.03.035`.

[34] Lauren E. Henke et al. "Stereotactic MR-Guided Online Adaptive Radiation Therapy (SMART) for Ultracentral Thorax Malignancies: Results of a Phase 1 Trial". *Advances in Radiation Oncology* 4.1 (2019), pp. 201–209. DOI: `10.1016/j.adro.2018.10.003`.

[35] Tobias Finazzi et al. "Clinical Outcomes of Stereotactic MR-Guided Adaptive Radiation Therapy for High-Risk Lung Tumors". *International Journal of Radiation Oncology*Biology*Physics* 107.2 (2020), pp. 270–278. DOI: `10.1016/j.ijrobp.2020.02.025`.

[36] Jan J. Lagendijk and Chris J. G. Bakker. "MRI guided radiotherapy: a MRI based linear accelerator". *Radiotherapy and Oncology* 56(Suppl) (2000). 19th Annual ESTRO Meeting, S60–S61. DOI: `10.1016/S0167-8140(00)81503-0`.

[37] Bas W. Raaymakers et al. "Integrating a 1.5 T MRI scanner with a 6 MV accelerator: proof of concept". *Physics in Medicine & Biology* 54.12 (2009), N229–N237. DOI: `10.1088/0031-9155/54/12/n01`.

[38] Gary P. Liney et al. "MRI-Linear Accelerator Radiotherapy Systems". *Clinical Oncology* 30.11 (2018), pp. 686–691. DOI: `10.1016/j.clon.2018.08.003`.

[39] Daniela Thorwarth and Daniel A. Low. "Technical Challenges of Real-Time Adaptive MR-Guided Radiotherapy". *Frontiers in Oncology* 11 (2021), p. 332. DOI: `10.3389/fonc.2021.634507`.

[40] Chiara Paganelli et al. "MRI-guidance for motion management in external beam radiotherapy: current status and future challenges". *Physics in Medicine & Biology* 63.22 (2018), 22TR03. DOI: `10.1088/1361-6560/aaebcf`.

[41] Bjorn Stemkens, Eric S. Paulson, and Rob H. N. Tijssen. "Nuts and bolts of 4D-MRI for radiotherapy". *Physics in Medicine & Biology* 63.21 (2018), 21TR01. DOI: `10.1088/1361-6560/aae56d`.

[42] *Company website ViewRay Inc.* `https://viewray.com/`. Accessed: 10th Mai 2021.

[43] *Company website Elekta AB.* `https://www.elekta.com/en/radiotherapy/treatment-delivery-systems/unity/`. Accessed: 10th Mai 2021.

[44] Indra J. Das et al. "Role and future of MRI in radiation oncology". *The British Journal of Radiology* 92.1094 (2019), p. 20180505. DOI: `10.1259/bjr.20180505`.

[45] Sebastian Klüter. "Technical design and concept of a 0.35 T MR-Linac". *Clinical and Translational Radiation Oncology* 18 (2019), pp. 98–101. DOI: `10.1016/j.ctro.2019.04.007`.

[46] Chiara Paganelli et al. "Feasibility study on 3D image reconstruction from 2D orthogonal cine-MRI for MRI-guided radiotherapy". *Journal of Medical Imaging and Radiation Oncology* 62.3 (2018), pp. 389–400. DOI: `10.1111/1754-9485.12713`.

[47] Chiara Paganelli et al. "Time-resolved volumetric MRI in MRI-guided radiotherapy: an in silico comparative analysis". *Physics in Medicine & Biology* 64.18 (2019), p. 185013. DOI: `10.1088/1361-6560/ab33e5`.

[48] Jürgen Biederer and Martin Heller. "Artificial Thorax for MR Imaging Studies in Porcine Heart-Lung Preparations". *Radiology* 226.1 (2003), pp. 250–255. DOI: `10.1148/radiol.2261011275`.

[49] Charis Kontaxis et al. "A new methodology for inter- and intrafraction plan adaptation for the MR-linac". *Physics in Medicine & Biology* 60.19 (2015), pp. 7485–7497. DOI: `10.1088/0031-9155/60/19/7485`.

[50] Martin J. Menten et al. "Automatic reconstruction of the delivered dose of the day using MR-linac treatment log files and online MR imaging". *Radiotherapy and Oncology* 145 (2020), pp. 88–94. DOI: `10.1016/j.radonc.2019.12.010`.

[51] Wilhelm C. Röntgen. "Über eine neue Art von Strahlen". *Sitzungsberichte der Physikalisch-Medicinischen Gesellschaft zu Würzburg* 137 (1895), pp. 132–141.

[52] Frank Herbert Attix. *Introduction to Radiological Physics and Radiation Dosimetry*. John Wiley & Sons, Ltd, 1986. DOI: `10.1002/9783527617135`.

[53] Martin J. Berger et al. "XCOM: Photon Cross Section Database". *NIST Standard Reference Database 8 (XGAM)* (2010). DOI: `10.18434/T48G6X`.

[54] John H. Hubbell. "Photon Cross Sections, Attenuation Coefficients, and Energy Absorption Coefficients from 10 keV to 100 GeV". *National Bureau of Standards Report NSRDS-NBS29, Washington DC* (1969).

[55] Albert Einstein. "Über einen die Erzeugung und Verwandlung des Lichtes betreffenden heuristischen Gesichtspunkt". *Annalen der Physik* 322.6 (1905), pp. 132–148. DOI: `10.1002/andp.19053220607`.

[56] Thorsten M. Buzug. *Computed Tomography: From Photon Statistics to Modern Cone-Beam CT*. Springer-Verlag Berlin Heidelberg, 2008. DOI: `10.1007/978-3-540-39408-2`.

[57] Arthur H. Compton. "A Quantum Theory of the Scattering of X-rays by Light Elements". *Physical Review* 21.5 (1923), pp. 483–502. DOI: `10.1103/PhysRev.21.483`.

[58] Oskar Klein and Yoshio Nishina. "Über die Streuung von Strahlung durch freie Elektronen nach der neuen relativistischen Quantendynamik von Dirac". *Zeitschrift für Physik* 52.11-12 (1929), pp. 853–868. DOI: `10.1007/BF01366453`.

[59] Patrick M. S. Blackett and Giuseppe P. S. Occhialini. "Some photographs of the tracks of penetrating radiation". *Proceedings of the Royal Society of London. Series A* 139.839 (1933), pp. 699–726. DOI: `10.1098/rspa.1933.0048`.

[60] M. J. Tahmasebi Birgani and S. M. Karbalaee. "Calculation of analytical expressions for measured percentage depth dose data in Megavoltage photon therapy". *Iranian Red Crescent Medical Journal* 11.2 (2009), pp. 140–144.

[61] Wolfgang Schlegel, Thomas Bortfeld, and Anca-Ligia Grosu. *New Technologies in Radiation Oncology*. Vol. 86. Springer, 2006.

[62] Jerrold T. Bushberg et al. *The Essential Physics of Medical Imaging*. Lippincott Williams & Wilkins, 2012.

[63] Robert Bujila, Artur Omar, and Gavin Poludniowski. "A validation of SpekPy: A software toolkit for modelling X-ray tube spectra". *Physica Medica* 75 (2020), pp. 44–54. DOI: `10.1016/j.ejmp.2020.04.026`.

[64] Godfrey N. Hounsfield. “Computerized transverse axial scanning (tomography): Part 1. Description of system”. *The British Journal of Radiology* 46.552 (1973), pp. 1016–1022. DOI: `10.1259/0007-1285-46-552-1016`.

[65] Willi A. Kalender et al. “Spiral volumetric CT with single-breath-hold technique, continuous transport, and continuous scanner rotation”. *Radiology* 176.1 (1990), pp. 181–183. DOI: `10.1148/radiology.176.1.2353088`.

[66] Johann Radon. “Über die Bestimmung von Funktionen durch ihre Integralwerte längs gewisser Mannigfaltigkeiten”. *Berichte über die Verhandlungen der Königlich-Sächsischen Gesellschaft der Wissenschaften zu Leipzig, Mathematisch-Physische Classe* 69 (1917), pp. 262–277.

[67] *Elekta Versa HD brochure*. `https://www.elekta.com/de/radiotherapy/treatment-delivery-systems/versa-hd/`. Accessed: 17th Mai 2021.

[68] Tilman Donath et al. “Toward clinical X-ray phase-contrast CT: demonstration of enhanced soft-tissue contrast in human specimen”. *Investigative Radiology* 45.7 (2010), pp. 445–452. DOI: `10.1097/RLI.0b013e3181e21866`.

[69] George Dedes et al. “Experimental comparison of proton CT and dual energy x-ray CT for relative stopping power estimation in proton therapy”. *Physics in Medicine & Biology* 64.16 (2019), p. 165002. DOI: `10.1088/1361-6560/ab2b72`.

[70] Michael M. Lell and Marc Kachelrieß. “Recent and upcoming technological developments in computed tomography: high speed, low dose, deep learning, multienergy”. *Investigative Radiology* 55.1 (2020), pp. 8–19. DOI: `10.1097/RLI.0000000000000601`.

[71] David A. Jaffray et al. “Flat-panel cone-beam computed tomography for image-guided radiation therapy”. *International Journal of Radiation Oncology*Biology*Physics* 53.5 (2002), pp. 1337–1349. DOI: `10.1016/S0360-3016(02)02884-5`.

[72] Nima Nabavizadeh et al. “Image Guided Radiation Therapy (IGRT) Practice Patterns and IGRT’s Impact on Workflow and Treatment Planning: Results From a National Survey of American Society for Radiation Oncology Members”. *International Journal of Radiation Oncology*Biology*Physics* 94.4 (2016), pp. 850–857. DOI: `10.1016/j.ijrobp.2015.09.035`.

[73] Lee A. Feldkamp, Lloyd C. Davis, and James W. Kress. “Practical cone-beam algorithm”. *Journal of the Optical Society of America A* 1.6 (1984), pp. 612–619. DOI: `10.1364/JOSAA.1.000612`.

[74] Chris C. Shaw. *Cone Beam Computed Tomography*. Taylor & Francis, 2014. DOI: `10.1201/b16465`.

[75] Kavitha Srinivasan, Mohammad Mohammadi, and Justin Shepherd. “Applications of linac-mounted kilovoltage Cone-beam Computed Tomography in modern radiation therapy: A review”. *Polish Journal of Radiology* 79 (2014), pp. 181–193. DOI: `10.12659/PJR.890745`.

[76] Christopher Kurz et al. “Investigating deformable image registration and scatter correction for CBCT-based dose calculation in adaptive IMPT”. *Medical Physics* 43.10 (2016), pp. 5635–5646. DOI: `10.1118/1.4962933`.

[77] David C. Hansen et al. “ScatterNet: A convolutional neural network for cone-beam CT intensity correction”. *Medical Physics* 45.11 (2018), pp. 4916–4926. DOI: `10.1002/mp.13175`.

[78] Susan Mercieca et al. “Interobserver variability in the delineation of the primary lung cancer and lymph nodes on different four-dimensional computed tomography reconstructions”. *Radiotherapy and Oncology* 126.2 (2018), pp. 325–332. DOI: `10.1016/j.radonc.2017.11.020`.

[79] Felix Bloch. “Nuclear Induction”. *Physical Review* 70 (1946), pp. 460–474. DOI: `10.1103/PhysRev.70.460`.

[80] Robert W. Brown et al. *Magnetic Resonance Imaging: Physical Principles and Sequence Design*. John Wiley & Sons, Ltd, 2014. DOI: `10.1002/9781118633953`.

[81] Piet Dirix, Karin Haustermans, and Vincent Vandecaveye. “The Value of Magnetic Resonance Imaging for Radiotherapy Planning”. *Seminars in Radiation Oncology* 24.3 (2014), pp. 151–159. DOI: `10.1016/j.semradonc.2014.02.003`.

[82] Jenny Bertholet et al. “Real-time intrafraction motion monitoring in external beam radiotherapy”. *Physics in Medicine & Biology* 64.15 (2019), 15TR01. DOI: `10.1088/1361-6560/ab2ba8`.

[83] Olaf Dietrich, Maximilian F. Reiser, and Stefan O. Schoenberg. “Artifacts in 3-T MRI: physical background and reduction strategies”. *European Journal of Radiology* 65.1 (2008), pp. 29–35. DOI: `10.1016/j.ejrad.2007.11.005`.

[84] Joseph Weygand et al. “Spatial precision in magnetic resonance imaging–guided radiation therapy: the role of geometric distortion”. *International Journal of Radiation Oncology*Biology*Physics* 95.4 (2016), pp. 1304–1316. DOI: `10.1016/j.ijrobp.2016.02.059`.

[85] Wolfgang Schlegel and Josef Bille. *Medizinische Physik 2*. Springer, Berlin, Heidelberg, 2002. DOI: `10.1007/978-3-642-56259-4`.

[86] Eite Tiesinga et al. “The 2018 CODATA Recommended Values of the Fundamental Physical Constants”. *National Institute of Standards and Technology (NIST)* (2020). URL: `http://physics.nist.gov/constants`.

[87] Michael Ingrisch. “Quantification of cerebral hemodynamics with dynamic contrast-enhanced MRI”. PhD thesis. Medical Faculty, LMU Munich, 2012.

[88] Matt A. Bernstein, Kevin F. King, and Xiaohong J. Zhou. *Handbook of MRI Pulse Sequences*. Elsevier, 2004. DOI: `10.1016/B978-0-12-092861-3.X5000-6`.

[89] Stewart C. Bushong and Geoffrey Clarke. *Magnetic Resonance Imaging: Physical and Biological Principles*. Elsevier Health Sciences, 2013.

[90] Marielle Philippens and Roberto García-Álvarez. “Functional MR Imaging”. *MRI for Radiotherapy*. Ed. by Gary Liney and Uulke van der Heide. Springer International Publishing, 2019. Chap. 5, pp. 73–94. DOI: `10.1007/978-3-030-14442-5_5`.

[91] Rick Keesman et al. “Correcting geometric image distortions in slice-based 4D-MRI on the MR-linac”. *Medical Physics* 46.7 (2019), pp. 3044–3054. DOI: `10.1002/mp.13602`.

[92] Olga L. Green et al. “First clinical implementation of real-time, real anatomy tracking and radiation beam control”. *Medical Physics* 45.8 (2018), pp. 3728–3740. DOI: `10.1002/mp.13002`.

[93] Yanle Hu et al. “Characterization of the onboard imaging unit for the first clinical magnetic resonance image guided radiation therapy system”. *Medical Physics* 42.10 (2015), pp. 5828–5837. DOI: `10.1118/1.4930249`.

[94] John S. Ginn et al. “Characterization of spatial distortion in a 0.35 T MRI-guided radiotherapy system”. *Physics in Medicine & Biology* 62.11 (2017), pp. 4525–4540. DOI: `10.1088/1361-6560/aa6e1a`.

[95] Siamak P. Nejad-Davarani et al. "Large field of view distortion assessment in a low-field MR-linac". *Medical Physics* 46.5 (2019), pp. 2347–2355. DOI: `10.1002/mp.13467`.

[96] Clarissa Kroll et al. "Improving the modelling of susceptibility-induced spatial distortions in MRI-guided extra-cranial radiotherapy". *Physics in Medicine & Biology* 64.20 (2019), p. 205006. DOI: `10.1088/1361-6560/ab447c`.

[97] Teo Stanescu and Jihong Wang. "Quality Assurance". *MRI for Radiotherapy*. Ed. by Gary Liney and Uulke van der Heide. Springer International Publishing, 2019. Chap. 3, pp. 43–54. DOI: `10.1007/978-3-030-14442-5_3`.

[98] Andrew Janke et al. "Use of spherical harmonic deconvolution methods to compensate for nonlinear gradient effects on MRI images". *Magnetic Resonance in Medicine* 52.1 (2004), pp. 115–122. DOI: `10.1002/mrm.20122`.

[99] Lei Dong, Jinzhong Yang, and Yongbin Zhang. "Image Processing in Adaptive Radiotherapy". *Image Processing in Radiation Therapy*. Ed. by Kristy K. Brock. CRC Press, 2013. Chap. 1, pp. 3–20. DOI: `10.1201/b15359`.

[100] Richard Speight. "MRI to CT Image Registration". *MRI for Radiotherapy*. Ed. by Gary Liney and Uulke van der Heide. Springer International Publishing, 2019. Chap. 2, pp. 21–42. DOI: `10.1007/978-3-030-14442-5_2`.

[101] Daniel Rueckert. "Nonrigid registration: Concepts, algorithms, and applications". *Medical Image Registration*. Ed. by Joseph V. Hajnal and Derek L. G. Hill. CRC Press, 2001. Chap. 13, pp. 281–301. DOI: `10.1201/9781420042474`.

[102] Raj Shekhar and William Plishker. "Parametric Image Registration". *Image Processing in Radiation Therapy*. Ed. by Kristy K. Brock. CRC Press, 2013. Chap. 5, pp. 75–84. DOI: `10.1201/b15359`.

[103] Daniel Rueckert et al. "Nonrigid registration using free-form deformations: application to breast MR images". *IEEE Transactions on Medical Imaging* 18.8 (1999), pp. 712–721. DOI: `10.1109/42.796284`.

[104] Kristy K. Brock et al. "Use of image registration and fusion algorithms and techniques in radiotherapy: Report of the AAPM Radiation Therapy Committee Task Group No. 132". *Medical Physics* 44.7 (2017), e43–e76. DOI: `10.1002/mp.12256`.

[105] He Wang. "Similarity Metrics". *Image Processing in Radiation Therapy*. Ed. by Kristy K. Brock. CRC Press, 2013. Chap. 4, pp. 65–74. DOI: `10.1201/b15359`.

[106] Saeed Ghahramani. *Fundamentals of Probability: With Stochastic Processes*. CRC Press, 2018.

[107] International Commission on Radiation Units and Measurements. "ICRU Report 83: Prescribing, recording, and reporting photon-beam intensity-modulated radiation therapy (IMRT)". *Journal of the International Commission on Radiation Units and Measurements* 10.1 (2010), pp. 1–112. URL: `https://www.icru.org/report/prescribing-recording-and-reporting-intensity-modulated-photon-beam-therapy-imrticru-report-83/`.

[108] Søren M Bentzen. "Theragnostic imaging for radiation oncology: dose-painting by numbers". *The Lancet Oncology* 6.2 (2005), pp. 112–117. DOI: `10.1016/S1470-2045(05)01737-7`.

[109] Daniela Thorwarth et al. "Hypoxia Dose Painting by Numbers: A Planning Study". *International Journal of Radiation Oncology*Biology*Physics* 68.1 (2007), pp. 291–300. DOI: `10.1016/j.ijrobp.2006.11.061`.

[110] Marcel van Herk et al. "The probability of correct target dosage: dose-population histograms for deriving treatment margins in radiotherapy". *International Journal of Radiation Oncology*Biology*Physics* 47.4 (2000), pp. 1121–1135. DOI: `10.1016/S0360-3016(00)00518-6`.

[111] Shalini K. Vinod et al. "Uncertainties in volume delineation in radiation oncology: A systematic review and recommendations for future studies". *Radiotherapy and Oncology* 121.2 (2016), pp. 169–179. DOI: `10.1016/j.radonc.2016.09.009`.

[112] Carlos E. Cardenas et al. "Advances in Auto-Segmentation". *Seminars in Radiation Oncology* 29.3 (2019), pp. 185–197. DOI: `10.1016/j.semradonc.2019.02.001`.

[113] Lawrence B. Marks et al. "Use of normal tissue complication probability models in the clinic". *International Journal of Radiation Oncology*Biology*Physics* 76.3 (2010), S10–S19. DOI: `10.1016/j.ijrobp.2009.07.1754`.

[114] Sekaran Sureka and Christina Armpilia. *Radiation Biology for Medical Physicists*. CRC Press, 2017.

[115] Hanno Krieger. *Strahlungsquellen für Technik und Medizin*. Springer Spektrum, 2013. DOI: `10.1007/978-3-658-00590-0`.

[116] Moritz Rabe et al. "Real-time 4DMRI-based internal target volume definition for moving lung tumors". *Medical Physics* 47.4 (2020), pp. 1431–1442. DOI: `10.1002/mp.14023`.

[117] Lukas Knybel et al. "Analysis of Lung Tumor Motion in a Large Sample: Patterns and Factors Influencing Precise Delineation of Internal Target Volume". *International Journal of Radiation Oncology*Biology*Physics* 96.4 (2016), pp. 751–758. DOI: `10.1016/j.ijrobp.2016.08.008`.

[118] Vincent Caillet, Jeremy T. Booth, and Paul Keall. "IGRT and motion management during lung SBRT delivery". *Physica Medica* 44 (2017), pp. 113–122. DOI: `10.1016/j.ejmp.2017.06.006`.

[119] Edward D. Brandner et al. "Motion management strategies and technical issues associated with stereotactic body radiotherapy of thoracic and upper abdominal tumors: A review from NRG oncology". *Medical Physics* 44.6 (2017), pp. 2595–2612. DOI: `10.1002/mp.12227`.

[120] Ming Yang and Robert Timmerman. "Stereotactic Ablative Radiotherapy Uncertainties: Delineation, Setup and Motion". *Seminars in Radiation Oncology* 28.3 (2018), pp. 207–217. DOI: `10.1016/j.semradonc.2018.02.006`.

[121] Jennifer Dhont et al. "The long- and short-term variability of breathing induced tumor motion in lung and liver over the course of a radiotherapy treatment". *Radiotherapy and Oncology* 126.2 (2018), pp. 339–346. DOI: `10.1016/j.radonc.2017.09.001`.

[122] Marco Schwarz, Giovanni M. Cattaneo, and Livia Marrazzo. "Geometrical and dosimetrical uncertainties in hypofractionated radiotherapy of the lung: A review". *Physica Medica* 36 (2017), pp. 126–139. DOI: `10.1016/j.ejmp.2017.02.011`.

[123] Eric C. Ford et al. "Respiration-correlated spiral CT: A method of measuring respiratory-induced anatomic motion for radiation treatment planning". *Medical Physics* 30.1 (2003), pp. 88–97. DOI: `10.1118/1.1531177`.

[124] Daniel A. Low et al. "A method for the reconstruction of four-dimensional synchronized CT scans acquired during free breathing". *Medical Physics* 30.6 (2003), pp. 1254–1263. DOI: `10.1118/1.1576230`.

[125] Tinsu Pan et al. "4D-CT imaging of a volume influenced by respiratory motion on multi-slice CT". *Medical Physics* 31.2 (2004), pp. 333–340. DOI: `10.1118/1.1639993`.

[126] Paul J. Keall et al. "Acquiring 4D thoracic CT scans using a multislice helical method". *Physics in Medicine & Biology* 49.10 (2004), pp. 2053–2067. DOI: `10.1088/0031-9155/49/10/015`.

[127] Gig S. Mageras et al. "Measurement of lung tumor motion using respiration-correlated CT". *International Journal of Radiation Oncology*Biology*Physics* 60.3 (2004), pp. 933–941. DOI: `10.1016/j.ijrobp.2004.06.021`.

[128] Heng Li and Joe Y. Chang. "Accounting for, Mitigating, and Choice of Margins for Moving Tumors". *Seminars in Radiation Oncology* 28.3 (2018), pp. 194–200. DOI: `10.1016/j.semradonc.2018.02.004`.

[129] Matthias Guckenberger et al. "Is a Single Respiratory Correlated 4D-CT Study Sufficient for Evaluation of Breathing Motion?" *International Journal of Radiation Oncology*Biology*Physics* 67.5 (2007), pp. 1352–1359. DOI: `10.1016/j.ijrobp.2006.11.025`.

[130] Sara St. James et al. "Quantifying ITV instabilities arising from 4DCT: a simulation study using patient data". *Physics in Medicine & Biology* 57.5 (2012), pp. L1–L7. DOI: `10.1088/0031-9155/57/5/l1`.

[131] Sara St. James et al. "Simulations using patient data to evaluate systematic errors that may occur in 4D treatment planning: A proof of concept study". *Medical Physics* 40.9 (2013), p. 091706. DOI: `10.1118/1.4817244`.

[132] Yolanda D. Tseng et al. "4D computed tomography scans for conformal thoracic treatment planning: is a single scan sufficient to capture thoracic tumor motion?" *Physics in Medicine & Biology* 63.2 (2018), 02NT03. DOI: `10.1088/1361-6560/aaa44e`.

[133] Elisabeth Steiner et al. "Both four-dimensional computed tomography and four-dimensional cone beam computed tomography under-predict lung target motion during radiotherapy". *Radiotherapy and Oncology* 135 (2019), pp. 65–73. DOI: `10.1016/j.radonc.2019.02.019`.

[134] Reinhart A. Sweeney et al. "Accuracy and inter-observer variability of 3D versus 4D cone-beam CT based image-guidance in SBRT for lung tumors". *Radiation Oncology* 7.1 (2012), p. 81. DOI: `10.1186/1748-717X-7-81`.

[135] Jochem W. H. Wolthaus et al. "Mid-ventilation CT scan construction from four-dimensional respiration-correlated CT scans for radiotherapy planning of lung cancer patients". *International Journal of Radiation Oncology*Biology*Physics* 65.5 (2006), pp. 1560–1571. DOI: `10.1016/j.ijrobp.2006.04.031`.

[136] Jochem W. H. Wolthaus et al. "Reconstruction of a time-averaged midposition CT scan for radiotherapy planning of lung cancer patients using deformable registration". *Medical Physics* 35.9 (2008), pp. 3998–4011. DOI: `10.1118/1.2966347`.

[137] Jochem W. H. Wolthaus et al. "Comparison of Different Strategies to Use Four-Dimensional Computed Tomography in Treatment Planning for Lung Cancer Patients". *International Journal of Radiation Oncology*Biology*Physics* 70.4 (2008), pp. 1229–1238. DOI: `10.1016/j.ijrobp.2007.11.042`.

[138] Di Yan et al. "Adaptive radiation therapy". *Physics in Medicine & Biology* 42.1 (1997), pp. 123–132. DOI: `10.1088/0031-9155/42/1/008`.

[139] Daniela Thorwarth. "Biologically adapted radiation therapy". *Zeitschrift für Medizinische Physik* 28.3 (2018), pp. 177–183. DOI: `10.1016/j.zemedi.2017.08.001`.

[140] Sahaja Acharya et al. "Online Magnetic Resonance Image Guided Adaptive Radiation Therapy: First Clinical Applications". *International Journal of Radiation Oncology*Biology*Physics* 94.2 (2016), pp. 394–403. DOI: `10.1016/j.ijrobp.2015.10.015`.

[141] Markus Glitzner et al. "Technical note: MLC-tracking performance on the Elekta Unity MRI-linac". *Physics in Medicine & Biology* 64.15 (2019), 15NT02. DOI: `10.1088/1361-6560/ab2667`.

[142] Jan J. W. Lagendijk et al. "MRI/linac integration". *Radiotherapy and Oncology* 86.1 (2008), pp. 25–29. DOI: `10.1016/j.radonc.2007.10.034`.

[143] Bas W. Raaymakers et al. "First patients treated with a 1.5 T MRI-Linac: clinical proof of concept of a high-precision, high-field MRI guided radiotherapy treatment". *Physics in Medicine & Biology* 62.23 (2017), pp. L41–L50. DOI: `10.1088/1361-6560/aa9517`.

[144] H. Omar Wooten et al. "Quality of Intensity Modulated Radiation Therapy Treatment Plans Using a ^{60}Co Magnetic Resonance Image Guidance Radiation Therapy System". *International Journal of Radiation Oncology*Biology*Physics* 92.4 (2015), pp. 771–778. DOI: `10.1016/j.ijrobp.2015.02.057`.

[145] Eric S. Paulson and Rob H. N. Tijssen. "Motion Management". *MRI for Radiotherapy*. Ed. by Gary Liney and Uulke van der Heide. Springer International Publishing, 2019. Chap. 7, pp. 107–116. DOI: `10.1007/978-3-030-14442-5_7`.

[146] Soumon Rudra et al. "Using adaptive magnetic resonance image-guided radiation therapy for treatment of inoperable pancreatic cancer". *Cancer Medicine* 8.5 (2019), pp. 2123–2132. DOI: `10.1002/cam4.2100`.

[147] Jason A. Dowling and Juha Korhonen. "MR-Only Methodology". *MRI for Radiotherapy*. Ed. by Gary Liney and Uulke van der Heide. Springer International Publishing, 2019. Chap. 9, pp. 131–151. DOI: `10.1007/978-3-030-14442-5_9`.

[148] Daniela Thorwarth et al. "Quantitative magnetic resonance imaging on hybrid magnetic resonance linear accelerators: Perspective on technical and clinical validation". *Physics and Imaging in Radiation Oncology* 16 (2020), pp. 69–73. DOI: `10.1016/j.phro.2020.09.007`.

[149] Svenja Ipsen et al. "Radiotherapy beyond cancer: Target localization in real-time MRI and treatment planning for cardiac radiosurgery". *Medical Physics* 41.12 (2014), p. 120702. DOI: `10.1118/1.4901414`.

[150] Phillip S. Cuculich et al. "Noninvasive Cardiac Radiation for Ablation of Ventricular Tachycardia". *New England Journal of Medicine* 377.24 (2017), pp. 2325–2336. DOI: `10.1056/NEJMoa1613773`.

[151] Michael Mayinger et al. "First magnetic resonance imaging-guided cardiac radioablation of sustained ventricular tachycardia". *Radiotherapy and Oncology* 152 (2020), pp. 203–207. DOI: `10.1016/j.radonc.2020.01.008`.

[152] Kathrin Spindeldreier et al. "Radiation dosimetry in magnetic fields with Farmer-type ionization chambers: determination of magnetic field correction factors for different magnetic field strengths and field orientations". *Physics in Medicine & Biology* 62.16 (2017), pp. 6708–6728. DOI: `10.1088/1361-6560/aa7ae4`.

[153] Stefan Pojtinger et al. "Experimental determination of magnetic field correction factors for ionization chambers in parallel and perpendicular orientations". *Physics in Medicine & Biology* 65.24 (2020), p. 245044. DOI: `10.1088/1361-6560/abca06`.

[154] Alexander J. E. Raaijmakers, Bas W. Raaymakers, and Jan J. W. Lagendijk. "Magnetic-field-induced dose effects in MR-guided radiotherapy systems: dependence on the magnetic field strength". *Physics in Medicine & Biology* 53.4 (2008), pp. 909–923. DOI: `10.1088/0031-9155/53/4/006`.

[155] Alexander J. E. Raaijmakers, Bas W. Raaymakers, and Jan J. W. Lagendijk. "Integrating a MRI scanner with a 6 MV radiotherapy accelerator: dose increase at tissue–air interfaces in a lateral magnetic field due to returning electrons". *Physics in Medicine & Biology* 50.7 (2005), pp. 1363–1376. DOI: `10.1088/0031-9155/50/7/002`.

[156] Charis Kontaxis et al. "Proof-of-concept delivery of intensity modulated arc therapy on the Elekta Unity 1.5 T MR-linac". *Physics in Medicine & Biology* 66.4 (2021), 04LT01. DOI: `10.1088/1361-6560/abd66d`.

[157] Dennis Winkel et al. "Adaptive radiotherapy: The Elekta Unity MR-linac concept". *Clinical and Translational Radiation Oncology* 18 (2019), pp. 54–59. DOI: `10.1016/j.ctro.2019.04.001`.

[158] Dong Nie et al. "Estimating CT Image from MRI Data Using 3D Fully Convolutional Networks". *Deep Learning and Data Labeling for Medical Applications*. 2016, pp. 170–178. DOI: `10.1007/978-3-319-46976-8_18`.

[159] Sebastian Neppl et al. "Evaluation of proton and photon dose distributions recalculated on 2D and 3D Unet-generated pseudoCTs from T1-weighted MR head scans". *Acta Oncologica* 58.10 (2019), pp. 1429–1434. DOI: `10.1080/0284186X.2019.1630754`.

[160] *Physics World article with image provided by MagnetTx*. `https://physicsworld.com/a/beams-eye-mri-could-guide-radiotherapy/`. Accessed: 11th Mai 2021.

[161] *ACRF Image X Institute website of the University of Sydney*. `https://image-x.sydney.edu.au/mri-linac/`. Accessed: 11th Mai 2021.

[162] *510(k) Premarket Notification by the U.S. Food and Drug Administration (FDA) for the MRIdian Linac System - 510(k) Number: K181989*. `https://www.accessdata.fda.gov/scripts/cdrh/cfdocs/cfpmn/pmn.cfm?ID=K181989`. Decision date: 20th February 2019.

[163] Sara Leibfarth et al. "Potentials and challenges of diffusion-weighted magnetic resonance imaging in radiotherapy". *Clinical and Translational Radiation Oncology* 13 (2018), pp. 29–37. DOI: `10.1016/j.ctro.2018.09.002`.

[164] Shmaryu Shvartsman et al. "Magnetic and RF Shielding of a Novel Compact 6 MeV S-Band Linac for MRI Guided Radiation Therapy System (poster)". *Proceedings of the International Society for Magnetic Resonance in Medicine, Scientific Meeting and Exhibition*. 2017. URL: `https://cds.ismrm.org/protected/17MProceedings/`.

[165] Brian Hargreaves. "Rapid gradient-echo imaging". *Journal of Magnetic Resonance Imaging* 36.6 (2012), pp. 1300–1313. DOI: `10.1002/jmri.23742`.

[166] Oliver Bieri and Klaus Scheffler. "Fundamentals of balanced steady state free precession MRI". *Journal of Magnetic Resonance Imaging* 38.1 (2013), pp. 2–11. DOI: `10.1002/jmri.24163`.

[167] Martin J. Menten et al. "The impact of 2D cine MR imaging parameters on automated tumor and organ localization for MR-guided real-time adaptive radiotherapy". *Physics in Medicine & Biology* 63.23 (2018), p. 235005. DOI: `10.1088/1361-6560/aae74d`.

[168] Lauren E. Henke et al. "Magnetic resonance image-guided radiotherapy (MRIgRT): A 4.5-year clinical experience". *Clinical Oncology* 30.11 (2018), pp. 720–727. DOI: `10.1016/j.clon.2018.08.010`.

[169] John R. van Sörnsen de Koste et al. "MR-guided gated stereotactic radiation therapy delivery for lung, adrenal, and pancreatic tumors: a geometric analysis". *International Journal of Radiation Oncology*Biology*Physics* 102.4 (2018), pp. 858–866. DOI: `10.1016/j.ijrobp.2018.05.048`.

[170] Taeho Kim et al. “Clinical experience of MRI4D QUASAR motion phantom for latency measurements in 0.35T MR-LINAC”. *Journal of Applied Clinical Medical Physics* 22.1 (2021), pp. 128–136. DOI: `10.1002/acm2.13118`.

[171] R. Botman et al. “The clinical introduction of MR-guided radiation therapy from a RTT perspective”. *Clinical and Translational Radiation Oncology* 18 (2019), pp. 140–145. DOI: `10.1016/j.ctro.2019.04.019`.

[172] Martin von Siebenthal et al. “4D MR imaging of respiratory organ motion and its variability”. *Physics in Medicine & Biology* 52.6 (2007), pp. 1547–1564. DOI: `10.1088/0031-9155/52/6/001`.

[173] Anagha Deshmane et al. “Parallel MR imaging”. *Journal of Magnetic Resonance Imaging* 36.1 (2012), pp. 55–72. DOI: `10.1002/jmri.23639`.

[174] Kieren G. Hollingsworth. “Reducing acquisition time in clinical MRI by data undersampling and compressed sensing reconstruction”. *Physics in Medicine & Biology* 60.21 (2015), R297. DOI: `10.1088/0031-9155/60/21/R297`.

[175] Joop J. Van Vaals et al. ““Keyhole” method for accelerating imaging of contrast agent uptake”. *Journal of Magnetic Resonance Imaging* 3.4 (1993), pp. 671–675. DOI: `10.1002/jmri.1880030419`.

[176] Chang M. Hyun et al. “Deep learning for undersampled MRI reconstruction”. *Physics in Medicine & Biology* 63.13 (2018), p. 135007. DOI: `10.1088/1361-6560/aac71a`.

[177] Jo Schlemper et al. “dAUTOMAP: Decomposing AUTOMAP to achieve scalability and enhance performance”. *arXiv preprint* (2019). URL: `https://arxiv.org/abs/1909.10995v2`.

[178] Moritz Rabe et al. “Porcine lung phantom-based validation of estimated 4D-MRI using orthogonal cine imaging for low-field MR-Linacs”. *Physics in Medicine & Biology* 66.5 (2021), p. 055006. DOI: `10.1088/1361-6560/abc937`.

[179] Jamie R. McClelland et al. “Respiratory motion models: A review”. *Medical Image Analysis* 17.1 (2013), pp. 19–42. DOI: `10.1016/j.media.2012.09.005`.

[180] Elena H. Tran et al. “Evaluation of MRI-derived surrogate signals to model respiratory motion”. *Biomedical Physics & Engineering Express* 6.4 (2020), p. 045015. DOI: `10.1088/2057-1976/ab944c`.

[181] Marco Müller, Chiara Paganelli, and Paul Keall. “A phantom study to create synthetic CT from orthogonal two-dimensional cine MRI and evaluate the effect of irregular breathing”. *2018 40th Annual International Conference of the IEEE Engineering in Medicine and Biology Society (EMBC)*. 2018, pp. 4162–4165. DOI: `10.1109/EMBC.2018.8513236`.

[182] Hadi J. Fayad et al. “A generic respiratory motion model based on 4D MRI imaging and 2D image navigators”. *2012 IEEE Nuclear Science Symposium and Medical Imaging Conference Record (NSS/MIC)*. 2012, pp. 4058–4061. DOI: `10.1109/NSSMIC.2012.6551927`.

[183] Wendy Harris et al. “Accelerating volumetric cine MRI (VC-MRI) using undersampling for real-time 3D target localization/tracking in radiation therapy: a feasibility study”. *Physics in Medicine & Biology* 63.1 (2017), 01NT01. DOI: `10.1088/1361-6560/aa9746`.

[184] Bjorn Stemkens et al. “Image-driven, model-based 3D abdominal motion estimation for MR-guided radiotherapy”. *Physics in Medicine & Biology* 61.14 (2016), pp. 5335–5355. DOI: `10.1088/0031-9155/61/14/5335`.

[185] Jamie R. McClelland et al. "A generalized framework unifying image registration and respiratory motion models and incorporating image reconstruction, for partial image data or full images". *Physics in Medicine & Biology* 62.11 (2017), pp. 4273–4292. DOI: `10.1088/1361-6560/aa6070`.

[186] Yvette Seppenwoolde et al. "Precise and real-time measurement of 3D tumor motion in lung due to breathing and heartbeat, measured during radiotherapy". *International Journal of Radiation Oncology*Biology*Physics* 53.4 (2002), pp. 822–834. DOI: `10.1016/S0360-3016(02)02803-1`.

[187] Emily Johnstone et al. "Systematic Review of Synthetic Computed Tomography Generation Methodologies for Use in Magnetic Resonance Imaging–Only Radiation Therapy". *International Journal of Radiation Oncology*Biology*Physics* 100.1 (2018), pp. 199–217. DOI: `10.1016/j.ijrobp.2017.08.043`.

[188] Jing Cai et al. "Reproducibility of Interfraction Lung Motion Probability Distribution Function Using Dynamic MRI: Statistical Analysis". *International Journal of Radiation Oncology*Biology*Physics* 72.4 (2008), pp. 1228–1235. DOI: `10.1016/j.ijrobp.2008.07.028`.

[189] Keiichi Harada et al. "Evaluation of the motion of lung tumors during stereotactic body radiation therapy (SBRT) with four-dimensional computed tomography (4DCT) using real-time tumor-tracking radiotherapy system (RTRT)". *Physica Medica* 32.2 (2016), pp. 305–311. DOI: `10.1016/j.ejmp.2015.10.093`.

[190] Kristy K. Brock and Laura A. Dawson. "Point: Principles of Magnetic Resonance Imaging Integration in a Computed Tomography–Based Radiotherapy Workflow". *Seminars in Radiation Oncology* 24.3 (2014), pp. 169–174. DOI: `10.1016/j.semradonc.2014.02.006`.

[191] Hersh Chandarana et al. "Emerging role of MRI in radiation therapy". *Journal of Magnetic Resonance Imaging* 48.6 (2018), pp. 1468–1478. DOI: `10.1002/jmri.26271`.

[192] Nicholas Koch et al. "Evaluation of internal lung motion for respiratory-gated radiotherapy using MRI: Part I - correlating internal lung motion with skin fiducial motion". *International Journal of Radiation Oncology*Biology*Physics* 60.5 (2004), pp. 1459–1472. DOI: `10.1016/j.ijrobp.2004.05.055`.

[193] Jane M. Blackall et al. "MRI-based measurements of respiratory motion variability and assessment of imaging strategies for radiotherapy planning". *Physics in Medicine & Biology* 51.17 (2006), pp. 4147–4169. DOI: `10.1088/0031-9155/51/17/003`.

[194] Erik Tryggestad et al. "4D tumor centroid tracking using orthogonal 2D dynamic MRI: Implications for radiotherapy planning". *Medical Physics* 40.9 (2013), p. 091712. DOI: `10.1118/1.4818656`.

[195] David H. Thomas et al. "Initial clinical observations of intra- and interfractional motion variation in MR-guided lung SBRT". *The British Journal of Radiology* 91.1083 (2018), p. 20170522. DOI: `10.1259/bjr.20170522`.

[196] Davide Cusumano et al. "Predicting tumour motion during the whole radiotherapy treatment: A systematic approach for thoracic and abdominal lesions based on real time MR". *Radiotherapy and Oncology* 129.3 (2018), pp. 456–462. DOI: `10.1016/j.radonc.2018.07.025`.

[197] Jing Cai et al. "Estimation of Error in Maximal Intensity Projection-Based Internal Target Volume of Lung Tumors: A Simulation and Comparison Study Using Dynamic Magnetic Resonance Imaging". *International Journal of Radiation Oncology*Biology*Physics* 69.3 (2007), pp. 895–902. DOI: `10.1016/j.ijrobp.2007.07.2322`.

[198] Gerhard Laub and Randall Kroeker. "syngo TWIST for dynamic time-resolved MR angiography". *Magnetom Flash* 3 (2006). Accessed: 16th July 2021, pp. 92–95. URL: `https://www.siemens-healthineers.com/magnetic-resonance-imaging/options-and-upgrades/clinical-applications/twist`.

[199] Nobuyuki Otsu. "A Threshold Selection Method from Gray-Level Histograms". *IEEE Transactions on Systems, Man, and Cybernetics* 9.1 (1979), pp. 62–66. DOI: `10.1109/TSMC.1979.4310076`.

[200] James A. Shackleford, Nagarajan Kandasamy, and Gregory C Sharp. "On developing B-spline registration algorithms for multi-core processors". *Physics in Medicine & Biology* 55.21 (2010), pp. 6329–6351. DOI: `10.1088/0031-9155/55/21/001`.

[201] Stefanie Ehrbar et al. "ITV, mid-ventilation, gating or couch tracking - A comparison of respiratory motion-management techniques based on 4D dose calculations". *Radiotherapy and Oncology* 124.1 (2017), pp. 80–88. DOI: `10.1016/j.radonc.2017.05.016`.

[202] Simon J. Thomas et al. "An evaluation of the mid-ventilation method for the planning of stereotactic lung plans". *Radiotherapy and Oncology* 137 (2019), pp. 110–116. DOI: `10.1016/j.radonc.2019.04.031`.

[203] Cristina Garibaldi et al. "Translational and rotational localization errors in cone-beam CT based image-guided lung stereotactic radiotherapy". *Physica Medica* 32.7 (2016), pp. 859–865. DOI: `10.1016/j.ejmp.2016.05.055`.

[204] Stephanie Lang et al. "Clinical application of flattening filter free beams for extracranial stereotactic radiotherapy". *Radiotherapy and Oncology* 106.2 (2013), pp. 255–259. DOI: `10.1016/j.radonc.2012.12.012`.

[205] Z. Henry Yu et al. "A comparison of tumor motion characteristics between early stage and locally advanced stage lung cancers". *Radiotherapy and Oncology* 104.1 (2012), pp. 33–38. DOI: `10.1016/j.radonc.2012.04.010`.

[206] Nadya Shusharina et al. "The clinical target distribution: a probabilistic alternative to the clinical target volume". *Physics in Medicine & Biology* 63.15 (2018), p. 155001. DOI: `10.1088/1361-6560/aacfb4`.

[207] Jürgen Biederer et al. "Magnetic resonance imaging and computed tomography of respiratory mechanics". *Journal of Magnetic Resonance Imaging* 32.6 (2010), pp. 1388–1397. DOI: `10.1002/jmri.22386`.

[208] Yasmin Korzets Ceder et al. "Stereotactic body radiotherapy for central lung tumors, yes we can!" *Radiation Oncology* 13.77 (2018), pp. 1–7. DOI: `10.1186/s13014-018-1017-y`.

[209] Baiqiang Dong et al. "Comparison of the outcomes of stereotactic body radiotherapy versus surgical treatment for elderly ($\geq$ 70) patients with early-stage non-small cell lung cancer after propensity score matching". *Radiation Oncology* 14.195 (2019), pp. 1–11. DOI: `10.1186/s13014-019-1399-5`.

[210] Anders S. Bertelsen et al. "First clinical experiences with a high field 1.5 T MR linac". *Acta Oncologica* 58.10 (2019), pp. 1352–1357. DOI: `10.1080/0284186X.2019.1627417`.

[211] Tobias Finazzi et al. "Stereotactic MR-guided adaptive radiation therapy for peripheral lung tumors". *Radiotherapy and Oncology* 144 (2020), pp. 46–52. DOI: `10.1016/j.radonc.2019.10.013`.

[212] Hilâl Tekatli et al. "Stereotactic ablative radiotherapy (SABR) for early-stage central lung tumors: New insights and approaches". *Lung Cancer* 123 (2018), pp. 142–148. DOI: `10.1016/j.lungcan.2018.07.002`.

[213] John S. Ginn et al. "Multislice motion modeling for MRI-guided radiotherapy gating". *Medical Physics* 46.2 (2019), pp. 465–474. DOI: `10.1002/mp.13350`.

[214] Troels Bjerre et al. "Three-dimensional MRI-linac intra-fraction guidance using multiple orthogonal cine-MRI planes". *Physics in Medicine & Biology* 58.14 (2013), pp. 4943–4950. DOI: `10.1088/0031-9155/58/14/4943`.

[215] Matteo Seregni et al. "Motion prediction in MRI-guided radiotherapy based on interleaved orthogonal cine-MRI". *Physics in Medicine & Biology* 61.2 (2016), pp. 872–887. DOI: `10.1088/0031-9155/61/2/872`.

[216] Nikolai J. Mickevicius and Eric S. Paulson. "Simultaneous orthogonal plane imaging". *Magnetic Resonance in Medicine* 78.5 (2017), pp. 1700–1710. DOI: `10.1002/mrm.26555`.

[217] Nikolai J. Mickevicius and Eric S. Paulson. "Simultaneous acquisition of orthogonal plane cine imaging and isotropic 4D-MRI using super-resolution". *Radiotherapy and Oncology* 136 (2019), pp. 121–129. DOI: `10.1016/j.radonc.2019.04.005`.

[218] Noemi Garau et al. "A ROI-based global motion model established on 4DCT and 2D cine-MRI data for MRI-guidance in radiation therapy". *Physics in Medicine & Biology* 64.4 (2019), p. 045002. DOI: `10.1088/1361-6560/aafcec`.

[219] Gregor Remmert et al. "Four-dimensional magnetic resonance imaging for the determination of tumour movement and its evaluation using a dynamic porcine lung phantom". *Physics in Medicine & Biology* 52.18 (2007), N401–N415. DOI: `10.1088/0031-9155/52/18/n02`.

[220] Jürgen Biederer et al. "4D-Imaging of the Lung: Reproducibility of Lesion Size and Displacement on Helical CT, MRI, and Cone Beam CT in a Ventilated Ex Vivo System". *International Journal of Radiation Oncology*Biology*Physics* 73.3 (2009), pp. 919–926. DOI: `10.1016/j.ijrobp.2008.09.014`.

[221] Philipp Mann et al. "3D dosimetric validation of motion compensation concepts in radiotherapy using an anthropomorphic dynamic lung phantom". *Physics in Medicine & Biology* 62.2 (2016), pp. 573–595. DOI: `10.1088/1361-6560/aa51b1`.

[222] Katharina Niepel et al. "Feasibility of 4DCBCT-based proton dose calculation: An ex vivo porcine lung phantom study". *Zeitschrift für Medizinische Physik* 29.3 (2019), pp. 249–261. DOI: `10.1016/j.zemedi.2018.10.005`.

[223] Stephen B. Edge et al. *AJCC Cancer Staging Manual*. Vol. 7. Springer New York, 2010.

[224] Matthew Newville et al. *LMFIT: Non-Linear Least-Square Minimization and Curve-Fitting for Python*. 2014. DOI: `10.5281/zenodo.11813`.

[225] Ziji Wu et al. "Evaluation of deformable registration of patient lung 4DCT with subanatomical region segmentations". *Medical Physics* 35.2 (2008), pp. 775–781. DOI: `10.1118/1.2828378`.

[226] Vivien Delmon et al. "Registration of sliding objects using direction dependent B-splines decomposition". *Physics in Medicine & Biology* 58.5 (2013), pp. 1303–1314. DOI: `10.1088/0031-9155/58/5/1303`.

[227] Giorgia Meschini et al. "Virtual 4DCT from 4DMRI for the management of respiratory motion in carbon ion therapy of abdominal tumors". *Medical Physics* 47.3 (2020), pp. 909–916. DOI: `10.1002/mp.13992`.

[228] Timothy D. Keiper et al. "Feasibility of real-time motion tracking using cine MRI during MR-guided radiation therapy for abdominal targets". *Medical Physics* 47.8 (2020), pp. 3554–3566. DOI: `10.1002/mp.14230`.

[229] James Shackleford, Nagarajan Kandasamy, and Gregory C. Sharp. “Accelerating MI-based B-spline registration using CUDA enabled GPUs”. *International Conference on Medical Image Computing and Computer-Assisted Intervention*. 2012. DOI: `10.1007/978-3-642-33415-3`.

[230] Se An Oh et al. “Optimal gating window for respiratory-gated radiotherapy with real-time position management and respiration guiding system for liver cancer treatment”. *Scientific Reports* 9.1 (2019), pp. 1–6. DOI: `10.1038/s41598-019-40858-2`.

[231] Emily Heath, Jan Unkelbach, and Uwe Oelfke. “Incorporating uncertainties in respiratory motion into 4D treatment plan optimization”. *Medical Physics* 36.7 (2009), pp. 3059–3071. DOI: `10.1118/1.3148582`.

[232] Min Rao et al. “Dosimetric Impact of Breathing Motion in Lung Stereotactic Body Radiotherapy Treatment Using Image-Modulated Radiotherapy and Volumetric Modulated Arc Therapy”. *International Journal of Radiation Oncology*Biology*Physics* 83.2 (2012), e251–e256. DOI: `10.1016/j.ijrobp.2011.12.001`.

[233] Dirk Boye, Tony Lomax, and Antje Knopf. “Mapping motion from 4D-MRI to 3D-CT for use in 4D dose calculations: A technical feasibility study”. *Medical Physics* 40.6 (2013), p. 061702. DOI: `10.1118/1.4801914`.

[234] Mirko Marx et al. “Simulation of spatiotemporal CT data sets using a 4D MRI-based lung motion model”. *International Journal of Computer Assisted Radiology and Surgery* 9.3 (2014), pp. 401–409. DOI: `10.1007/s11548-013-0963-y`.

[235] Yuxin Yang et al. “A hybrid approach for fusing 4D-MRI temporal information with 3D-CT for the study of lung and lung tumor motion”. *Medical Physics* 42.8 (2015), pp. 4484–4496. DOI: `10.1118/1.4923167`.

[236] Joshua N. Freedman et al. “Synthetic 4D-CT of the thorax for treatment plan adaptation on MR-guided radiotherapy systems”. *Physics in Medicine & Biology* 64.11 (2019), p. 115005. DOI: `10.1088/1361-6560/ab0dbb`.

[237] Jinzhong Yang et al. “Technical Note: Density correction to improve CT number mapping in thoracic deformable image registration”. *Medical Physics* 46.5 (2019), pp. 2330–2336. DOI: `10.1002/mp.13502`.

[238] Evan Maynard et al. “Evaluation of accuracy and precision in polymer gel dosimetry”. *Medical Physics* 44.2 (2017), pp. 736–746. DOI: `10.1002/mp.12080`.

[239] Miriam Krieger et al. “Impact of internal target volume definition for pencil beam scanned proton treatment planning in the presence of respiratory motion variability for lung cancer: A proof of concept”. *Radiotherapy and Oncology* 145 (2020), pp. 154–161. DOI: `10.1016/j.radonc.2019.12.001`.

[240] Kenneth A. Wikström et al. “Evaluation of irregular breathing effects on internal target volume definition for lung cancer radiotherapy”. *Medical Physics* 48.5 (2021), pp. 2136–2144. DOI: `10.1002/mp.14824`.

[241] Borna Maraghechi et al. “Dose uncertainty and resolution of polymer gel dosimetry using an MRI guided radiation therapy system’s onboard 0.35 T scanner”. *Physica Medica* 73 (2020), pp. 8–12. DOI: `10.1016/j.ejmp.2020.04.004`.

[242] Cornelis Ph. Kamerling et al. “Real-time 4D dose reconstruction for tracked dynamic MLC deliveries for lung SBRT”. *Medical Physics* 43.11 (2016), pp. 6072–6081. DOI: `10.1118/1.4965045`.

[243] Keith Wachowicz, Bradley Murray, and B. Gino Fallone. "On the direct acquisition of beam's-eye-view images in MRI for integration with external beam radiotherapy". *Physics in Medicine & Biology* 63.12 (2018), p. 125002. DOI: `10.1088/1361-6560/aac5b9`.

[244] Xingyu Nie, Andreas Rimner, and Guang Li. "Feasibility of MR-guided radiotherapy using beam-eye-view 2D-cine with tumor-volume projection". *Physics in Medicine & Biology* 66.4 (2021), p. 045020. DOI: `10.1088/1361-6560/abd66a`.

[245] Fei Han et al. "Respiratory motion-resolved, self-gated 4D-MRI using Rotating Cartesian K-space (ROCK): Initial clinical experience on an MRI-guided radiotherapy system". *Radiotherapy and Oncology* 127.3 (2018), pp. 467–473. DOI: `10.1016/j.radonc.2018.04.029`.

[246] Davide Cusumano et al. "Artificial intelligence in magnetic resonance guided radiotherapy: Medical and physical considerations on state of art and future perspectives". *Physica Medica* 85 (2021), pp. 175–191. DOI: `10.1016/j.ejmp.2021.05.010`.

[247] Chenyang Shen et al. "An introduction to deep learning in medical physics: advantages, potential, and challenges". *Physics in Medicine & Biology* 65.5 (2020), 05TR01. DOI: `10.1088/1361-6560/ab6f51`.

[248] Maarten L. Terpstra et al. "Deep learning-based image reconstruction and motion estimation from undersampled radial k-space for real-time MRI-guided radiotherapy". *Physics in Medicine & Biology* 65.15 (2020), p. 155015. DOI: `10.1088/1361-6560/ab9358`.

[249] Laura I. Cerviño, Jiang Du, and Steve B. Jiang. "MRI-guided tumor tracking in lung cancer radiotherapy". *Physics in Medicine & Biology* 56.13 (2011), pp. 3773–3785. DOI: `10.1088/0031-9155/56/13/003`.

[250] Bryson Dietz et al. "Single patient convolutional neural networks for real-time MR reconstruction: a proof of concept application in lung tumor segmentation for adaptive radiotherapy". *Physics in Medicine & Biology* 64.19 (2019), p. 195002. DOI: `10.1088/1361-6560/ab408e`.

[251] Jihyun Yun et al. "Neural-network based autocontouring algorithm for intrafractional lung-tumor tracking using Linac-MR". *Medical Physics* 42.5 (2015), pp. 2296–2310. DOI: `10.1118/1.4916657`.

[252] Jihyun Yun et al. "An artificial neural network (ANN)-based lung-tumor motion predictor for intrafractional MR tumor tracking". *Medical Physics* 39.7 (2012), pp. 4423–4433. DOI: `10.1118/1.4730294`.

[253] Jihyun Yun et al. "First demonstration of intrafractional tumor-tracked irradiation using 2D phantom MR images on a prototype linac-MR". *Medical Physics* 40.5 (2013), p. 051718. DOI: `10.1118/1.4802735`.

[254] Paul Z. Y. Liu et al. "First experimental investigation of simultaneously tracking two independently moving targets on an MRI-linac using real-time MRI and MLC tracking". *Medical Physics* 47.12 (2020), pp. 6440–6449. DOI: `10.1002/mp.14536`.

[255] Vanessa Da Silva Mendes et al. "Dosimetric comparison of MR-linac-based IMRT and conventional VMAT treatment plans for prostate cancer". *Radiation Oncology* 16.1 (2021), pp. 1–12. DOI: `10.1186/s13014-021-01858-7`.

[256] Bradley M. Oborn et al. "Future of medical physics: Real-time MRI-guided proton therapy". *Medical Physics* 44.8 (2017), e77–e90. DOI: `10.1002/mp.12371`.

[257] Aswin Hoffmann et al. "MR-guided proton therapy: a review and a preview". *Radiation Oncology* 15 (2020), pp. 1–13. DOI: `10.1186/s13014-020-01571-x`.

[258] Bas W. Raaymakers, Alexander J. E. Raaijmakers, and Jan J. W. Lagendijk. "Feasibility of MRI guided proton therapy: magnetic field dose effects". *Physics in Medicine & Biology* 53.20 (2008), pp. 5615–5622. DOI: `10.1088/0031-9155/53/20/003`.

[259] Sonja M. Schellhammer et al. "Integrating a low-field open MR scanner with a static proton research beam line: proof of concept". *Physics in Medicine & Biology* 63.23 (2018), 23LT01. DOI: `10.1088/1361-6560/aaece8`.

[260] Chonnipa Nantavithya et al. "Phase 2 Study of Stereotactic Body Radiation Therapy and Stereotactic Body Proton Therapy for High-Risk, Medically Inoperable, Early-Stage Non-Small Cell Lung Cancer". *International Journal of Radiation Oncology*Biology*Physics* 101.3 (2018), pp. 558–563. DOI: `10.1016/j.ijrobp.2018.02.022`.

List of Publications

Peer-reviewed articles as first author in the scope of this thesis

M. Rabe, C. Paganelli, H. Schmitz, G. Meschini, M. Riboldi, J. Hofmaier, J. Dinkel, M. Reiner, K. Parodi, C. Belka, G. Landry, C. Kurz, and F. Kamp. "Continuous time-resolved estimated synthetic CTs for dose reconstruction of lung tumor treatments at the low field MR-Linac". *Manuscript in preparation*.

M. Rabe, C. Paganelli, M. Riboldi, D. Bondesson, M. J. Schneider, T. Chmielewski, G. Baroni, J. Dinkel, M. Reiner, G. Landry, K. Parodi, C. Belka, F. Kamp, and C. Kurz. "Porcine lung phantom-based validation of estimated real-time 4D-MRI using orthogonal cine MRI for low-field MR-Linacs". *Physics in Medicine & Biology* 66.5 (2021), p. 055006. DOI: `10.1088/1361-6560/abc937`.

M. Rabe, C. Thieke, M. Düsberg, S. Neppl, S. Gerum, M. Reiner, N. H. Nicolay, H. P. Schlemmer, J. Debus, J. Dinkel, G. Landry, K. Parodi, C. Belka, C. Kurz, and F. Kamp. "Real-time 4DMRI-based internal target volume definition for moving lung tumors". *Medical Physics* 47.4 (2020), pp. 1431–1442. DOI: `10.1002/mp.14023`.

Peer-reviewed topical review as co-author

C. Kurz, G. Buizza, G. Landry, F. Kamp, **M. Rabe**, C. Paganelli, G. Baroni, M. Reiner, P. J. Keall, C. A. T. van den Berg, and M. Riboldi. "Medical physics challenges in clinical MR-guided radiotherapy". *Radiation Oncology* 15.93 (2020), pp. 1–16. DOI: `10.1186/s13014-020-01524-4`.

Peer-reviewed articles as co-author

L. Nierer, F. Kamp, M. Reiner, S. Corradini, **M. Rabe**, O. Dietrich, K. Parodi, C. Belka, C. Kurz, and G. Landry. "Evaluation of an anthropomorphic ion chamber and 3D gel dosimetry head phantom at a 0.35 T MR-linac". *Under review*.

H. Schmitz, **M. Rabe**, G. Janssens, D. Bondesson, S. Rit, K. Parodi, C. Belka, J. Dinkel, C. Kurz, F. Kamp, and G. Landry. "Validation of proton dose calculation accuracy on scatter corrected 4D cone beam computed tomography using a porcine lung phantom". *Physics in Medicine & Biology* (2021), *In press*. DOI: `10.1088/1361-6560/ac16e9`.

S. Neppl, C. Kurz, D. Köpl, I. Yohannes, M. J. Schneider, D. Bondesson, **M. Rabe**, C. Belka, O. Dietrich, G. Landry, K. Parodi, and F. Kamp. "Gel measurement-based range evaluation for quality assurance of CBCT-based dose calculations in adaptive proton therapy". *Medical Physics* 48.8 (2021), pp. 4148–4159. DOI: `10.1002/mp.14995`.

D. Bondesson, A. Meijers, G. Janssens, S. Rit, **M. Rabe**, F. Kamp, K. Niepel, L. A. den Otter, S. Both, S. Brousmiche, J. Dinkel, C. Belka, K. Parodi, A. Knopf, C. Kurz, and G. Landry. "Anthropomorphic lung phantom based validation of in-room proton therapy 4D-CBCT image correction for dose calculation". *Zeitschrift für Medizinische Physik* (2020), *In press.* DOI: `10.1016/j.zemedi.2020.09.004`.

A. Meijers, C. S. Oria, J. Free, D. Bondesson, **M. Rabe**, K. Parodi, G. Landry, J. A. Langendijk, S. Both, C. Kurz, and A. C. Knopf. "Assessment of range uncertainty in lung-like tissue using a porcine lung phantom and proton radiography". *Physics in Medicine & Biology* 65.15 (2020), p. 155014. DOI: `10.1088/1361-6560/ab91db`.

F. Hueso-González, **M. Rabe**, T. A. Ruggieri, T. Bortfeld, and J. M. Verburg. "A full-scale clinical prototype for proton range verification using prompt gamma-ray spectroscopy". *Physics in Medicine & Biology* 63.18 (2018), p. 185019. DOI: `10.1088/1361-6560/aad513`.

Conference contributions as first author

M. Rabe, C. Paganelli, H. Schmitz, G. Meschini, M. Riboldi, J. Hofmaier, J. Dinkel, M. Reiner, K. Parodi, C. Belka, G. Landry, C. Kurz, and F. Kamp. "Experimental validation of time-resolved estimated synthetic CTs at 3.65 Hz for MR-guided lung tumor treatments". Oral presentation at the *Joint Conference of the ÖGMP, DGMP and SGSMP* (2021), virtual conference.

M. Rabe, C. Paganelli, H. Schmitz, G. Meschini, M. Riboldi, J. Hofmaier, J. Dinkel, M. Reiner, K. Parodi, C. Belka, G. Landry, C. Kurz, and F. Kamp. "Time-resolved estimated synthetic CTs based on orthogonal cine MRI for low-field MR-Linac treatments". Oral presentation at the *Virtual AAPM 63rd Annual Meeting & Exhibition* (2021), virtual conference.

M. Rabe, C. Paganelli, M. Riboldi, D. Bondesson, M. J. Schneider, T. Chmielewski, J. Dinkel, M. Reiner, G. Landry, K. Parodi, C. Belka, F. Kamp, and C. Kurz. "Experimental validation of generating 4 Hz 4D-MRI from orthogonal cine-MRI on a 0.35 T MR scanner". Oral presentation in the Young Investigator Session at the *Virtual 8th MR in RT Symposium* (2021), virtual conference.

M. Rabe, C. Paganelli, M. Riboldi, D. Bondesson, M. J. Schneider, T. Chmielewski, J. Dinkel, M. Reiner, G. Landry, K. Parodi, C. Belka, F. Kamp, and C. Kurz. "Erzeugung von geschätzten 4D-MRT basierend auf orthogonaler 2D cine-MRT für den MR-Linac – experimentelle Validierung mit einem Schweinelungenphantom". Oral presentation in the Young Investigator Forum at the *51. Jahrestagung der DGMP – digitaler Kongress* (2020), virtual conference.

M. Rabe, C. Paganelli, M. Riboldi, D. Bondesson, M. J. Schneider, T. Chmielewski, J. Dinkel, M. Reiner, G. Landry, K. Parodi, C. Belka, F. Kamp, and C. Kurz. "Experimental validation of estimated 4D-MRI for MR-guided radiotherapy based on orthogonal cine-MRI with a porcine lung phantom". Oral presentation at the *Joint AAPM | COMP Virtual Meeting* (2020), virtual conference.

M. Rabe, C. Thieke, M. Düsberg, S. Neppl, S. Gerum, M. Reiner, N. H. Nicolay, H. P. Schlemmer, J. Debus, J. Dinkel, G. Landry, K. Parodi, C. Belka, C. Kurz, and F. Kamp.

"Investigating the robustness of ITV and mid-ventilation concepts against interfractional changes using real-time 4D-MRI". Poster presentation at the *4D Treatment Workshop for Particle Therapy* (2019), Krakow, Poland.

M. Rabe, C. Thieke, M. Düsberg, S. Neppl, S. Gerum, M. Reiner, N. H. Nicolay, H. P. Schlemmer, J. Debus, J. Dinkel, G. Landry, K. Parodi, C. Belka, C. Kurz, and F. Kamp. "Geometrical analysis of interfractional changes of internal target volumes using real-time 4D-MRI of moving lung tumors". Oral presentation at the *7th MR in RT Symposium* (2019), Toronto, Canada.

M. Rabe, C. Thieke, M. Düsberg, S. Neppl, S. Gerum, M. Reiner, N. H. Nicolay, H. P. Schlemmer, J. Debus, J. Dinkel, G. Landry, K. Parodi, C. Belka, C. Kurz, and F. Kamp. "Real-time 4D-MRI-based geometrical analysis of interfractional changes of internal target volumes of moving lung tumors". Poster presentation at the *Biology-Guided Adaptive Radiotherapy (BiGART) 18th Acta Oncologica conference* (2019), Aarhus, Denmark.

M. Rabe, F. Hueso-González, T. Bortfeld, and J. M. Verburg. "Modeling the prompt gamma-ray emission in proton therapy — a key for absolute range verification". Oral presentation at the *49. Jahrestagung der DGMP und 21. Jahrestagung der ISMRM-DS* (2018), Nuremberg, Germany.

Conference contributions as co-author

Y. Xiong, **M. Rabe**, S. Corradini, C. Belka, M. Riboldi, G. Landry, and C. Kurz. "Intrafractional prostate motion analysis during MR-guided radiotherapy". Oral presentation at the *Joint Conference of the ÖGMP, DGMP and SGSMP* (2021), virtual conference.

H. Schmitz, **M. Rabe**, G. Janssens, D. Bondesson, S. Rit, K. Parodi, C. Belka, J. Dinkel, C. Kurz, F. Kamp, and G. Landry. "Experimental lung phantom based validation of scatter corrected 4D cone beam computed tomography for proton dose calculations". ePoster presentation at the *Joint Conference of the ÖGMP, DGMP and SGSMP* (2021), virtual conference.

S. Neppl, C. Kurz, D. Köpl, I. Yohannes, M. Schneider, D. Bondesson, **M. Rabe**, C. Belka, O. Dietrich, G. Landry, K. Parodi, and F. Kamp. "Measurement-based range evaluation for image quality assurance in adaptive proton radiotherapy". Oral presentation at the *Joint Conference of the ÖGMP, DGMP and SGSMP* (2021), virtual conference.

S. Neppl, C. Kurz, D. Köpl, I. Yohannes, M. Schneider, D. Bondesson, **M. Rabe**, C. Belka, O. Dietrich, G. Landry, K. Parodi, and F. Kamp. "Gel dosimetry-based range evaluation as quality assurance tool for adaptive proton therapy". Poster presentation at *ESTRO 2021* (2021), hybrid conference in Madrid, Spain and virtual.

H. Schmitz, **M. Rabe**, G. Janssens, J. Dinkel, S. Rit, K. Parodi, C. Belka, C. Kurz, F. Kamp, and G. Landry. "Scatter Correction of 4D Cone Beam Computed Tomography for Time-Resolved Proton Dose Calculation: Porcine Lung Phantom Validation". Oral presentation at the *Virtual AAPM 63rd Annual Meeting & Exhibition* (2021), virtual conference.

A. Meijers, C. Seller Oria, J. Free, D. Bondesson, **M. Rabe**, K. Parodi, G. Landry, J. A. Langendijk, S. Both, C. Kurz, and A. C. Knopf. "Range Uncertainty Assessment in Lung-Like

Tissue Using Porcine Lung and Proton Radiography". Oral presentation at the *Joint AAPM | COMP Virtual Meeting* (2020), virtual conference.

F. Kamp, S. Neppl, **M. Rabe**, L. Nierer, C. Kurz, M. Reiner, and C. Belka. "MR-guided radiotherapy at the LMU in Munich: Preliminary studies". Oral presentation at the *European Congress of Medical Physics (ECMP)* (2018), Copenhagen, Denmark.

F. Hueso-González, **M. Rabe**, T. Ruggieri, T. Bortfeld, and J. M. Verburg. "Development of a Clinical Prototype for Range Verification in Proton Therapy based on Prompt Gamma-Ray Spectroscopy". Oral presentation and conference proceeding at the *IEEE Nuclear Science Symposium and Medical Imaging Conference (NSS/MIC)* (2018), Sydney, Australia.

J. M. Verburg, T. Ruggieri, P. Botas, E. Cascio, F. Hueso-González, **M. Rabe**, and T. Bortfeld. "Clinical Translation of Prompt Gamma-Ray Spectroscopy for In Vivo Proton Range Verification". Oral presentation at the *AAPM 59th Annual Meeting & Exhibition* (2017), Denver, Colorado, USA.

Acknowledgments

I feel fortunate to have stumbled across the field of Medical Physics and Radiotherapy during the Summer Student Program at GSI more than seven years ago. I appreciate working in this exciting research field and found pursuing a Ph.D. in this area – with all its ups and downs – very interesting and rewarding. Over the last few years, I have received tremendous support from many people that I would like to acknowledge at this point.

First of all, I would like to thank Prof. Katia Parodi for supervising my thesis, for her valuable advice and input for my research projects, and for supporting my academic development. I am truly impressed by your commitment, dedication, and passion for the field of Medical Physics research.

I want to thank Prof. Daniela Thorwarth for taking the time to review this thesis as the second referee.

Next, I would like to express my deep gratitude to Dr. Florian Kamp and Dr. Christopher Kurz for not only being supervisors but mentors throughout these years. Thank you for all your help, guidance, and advice, for all the scientific and non-scientific discussions, for investing countless hours in the many – sometimes successful, sometimes failed – experiments, for involving me in research projects beyond my own, for the opportunity to pursue my ideas, for supporting my academic career and for all the good times and jokes. My highlight during my Ph.D. – the measurement campaign in Cleveland, Ohio – would not have been possible or that much fun without you. When looking back, I am astonished by what I have learned over the last few years and what you have taught me, and I am looking forward to continuing working with you in the future.

I highly value working in this interdisciplinary field in a clinical environment, in close contact with clinical medical physicists, physicians, and RTTs, and having the opportunity to conduct experiments at the MR-Linac, linacs, and the CT scanner. I want to thank Prof. Claus Belka, Dr. Michael Reiner, and PD Dr. Dr. Christian Thieke for providing this inspiring research setting and for giving me the opportunity to participate in this many conferences, summer schools, and workshops, which I found to be very valuable experiences.

I had the great pleasure to work in a young and dynamic research group led by Prof. Guillaume Landry, whom I would like to thank for his valuable ideas and feedback on my Ph.D. projects. Thank you for supporting my academic development and for giving me the opportunity to continue working on exciting research projects in this group. I am very much looking forward to the upcoming years as a postdoctoral researcher.

An essential aspect of research that I enjoy very much is collaborating with other academic institutions and industrial partners. None of my research projects would have been possible without the contribution and support of my collaborators. I want to express my thanks to Prof. Julien Dinkel for sharing the unique 4D-MRI datasets and for lending us the porcine lung phantom, to Dr. Moritz Schneider and Dr. David Bondesson for their technical support with the MRI scanners and the porcine lung phantom, to Prof. Marco Riboldi for helping us to conceptualize the research projects and for all the scientific advice and input, to Dr. Chiara Paganelli for sharing her code and for helping to further develop the propagation method, and to Dr. Giorgia Meschini for her support on the tresCT research project and for the time when we shared an office. Furthermore, Dr. Thomas Chmielewski, Tim Lin, Dr.

Thomas Cull, and Dr. Michael Thompson are acknowledged for their organizational and technical support during the measurement campaign at ViewRay Inc. in Cleveland, Ohio.

Thank you to all my current and former colleagues at the Department of Radiation Oncology at the University Hospital, LMU Munich, who are or were working in our research group and in the clinic, and majorly contributed to making these past few years memorable and really enjoyable. Thank you all for the coffee breaks, discussions, and for all the fun times we shared. In particular, I would like to thank my long-time fellow Ph.D. students and co-authors Jan Hofmaier, Sebastian Neppl, and Henning Schmitz, and the MR-Linac team, including Lukas Nierer, Vanessa da Silva Mendes, Dr. Helmut Weingandt, and Dr. Katrin Straub for all the technical support for the experiments and their scientific input and contribution.

This work was supported by the German Research Foundation (DFG) within the Research Training Group GRK 2274 *Advanced Medical Physics for Image-Guided Cancer Therapy* and the Friedrich-Baur-Stiftung. I am grateful for having been a member of the GRK and having had the chance to participate in all the different seminars, summer schools, retreats, and courses where I learned about many different Medical Physics topics beyond radiotherapy. For these great experiences, I would like to thank the coordination and management team of the GRK2274, Karin Kleinstück, Veronica Bodek, and PD Dr. Dr. Christian Thieke, as well as my fellow doctoral candidates within the GRK.

Special thanks go to all the butchers in the Landkreis Starnberg and near Cleveland, Ohio, who helped me with my special request for “porcine lungs without tissue damages and the trachea still attached” and for supporting our research projects in this way.

On a more personal note, I would like to thank my family for all their love and continuous support throughout my Ph.D. studies.

Thank you, Oskari Pakari, for convincing me early on to pursue a Ph.D. after my Master’s studies and for taking the time to proofread this thesis.

Last but not least, I would like to deeply thank my wife Johanna Rabe for all the love, support, and understanding, who was always there for me in good times and bad times, after long working days, during stressful times before deadlines, for celebrations of the successes, and who even tolerated keeping porcine lungs in our fridge and freezer. Dear Lina, thank you for enriching my life beyond measure and for all your love.